Periodic Modelling Solutions for Railway Track Structures

Angie Catalina Lamprea Pineda

Submitted in accordance with the requirements for the degree of
Doctor of Philosophy

The University of Leeds

School of Civil Engineering

Institute for High Speed Rail and System Integration

June, 2024

Declaration

I confirm that the work submitted is my own and that appropriate credit has been given where reference has been made to the work of others. The information contained in the Chapters of this thesis has been previously published in research articles written by the author of this thesis who also appears as the lead author in all published papers. The research has been supervised and guided by Professor David P. Connolly who appears as the co-author in all the published articles. All the materials included in this document are of the author's intellectual ownership. Contributions of all authors and publication's status is indicated below:

Paper No. 1

Details:	**A.C. Lamprea-Pineda**[1], D.P. Connolly[2] and M.F.M. Hussein[3], 'Beams on elastic foundations – A review of railway applications and solutions', in Transportation Geotechnics, vol. 33, 100696, 2022.
Type:	Journal paper
Status:	Published
Authors' Contribution:	1. Methodology, Software, Validation, Investigation, Writing – Original Draft, Writing – Review and Editing. 2. Conceptualization, Methodology, Software, Validation, Resources, Writing – original Draft, Writing – review and editing, Supervision, Funding acquisition. 3. Conceptualization, Methodology, Software, Supervision, Writing – Review and Editing.
Thesis' chapters:	• Chapter 2. Railway Track Modelling. • Chapter 3. Periodic approaches for railway track simulation.

Paper No. 2

Details: **A. C. Lamprea-Pineda**[1], D. P. Connolly[2], A. Castanheira-Pinto[3], M. F.M. Hussein[4], P. Alves-Costa[5], and P. K. Woodward[6], 'On railway track receptance', in Soil Dynamics and Earthquake Engineering, vol. 177, 108331, 2024.

Type: Journal paper

Status: Published

Authors' Contribution:
1. Methodology, Software, Validation, Investigation, Writing – Original Draft, Writing – Review and Editing.
2. Conceptualization, Methodology, Software, Validation, Resources, Writing – original Draft, Writing – review and editing, Supervision, Funding acquisition.
3. Conceptualization, Software, Supervision.
4. Conceptualization, Writing – Review and Editing.
5. Conceptualization, Writing – Review and Editing.
6. Supervision.

Thesis' chapters:
- Chapter 1. Introduction.
- Chapter 4. Development of a Periodic Track Model.
- Chapter 5. DPM model verification.
- Chapter 6. Model refinement for receptance applications.
- Chapter 7. Sensitivity Study.

Paper No. 3

Details: **A.C. Lamprea-Pineda**[1], C. Charoenwong[2], P. Chumyen[3], D.P. Connolly[4], P. K. Woodward[5], and P. Alves-Costa[6], 'Track-ground coupling techniques for the analysis of railway track vibrations', 27th International Congress on Sound and Vibration, 11-16 July, 2021.

Type: Conference paper

Status: Published

Authors' Contribution:
1. Methodology, Software, Validation, Investigation, Writing – Original Draft, Writing – Review and Editing.
2. Conceptualization.
3. Conceptualization.
4. Methodology, Software, Validation, Resources, Writing – review and editing, Supervision, Funding acquisition.
5. Supervision.
6. Software, Conceptualization.

Thesis' chapters:
- Chapter 2. Railway Track Modelling.
- Chapter 3. Periodic approaches for railway track simulation.

Paper No. 4

Details:	**A.C. Lamprea-Pineda**[1], D.P. Connolly[2], P.K. Woodward[3], M.F.M. Hussein[4], and P. Alves-Costa[5], 'Semi-analytical study of train induced ground borne-vibrations effects', 28th International Congress on Sound and Vibration (Singapore), 04-05 August, 2022.
Type:	Conference paper
Status:	Published
Authors' Contribution:	1. Methodology, Software, Validation, Investigation, Writing – Original Draft, Writing – Review and Editing. 2. Conceptualization, Methodology, Software, Validation, Resources, Writing – review and editing, Supervision, Funding acquisition. 3. Supervision. 4. Conceptualization, Methodology, Supervision. 5. Software, Conceptualization.
Thesis' chapters:	• Chapter 2. Railway Track Modelling. • Chapter 3. Periodic approaches for railway track simulation.

Paper No. 5

Details:	**A.C. Lamprea-Pineda**[1], D. P. Connolly[2], M.F.M. Hussein[3], P. Alves-Costa[4], and P. K. Woodward[5], 'Modelling the Critical Speed Amplification Effect on Railway Track-Ground Systems', The fifth International Conference on Railway Technology: Research, Development and Maintenance (Montpellier, France), 22-25 August, 2022.
Type:	Conference paper
Status:	Published
Authors' Contribution:	1. Methodology, Software, Validation, Investigation, Writing – Original Draft, Writing – Review and Editing. 2. Conceptualization, Methodology, Software, Validation, Resources, Writing – review and editing, Supervision, Funding acquisition. 3. Conceptualization, Methodology, Supervision. 4. Software, Conceptualization. 5. Supervision.
Thesis' chapters:	• Chapter 2. Railway Track Modelling. • Chapter 3. Periodic approaches for railway track simulation.

Paper No. 6

Details:	**A. C. Lamprea-Pineda**[1], A. Castanheira-Pinto[2], P. Alves-Costa[3], P. K. Woodward[4], M. F.M. Hussein[5], and D. P. Connolly[6], 'Railway track structural dynamics via periodic approaches', COMPDYN 2023, 9th ECCOMAS Thematic Conference on Computational Methods in Structural Dynamics and Earthquake Engineering (Athens, Greece), 12-14 June, 2023.
Type:	Conference paper
Status:	Published
Authors' Contribution:	1. Methodology, Software, Validation, Investigation, Writing – Original Draft, Writing – Review and Editing. 2. Conceptualization, Software, Supervision. 3. Conceptualization, Writing – Review and Editing. 4. Supervision. 5. Conceptualization, Writing – Review and Editing. 6. Conceptualization, Methodology, Software, Validation, Resources, Writing – original Draft, Writing – review and editing, Supervision, Funding acquisition.
Thesis' chapters:	• Chapter 4. Development of a Periodic Track Model. • Chapter 5. DPM model verification.

Acknowledgments

I take this opportunity to express my gratitude to my main supervisor, Professor **David Connolly,** for his constant guidance and support throughout my PhD research. His motivation, suggestions, expertise and experience have been instrumental in shaping my research. Thank you for your invaluable support and for providing me with this remarkable opportunity – none of this would have been possible without you.

I would also like to extend my heartfelt thanks to Professor **Peter Woodward** for serving as my second supervisor and contributing significantly to my research. I am grateful to the **University of Leeds** for sponsoring my studies and to the **Leverhulme Trust UK (PLP-2016-270)** for their financial support.

My appreciation goes to Professor **Mohammed M.H. Hussein** from Qatar University. Thank you for your continuous support and for generously sharing your time and knowledge with me. My sincere thanks to the University of Porto team, especially Professor **Pedro Alves-Costa** and **Alexandre Castanheira-Pinto**. Your expertise has been a fundamental part of my research.

I would also like to express my gratitude to my mentor and advisor, Professor **Nikolaos Nikitas**, and the **George Earle Heavy Structures laboratory team**. I greatly appreciate your support during my lab work.

I extend my thanks to my colleagues **Chonlatis Charoenwong**, **Panudech Chumyen**, and **Chutiphon Moranon** for their help and support during my PhD journey.

Special thanks to my friends **Pablo**, **Johan**, **Ana**, **Rodrigo** and **Tatiana**, my small latin/hyspanic family in Leeds. Your friendship, cheerfulness and support have been invaluable. Thanks to **Angela**, **Cindy** and **Carlos**, my friends outside the UK, who were always there for a call despite the time zone difference.

Lastly, I am incredibly thankful to **my family** for encouraging me in all of my pursuits and inspiring me to follow my dreams. You are all my role models.

Abstract

Understanding dynamic track stiffness is crucial for addressing railway dynamics issues such as ground-borne noise, track dynamics, and rolling noise. This parameter is often analysed through its inverse, receptance, which is the ratio of the structure's deformations to a unit force. Studies on receptance offers valuable information for assessing the track's mechanical behaviour, developing control strategies, and optimising the design of new systems.

Despite its importance, most comprehensive studies on railway track components typically employ analytical approaches. While these methods simplify modelling, they often lack the complexity needed to accurately capture the structure's response and cannot fully replicate 3D wave propagation effects. Although numerical approaches provides more flexibility, they are computationally intensive. Alternatively, periodic strategies, offer a promising solution by reducing computational effort while accurately modelling the structure's behaviour. Thus, this research employs a periodic strategy to develop a computational tool for calculating the dynamic performance of ballasted railway track structures.

First, several modelling strategies for the track's behaviour study are review and compared based on their ability to simulate different railway engineering problems. This comparison allowed for the selection of a periodic formulation, which can be coupled with perfectly matched layers to replicate wave propagation effects. Using this periodic approach, the model is refined for receptance applications by considering the effects of two common modelling assumptions: beam-on-elastic foundation and symmetry. The findings indicate that neglecting wave propagation in subgrade-earthwork layers results in errors of approximately $80\% - 300\%$ at frequencies below 200 Hz, and around 30% between $200 - 440$ Hz. Additionally, assuming symmetry along the track centreline overlooks certain track bending modes, leading to errors of about 20% up to 1000 Hz. This new model facilitates a parametric study on ballasted track components, providing insights into their typical frequency ranges and enabling the formulation of new empirical equations.

Table of Contents

List of Figures

List of Tables

List of Symbols

The following lists presents an overview of the most commonly adopted abbreviations, notations used throughout the thesis.

Abbreviations

1D	One-dimensional
2D	Two-dimensional
2.5D	Two-and-a-half-dimensional
3D	Three-dimensional
FE(M)	Finite Element (Method)
BE(M)	Boundary Element (Method)
BOEF	Beam on Elastic Foundation
DOF	Degree-of-Freedom
DPM	Direct Periodic Method
TLM	Thin Layer Method
PML	Perfectly Matched Layer
TMM	Transfer Matrix Method
FFT	Fast Fourier Transformation
IFFT	Inverse Fast Fourier Transformation
FRA	Federal Railroad Administration
PSD	Power Spectral Density
DSM	Dynamic Stiffness Matrix
USP	Under-Sleeper Pad
UIC□	Rail model standard type □ of International Union of Railways

General Notations

x	Space coordinate in the longitudinal direction
y	Space coordinate in the vertical direction
z	Space coordinate in the transversal direction

$s = \{x, y, z\}$	Global-Cartesian coordinates
$\tilde{s} = \{\tilde{x}, \tilde{y}, \tilde{z}\}$	Local-Cartesian coordinates
β_x	Wavenumber in the longitudinal direction or Fourier image of x
β_y	Wavenumber in the vertical direction or Fourier image of y
β_z	Wavenumber in the transversal direction or Fourier image of z
t	Instance of time
f	Circular frequency
f_{subgrade}	Subgrade frequency of resonance
$f_{\text{full-track}}$	Full-track frequency of resonance
f_{rail}	Rail frequency of resonance
f_{railpad}	Railpad frequency of resonance
f_{sleeper}	Sleeper frequency of resonance
$f_{\text{pin-pin}}$	Pin-pin frequency of resonance
ω	Angular frequency
$i = \sqrt{-1}$	Imaginary unit or number
$\square(s, t)$	Function $\square$ in the space-time-domain
$\hat{\square}(s, \omega)$	Function $\square$ in the space-frequency-domain
$\overline{\square}(\beta, t)$	Function $\square$ in the wavenumber-time-domain
$\hat{\overline{\square}}(\beta, \omega)$	Function $\square$ in the wavenumber-frequency-domain
$\breve{\square}(s, \beta, \omega)$	Function $\square$ in the space-wavenumber-frequency-domain
$\delta(\square)$	Dirac Delta or impulse function with respect to variable $\square$
$\displaystyle\sum_{j=1}^{j=j_{\text{end}}} \square_j$	Sum of $\square_j$, from $j = 1$ to $j = j_{\text{end}}$
$\dot{\square}$	First derivative of function $\square$
$\ddot{\square}$	Second derivative of function $\square$
$\square^{\text{IV}}$	Fourth derivative of function $\square$
$\partial^n \square / \partial \square^n$	n^{th}-order partial derivative of function $\square$ with respect to variable $\square$
$\{\square\}$	Vector $\square$
$[\square]$	Matrix $\square$
$\{u\}$	Vector of displacements (and rotations)
$\{F\}$	Vector of forces (and moments)
$[D]$	Dynamic Stiffness Matrix or DSM
$[K]$	Stiffness matrix
$[M]$	Mass matrix
$[C]$	Damping matrix
$\alpha(\square)$	Receptance or compliance function
$Y(\square)$	Mobility or admittance function
$\chi(\square)$	Accelerance or inertance function
Ω	Global or periodic-domain
$\tilde{\Omega}$	Generic or reference cell domain
d	Periodic length or thickness of the reference cell

General Material Parameters

E	Young's modulus
I	Second moment of inertia
ρ	Density
m	Mass (per unit length when continuous)
ν	Poisson's ratio
k	Real stiffness (per unit length when continuous)
k^*	Complex stiffness (per unit length when continuous)
G	Shear modulus
A	Cross Sectional area
c	Damping coefficient
ξ	Damping ratio
η	Loss factor or hysteretic damping

Train Model Parameters

$F(\square)$	Force function
P	Force magnitude (per unit length when continuous)
v	Train speed
ϖ	Driving oscillating frequency
C_{HZ}	Hertzian constant
K_{HZ}	Hertzian spring or contact stiffness
$r(\square)$	Roughness function
C^T	Track compliance
C^V	Vehicle compliance
r	Rail irregularity, roughness or unevenness

Track Model Parameters

$\square_t$	Combined track parameters $\square$
$\square_{tb}$	Track bed parameter $\square$
$\square_r$	Rail parameter $\square$
$\square_{rp}$	Railpad parameter $\square$
$\square_s$	Sleeper parameter $\square$
$\square_b$	Ballast parameter $\square$
$\square_{sb}$	Sub-ballast parameter $\square$
$\square_e$	Embankment parameter $\square$
l_x	Element length in the longitudinal direction
l_y	Element length in the vertical direction
l_z	Element length in the transversal direction

Elastodynamic Parameters

$\square_{sg}$ Subgrade parameter
C_s Shear wave speed
C_p Longitudinal or dilatational wave speed

Chapter 1
Introduction

1.1 Background and Motivation

The dynamic characteristics of a railway track play an important role in its interaction with rolling stock and are closely connected to short term and long term behaviour (settlement) [1,2]. Thus, dynamic stiffness is key parameter reflecting the entire system's quality and performance, which depends on its component's individual and collective behaviour. Track stiffness can be divided into two categories: static and dynamic. In both cases, it is expressed as the ratio between the applied force and the corresponding deformation of the structure [3–5]. However, the force and its resulting deflection are static in the former instance, whereas dynamic and frequency-dependent in the second case. Although both are relevant for track design and maintenance, dynamic stiffness is a key parameter for understanding railway dynamics issues. These include ground-borne noise and vibration at low-frequencies, track dynamics problems at mid-frequencies, and rolling noise issues at high-frequency ranges [6,7] – see **Figure 1-1**.

Dynamic stiffness is commonly studied via its inverse, 'receptance' (also referred to as 'compliance', 'dynamic flexibility' or 'force-displacement transfer function'). Receptance analysis enables the characterisation of railway systems and their components in terms of frequencies influencing the track behaviour. These frequencies are typically referred to as frequencies of resonance and are associated to a 'mode' of the structural vibration. Receptance can be used to identify various structural properties such as stiffness, damping and potentially component dimensions, as well as changes in these parameters and their overall relationship with the global system behaviour. This information has the potential to be used for assessing the mechanical behaviour of the track structure, define control strategies for several railway issues, and optimise design of new systems.
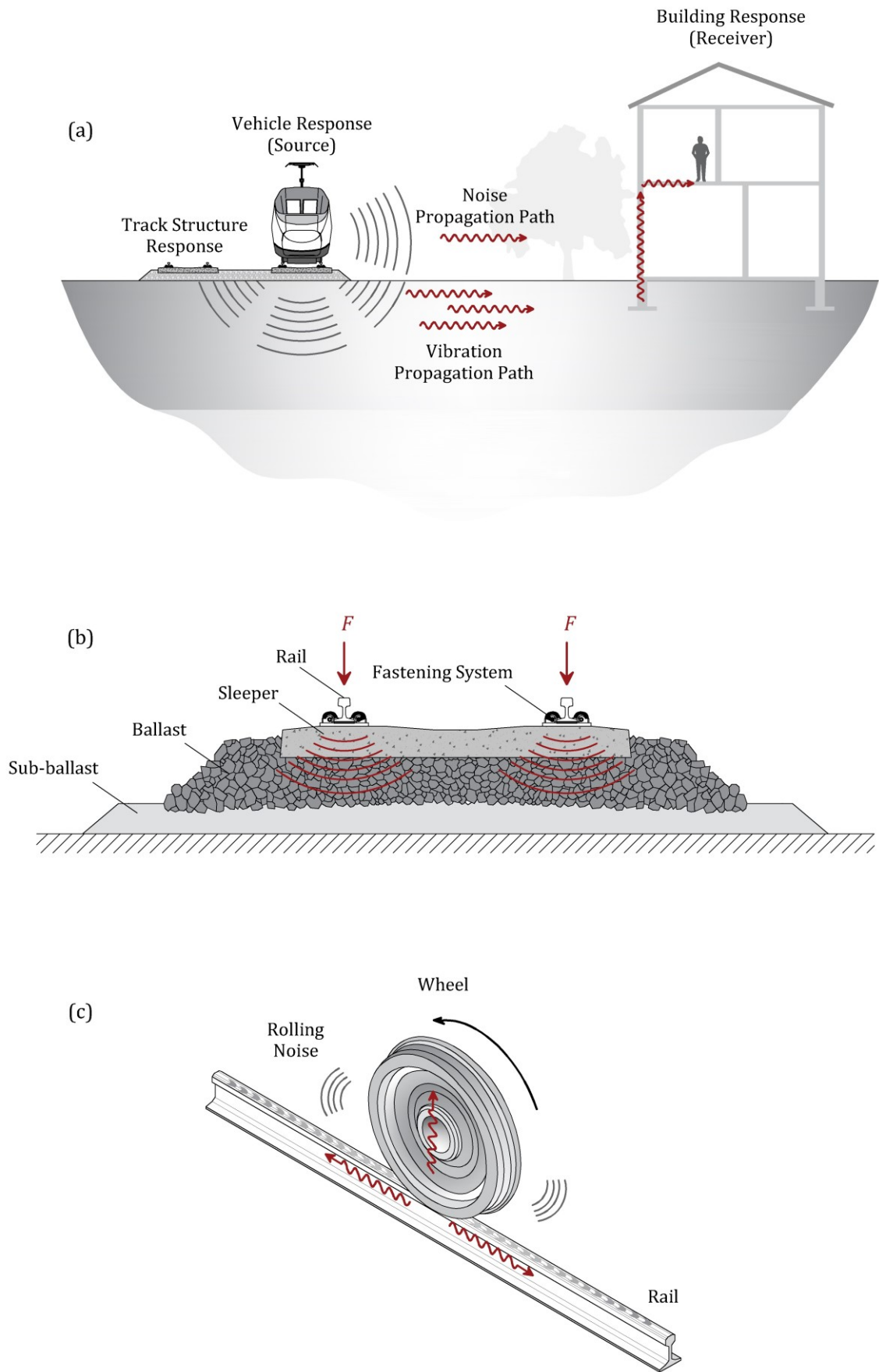
Figure 1-1. Typical railway dynamic issues: (a) ground-borne noise and vibration, (b) track dynamics, and (c) rolling noise

Receptance studies have proposed analytical, semi-analytical and numerical approaches to assess the track structure and its components. Perhaps the most comprehensive sensitivity studies on railway track components' behaviour have been conducted using analytical methods, such as Beam on Elastic Foundation (BOEF) formulations. These studies have examined the effect of the excitation position, number of layers, element formulations (beam and damping models), material properties, and support effect [8–11]. This range of analysis is possible due to the simplified modelling approach, which characterises the track system components as beams, a series of elastic elements, and lumped masses. These studies have shown that analytical methods require a certain degree of complexity in their simulation, including a minimum of two layers and discrete supports, in order to be able to capture the main vibration modes [9].

Analytical approaches are unable to fully capture 3D wave propagation effects because they are limited in the structural elements they can be formed from. Therefore, they are well suited to cases where the assumption of a rigid foundation is applicable (e.g. directly-fixed railway track in a tunnel) or noise modelling where vibration is confined within the upper track structure. In an attempt to approximate 3D ground wave propagation, [12] implemented flexibility matrices in the track sub-structure, defined in the frequency-domain, thus enabling subgrade simulation. Different track support models resting on homogeneous and layered-homogenous mediums were compared with simpler analytical models. Results demonstrated the importance of modelling the ground at frequencies below 400 Hz, yielding a receptance result that the viscoelastic foundation of the analytical model could not replicate.

Nevertheless, receptance analyses conducted via analytical or semi-analytical strategies rely on several important approximations of the railway system. For instance, railpad complex geometries are usually simplified into viscoelastic point supports – elements described using minimal material parameters (i.e. stiffness and damping only, in absence of geometrical dimensions); track layers are often combined with equivalent parameters used instead; supporting ground is often simulated via springs-in-series assumptions; among other track components' behaviour ignored during simulation that affects the overall dynamic response.

Beam on Elastic Foundation (BOEF) approaches are widely employed when studying railway track dynamics. Most commonly they assume the track response can be approximated using a single-layer continuous beam supported by springs-in-series (representing the rails and the underlying track layers, respectively), thus, offering a straightforward and computationally efficient approach.

The underlying formulation can be extended to incorporate discrete sleeper effect and additional track components. The former is achieved by assuming the support arrangement is constant in the train passage direction, i.e. the fundamental continuous BOEF formulation includes a certain degree of periodicity. In the second case, additional excitation mechanisms are included within the BOEF model through lumped masses and elastic layers. Despite these, it is difficult to accurately capture 3D wave propagation within the track, which is crucial for simulating receptance.

To address this, numerical approaches such as the Finite Element (FE) and boundary element (BE) methods have also been used to compute receptance. Numerical techniques can be solved in both frequency and time-domain [13]. In the former, receptance is computed by enforcing Fourier transformations during the formulation of the algorithms. Approaches in this domain are widely employed in simulations since they provide a straightforward algebraic formulation. In contrast, time-domain methodologies are solved via iterative integration schemes [14,15]. Following the latter methodology, [16] conducted an extensive investigation of the dynamic behaviour of the track, assessing the support effect, material properties, and the location of excitation and observation points on different track types, and comparing the results against field tests. This numerical time-domain model was then combined with sensitivity studies on ballasted tracks to derive equations of the resonant frequencies in [17]. Similarly, [18] used a 3D FEM solved in the time-domain to compare two different railpad elements: viscoelastic and solid. However, as the frequency range of interest started at 300 Hz, the soil behaviour was not included in the simulation. This sensitivity analysis on railpads was extended in [19], including parameters such as the toe load, temperature effect, aging conditions, and railpad type. Additionally, [20] studied the wheel-rail impact problem in the time-domain by comparing two wheel-track interaction models, the beam and continuum FE. The former used a discretised Timoshenko beam in the rail and sleeper formulation, whereas the latter employed 3D solid elements. Although both cases simulated railpad and ballast via spring elements, the rail is supported at a single point in the beam model and over an area in the solid model. Overall, findings indicated that solid elements can approximate receptance more accurately than the beam model. The frequency range was broader in this case, ranging from 10 to 3000 Hz and the subgrade was not included in the formulation.

Although numerical methods potentially provide more flexibility to model the true geometry of a railway track compared to analytical and semi-analytical methods, they are computationally demanding. In order to reduce the computational effort while still delivering accurate approximations of the structure's behaviour, periodic strategies are a promising solution. These approaches take advantage of the periodic or repetitive characteristics of the system, thus reducing the domain under

consideration and, in turn, reducing the computational resources and increasing the computational efficiency.

1.2 Aim and Objectives

This research aims to develop a computational tool to calculate the dynamic performance of ballasted periodic railway track structures.

For the fulfilment of the project aim, the following objectives are proposed:

1. Conduct a review of literature of the different railway modelling strategies for continuous and periodic Beams on Elastic Foundations.

2. Develop a 3D periodic numerical model of railway track structures subjected to static, quasi-static and dynamic excitations.

3. Optimise the new 3D periodic numerical approach for receptance calculation.

4. Analyse the receptance characteristics of high-speed ballasted tracks.

1.3 Novelty of the Research

The original contributions of this work can be summarised in **Table 1-1**.

Current state of the art	Research project advancement
Objective 1: Existing BOEF review papers include general and brief information, typically evaluating only one track modelling and analysis strategy. Furthermore, current periodic strategies have not been properly reviewed. Assessment is usually focused on one periodic strategy and other methods are briefly evaluated.	Review will be performed from the simplest BOEF formulation to more complex models and analysis strategies. Although the review will consider brief information for each revised strategy, it will include several current techniques that will be compared through simple BOEF models. Additionally, a periodic modelling revision will be performed. It will include an evaluation between methods. Finally, a critical assessment of the modelling methods for BOEF and periodic formulations will be provided depending

on depending on their ability to simulate different railway engineering problems.

This comprehensive review of methodologies and the study of various railway effects allowed for the selection of a periodic formulation suitable for studying standstill receptance applications for discrete ballasted railway tracks.

Objective 2: Typically, railway track analyses assume an invariant domain in a given direction, i.e., a periodic behaviour. However, this feature is often ignored, leading to longer simulations.

Generally, studying the entire track is computationally inefficient, as it requires analysing a large number of elements. To mitigate high computational demands, numerical models often limit the track structure to a small Section, reducing the number of elements at the cost of accuracy.

While the periodic approach has been studied before, it remains a relatively new technique. Current 3D periodic modelling has primarily focused on examining the dynamic behaviour of the track-soil structure and its validation through measured data and other strategies, without further assessment

Among the various periodic approaches, the 2.5D Finite Element (FE) method has been widely used for railway track simulations [21–25]. This technique simplifies the structure into a 2D slice and then recovers the full 3D response using Fourier transformations. While this offers computational benefits, the 2.5D method only meshes the cross-Section of the structure and assumes homogeneous behaviour along its length, failing to capture discrete rail support effects.

An alternative to the 2.5D approach is the 3D FE wave propagation technique, which can simulate discrete support behaviour [26–28]. This method discretises the structure into a 3D slice and uses Floquet transformations solved through Eigenvalue (modal) analysis. Although this approach allows for flexible geometry, it requires extracting Eigenmodes and implementing additional strategies to optimise the

The periodic nature of ballasted tracks will be utilised to construct and analyse a 3D numerical model, reducing the study domain to a single slice, also known as unit or reference cell, for computational efficiency.

For this purpose, the Direct Periodic Method (DPM) will be employed. The DPM is a highly efficient technique able to retrieve the total structure response via a direct inversion and the application of Floquet's theorem.

Additionally, the DPM will be combined with 3D Finite Element (FE) and Perfectly Matched Layer (PML) techniques (3D DPM-FE-PML). This combination allows for the inclusion of complex geometries, additional track components' mechanical behaviour, and wave propagation effects.

Also, as the wave propagation effect within the ground will be simulated via PML, the simulation is further optimise since responses very far away from the track are not considered and only a small soil domain is required in the simulation.

solution process, which is computationally demanding.

Objective 3: Receptance calculation models presented in the literature often make assumptions regarding the track to improve computational efficiency. One common assumption is the track support can be modelled as a rigid boundary condition rather than a flexible condition representative of the underlying earthworks. Another is that symmetry can be assumed along the track centreline, meaning both rails are excited rather than one, which is unlikely to be the case when field testing.

The 3D DPM-FE-PML will be refined to study track bed support and symmetry conditions, thereby closely approximating real railway infrastructure and receptance testing conditions. This refinement will enable a new numerical approach specifically designed for receptance calculation on ballasted tracks.

In the case of support conditions, both track resting on a semi-infinite ground and on a rigid support will be compared. Alternatively, when studying symmetric conditions, receptance will be compared for fully-symmetric and asymmetric loading conditions.

Note that although only receptance will be analysed, the selected periodic formulation can be expanded to replicate various effects, such as moving quasi-static and dynamic contributions, far-field effects, long term deformations, etc.

Objective 4: Perhaps the most comprehensive sensitivity studies on railway track components' behaviour have been conducted using analytical methods, such as BOEF. These formulations rely on simplified modelling approaches that must incorporate a certain level of complexity to capture the main vibration modes [9]. However, analytical approaches are limited in their ability to fully capture 3D wave propagation effects due to restrictions in the structural elements they can model.

Although some periodic approaches have studied receptance issues – e.g. [21,29], these approaches are relatively new and no comprehensive analysis have been performed using these techniques.

A sensitivity study on the most common high-speed railway ballasted track components will be performed. For this, the refined 3D DPM-FE-PML model tailored to receptance of ballasted tracks will be employed.

Then, using this information, new knowledge regarding the typical frequency ranges associated to each track component and new empirical equations, will be obtained.

Table 1-1. Novelty of the research

1.4 Outline of the Thesis

The thesis can be divided into four Sections: (1) theory, (2) methodology, (3) main model, and (4) simulations and assessment. The first Section introduces the research context, outlining its motivation, objectives, and relevant literature.

Section 2 details the selected approach, the Direct Periodic Method (DPM), and its validation. Using the presented methodology, Section 3 presents a new numerical model designed to receptance applications. Finally, Section 4 describes the simulations conducted with the previous model, assessing the results and presenting novel insights concerning receptance applications. **Figure 1-2** shows the visual outline of the thesis structure.

Chapter 1 provides a brief introduction to the problems faced in simulating railway infrastructure and the motivations for this work. It then describes the main research aim, objectives, and contributions, followed by the outline of the thesis.

Chapter 2 presents a technical review of various BOEF approaches and their application to railway engineering problems. It discusses solutions and practicalities of different BOEF approaches focusing on track, track-ground, and train-track dynamic behaviour. Then, using BOEF models, benchmark solutions for two common railway engineering problems: railway track dynamics and railway ground-borne vibration. Finally, this Chapter outlines the challenges associated with BOEF approaches and how they can be overcome with periodic and FEM techniques.

Chapter 3 introduces the framework of periodic approaches. It reviews the literature on various solutions for periodic track structures, including considerations for semi-periodic structures. Additional examples of applications for two common railway problems are presented. The challenges associated with the fundamental periodic approach are then introduced. Finally, the studied periodic approaches are compared against the analytical and semi-analytical techniques introduced in Chapter 2, and the solution techniques are classified and ranked according to their suitability for the study of railway engineering problems.

Chapter 4 describes the development of a track-ground model based on the Direct Periodic Method (DPM), a computationally efficient approach that takes advantage of the periodic nature of the railway structure. The proposed model integrates 3D Finite Element (FE) and Perfectly Matched Layer (PML) techniques (i.e. 3D FE-PML-DPM), thus allowing considering complex geometries, mechanical behaviours of additional track components, and wave propagation.

Chapter 5 validates the model's capability to replicate the railway track behaviour under various excitation conditions and the propagation effects of waves within the subgrade component. For this purpose, four numerical verifications are presented: track model under non-moving excitations, under moving excitations, moving dynamic and multiple-axle contributions, and the effect of ground vibrations.
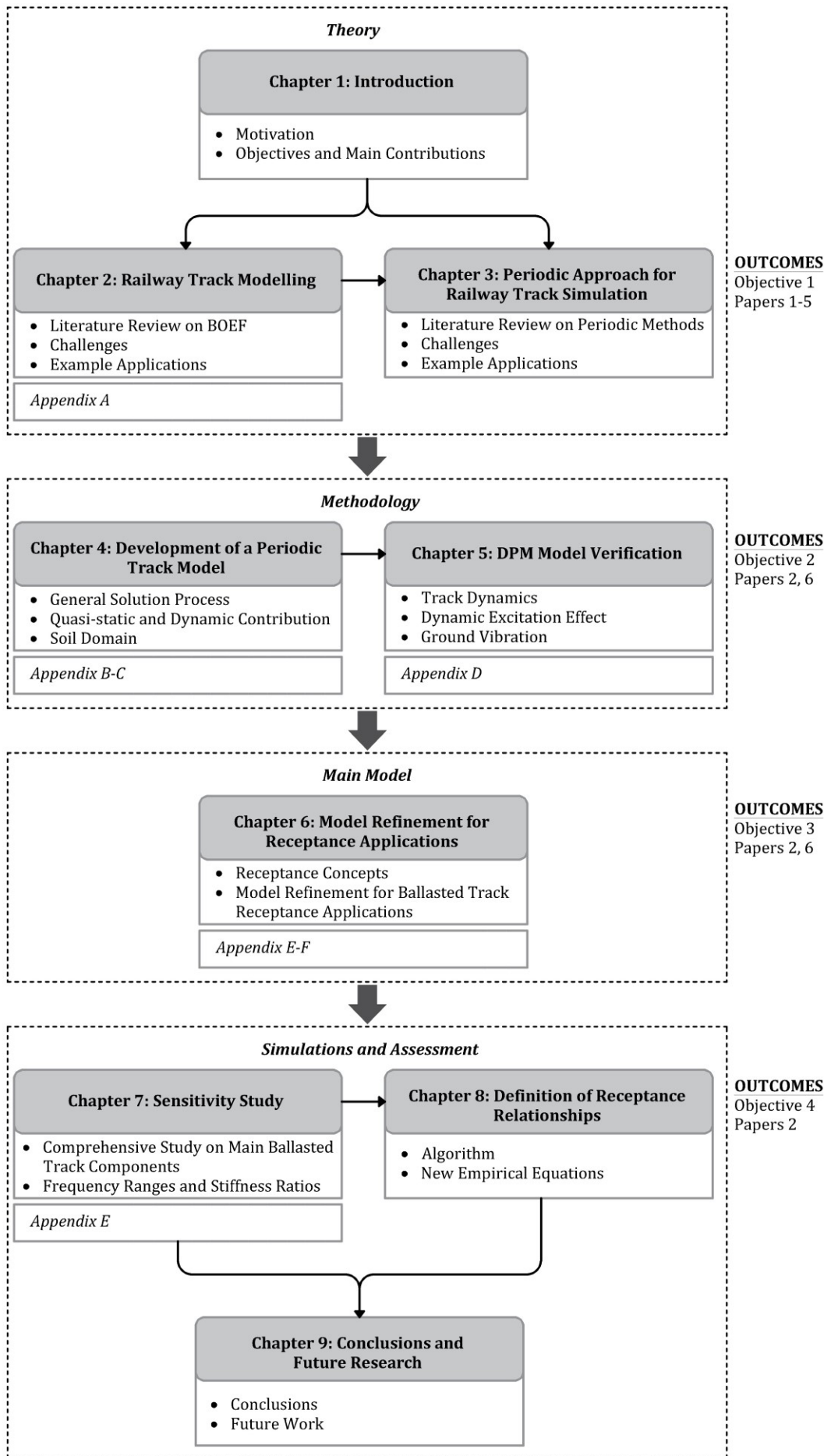
Figure 1-2. Thesis structure. Visual outline

Chapter 6 introduces the theory of receptance, an important quantity that affects the track's dynamic response under moving trains and noise and vibration characteristics. Then, the model presented in Chapter 4 is refined by incorporating common track modelling assumptions: track bed support, and symmetry conditions. Thus introducing a new numerical approach tailored to receptance calculation on ballasted tracks. The refined model is described by a stiff track supported by well-compacted earthworks, representing the characteristics of a modern high-speed track.

Chapter 7 employs the refined model proposed in Chapter 6 to perform a sensitivity study on the most common ballasted track components. These include the effects of rail Sections, railpad stiffness, sleeper material, Under-Sleeper Pads (USP) application, ballast stiffness and thickness, embankment simulation, and subgrade stiffness. Multiple permutations considered for this comprehensive analysis are compared against the base case described by stiff track properties typical of modern high-speed track structures. Finally, new knowledge is presented regarding the typical frequency ranges and stiffness ratios associated with each track component.

Chapter 8 employs the sensitivity study information from Chapter 7 to formulate new empirical equations tailored for receptance applications. For this, a three-step procedure is developed, which involves (1) defining initial relationships using power regression methods, (2) identifying the crucial parameters influencing the response, and (3) formulating the final empirical equations through optimization techniques. Finally, equation results are compared with those obtained via sensitivity analysis.

Chapter 9 summarises the results of this thesis and provides recommendations for future work.

Chapter 2
Railway Track Modelling

2.1 Introduction

The behaviour of railway tracks is commonly studied using Beam on Elastic Foundation (BOEF) theory. Initially proposed by Winkler [30], the general approach typically uses beams to simulate the response of railway rails, supported by spring and dashpot elements that represent the combined effect of the various track components and the ground. The simplicity of the BOEF approach provides a straightforward and efficient computational framework for understanding railway track behaviour.

Thus, this Chapter presents a technical review of a wide variety of BOEF approaches and their application to railway engineering problems. First, Section 2.2 explores a range of BOEF modelling strategies. Next, Section 2.3 discuss solutions and practicalities of different BOEF approaches with a focus on track, track-ground, and train-track dynamic behaviour. Then, using BOEF models, Section 2.4 presents benchmark solutions for two common railway engineering problems: railway track dynamics and railway ground-borne vibration. Finally, Section 2.5 outlines the challenges associated to BOEF approaches, and Section 2.6 highlights the conclusions for this Chapter.

2.2 BOEF Modelling Strategies

2.2.1 Track Models

2.2.1.1 Track Types

BOEF theory allows for the modelling of a range of track types, including ballasted and slab. A typical single-layer BOEF model uses a beam to simulate the rail, and a single layer of springs and dashpots to represent the track support [9,31,32]. However, additional degrees of freedom can also be simulated by adjusting the rail support conditions. For instance, a two-layer model can be used to simulate ballasted track sleepers, via lumped continuous or discrete masses [8,9]. Alternatively, a second beam element, similar to the rail, can be used to simulate a slab track (e.g. concrete or asphalt), by taking its bending stiffness into account when calculating track response [33–36].

2.2.1.2 Track Structure

The traditional Winkler formulation [30] employed in the single-layer BOEF track model simulates the rail as a continuous beam and the track substructure as an elastic foundation, with the latter represented via evenly distributed linear springs [37]. Typically, this elastic foundation is homogeneous and accounts for multiple components via a combination of their properties, calculated using a 'springs-in-series' approach. For instance, the stiffness foundation can be employed to model the effect of the different track components: railpad, sleepers, ballast, sub-ballast and soil [31,38–41]. **Eq.** (2-1) shows the track system stiffness k_t obtained by combining the stiffness of the railpad k_{rp} and the track bed k_{tb}, using the springs-in-series approach [34,37,42,43].

$$\frac{1}{k_t} = \frac{1}{k_{rp}} + \frac{1}{k_{tb}}$$

(2-1)

This assumption is limiting because multiple components are approximated using a single layer. Therefore, to account for more complex track behaviour, the BOEF can be extended to have an increased number of layers – see **Figure 2-1**.

A second track layer – e.g. **Figure 2-1**(b), allows the model to more accurately simulate railpads, sleepers and ballast [8,34,44,45]. In this, the railpads and ballast are commonly represented as elastic or viscoelastic massless components (i.e. springs or springs-dashpots elements, respectively). Additional flexibility can

further be achieved using a three-layer model – see **Figure 2-1**(c), in which the ballast behaviour is modelled as a mass element with dashpots and springs – accounting for the damped elastic behaviour of the ballast and the subgrade [46–48].

Replacing the traditional Euler-Bernoulli beam formulation with a Timoshenko beam [49] allows for the capture of shear deformation and rotational inertia effects, which are important at higher frequencies [10,50,51].

Regardless of the number of layers or beam formulation employed, it should be noted that models with homogenous or continuous support conditions struggle to simulate the discrete nature of the rail supports [7,9,12,52]. This discrete behaviour is also important when modelling track structures resting on both rigid and soft foundations at high frequencies.

Shortcomings of continuously supported models include difficulties in providing accurate results near the so-called 'pinned-pinned' resonance frequency. This is important because the magnitude of response around this frequency decreases as the vehicle speed increases [53], thus requiring the simulation of the discrete effect of the sleepers [8,45] – see **Figure 2-2**. Nevertheless, when studying the dynamic effect of railway track at lower frequencies, both models provide similar predictions, regardless of the vehicle speed. In general, continuous support models can effectively predict the track response at frequencies below $\approx$ 500 Hz [9].

2.2.2 Foundation Models

Considering a purely elastic Winkler formulation [30] to represent the track support, this model simulates the foundation properties through a series of independent and closely spaced linear springs. It also assumes that the reaction at a point on the foundation is proportional to the deflection at that point only [54–56]. **Eq.** (2-2) describes the load-deflection relationship for a Winkler foundation:

$$p(x,y) = ku(x,y) \qquad\qquad (2\text{-}2)$$

where p is the pressure, k is the foundation coefficient (i.e. the spring stiffness), and u is the deflection. Although it is capable of modelling the foundation behaviour, the Winkler approach is unable to represent the continuous nature of a railway track. This is due to the linear one-parameter assumption involved in its formulation (only considering stiffness in the pressure-deflection relation) [38,56–58]. **Figure 2-3**(a) shows the localised deflection due to an external load applied on a Winkler foundation – note how the model fails to describe a continuous response.
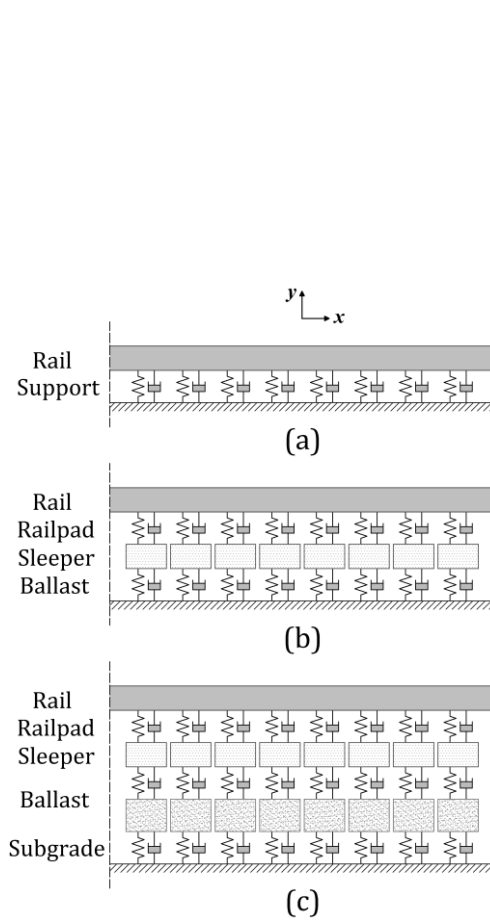
Figure 2-1. Continuously supported railway track models: (a) Single-layer model, (b) Two-layer model, and (c) Three-layer model
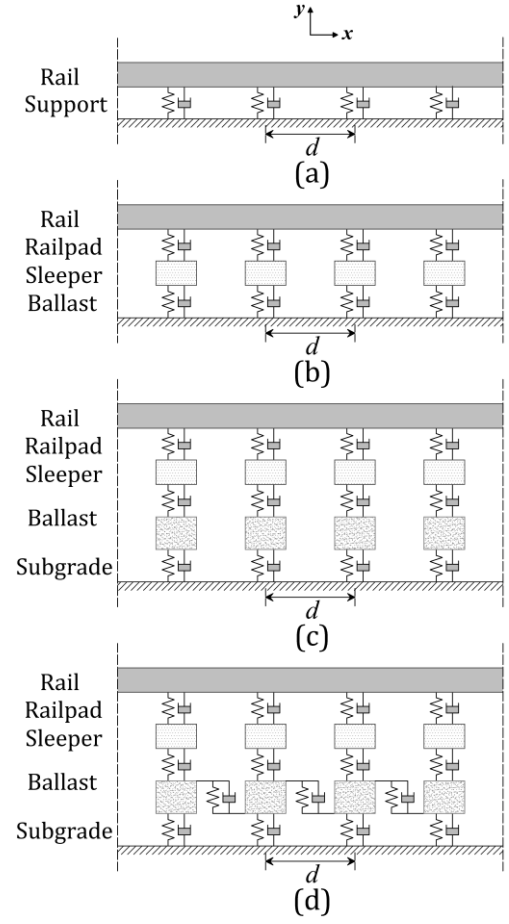
Figure 2-2. Discretely supported railway track models: (a) Single-layer model, (b) Two-layer model, (c) Three-layer model, and (d) Three-layer model with horizontal damped elastic layer

Alternatively, interaction between the linear elastic springs can be simulated through a stretched elastic membrane. This upgraded version of the Winkler model is known as the Filonenko-Borodich foundation [59]. Thus, accounting for the additional parameter in the model described in **Eq.** (2-2), the load-deflection relation is [55,56,59]:

$$p(x,y) = ku(x,y) - T\nabla^2 u(x,y) \qquad (2-3)$$

where T is the constant tension force of the membrane and $\nabla^2 = \frac{\partial^2}{\partial x^2} + \frac{\partial^2}{\partial y^2}$ is a differential operator defined in x and y, also known as the Laplace operator. **Figure 2-3**(b) shows the coupling effect introduced by the inclusion of the membrane. This effect between the linear springs can also be achieved through the foundation model proposed by Hetényi [38]. This model considers foundation interaction through an elastic plate of flexural rigidity D [38,56–58], as shown in **Figure 2-3**(c). The force-deflection relationship is therefore defined by:

$$p(x,y) = ku(x,y) + D\nabla^2\nabla^2 u(x,y) \qquad (2\text{-}4)$$

where $\nabla^2\nabla^2$ is the bi-harmonic or bi-Laplacian operator ∇^4 [60,61]. The Pasternak foundation [62] assumes that the interaction of the linear spring is obtained through a shear layer of unit thickness [37,55,56] – see **Figure 2-3**(d). Through the inclusion of this layer in the Winkler foundation model – **Eq.** (2-2), the Pasternak approach allows for both the representation of the compressibility and the shear stiffness of the foundation [57]. Therefore, assuming a homogenous and isotropic foundation, the force-deflection relationship includes the shear deformation effect G:

$$p(x,y) = ku(x,y) - G\nabla^2 u(x,y) \qquad (2\text{-}5)$$

Additionally, a third parameter can be included to expand the Pasternak formulation, incorporating an additional layer of elastic springs (Kerr [56,63]). Thus, the coupling of both layers is achieved through the shear layer placed in the middle of the model. **Eq.** (2-6) gives the differential equation of motion:

$$\left(1 + \frac{k_1}{k_2}\right)p = \frac{G}{k_1}\nabla^2 p + k_2 u - G\nabla^2 u \qquad (2\text{-}6)$$

where k_1 and k_2 are the spring constants for the first and second layer, respectively – see **Figure 2-3**(e). In general, this foundation allows for more modelling flexibility due to the third parameter (i.e. the additional layer) in its formulation [55,57,58].
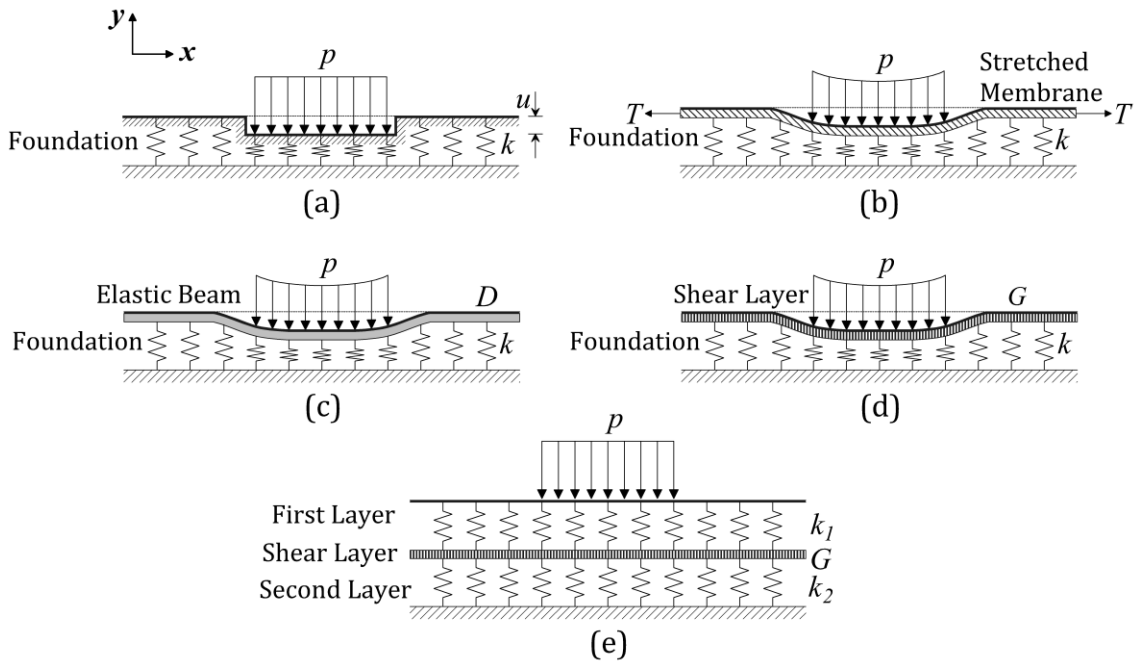
Figure 2-3. Mechanical foundation models: (a) Winkler foundation [30], (b) Filonenko-Borodich foundation [59], (c) Hetényi foundation [38], (d) Pasternak foundation [62], and (e) Kerr foundation [56,63]

Overall, improvement of the single-parameter foundation model proposed by Winkler, in which only the stiffness foundation k is considered, is achieved by including various foundation parameters into its equation of motion – see **Eq.** (2-2), thus allowing for different effects to be simulated. For instance, the two- and three-parameter models allow for continuity of the elastic foundation through simulation of the additional material behaviours, such as tension T (Filonenko-Borodich [59]), flexural rigidity D (Hetényi [38]), and shear deformation G (Pasternak [62] and Kerr [56,63]).

Further improvement of the previous foundation models can be obtained through the inclusion of damping behaviour. To do so, the formulation is extended to include a viscoelastic foundation, by placing viscous elements (i.e. dashpots) in a variety of arrangements [55,56], which allow for damping of the model response. **Figure 2-4**(a) shows the parallel arrangement of elastic and viscous elements, known as the Kelvin-Voight model. **Figure 2-4**(b) depicts the Maxwell model, in which the elements are placed in series. Further, different combinations of both parallel and series arrangements are shown in **Figure 2-4**(c)-(d). These are known as Zener, Poynting-Thomson type 1 and Poynting-Thomson type 2, respectively [55–57,64].

The effect of track subgrade can also be combined with the above approaches [65–68]. For example, the foundation can be simulated as an elastic and continuum medium with infinite dimensions. The equations of motion in the different directions x, y and z of the half-space are defined as [31,55,69,70]:

$$(\lambda + G)\frac{\partial \Theta}{\partial x_i} + G\nabla^2 u_i + F_i = \rho\frac{\partial^2 u_i}{\partial t^2}, \quad i = 1,2,3$$

$$\Theta = \sum_{j=1}^{j=3}\frac{\partial u_j}{\partial x_j}, \qquad \nabla^2 = \sum_{j=1}^{j=3}\frac{\partial^2}{\partial x_j^2} \tag{2-7}$$

where u_i and F_i are the displacement and force per volume in the axis x_i, respectively. λ and G are the Lamé constants, Θ is the volumetric strain, and ρ is the density of the material. Furthermore, **Eq.** (2-7) gives the equations of motion of the system in the three axis $x_{i=1} = x$, $x_{i=2} = y$ and $x_{i=3} = z$.

(a)   (b)   (c)   (d)   (e)
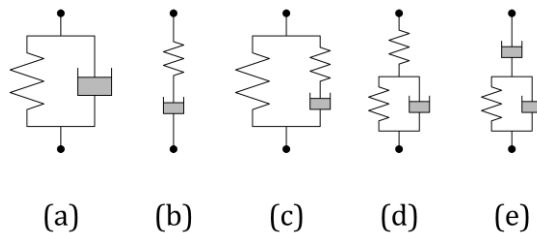
Figure 2-4. Spring-dashpot arrangement: (a) Kelvin–Voight model, (b) Maxwell model, (c) Zener model, (d) Poynting-Thomson model type 1, and (e) Poynting-Thomson type 2

Half-space foundation models are useful for simulating wave propagation in the supporting soil, which the previous models cannot accurately describe solely using springs. This wave propagation is important to consider when modelling ground vibration problems, and when train speeds are high relative to the track-ground 'critical velocity' [71–74]. When analysing such problems it is important to simulate the effect of soil layering [66,68,71,75]. For example, **Figure 2-5**(a) shows a homogenous half-space with boundaries extending to infinity (i.e. $-\infty < x < \infty, -\infty < y < \infty, 0 < z < \infty$), while **Figure 2-5**(b) shows a three layered soil with the lowest layer extending to infinity.

(a)   (b)
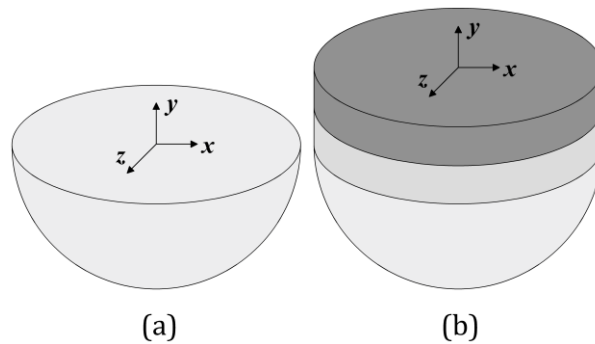
Figure 2-5. Continuous foundation model: (a) Homogeneous half-space model, and (b) Multi-layer half-space

2.2.3 Vehicle Models

Train excitation is a combination of both quasi-static and dynamic loading. Quasi-static loading is due to the self-weight of the rolling stock and acts as a load sliding on the rail surface. Therefore the deflection bowl shape is identical in shape and magnitude regardless of position along an infinite rail. At speeds below the critical velocity, the deflection response is relatively uniform and symmetrical, and wave propagation does not occur – see **Figure 2-6**(a). However, above this speed perturbations are generated in the wake of the load [71,72,74,76], which can be magnified significantly due to superposition if multiple axles are considered [35,77] – as seen in the trailing oscillations behind the loads ($t < 0$ s) in **Figure 2-6**(b). Note that the maximum deflections at the time instant t_l, are related to the position x_l of the lth axle and the speed v – i.e. the speed-space-time relationship is enforced: $t_l = x_l/v$.

In contrast, dynamic loading is due to the interaction of rolling-stock with the track [78,79]. On a perfectly smooth track with uniform support, a vehicle's suspension and mass are not excited and the train glides across the track, thus inducing a track response identical to the quasi-static case. However, in reality, irregularities (e.g. rail unevenness) excite the vehicle system, resulting in dynamic excitation, which is amplified with increasing train speed [80]. These dynamic train-track interactions

effects result in increased dynamic contact forces [81,82], increased noise generation [10], and vibration amplification in both the track and ground [82].
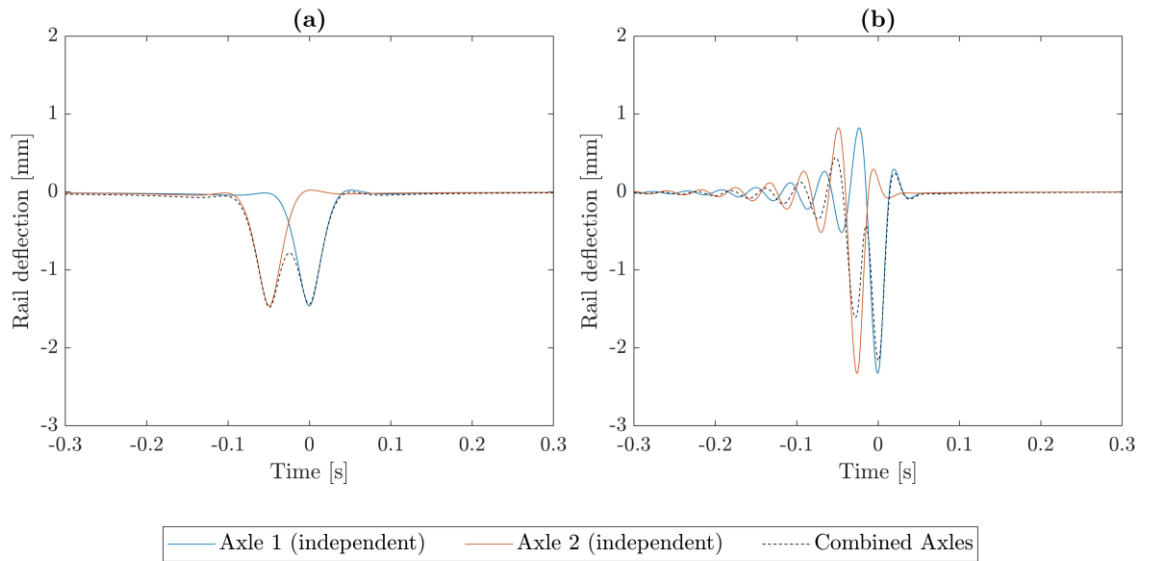
Figure 2-6. Track response due to quasi-static excitation: (a) below the critical speed, and (b) above the critical speed

Considering the differing characteristics of quasi-static and dynamic excitation, if the system is considered linear elastic, each excitation mechanism can be modelled separately and then added to obtain the combined response [78,83]. This is shown in **Figure 2-7** considering a sprung mass of 2003 kg on a BOEF. Notice that when the track unevenness is high, the dynamic component of the excitation becomes increasingly dominant.
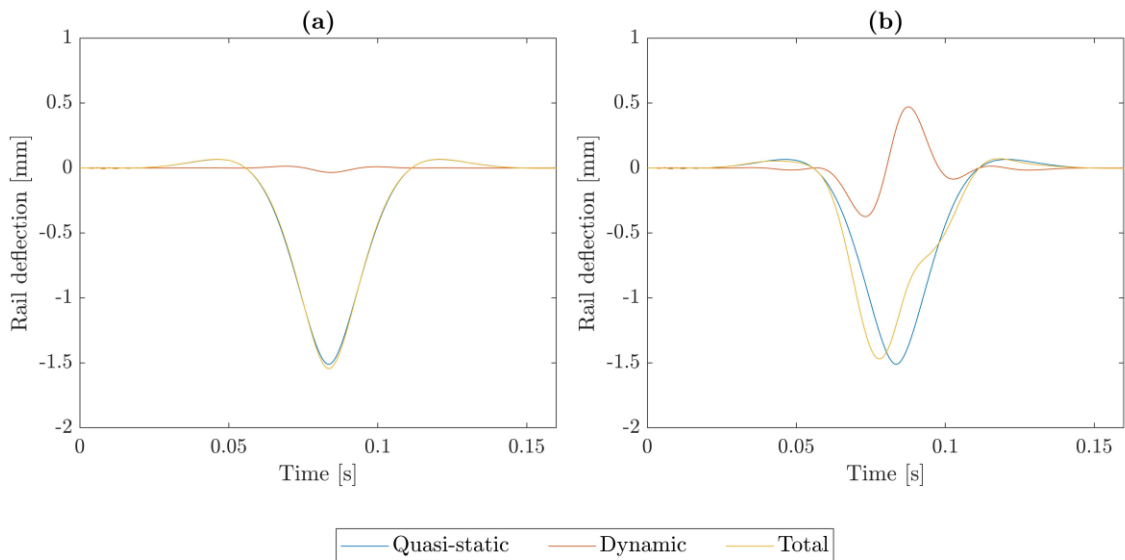
Figure 2-7. Track response due to quasi-static and dynamic excitation for: (a) low unevenness, and (b) high unevenness

2.2.3.1 Moving Points

Perhaps the simplest representation of track loading is achieved assuming a stationary ($v = 0$) and constant load F [13,31], see **Figure 2-8**.
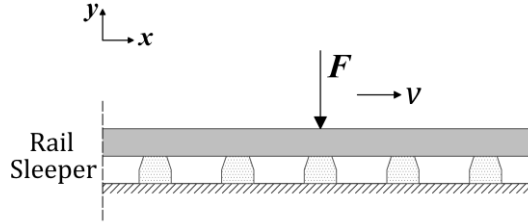
Figure 2-8. Track subjected to a moving point load

Inclusion of a Dirac Delta function $\delta(\cdot)$ allows for the representation of an impulse or transient force. With this function, an excitation is defined only at a specific position (x) or instance of time (t). **Eq.** (2-8) depicts the stationary impulse force, equal to P at $x = 0$ and $t = 0$, and equal to zero elsewhere. This definition can be extended to a moving load as described by [8,9,31,84,85], and the impulse force is defined using a moving frame of reference, $x - vt$, which relates the space and time through the velocity v. **Eq.** (2-9) presents the moving impulse excitation equal to P at $x = vt$, and equal to zero elsewhere.

$$F = P\delta(x)\delta(t) \tag{2-8}$$

$$F = P\delta(x - vt) \tag{2-9}$$

where $\delta(x)$ and $\delta(t)$ are the impulse functions in space and time, respectively, while $\delta(x - vt)$ is the moving impulse function. The harmonic oscillating nature of the force can be considered by including the complex exponential function $e^{i\varpi t}$ in **Eqs.** (2-8)-(2-9) [9,36,86]. In this way, the load is no longer constant (in amplitude) and the oscillatory nature of the unsprung/sprung train can be approximated. **Eqs.** (2-10) and (2-11) show the non-moving and the moving oscillating load with driving oscillating frequency ϖ, respectively [31,84,86,87].

$$F = Pe^{i\varpi t} \tag{2-10}$$

$$F = Pe^{i\varpi t}\delta(x - vt) \tag{2-11}$$

Combining multiple Dirac Delta functions allows for the simulation of more complex effects such as wheel-rail irregularities [79,88,89] and discrete supports [90–93]. These effects are simulated via the summation of the reaction forces, resulting from a single axle load, at each sleeper n, evenly spaced by a distance $x = nd$ – as shown in **Eq.** (2-12) where d is the sleeper spacing.

$$F = \sum_{n=-\infty}^{n=+\infty} P\delta(x - nd) \tag{2-12}$$

Note that **Eq.** (2-12) considers a repetitive arrangement of sleeper via the constant spacing d, which can be defined as a periodic length.

Considering a linear system, the response due to multiple axle loads can be achieved through superposition, i.e. either by summing each loading or their single response, according their location in the structure (**Figure 2-6**).

Despite allowing for an oscillating and moving representation of the excitation source, point load and quasi-static models cannot describe the aspects of the loading induced by train dynamics. Nevertheless, these type of loads enable characterisation and understanding of structural behaviour, and provide the framework to solve more complex problems such as train-track interaction.

2.2.3.2 Multi-Body Systems

Vehicle behaviour can alternatively be simulated using multi-body dynamics. Flexible and rigid body assumptions can be combined with BOEF approaches, however, perhaps the most common is the assumption of rigidity. Models typically consist of:

- Masses to describe the wheelsets, bogie frames, and car body.
- Viscoelastic elements (i.e. springs and dampers/dashpots) to model the primary and secondary suspension, and the contact between the wheel and rail.

One simple multi-body system is that of a single degree-of-freedom system [94,95]. In this model, 1/4 of a moving train with four axles and two bogie frames is considered through a moving mass M_w (wheelset with vertical displacement u_w) connected to the rail (i.e. the contact point) through a Hertzian spring K_{Hz}, with vertical displacement u_r at its base – see **Figure 2-9**(a).

An additional degree-of-freedom (vertical displacement u_b) can be accounted through a moving mass representing the bogie [96–99], as indicated in **Figure 2-9**(b). Note that since only a quarter of the vehicle is modelled, the system includes a single axle and half of a bogie, and both moving masses are connected via a viscoelastic element k_1-c_1 (primary suspension). A quarter of the car body is included in the form of a static force P.

Further degrees-of-freedom can be included in the system by adding more components of the train and including the pitch rotation φ_i of the rigid masses. For instance, half of a moving train with two moving wheelsets and a moving bogie

yields a four-degree-of freedom system [21,100], whereas a five-degree-of-freedom model is achieved with the inclusion of half of the moving car body [101,102] – see **Figure 2-9**(c) and (d), respectively.

Finally, an entire train can be modelled using larger multi-body systems [46,103–105]. The model shown in **Figure 2-9**(e) considers four wheelsets (M_{wi}) connected via the primary suspension (k_1,c_1) to two bogie frames (M_{bi}), which at the same time are connected to a complete car body (M_{cb}) through a secondary suspension (k_1,c_2).
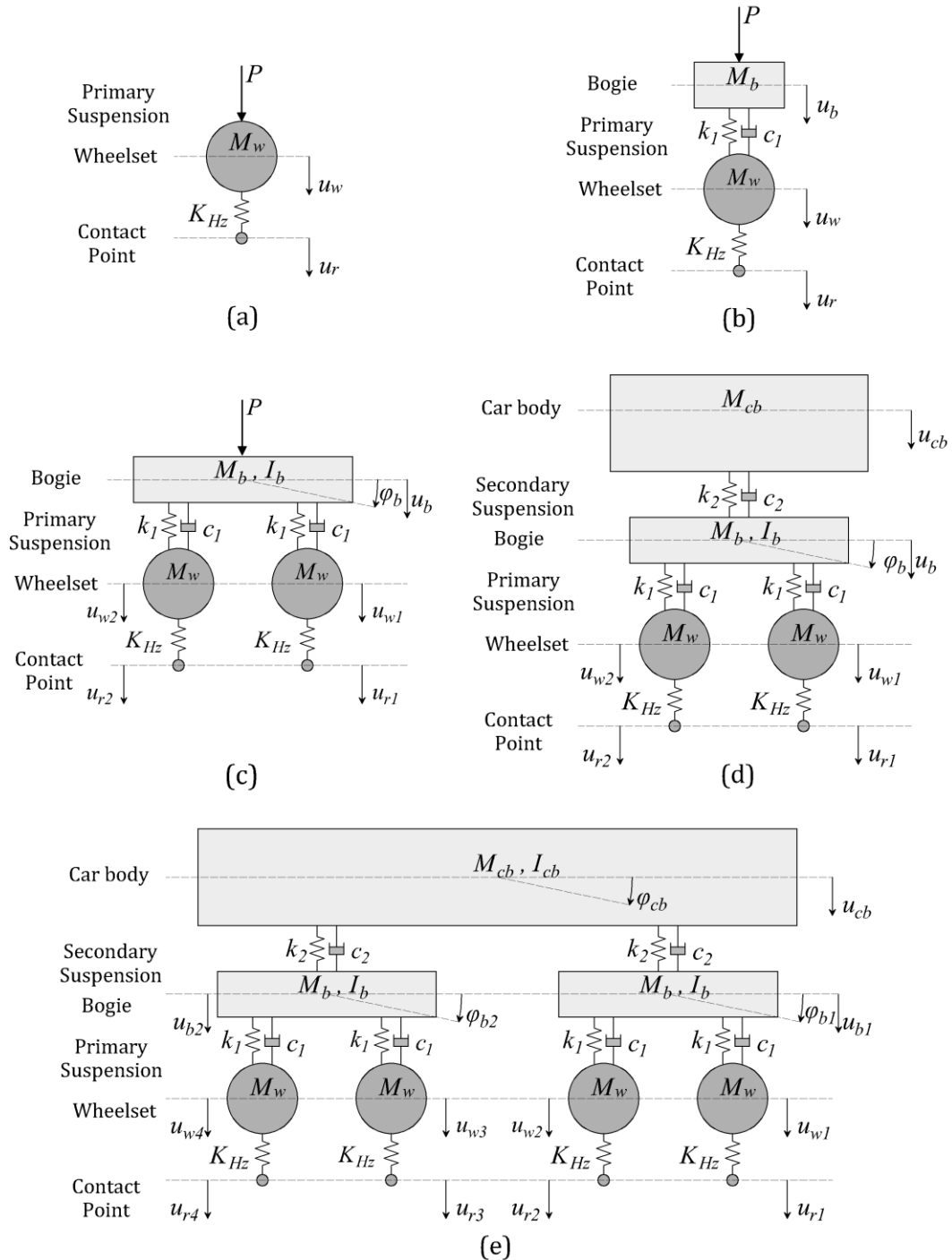
Figure 2-9. Train multi-body system: (a) one-degree-of-freedom model, (b) two-degree-of-freedom model, (c) four-degree-of-freedom model, (d) five-degree-of-freedom model, and (e) ten-degree-of-freedom model

The selection of the model should depend upon the purpose of the simulation [44,106]. For instance, a four-degree-of-freedom system (without secondary suspension and car body) is typically sufficient to study railway-traffic induced vibrations at frequencies above 3 Hz [107]. On the other hand, studies have shown that at frequencies higher than a few Hertz, the train's primary and secondary suspension isolate the bogie and the vehicle body from the wheelset, allowing the vehicle model to be limited to only its unsprung mass component (i.e. the wheelset) [9]. Thus, for some applications, reduced degree-of-freedom vehicle models, with fewer elements, can give similar results with reduced computational effort. However, it should be noted that this depends upon vehicle characteristics. For example, the stiff suspension commonly found on freight vehicles means that this type of rolling stock may need to be simulated using a larger number of degrees-of-freedom in comparison to passenger vehicles.

It should also be noted that the strategies described in this Section make use of rigid-body models (i.e. negligible deformations of elements). However, flexible-body systems (i.e. deformable elements) can also be implemented in vehicle simulations, particularly when interested in vehicle dynamics rather than track dynamics [108–110].

2.3 Solution Methods

2.3.1 Equations of Motion

A Euler-Bernoulli beam resting on Winkler springs and subject to an external dynamic force $F(x,t)$ can be described by the following equation of motion in the space-time-domain (x,t) [31,40,111]:

$$E_r I_r u_r^{IV} + m_r \ddot{u}_r + k_f u_r = F$$
$$u_r^{IV} = \frac{\partial^4 u_r(x,t)}{\partial x^4}, \ddot{u}_r = \frac{\partial^2 u_r(x,t)}{\partial t^2} \tag{2-13}$$

and where $E_r I_r$ and m_r are the flexural bending and the mass per unit length of the rail 'r', respectively. k_f is the stiffness of the foundation per unit length 'f', and F is the force per unit length. The corresponding partial derivatives of the rail deflection $u_r(x,t)$ with respect to space x and time t are depicted by u_r^{IV} and $\ddot{u}_r$, respectively. **Figure 2-10** shows a diagram of the system used to formulate **Eq.** (2-13) for a single-layer continuously supported model (bending component excluded for brevity).

Eq. (2-13) is formulated from D'Alembert's principle [31,37,40], and every term on the left-hand side represents a force whose sum equals the external dynamic force

at the right-hand side, i.e. the system is in equilibrium. In general, reading from the left, the first two terms correspond to the beam's flexural bending (internal forces) and mass (Newton's law) contribution, while the third term is the force exerted by the linear spring describing the elastic foundation. Following this, the damping effect of the foundation is included using linear dashpot elements. The contribution of the new elements to the system is similar to that provided by the springs, however, is proportional to the velocity $\dot{u}_r$:

$$E_r I_r u_r^{IV} + m_r \ddot{u}_r + c_f \dot{u}_r + k_f u_r = F$$
$$\dot{u}_r = \frac{\partial u_r(x,t)}{\partial t} \tag{2-14}$$

where c_f is the damping of the foundation. **Eqs.** (2-13) and (2-14) depict a simple railway-track model with a continuously supported single-layer. The simplicity of these models restricts the study of additional degrees-of-freedom in the track, which can be considered through the incorporation of more layers in the foundation model [10,34,51]. For instance, the second layer allows for the representation of the railpad, sleepers, and ballast elements (**Figure 2-1**), and the computation of the response at the sleeper level u_s:

$$E_r I_r u_r^{IV} + m_r \ddot{u}_r + k_{rp}(u_r - u_s) + c_{rp}(\dot{u}_r - \dot{u}_s) = F$$
$$m_s \ddot{u}_s - k_{rp}(u_r - u_s) + k_{rb} u_s - c_{rp}(\dot{u}_r - \dot{u}_s) + c_b \dot{u}_s = 0 \tag{2-15}$$

where $k_{rp,b}$ and $c_{rp,b}$ are the stiffness per unit length and damping per unit length, of the railpad 'rp' and the ballast 'b', respectively; and m_s is the mass of the sleeper 's'. **Figure 2-11** shows the Section employed to formulate the set of dynamic equations of motion – see **Eq.** (2-15), for a two-layer model continuously supported.

The previously described models follow Euler-Bernoulli theory, which neglects shear and rotational effects, while assuming the beam's plane Section remains plane and normal to its longitudinal axis, making them suitable in the study of thinner or larger length-to-thickness ratio beam elements.

Alternatively, Timoshenko's theory [49] is used when considering shear deformation and rotational inertial contributions, assuming that the plane section remains plane but no longer normal to the beam axis, which makes it appropriate to study thicker beam elements [10,49,50]. **Eq.** (2-15) describes the dynamic equations of motion for a Timoshenko beam resting on Winkler springs, using a system analogous to **Eq.** (2-13):

$$G_r A_r \kappa_r(\phi_r^I - u_r^{II}) + k_f u_r + m_r \ddot{u}_r = F$$
$$G_r A_r \kappa_r(\phi_r - u_r^I) - E_r I_r \phi_r^{II} + \rho_r I_r \ddot{\phi}_r = 0$$
$$\phi_r^I = \frac{\partial \phi_r(x,t)}{\partial x}, \phi^{II} = \frac{\partial^2 \phi_r(x,t)}{\partial x^2}, \ddot{\phi}_r = \frac{\partial^2 \phi_r(x,t)}{\partial t^2} \tag{2-16}$$

where ϕ_r is the bending rotation, A_r is the cross-sectional area, ρ_r is the density, m_r is the mass per unit length, E_r is the Young's modulus, G_r is the shear modulus, and κ_r is the shear coefficient.
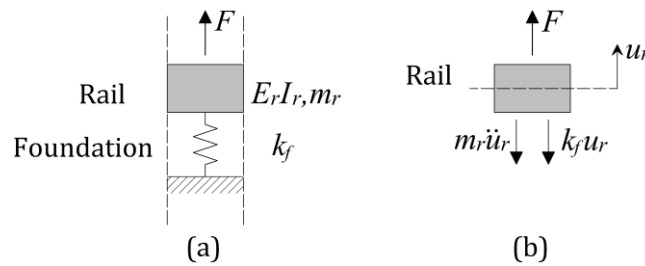
Figure 2-10. Continuous single-layer model: (a) discrete Section, and (b) free-body-diagram
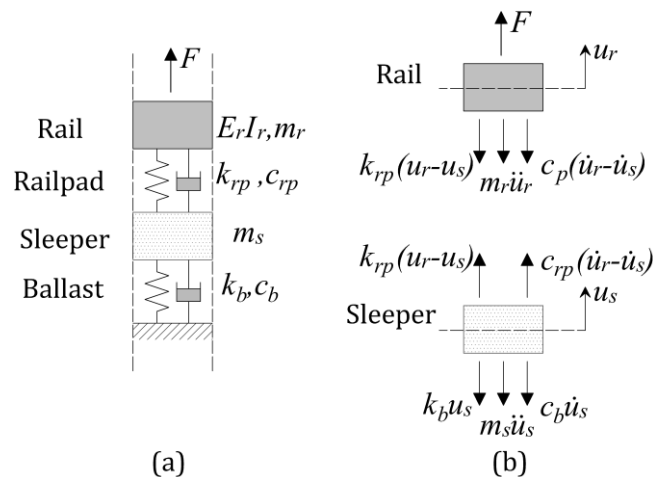
Figure 2-11. Continuous two-layer model (bending component excluded for brevity): (a) discrete Section, and (b) free-body-diagram

2.3.2 Damping Formulations

Damping is the process via which a structure's energy – kinetic and strain, is dissipated. Its inclusion in the dynamic modelling of the system allows for the representation of the decay of structural vibration [112].

Among the various damping mechanisms, the two most commonly used for BOEF applications are viscous and structural/hysteretic. The first case is used for time- and frequency-domain analysis. In contrast, structural damping is constant at all frequencies and is thus restricted to frequency-domain simulations due to the causality problems it causes in the time-domain [10,51]. Although both types of damping can yield similar results in structures with strong natural frequencies, viscous damping is often preferred when describing railpad behaviour in time-domain simulations, which is highly damped in comparison to the other track elements. In contrast, hysteretic damping can give a better approximation within a

limited frequency range, which makes it commonly used for soil modelling [10], and suitable for railpad modelling in the frequency-domain.

2.3.2.1 Viscous Damping

Viscous damping models represent a linear dissipative behaviour using massless dashpot elements, with a constant viscous damping coefficient c, which produces a force F_d proportional to velocity $\dot{u}$ in the time-domain [51,112]:

$$F_d(t) = c\dot{u}(t) \tag{2-17}$$

Viscous damping can be employed in frequency-domain problems after transforming **Eq.** (2-17) from the time- to frequency-domain:

$$\tilde{F}_d(\omega) = i\omega c\tilde{u}(\omega) \tag{2-18}$$

where $\tilde{F}_d$ and $\tilde{u}$ are the damping force and the deflection in frequency-domain ω, respectively. Often, a complex stiffness $k^*(\omega) = (k + i\omega c)$ is used to describe the dynamic stiffness behavior of the system, which is a combination of the real stiffness k and the imaginary damping $i\omega c$:

$$\tilde{F}_k(\omega) + \tilde{F}_d(\omega) = k\tilde{u}(\omega) + i\omega c\tilde{u}(\omega) \tag{2-19}$$

where $\tilde{F}_k(\omega)$ is the force provided by the linear spring, with stiffness k.

The proportional damping proposed by Rayleigh [113] is a particular case of viscous damping typically employed when performing a modal analysis of classically damped systems. This model assumes the damping $[C]$ is a linear combination of the mass $[M]$ and/or stiffness $[K]$ [112,114]:

$$[C] = \alpha_1[M] + \alpha_2[K]$$
$$\alpha_1 = \zeta_n\omega_n, \qquad \alpha_2 = \frac{\zeta_n}{\omega_n} \tag{2-20}$$

where α_1 and α_2 are real coefficients related to the mass and damping, respectively; ζ_n and ω_n are the damping ratio and the frequency of the nth mode. Moreover, when $\alpha_1 = 0$ and $\alpha_2 \neq 0$ the system is said to have stiffness-proportional damping. On the contrary, when $\alpha_1 \neq 0$ and $\alpha_2 = 0$, the damping is mass-proportional.

For structures described by low-order modes or with a low number of degrees-of-freedom, the lowest natural modes are able to represent the vibration modes of the total system and ensure reliable Raylei gh parameters α_1 and α_2. However, for complex systems (with larger number of degrees-of-freedom) whose dynamic

behavior is controlled by a large number of modes, determination of these parameters represents a challenge [112,115].

A generalised form of Rayleigh damping is achieved by including specific damping ratios for more than two modes; thus allowing the simulation of a particular damping value over a frequency range [112,116,117]. This model, known as Caughey damping, is described by:

$$[C] = [M] \sum_{j=0}^{j=N-1} \alpha_j ([M]^{-1}[K])^j$$
$$\zeta_n = \frac{1}{2} \sum_{j=0}^{j=N-1} \alpha_j \, \omega_n^{2j-1}$$

(2-21)

where N is the studied number of modes and α_j are the coefficients related to the damping ratios ζ_n.

2.3.2.2 Structural/Hysteretic Damping

Structural damping (aka hysteretic or rate-independent linear damping) assumes that a structure's energy dissipation is almost independent of frequency, and is caused by cyclic internal deformation and restoration to its original shape. A dashpot element defining structural damping is described by [112]:

$$c = \frac{k\eta}{\omega}$$

(2-22)

where c is the damping coefficient proportional to the damping loss factor η and stiffness k, and is inversely proportional to frequency ω. Thus, according to **Eq.** (2-22), the damping effect can be considered in the form of a complex stiffness k^*, by means of η and k [10,51,114]:

$$k^* = k(1 + i\eta), \eta \ll 1$$

(2-23)

In frequency-domain analysis, a system with hysteretic damping is compatible with the causality principle, i.e. its response due to an external force does not occur before the application of the force. However, in time-domain analysis, an undesirable characteristic of hysteretic damping is that it typically violates this principle, meaning the force anticipates the system response. In such a case the model is referred to as non-causal [118,119], and to avoid this, hysteretic damping is usually confined to frequency-domain solutions. The inclusion of a signum function in frequency, sgn(ω) [120] can help correct the mathematical formulation, as shown in **Eq.** (2-24).

$$k^* = k\big(1 + i\eta\,\mathrm{sgn}(\omega)\big), \; \mathrm{sgn}(\omega) = \begin{cases} \eta, & \text{for } \omega > 0 \\ 0, & \text{for } \omega = 0 \\ -\eta, & \text{for } \omega < 0 \end{cases} \qquad (2\text{-}24)$$

Note that when considering non-moving fore contributions, symmetry of the response is often exploited (in the transformed domain – see Section 2.3.3.2.2). Thus, only ω > 0 values are considered and ω < 0 are disregarded. Alternatively, moving contributions struggle exploiting the symmetry assumption, thus negative frequencies are of major importance in the response computation of the structure.

Alternative approaches have also been developed to reduce non-causal behaviour, or enforce causality in the damping formulation. For instance, in the first case, iteration procedures involving Hilbert transformations can be performed [121,122]. For the latter, both the real and imaginary components in **Eq.** (2-24) are modified and an arbitrary constant ε is introduced [118], as shown in **Eq.** (2-25):

$$k^* = k\left(1 + \frac{2}{\pi}\eta \ln\left|\frac{\omega}{\varepsilon}\right| + i\,\eta\,\mathrm{sgn}\left(\frac{\omega}{\varepsilon}\right)\right) \qquad (2\text{-}25)$$

2.3.3 Track Dynamics

A variety of modelling strategies have been proposed to compute railway track dynamic behaviour. These include empirical, analytical, numerical, and semi-analytical strategies. Regarding empirical, these approaches are based upon past experience and often restricted to specific conditions such as certain train speed ranges or ground conditions [17,123]. For analytical strategies, models are created based upon idealised track conditions, thus allowing closed-form solutions to be derived. Often, these methods are based upon BOEF models, in which the rail rests on either continuous or discrete supports. However, when dealing with complex track problems such as the spatial variation of geometry and material properties, analytical solutions are not always practical to obtain. Instead, these limitations can be overcome by using numerical or semi-numerical strategies. However, despite the benefits of increased accuracy and flexibility, numerical approaches require additional computational expense. A selection of the more commonly used approaches is now discussed.

2.3.3.1 Multi-Purpose Solution Approaches

2.3.3.1.1 Finite Element Method

The Finite Element Method (FEM), is a numerical technique that calculates structural response by subdividing the domain (i.e. the overall structure) into

several sub-domains or Finite Elements, interconnected at their nodal points, and selecting appropriate functions to describe their physical behaviour. Each nodal point is defined by a number of nodal or generalised displacements which provide the degrees-of-freedom (DOF) of the problem. This allows the governing partial differential equations of motion to be reformulated in terms of the N number of DOFs present in the overall structure [112,114,124].

The FEM allows the formulation and solution of a structural system in either the time or frequency-domain, the latter defined after performing domain transformation of the former. **Eqs.** (2-26) and (2-27) depict the time- and frequency-domain dynamic equations of motion in matrix format respectively:

$$[M]\{\ddot{u}(t)\} + [C]\{\dot{u}(t)\} + [K]\{u(t)\} = \{F(t)\} \tag{2-26}$$

$$-\omega^2[M]\{\hat{u}(\omega)\} + i\omega[C]\{\hat{u}(\omega)\} + [K]\{\hat{u}(\omega)\} = \{\hat{F}(\omega)\} \tag{2-27}$$

where $[M]$, $[C]$ and $[K]$ are the $(N \times N)$ mass, damping and stiffness matrices of the track structure, respectively; $\{\ddot{u}\}$, $\{\dot{u}\}$, $\{u\}$ and $\{F\}$ are the $(N \times 1)$ vectors of acceleration, velocity, displacement and force in the time-domain t; while $\{\hat{u}\}$ and $\{\hat{F}\}$ are the vectors of displacement and force in the frequency-domain ω. Furthermore, when formulated in the frequency-domain, **Eq.** (2-27) can be expressed in terms of the dynamic stiffness matrix, which relates the displacement-force vectors at a particular frequency value [125]:

$$([K] + i\omega[C] - \omega^2[M])\{\hat{u}(\omega)\} = \{\hat{F}(\omega)\}$$
$$[D] = [K] + i\omega[C] - \omega^2[M] \tag{2-28}$$

One-dimensional FE track models make use of two node (i.e. line) beam elements lying on elastic springs, representing the rail and the support, respectively. **Figure 2-12**(a) shows a 1D FE track structure with j nodes and element length l_e resting on a layer of continuous springs, and the corresponding DOFs u and φ.

Further flexibility is achieved via two-dimensional Finite Element models. 2D FEM allows for the representation of 2D solids and deflection in the plane of study. Thus, additional nodal points (e.g. 4 nodes for rectangular elements) and their corresponding DOFs can be included – see for instance [126–129]. **Figure 2-12**(b) illustrates a 2D BOEF-FE model which employs 8-node quadrilateral elements of length l_e resting on springs.

By neglecting the stress or strain in the out-of-plane direction, 2D methods attempt to approximate the results achieved using fully 3D models. If considering a plane stress assumption, then in-plane stresses ($x - y$ direction) are allowed and out-of-plane stresses (z direction) or 'through thickness shear stresses' are disregarded, making the assumption suitable for thinner structures – see for instance [130].

Alternatively, if considering plane strain, this assumes non-zero in-plane, and zero out-of-plane strains. It allows for stresses in the z direction to be simulated, which makes it appropriate for studying thicker bodies (e.g. [131–133]).

Alternatively, 3D FE models are capable of a closer geometrical representation of an actual track structure – see for instance [27,127,134–136]. This allows for modelling of 3D solids, including complex railhead geometries if desired [137–141]. **Figure 2-12**(c) shows a 3D FE model approximating the rail as a cuboidal shape, using 20-node quadratic elements of length l_e, resting on springs.
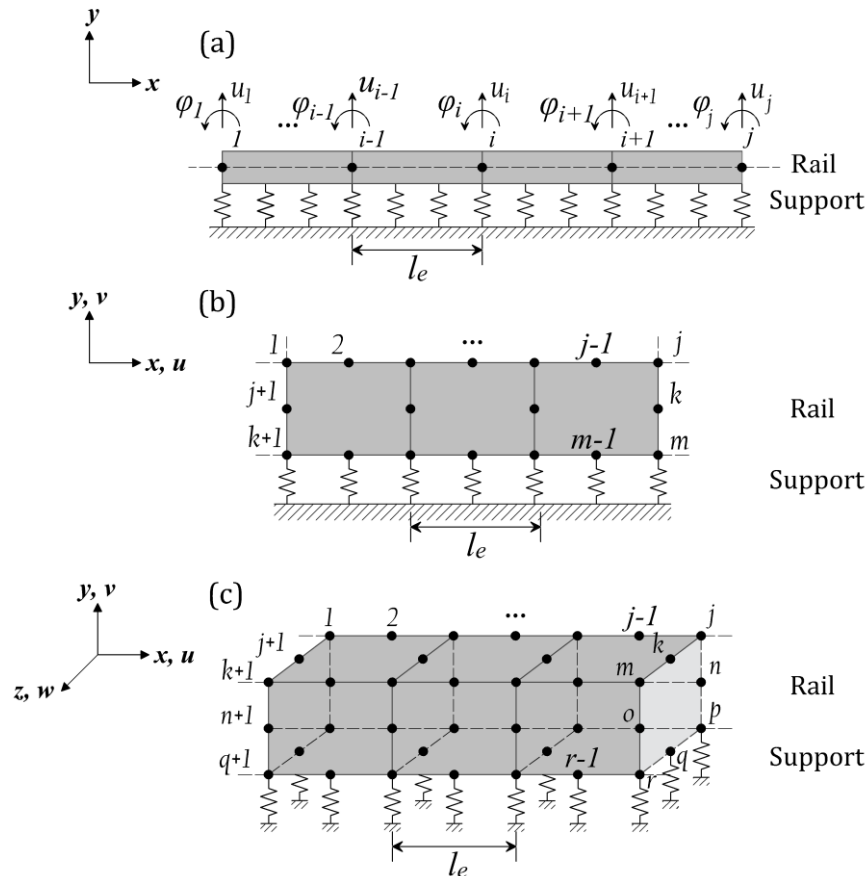
Figure 2-12. Finite Element models: (a) 1D, (b) 2D, and (c) 3D

2.3.3.1.1.1 Numerical Integration

Time-domain approaches are most commonly employed when aspects of the domain are non-linear [85]. In general, time-domain solutions employ numerical integration methodologies to solve the governing differential equation of motion of the track structure defined in **Eq.** (2-26). In this formulation, numerical integration requires time discretisation in the form of a time step or increment Δt, leading to the computation at a specific time interval t_j and its consecutive interval $t_{j+1} = t_j + \Delta t$ [112].

The integration procedure can be categorised as either explicit or implicit. The former computes the response at time t_{j+1} depending only on the known response

at the previous time t_j (i.e. at t_{j+1}, the solution is independent of t_{j+1}). In contrast, implicit procedures involve values at both times t_j and t_{j+1}, which results in the formulation of an additional system of equations, usually in matrix format, that must be inverted in order to compute the response at t_{j+1} [66]. Further distinction between numerical integration schemes can be made depending on the system to be solved. Thus, when solving the equation of motion (2-26) with no changes in its form, the numerical integration is said to be 'direct'. 'Indirect' integration procedures require the reformulation of **Eq.** (2-26) into an equivalent time-space system which is instead solved [66,142].

Direct integration procedures often employ the finite difference method [124]. The Newmark method and the central difference method, are examples of direct-implicit and direct-explicit integration methods, respectively. In contrast, the explicit Runge-Kutta and the implicit Crank-Nicolson, are common indirect integration procedures [66,112,124].

2.3.3.2 Solution Methods for Continuous Track Structures

2.3.3.2.1 Time-Space-Domain Approaches

2.3.3.2.1.1 Analytical Time-Space Solution

An analytical, time-space, single-layered, BOEF model is perhaps the most commonly used simulation approach in the railway industry. The computation involves the solution of a homogenous differential equation of motion in which the rail rests on a continuous elastic support, defined by a track modulus or stiffness k_f [126,143]:

$$E_r I_r u_r^{IV} + k_f u_r = 0 \qquad (2\text{-}29)$$

Note that although **Eq.** (2-29) is similar to **Eq.** (2-14), the former ignores dynamic effects (i.e. inertial components) and computes the response for the homogenous part of the differential equation (i.e. for a force, $F = 0$). Solution of **Eq.** (2-29) can be obtained through analytical formulations [45,126,143,144] and expressed in terms of space and time, via the speed-space-time relationship, $v = x/t$, as shown in **Eq.** (2-30) and **Eq.** (2-31) – see [13], respectively:

$$u_r(x) = \frac{F}{\left(64 E_r I_r k_f^{\,3}\right)^{1/4}} e^{-|\delta x|} (\cos|\delta x| + \sin|\delta x|) \qquad (2\text{-}30)$$

$$u_r(x,t) = \frac{F}{8 E_r I_r \delta^3} e^{-\delta|x-vt|} [\cos(\delta|x-vt|) + \sin(\delta|x-vt|)] \qquad (2\text{-}31)$$

$$\delta = \left(\frac{k_f}{4E_r I_r}\right)^{1/4} = \frac{1}{L_e}$$ (2-32)

where $u_r(x,t)$ is the rail deflection at track position x and time t, due to a quasi-static force F, and δ is the inverse of the characteristic length, L_e, a parameter that measures the extension of the deflection bowl of the rail.

2.3.3.2.2 Frequency-Wavenumber-Domain Approaches

Frequency-domain based approaches are typically employed for the study of linear structures. When computing a railway structure's response in terms of frequency, the time-domain differential equations are simplified to an algebraic problem, thus making them more straightforward to solve.

2.3.3.2.2.1 Fourier Transform Method

The Fourier transform method allows for a domain conversion through integrals or sums of sinusoidal waves, before converting into the time-domain. The most common Fourier transformations and corresponding inverse Fourier transformations used for railway problems are shown in **Eqs.** (2-33)-(2-36):

$$\hat{\mathcal{F}}(x,\omega) = \int_{-\infty}^{+\infty} \mathcal{F}(x,t)e^{-i\omega t}\mathrm{d}t$$ (2-33)

$$\mathcal{F}(x,t) = \frac{1}{2\pi}\int_{-\infty}^{+\infty} \hat{\mathcal{F}}(x,\omega)e^{i\omega t}\mathrm{d}\omega$$ (2-34)

$$\tilde{\mathcal{F}}(\beta,\omega) = \int_{-\infty}^{+\infty} \hat{\mathcal{F}}(x,\omega)e^{-ix\beta}\mathrm{d}x$$ (2-35)

$$\hat{\mathcal{F}}(x,\omega) = \frac{1}{2\pi}\int_{-\infty}^{+\infty} \tilde{\mathcal{F}}(\beta,\omega)\,e^{ix\beta}\mathrm{d}\beta$$ (2-36)

where the wavenumber β and the angular frequency ω are the Fourier images of space x and time t, respectively; $\hat{\mathcal{F}}(x,\omega)$ represents the Fourier transform of function $\mathcal{F}(x,t)$ or the inverse Fourier transformation of function $\tilde{\mathcal{F}}(\beta,\omega)$; $\mathcal{F}(x,t)$ is the inverse Fourier transformation of function $\hat{\mathcal{F}}(x,\omega)$; and $\tilde{\mathcal{F}}(\beta,\omega)$ the Fourier transform of function $\hat{\mathcal{F}}(x,\omega)$.

Fourier transform methods are widely employed for the solution of continuously supported tracks (see, for instance [84,90,92,145]). Through this approach, firstly the original partial differential equation in space-time-domain (x,t) – **Eq.** (2-37), is analytically transformed into an algebraic equation system in the wavenumber-frequency-domain(β,ω)– **Eq.** (2-38):

$$E_r I_r \frac{\partial^4 u_r(x,t)}{\partial x^4} + \rho_r A_r \frac{\partial^2 u_r(x,t)}{\partial t^2} + c_{rp} \frac{\partial u_r(x,t)}{\partial t} + k_{rp} u_r(x,t)$$
$$= F(x,t) \tag{2-37}$$

$$E_r I_r \beta^4 \tilde{u}_r(\beta,\omega) - \omega^2 \rho_r A_r \tilde{u}_r(\beta,\omega) + i\omega c_{rp} \tilde{u}_r(\beta,\omega) + k_{rp} \tilde{u}_r(\beta,\omega)$$
$$= \tilde{F}(\beta,\omega) \tag{2-38}$$

where E_r, I_r, ρ_r and A_r are the Young's modulus, the second moment of inertia, the density and the cross-sectional area of the rail ('r'), respectively; k_{rp} and c_{rp} are the stiffness per unit length and damping factor of the railpad (subscript 'rp'), respectively; $u(x,t)$ and $F(x,t)$ represent the displacement and force in the space-time-domain (x,t), and displacement $\tilde{u}_r(\beta,\omega)$ and force $\tilde{F}(\beta,\omega)$ are the corresponding Fourier transformations in wavenumber-frequency-domain (β,ω). After the track response is computed in the frequency-domain, an inverse Fourier transform is used in order to transform the results back into the desired domain.

2.3.3.2.2.2 Filon Quadrature Method

The Filon quadrature [146], is a numerical method that allows for the domain transformation of a function by limiting the number of points in the integration. Thus, instead of solving for an infinite sampling, as required by Fourier, Filon quadrature makes use of a finite ascending sampling σ which does not need to be evenly spaced. The method can evaluate highly oscillatory integrals whose integrands are smooth and non-oscillatory functions $\tilde{G}(\sigma)$ multiplying a oscillatory function traditionally involving trigonometric functions [147,148]. Different representations have been developed for the domain transformation of a function through this procedure, for instance, **Eqs.** (2-39)-(2-41) describe the Filon quadrature of Fourier cosine, Fourier sine and Fourier integral, respectively [148–151]:

$$g(r) = \int_{\xi_1}^{\xi_{end}} \tilde{G}(\sigma) \cos(\sigma r) \, d\sigma \tag{2-39}$$

$$g(r) = \int_{\xi_1}^{\xi_{end}} \tilde{G}(\sigma) \sin(\sigma r) \, d\xi \tag{2-40}$$

$$g(r) = \int_{\xi_1}^{\xi_{end}} \tilde{G}(\sigma) e^{\sigma r} \, d\sigma \tag{2-41}$$

where $g(r)$ is the Filon quadrature or transformed function computed at sampling point r, $\tilde{G}$ is the continuous function to transform in the interval (σ_1, σ_{end}) of the sampling σ. Thus, for a transformation from wavenumber- to space-domain, it is noticeable that $g(r)$ corresponds to the integral in **Eq.** (2-36) at a particular point

$x = r$. This allows for the computation of the correspoding transformed function $\hat{\mathcal{F}}(r)$ at r through [149]:

$$\hat{\mathcal{F}}(r) = \frac{1}{2\pi} g(r) \tag{2-42}$$

2.3.3.2.2.3 Contour Integration Method

The contour integration is an analytical method that solves an integral around a contour or closed path in the complex plane. The integration around this contour can be split into an integral along the real axis from $-R \to -\infty$ to $+R \to +\infty$ (i.e. a straight path), plus the integration of a semicircle 'CR' connecting the two ends of the previous path [31,152,153]. Furthermore, the contour domain encloses special points, known as poles, whose properties allow for the computation of the closed domain integral, which can be solved through residue theorem [10,92,152,153]. **Eq.** (2-43) depicts the contour integration of function $\tilde{G}(\sigma)$ evaluated through the summation of its residues Res $\tilde{G}(\sigma)$ at the j poles σ_j.

$$\oint_C \tilde{G}(\sigma)\mathrm{d}\xi = \lim_{R\to\infty} \int_{-R}^{+R} \tilde{G}(\sigma)\mathrm{d}\sigma + \int_{CR} \tilde{G}(\sigma)\mathrm{d}\sigma$$
$$= 2\pi i \sum_{j=1}^{j=j_{\mathrm{end}}} \mathrm{Res}\,\tilde{G}(\sigma)|_{\sigma=\sigma_j} \tag{2-43}$$

For instance, transforming the rail response $\tilde{u}_r(\beta,\omega)$ in **Eq.** (2-38) from wavenumber-frequency-domain – as shown in **Eq.** (2-44), to space-frequency-domain through the inverse Fourier transformation in **Eq.** (2-45), it is possible to realise that $\tilde{G}(\sigma) = \tilde{G}(\beta)$:

$$\tilde{u}_r(\beta,\omega) = \frac{\tilde{F}(\beta,\omega)}{E_r I_r \beta^4 - \omega^2 \rho_r A_r + i\omega c_{rp} + k_{rp}} \tag{2-44}$$

$$\hat{u}_r(x,\omega) = \frac{1}{2\pi} \int_{-\infty}^{+\infty} \tilde{G}(\beta)\mathrm{d}\beta$$
$$\tilde{G}(\sigma) = \tilde{G}(\beta) = \tilde{u}_r(\beta)e^{-ix\beta} \tag{2-45}$$

Furthermore, the points at which function $\tilde{G}$ becomes singular (i.e. no longer analytical), are the poles. For this particular example, the poles corresponds to the four wavenumber roots β_j:

$$\beta^4 = \frac{\omega^2 \rho_r A_r - i\omega c_{rp} - k_{rp}}{E_r I_r} = \begin{cases} \beta_1 = \beta \\ \beta_2 = i\beta_1 = i\beta \\ \beta_3 = i\beta_2 = -\beta \\ \beta_4 = i\beta_3 = -i\beta \end{cases} \tag{2-46}$$

Thus, dropping ω for convenience and considering a unit force $\tilde{F}(\beta, \omega) = 1$, the residues of function $\tilde{G}(\beta_j)$ and the transformed response $\hat{u}_r(x, \omega)$ can be defined [10,92,153]:

$$\text{Res } \tilde{G}(\beta_j) = \lim_{\beta \to \beta_j} (\beta_j - \beta_j) \frac{e^{-ix\beta}}{E_r I_r (\beta_j - \beta_1)(\beta_j - \beta_2)(\beta_j - \beta_3)(\beta_j - \beta_4)}$$
$$= \frac{e^{-ix\beta}}{4 E_r I_r \beta_j^3} \tag{2-47}$$

$$\hat{u}_r(x, \omega) = \frac{1}{2\pi} \oint_C \tilde{G}(\beta) d\beta = \pm i \sum_{j=1}^{j=j_{\text{end}}} \frac{e^{-ix\beta}}{4 E_r I_r \beta_j^3} \tag{2-48}$$

where the sign in **Eq.** (2-48) depends upon the chosen contour, which in turn is based on the poles' position in the complex plane [10,31,92,153] – see **Figure 2-13**. Thus, poles in the first and second quadrant are enclosed in the upper anti-clockwise semicircle, giving a positive sign in **Eq.** (2-48) and corresponding to positions at $x \geq 0$. Alternatively, poles in the third and fourth quadrant in the lower clockwise domain result in a negative sign in **Eq.** (2-48), corresponding to $x \leq 0$. However, for the case where the poles are purely real, the contour must be rearranged to include or exclude the points lying on the real axis.
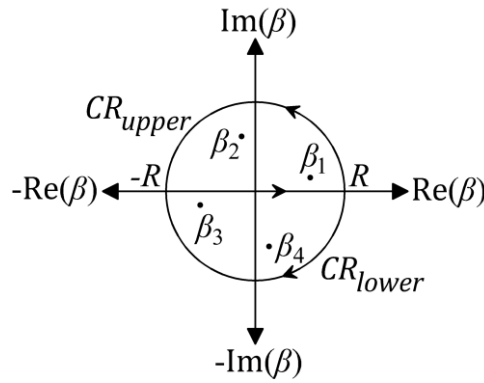
Figure 2-13. Upper and lower contour integration paths [153]

2.3.3.2.2.4 Boundary Value Method

The boundary value method is an analytical solution approach which computes the global track response by utilising symmetry in the moving direction, and making assumptions about the characteristics of wave energy. The method computes an infinite and constant track response, by treating the external load as part of the boundary conditions instead of part of the equations of motion, thus only considering the homogeneous part of the ordinary differential equation [153]. Therefore, by solving the homogeneous part of the equation of motion, and assuming harmonic excitation, the track deflection can be computed using **Eq.** (2-49) [10,111,153]:

$$\hat{u}_r(x,\omega) = \left(\sum_{j=1}^{j=j_{end}} E_j C_j e^{i\beta_j x} \right) e^{i\omega t} \tag{2-49}$$

where $\hat{u}_r(x,\omega)$ is the rail displacement in the space-frequency-domain, E_j is the eigenvector corresponding to the decaying eigenvalues $|\lambda_j| < 1$ (i.e. the decaying solutions); C_j is the amplitude of the wave components (arbitrary constants in the homogeneous equation [66]), and β_j is the wavenumber root. Furthermore, the response can be assumed to be symmetrical around the loading point, making it possible to take advantage of track symmetry. Therefore, only half of the track response requires computation.

Next, insertion of **Eq.** (2-49) in the homogeneous differential equation provides the characteristic polynomial, which must be solved to obtain the deflection. However, since symmetry is enforced, the problem is considerably simplified, and only half of the coefficients are taken into account in the formulation. Therefore, only the wavenumbers associated with the studied portion of the structure (right-hand side: $x > 0$, or left-hand side: $x < 0$) are accounted for in the solutions [10,153].

For an infinite and constant track, only decaying/propagating wave components must be considered. This is because waves that increase in magnitude as they propagate cannot exist and so are ignored. Thus, for $x > 0$, the β_j roots which lie in the first and the second quarter – see **Figure 2-14**(a), excluding the positive real axis, are included in the response [153], i.e. decaying waves propagating to the right-side. Whereas at $x < 0$, the β_j roots which lie in the third and fourth quarter – see **Figure 2-14**(b), excluding the negative real axis, must be considered in the response computation [153], i.e. increasing waves propagating to the left-side. Finally, the solution is calculated by enforcing the boundary conditions at $x = 0$ (i.e. at the point of load application).
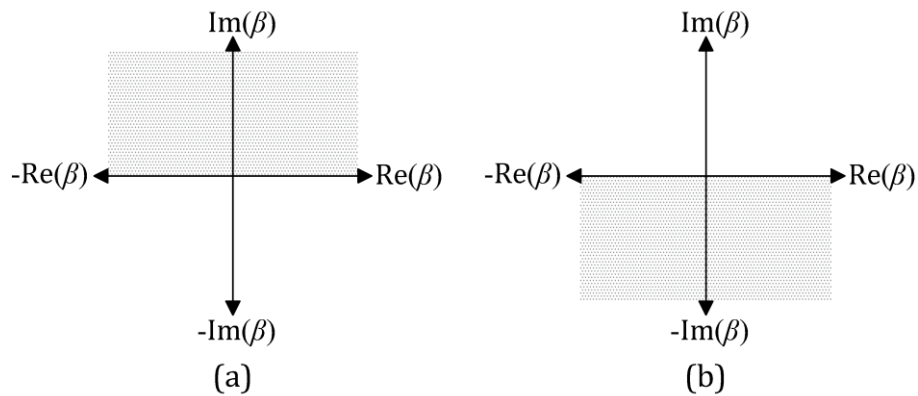
Figure 2-14. Wavenumber solutions [153]: (a) first and second quarter solutions (for $x > 0$), and (b) third and fourth quarter solutions (for $x < 0$)

Note that the considered roots are obtained for an infinite-infinite problem, which is solved by subdividing the domain into two sub-systems: infinite-finite ($x < 0$) and finite-infinite ($x > 0$) problem. Thus, only half of the roots are used in each case. However, when considering a finite-finite problem, all roots must be employed as the waves decay and propagate to the right-side, but then they are reflected back and increase to the left-side. For this type of problem, please refer to semi-periodic structures in Section 3.3.

2.3.4 Track-Ground Coupling

Track-ground coupling is required to represent the dynamic interaction between the railway track and the soil system. This can be achieved using different approaches which allow the track and the soil to be coupled through compatibility conditions at their interface.

Although BOEF models allow for a soil representation via spring-dampers, they cannot accurately describe wave propagation effects. This is in-part because these elements are typically defined using minimal parameters, which are assumed to be constant in space and time, and yet describe multiple supporting components, including railpads, sleepers, ballast and soil – see **Eq.** (2-1).

Compared to the continuous single-layered BOEF models, the discrete representation of foundation components provides a better approximation of the ground-track response. For instance, the time-domain discrete lumped parameter models shown in **Figure 2-2**(d) [154–156], account for the mass participating in the ground vibration and provide a better representation of the track-ground interaction and the nearby ground response [154]. Despite these advantages, computation of the discrete foundation parameters requires either additional soil measurements or numerical simulations [157] – the latter often performed in frequency-domain and then fitted into the time-domain interaction model [154,156].

In order to introduce a better approximation of the soil response (i.e. variable spring foundation properties) in BOEF models, the frequency-domain can be used, where the soil response is obtained via Fourier or Hankel transformations, and Green's formulations. Although the soil response can be obtained at different locations, only results at its surface below the track are needed when coupled to the BOEF track. This is because, at this location, the soil surface and the lowermost components of the track are in contact. The various analytical and semi-analytical methods used to study layered ground behaviour in the frequency-domain, include the Haskell-Thomson method [158,159], the direct stiffness method [160–162], the domain

transformation (DT) approach proposed by Sheng [68,70], and the thin layered method (TLM) [163,164].

Regarding Haskell-Thomson, the displacements and stresses of one side of each soil layer are related to the other side via a transfer matrix built upon shape functions computed from Navier's equations. In contrast, the Direct Stiffness Matrix method rearranges the previous transfer matrix into a stiffness matrix system that relates displacements and stresses between each layer. Alternatively, Sheng's method computes the 3D soil behaviour by relating each layer response via a global flexibility matrix (i.e. the inverse of the soil stiffness) which couples displacements and stresses of each element. The use of a flexibility matrix allows for the improvement in the computational efficiency by limiting the mathematical order of the problem, reducing numerical difficulties, exploiting symmetry relationships, and providing an explicit analytical formulation of the problem. However, numerical difficulties may arise when studying certain layer thicknesses [68,70].

This problem is avoided in the TLM method by discretising the layered soil domain with respect to the smallest relevant wavelength [75,165] – see **Figure 2-15**. The TLM computes the 3D soil response by combining its analytical formulation (in the two horizontal soil directions) with numerical techniques in the vertical soil direction [75,163]. Despite obtaining the soil response by relating the displacements to the stresses at both sides of the same layer (akin to the direct stiffness method), the stiffness matrices in the TLM are built upon FE approaches.
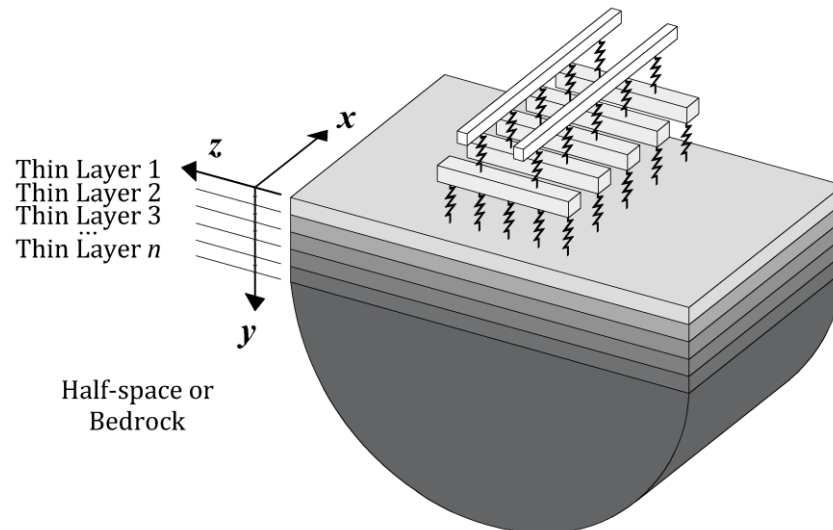
Figure 2-15. Track coupled with multi-layer soil model

Regardless of the solution approach, once the soil response is obtained, soil-track coupling can be achieved via Green's formulations that transform the soil's response into an equivalent soil stiffness $\tilde{k}_{eq}(\beta_x, \omega)$ or soil flexibility $\tilde{H}(\beta_x, \omega)$, which can be included in the BOEF model as its foundation parameter [72,75,166]:

$$\tilde{k}_{eq}(\beta_x, \omega) = \frac{1}{\tilde{H}(\beta_x, \omega)} = \frac{2\pi}{\int_{-\infty}^{+\infty} \tilde{u}^G(\beta_x, y = 0, \beta_z, \omega) \, C_{tg} \, d\beta_x}$$

$$C_{tg} = \begin{cases} \dfrac{\sin(\beta_z B)}{\beta_z B}, & \text{Ballasted track} \\[2mm] \dfrac{\sin(\beta_z B)^2}{(\beta_z B)^2}, & \text{Slab track} \end{cases} \qquad (2\text{-}50)$$

where $\tilde{u}^G$ is the Green's function related to the deflection of the soil surface ($y = 0$) in the wavenumber-frequency-domain (β_x, β_z, ω), and C_{tg} is the scaling factor for the coupling between the track and the soil which depends upon the track type, the track width B, and the track-soil compatibility conditions (compatibility of displacements at the centre point for ballasted tracks and compatibility of the average displacements for slab tracks [68,167–169]).

2.3.5 Train-Track Interaction

When studying train-track interaction, a system comprising a train, a track, and a wheel-track contact model are used, such as that shown in **Figure 2-16**. The train and the track models depict the dynamic behaviour of the overall system. The contact model represents the interaction between the wheel and the rail, and accounts for discrete irregularities (e.g. roughness) affecting these systems [170–172].
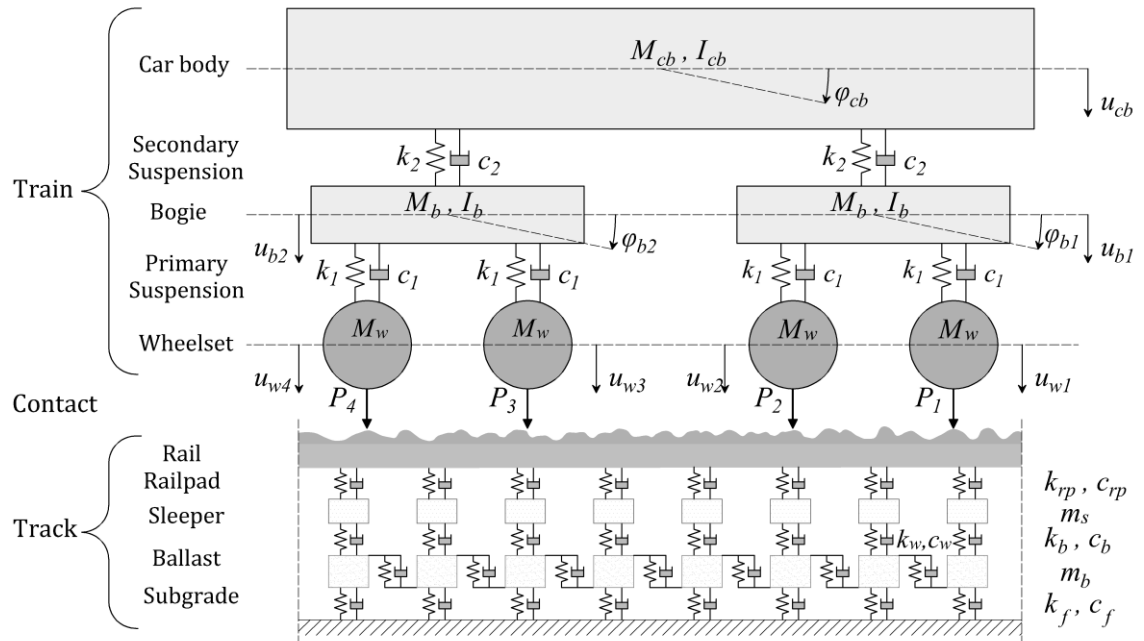
Figure 2-16. Train-Track interaction model [173,174]

2.3.5.1 Time-Domain Interaction Approaches

Time-domain approaches are often employed when analysing the non-linear aspects of wheel-rail contact. To determine the train-track interaction response, the dynamic equations of motion of both the train and the track are combined into an ordinary differential equation of the overall system [174–177]. To solve the interaction problem, compatibility of forces at the wheel-rail boundary is enforced. This procedure is performed through contact theory, which allows for the computation of the interaction forces $F_i(t)$.

Alternatively, the train-track system of equations can be solved as two coupled systems. In this case, iterative methods are employed to compute the response of the train and the track separately. To do so, compatibility conditions (i.e. continuity of displacements and equilibrium of forces) at the wheel-rail interface are enforced to couple both systems. Next, the total response is computed by convergence of train and track systems at the contact point [27,82,178,179].

Regardless of the employed approach, the response computation often involves traditional time-stepping integration procedures such as Newmark [157], Runge-Kutta or Wilson's method [9,27,174,180]. Additionally, some authors have developed different methods to reduce the duration and improve the computational effort of these methods. For instance, the modified Newmark method proposed by Zhai [173,174]; the algorithm developed by Sadeghi et al. [176,181,182] which combines the Newton–Raphson iterative procedure with the Newmark integration method; and approaches which use precise integration methods (PIM) [175,183].

2.3.5.2 Frequency-Domain Interaction Approaches

Frequency-domain approaches only allow for the analysis of structures whose behaviour can be approximated as linear [107,184–186]. Computation of train-track interaction requires the transformation of the time-domain ordinary differential equation of the system into a frequency-domain algebraic one:

$$[[K] - \omega^2[M] + i\omega[C]]\{\tilde{u}(\omega)\} = \{\tilde{F}(\omega)\} \qquad (2\text{-}51)$$

where $[M]$, $[C]$ and $[K]$ describe the mass, damping and stiffness matrices, respectively. $\{\tilde{u}(\omega)\}$ and $\{F(\omega)\}$ define the vector of displacements and forces as functions of the angular frequency ω. In general, the frequency-domain equation of motion can be derived by either applying the Fourier transformation or by assuming the following harmonic solution [8,170]:

$$\{u(t)\} = \{\tilde{u}(\omega)\}e^{i\omega t} \qquad (2\text{-}52)$$

In a similar manner to time-domain approaches, both the train and the track systems are coupled at the contact interaction points through compatibility conditions. Furthermore, since the solution is obtained in the frequency-domain, this involves the computation of receptance functions which describe the dynamics of the overall system composed by the train, the track and the contact models [78,83].

2.3.5.3 Wheel-Rail Contact Interaction

2.3.5.3.1 Linear vs Non-Linear Contact

A Hertzian contact spring can be modelled between each wheelset and rail to couple the train and the track systems, and account for the wheel-rail contact interaction [180,187] – see **Figure 2-17**. However, the contact model depends on the train-track system behaviour. Thus, for a non-linear system (i.e. time-domain problem), Hertzian non-linear elastic contact theory can be employed to define the wheel-rail contact force P in the time-domain [46,180,188,189]:

$$P(t) = \begin{cases} C_{Hz} \cdot \delta(t)^{3/2}, & \delta(t) > 0 \\ 0\ , & \delta(t) \leq 0 \end{cases} \tag{2-53}$$

$$\delta(t) = u_w(t) - u_r(t) - r(t) \tag{2-54}$$

where C_{Hz} is the Hertzian constant, and $\delta(t)$ is the material deformation or contact deflection which relates the relative displacement between the wheel $u_w(t)$ and the rail $u_r(t)$ with the roughness $r(t)$, as described in equations **Eqs.** (2-53) and (2-54).
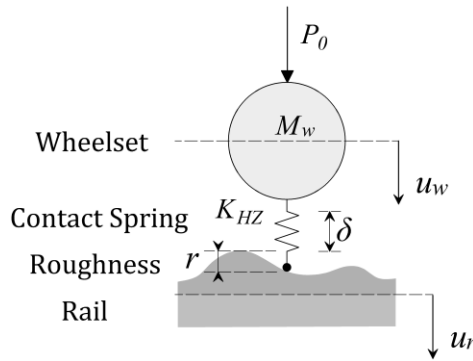
Figure 2-17. Wheel-Rail contact model [180]

Alternatively, when dealing with linear systems, (e.g. frequency-domain solutions) this Hertzian non-linear contact spring must be linearised. Firstly, assuming that the wheelset and the rails are always in contact, it is possible to define the dynamic displacement of the wheelset $u_w(\omega)$ [170,188,190,191], as shown in **Eq.** (2-55):

$$u_w(\omega) = u_r(\omega) + r(\omega) + \frac{\tilde{P}(\omega)}{K_{Hz}} \tag{2-55}$$

where $u_r(\omega)$ and $r(\omega)$ are the displacements at the rail level and at the wheel-rail contact point (roughness), $\tilde{P}(\omega)$ is the contact loading, and K_{Hz} is the linear Hertzian spring. Next, by inverting **Eq.** (2-55), the contact force in the frequency-domain is defined as:

$$\tilde{P}(\omega) = -\frac{r(\omega)}{\alpha_w(\omega) + \alpha_r(\omega) + \alpha_c(\omega)} \tag{2-56}$$

$$\alpha_c(\omega) = \frac{1}{K_{Hz}} \tag{2-57}$$

where $r(\omega)$ is the roughness excitation; and $\alpha_w(\omega)$, $\alpha_r(\omega)$ and $\alpha_c(\omega)$ define the receptance of the wheel, the rail, and receptance at the contact spring, respectively. Linearization of the contact force can be defined assuming small variations in the length of the contact spring [13,79,192]:

$$P = P_0 + dP \tag{2-58}$$

$$dP = K_{Hz} \cdot d\delta \tag{2-59}$$

where P_0 is the nominal preload, and dP is the varying contact force which relates the Hertzian linear spring K_{Hz} and the variation of the contact deflection $d\delta$, as depicted by **Eq.** (2-59). **Figure 2-18** presents the non-linear contact force/deflection relationship with its linear approximation.
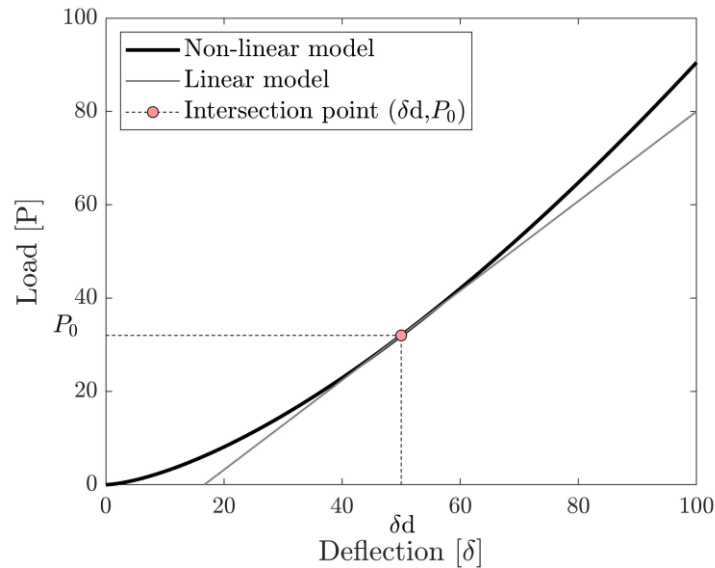
Figure 2-18. Linear vs Non-linear wheel-rail contact models [192]

In general, the previous contact models follow Hertzian contact theory, which is formulated using the theory of elastic half-space bodies. Therefore, it assumes that the bodies under contact are infinitely large half-spaces with perfectly linear elastic behaviour, perfectly smooth surfaces, no friction at the contact point, and can be

defined through quadratic (parabolic) functions in the contact point's vicinity [172,193,194]. These assumptions do not fully describe the real behaviour of wheel-rail bodies in contact. Thus, to allow for a closer representation of the wheel-rail contact behaviour, non-Hertzian theory can be employed [194–197]. Perhaps the most commonly used formulation is that developed by Kalker [195], in which a potential contact area is arbitrarily defined and discretised into several rectangular elements of constant magnitudes (i.e. deflections and displacements).

2.3.5.4 Irregularities

2.3.5.4.1 Track Irregularities

There are a variety of types of rail irregularities/unevenness, including longitudinal, lateral, cross-level, and gauge. These irregularities can be simulated in computational models using data collected directly from track-recording vehicles (TRV) [198–200], or synthetically generated using stochastic methods (e.g. Power Spectral Density (PSD)) [13,199,201,202]. BOEF models are frequently used to investigate vertical response (i.e. rather than lateral), and therefore longitudinal irregularities are most commonly studied [95,203–205].

Singular rail irregularities include joints, switches and crossings, and although they form part of the longitudinal profile, they generate isolated and much higher impact forces compared to standard rail unevenness [206]. Therefore these require additional modelling consideration, typically using time-domain models to simulate the non-linear, high frequency, wheel-rail contact [79,156,207,208].

2.3.5.4.2 Wheel Irregularities

Wheel defects lead to increased noise, vibration, impact forces and passenger discomfort. These defects are known as out-of-roundness (OOR) irregularities, and include: eccentricity of the wheel, discrete defects (wheel radius deviation), wheel corrugation and wheel-flats [97,209–211]. In general, wheel-rail contact can be approximated as linear for small OOR values, and thus modelled as an equivalent rail unevenness. However, larger levels of OOR (e.g. wheel-flats) generate rapid changes in force as the wheel spins, meaning their simulation requires the use of non-linear contact models [188,189].

2.4 Example Application of Solution Methods

BOEF models can be used to study a wide range of railway engineering problems. This Section addresses two common applications, solving them using a selection of the methods discussed previously:

1. *Track-ground dynamics* - the effect of train speed on track deflection is analysed. Ballast and slab track models are considered.
2. *Ground-borne vibration* – the effect of ballast and slab tracks on ground-borne vibration is considered. Track receptance and free-field transfer functions are analysed.

Table 2-1 summarises the solution methods used for each application and the results shown.

No.	Application	Results	Solution Methods
1	Track Dynamics	Track deflection Ground surface contour Dynamic amplification	Thin-layer method
2	Ground-Borne Vibration	Track receptance Ground transfer Free-field transfer function	Domain transformation method

Table 2-1. Results and solution methods used in each application

2.4.1 Application no. 1: Track-Ground Dynamics

The response of the ballasted track model developed in Alves-Costa [167,169] is compared to the response of a slab track model [75,169] – see Appendix A. Both track models are subject to a constant moving force $F = 150$ kN (i.e. zero riding frequency, $\bar{f} = 0$ Hz). Regarding the soil, a layered ground resting on a half-space is coupled to the track through compatibility conditions (i.e. equilibrium of forces and continuity of displacements). **Table 2-2** and **Table 2-3** present the track components and soil properties employed, respectively. Note that the material and geometrical values employed in both application described in this Chapter, are based on examples depicted by [10,51,75,170,212] in the case of the track and [68,70,75,170] in the soil.

Component	Parameter		Units	Value
(One) Rail	$E_r I_r$	Bending moment	[MNm^2]	6.38
	m_r	Mass per unit length	[kg/m]	60.23
Railpad	k_{rp}	Stiffness per unit length	[MN/m^2]	350
	η_{rp}	Damping loss factor (hysteretic)	[−]	0.15
	c_{rp}	Damping (viscous)	[Ns/m]	3.84E+04
(Half) Sleeper	m_s	Mass per unit length of rail	[kg/m]	245
Ballast	k_b	Stiffness per unit length	[MN/m^2]	180
	c_b	Damping (viscous)	[Ns/m]	2.34E+05
	H_b	Height	[m]	0.35
	E_b	Young's modulus	[MPa]	140
	ρ_b	Density	[kg/m^3]	1700
	C_p	Compression wave speed	[m/s]	3.33E+02
	B	Track width	[m]	2.5
	m_b	Mass per unit length of rail	[kg/m]	1695.80
Slab	L_{sb}	Length	[m]	2.5
	H_{sb}	Thickness	[m]	0.25
	E_{sb}	Young's modulus	[GPa]	30
	ρ_{sb}	Density	[kg/m^3]	2500
	m	Mass per unit length	[kg/m]	1250
	I_{sb}	Inertia	[m^4]	3.26E-03
	$E_{sb}I_{sb}$	Bending stiffness	[MNm^2]	97.7

Table 2-2. Continuous track components

Layer	Depth h [m]	Young's modulus E [MPa]	Poisson's ratio ν [−]	Density ρ [kg/m^3]	Loss factor η [−]
1	2	60	0.35	1500	0.06
Half-space	∞	200	0.35	1800	0.06

Table 2-3. Soil parameters

An appropriate model discretisation is required to obtain accurate space-time results. In the case of the wavenumber sampling β, typically, this is defined via the wavelength λ by [213,214]:

$$\beta_{\max} = \frac{2\pi}{\lambda_{\min}} \tag{2-60}$$

where $\beta_{\max}$ is the maximum wavenumber and $\lambda_{\min}$ is the shortest wavelength defined as $\lambda_{\min} \approx 8l_e$, with l_e being the node spacing – see [213]. For this particular case, it is assumed that $\lambda_{\min} \approx 0.6$ m, thus resulting in $\beta_{\max} \approx 10$ rad/m. Regarding

wavenumber increment, a total of 2049 values were considered enough to capture the response of the structure. **Eq.** (2-61) shows the total symmetric wavenumber sampling employed in the following simulations:

$$\beta_x = [-\beta_{max} : \beta_{max}/1024 : \beta_{max}] \tag{2-61}$$

Dynamic amplification curves for both the ballast and slab tracks resting on layered soil, excited by a moving constant force F are presented in **Figure 2-19**. It is shown that the ballasted track gives a lower critical speed v_{cr} compared to the slab case, 135 m/s and 171 m/s, respectively. This is due to the additional bending stiffness provided by slab track, which also results in reduced rail deflections compared to the ballasted track case. This effect is also evident in the rail deflections shown in **Figure 2-20**, in which the track response is computed at 100% and 50% of the critical speed for both track types. Note that the maximum deflection occurs at $t = 0$ s, corresponding to the observation point and the location of the force. Around this instant of time, there are trailing oscillations behind the load (i.e. $t < 0$ s).

Surface contours of the layered soils below the track are shown in **Figure 2-21** and **Figure 2-22**, for the ballasted and slab track, respectively. In each case, results are presented for two different speeds: (a) 50% and (b) 100% of the critical value. It is evident that the higher speed results in a larger deflection. The contour shapes are also different, with the higher speed exhibiting conical shaped waves and trailing oscillations, which are absent at the lower speed [169,212].
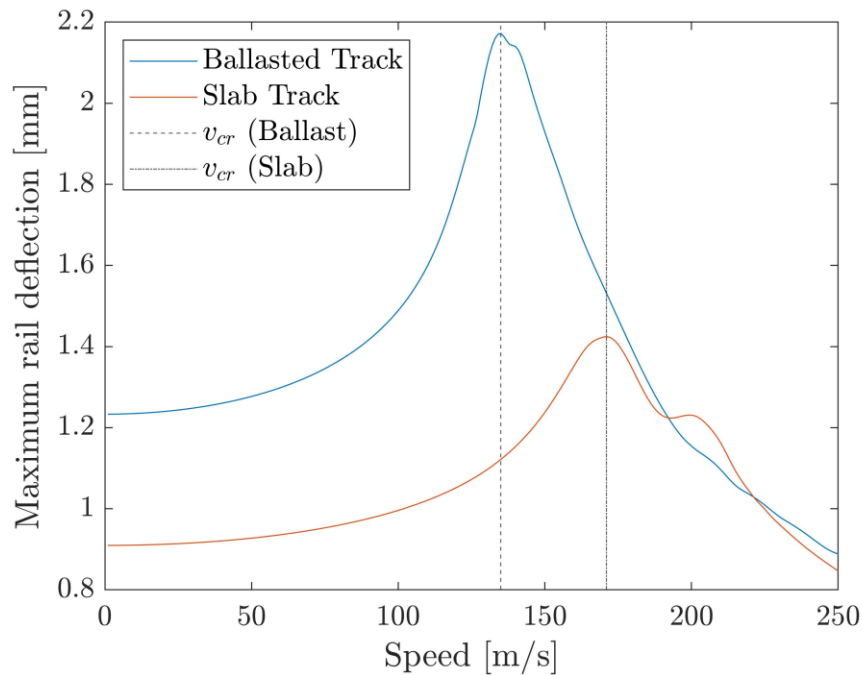
Figure 2-19. DAF of ballasted and slab tracks resting on layered soil due to a moving constant force $F = 150$ kN
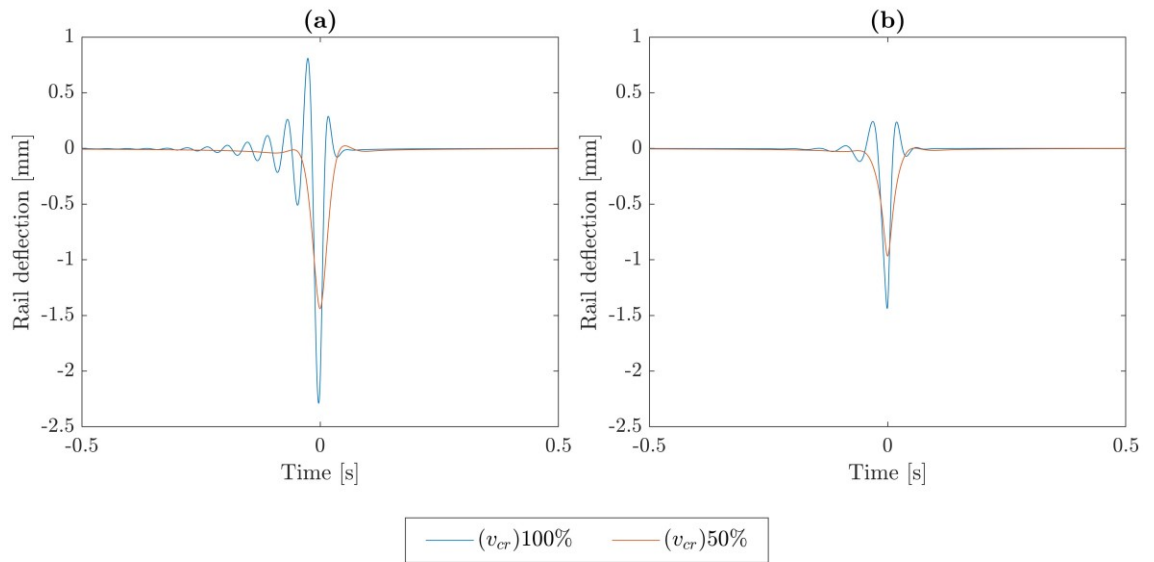
Figure 2-20. Track response on layered soil at 100% and 50% of the critical speed:
(a) ballasted track, and (b) slab track
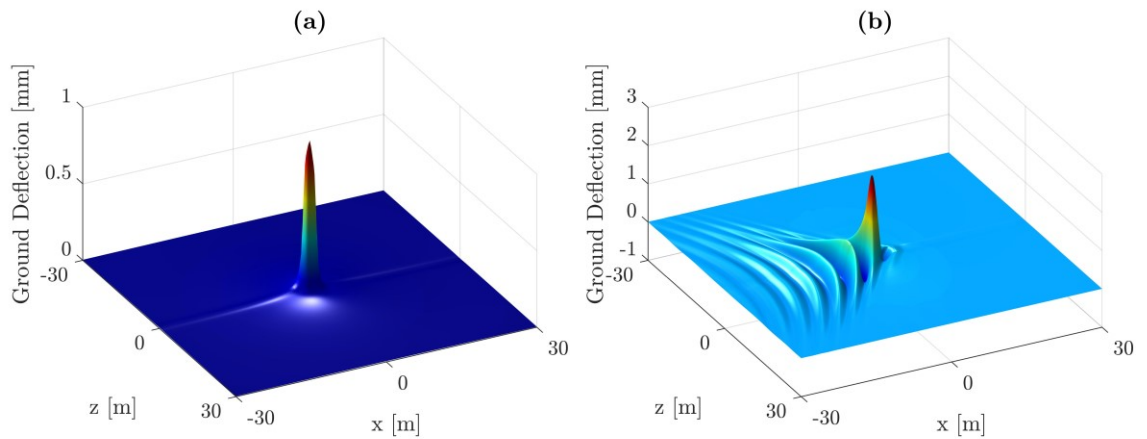
Figure 2-21. Ground contour due to ballasted track, resting on layered soil at:
(a) 50% of the critical speed, and (b) 100% of the critical speed
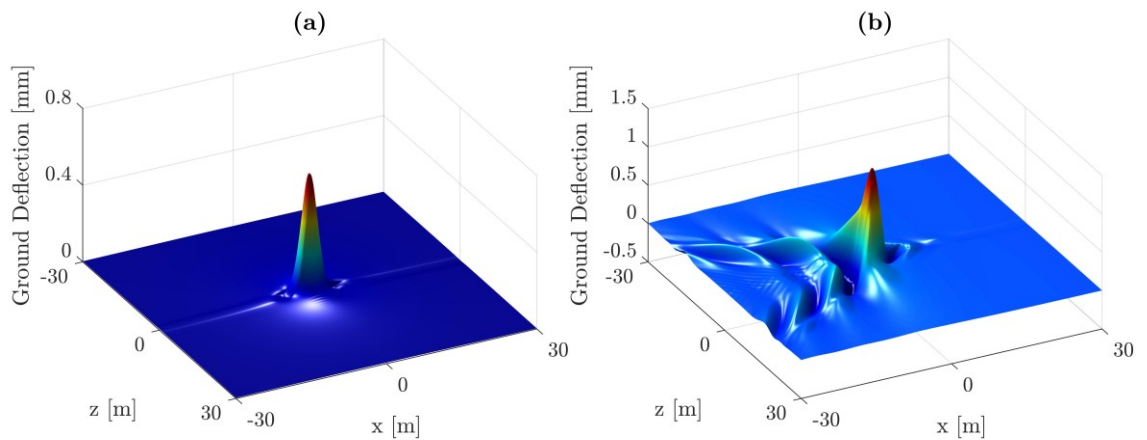
Figure 2-22. Ground contour due to slab track resting on layered soil at:
(a) 50% of the critical speed, and (b) 100% of the critical speed

2.4.2 Application no. 2: Ground-Borne Vibration

Train-induced ground vibrations have two excitation components: quasi-static and dynamic. Although the former plays an important role at lower frequencies in the near-field, the dynamic excitation, resulting from train-track interaction, is a key contributor to ground vibration levels [215,216]. Thus, to study ground-borne vibration dynamics, a sprung mass moving on a track with a rough rail is considered. The sprung mass has $M_w = 2003$ kg and a Hertzian contact stiffness of $K_{Hz} = 1940$ MN/m. It moves with a constant speed on an uneven track profile of class 5, defined according to the Federal Railroad Administration (FRA) [217]. The ballasted track model and layered soil properties from application no. 1 are reused. Alternatively, the soil response is computed through the flexibility method proposed by Sheng and coupled to the track as described in **Eq.** (2-50) [68,70]. Once both the dynamic and quasi-static excitations are obtained, the free-field vibration of the ground is computed at different points from the centreline of the track. Note that some problems (e.g. wear) justify the need for non-Hertzian contact models, however for most of the BOEF applications discussed in this study, the programming effort, additional input parameters, and computational resources required to implement such an approach outweigh the limited improvement in accuracy.

Component	Parameter		Units	Value
Slab	H_{sb}	Thickness	[m]	0.35
	m_{sb}	Mass per unit length	[kg/m]	2188
	I_{sb}	Inertia	[m^4]	8.93E-03
	$E_{sb}I_{sb}$	Bending stiffness	[MNm^2]	268

Table 2-4. Additional track parameters

Layer	Depth h [m]	Young's modulus E [MPa]	Poisson's ratio ν [$-$]	Density ρ [kg/m^3]	Loss factor η [$-$]
Half-space	∞	75	0.35	1800	0.06

Table 2-5. Soil parameters

For the computation of the irregularity profile, the following equations in the wavenumber-domain are employed:

$$\hat{r}(\beta) = \left(\sqrt{2S(\beta)\Delta\beta} \right) e^{i(\beta a - \theta_j)} \tag{2-62}$$

$$S(\beta) = \frac{A\rho_3^2(\beta^2 + \rho_2^2)}{\beta^4(\beta^2 + \rho_3^2)} \tag{2-63}$$

in which $\hat{r}$ is the unevenness function in the wavenumber-domain β, a is the axle position (here assumed to be a $= 0$ m), $\Delta\beta$ is the resolution retained for the spatial frequency, θ is the phase angle taken as a random variable with uniform distribution in the range 0 to 2π. S is the Power Spectral Density (PSD) function defined by the FRA, ρ_2 and ρ_3 are the break spatial frequencies, and A is the roughness constant [13]. Refer to Section 4.2.1.4.1 for more information regarding the definition of the track irregularities.

Figure 2-23 shows the one-third octave band far-field velocity due to the ballasted track resting on a layered soil and excited by a single load moving at 50% of the critical speed, i.e. $v = 135$ m/s $\times 50\% = 68$ m/s. Often, the frequency of interest for the perception of the ground-borne vibration lies within the range $\bar{f} = [1 - 80]$ Hz – see [218–220]. However, since frequencies close to this limit might also contribute to the response, the limit is extended to $\bar{f} = [0.5 - 150]$ Hz (range similar to the used in [78,83]), corresponding to a wavelength range of $\lambda = [0.45 - 135]$m. **Figure 2-23**(a) compares the dynamic, the quasi-static and the total surface response at 20 m from the track axle (i.e. $x = 0$ m, $y = 0$ m, $z = 15$ m). It can be seen that at lower frequency ranges, the quasi-static contribution is large compared to the dynamic case. However, at higher frequencies, the quasi-static response decreases while the dynamic response increases. Overall, the maximum amplitude of the velocity occurs in higher frequencies and is dominated by the dynamic response, a result consistent with the findings of [78]. Alternatively, **Figure 2-23**(b) compares the total response at different positions from the track centreline: 5 m, 10 m and 15 m. It can be seen that the closer to the track, the larger the response. Again, results show that the maximum velocity occurs in the higher frequency range.

To further study soil and track type effects, the track receptance and the track-ground transfer function are computed. To do so, the ballasted track properties presented in **Table 2-2** are again used, however the two-layered ballasted track model proposed by Sheng [68,70] is instead studied – see Appendix A. For the slab track, the same model is employed, however with thickness as shown in **Table 2-4**. The layered soil properties are shown in **Table 2-3**, and the homogenous half-space ones shown in **Table 2-5**.
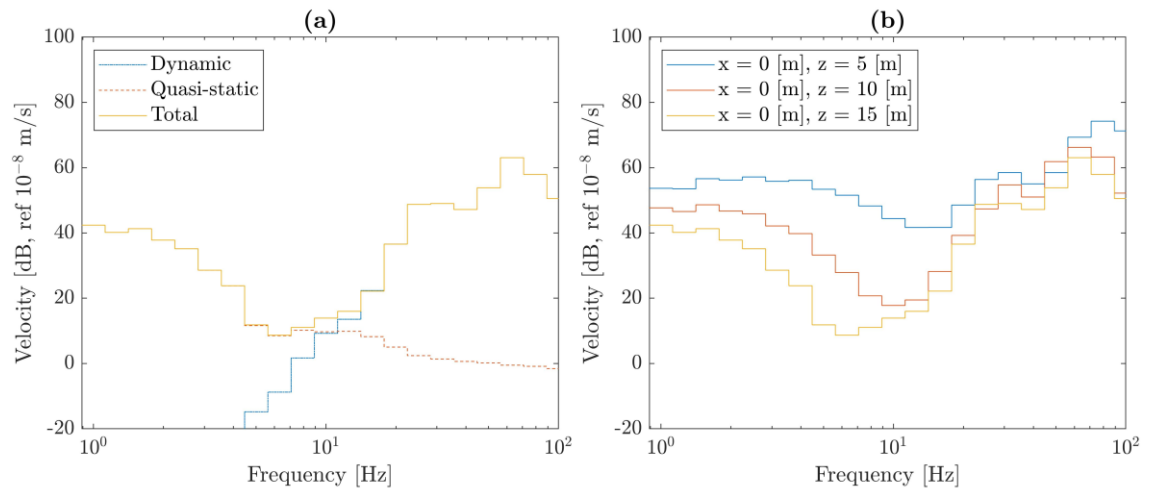
Figure 2-23. Far-field response due to ballasted track model resting on layered soil – 50% of the critical speed: (a) 15m from the track axis; and (b) 5m, 10m and 15m from the track axis

Figure 2-24 present the absolute deflection of (a) the ground and (b) track to a unit harmonic force applied on the rail, i.e. the transfer function of the ground and the track receptance, respectively. In the first case, **Figure 2-24**(a), deflections are measured on the ground's surface below the force application's location (same transversal and longitudinal point, but different vertical coordinate), i.e. the response is a transfer function. Alternatively, in **Figure 2-24**(b), results are computed at the same point where the force is applied, i.e. the response is a track receptance.

Notice that for all track types resting on the layered soil, the first cut-on-frequency occurs in the range $18 - 20$ Hz and yields the maximum response of the soil-track system. Alternatively, the ground and track response corresponding to the homogenous half-space is constant around these frequencies, and its magnitude is lower than the layered case. However, above the cut-on-frequency, the response of both soil cases reduces. In both cases, the maximum deflection at approximately 20 Hz corresponds to the amplification effect of the subgrade's response, occurring at the subgrade's resonance frequency.

Overall, **Figure 2-24** shows the effect of soil layering, and the potential discrepancies introduced when approximating a layered soil as homogenous. Furthermore, regardless of soil properties, the largest rail deflection is obtained for ballasted tracks rather than slab.

Figure 2-25 and **Figure 2-26** show the ground surface response due to the ballasted track model at its corresponding cut-on-frequency (20 Hz) for both homogenous half-space and layered soil cases, respectively. In both cases, the absolute response drops quickly beyond the edges of the track, particularly along the perpendicular z axis. However, the layered soil gives larger deflections than the homogenous half-

space. In addition, the real components in both soil cases show an oscillating behaviour, again larger for the layered soils compared to the homogenous half-spaces.
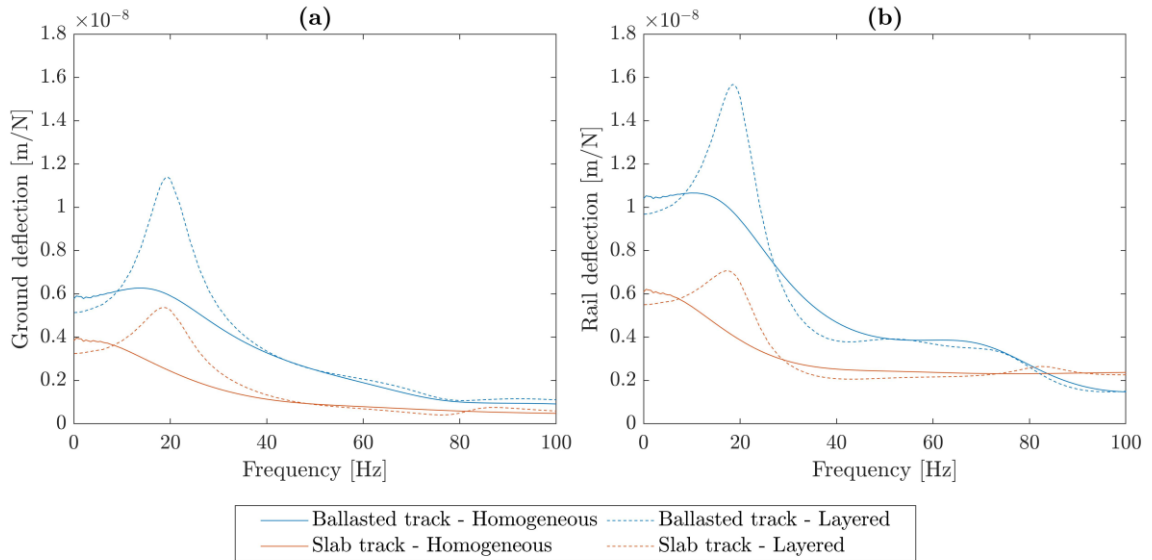
Figure 2-24. Response due to track resting on homogenous half-space and layered soil: (a) ground deflection, and (b) track deflection

Although the layered effect is crucial for accurately representing the supporting soil, it is not included in this thesis's analysis performed in the following Chapters – see Chapter 6 and Chapter 7. This decision is due to the increased programming effort, additional input parameters, the large number of permutations required in the analysis, and computational resources required to model the layered effect.
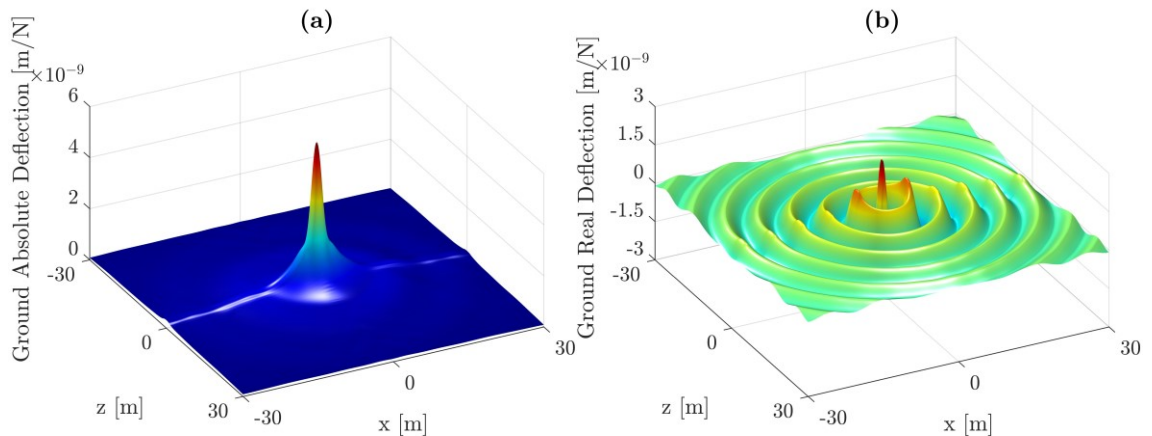
Figure 2-25. Homogenous half-space soil response – ballasted track model: (a) absolute response, and (b) real response
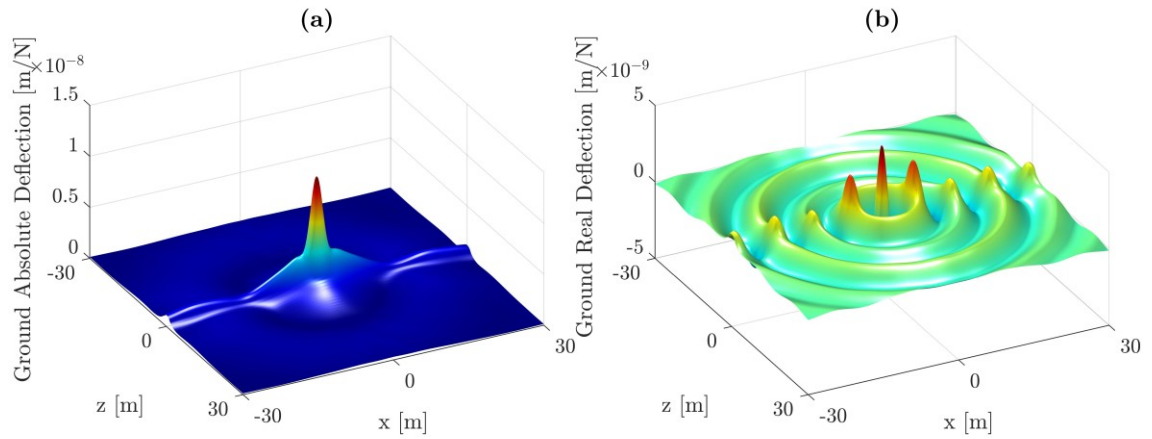
Figure 2-26. Layered soil response – ballasted track model: (a) absolute response, and (b) real response

2.5 Challenges associated to BOEF Approaches

Beam on Elastic Foundation (BOEF) approaches are widely employed when studying railway track dynamics. Most commonly they assume the track response can be approximated using a single-layer continuous beam supported by continuous springs-in-series (representing the rails and the underlying track layers, respectively), thus, offering a straightforward and computationally efficient approach. While the fundamental BOEF formulation can be extended to incorporate additional track components such as lumped masses and elastic layers, addressing the discrete support effect and accurately replicating 3D wave propagation within the track demands supplementary methodologies. These factors are particularly critical for railway analysis at both higher and lower frequency ranges.

To overcome this, the track requires incorporation of a certain degree of periodicity and/or 3D simulations to faithfully capturing the discrete support effect and geometry of each track component. The challenges associated with the basic BOEF formulation and how they are overcome using periodic and/or 3D modelling are:

- *Rail support conditions.* The fundamental BOEF formulation employs continuous support conditions to represent railpads and sleepers, both track components exhibiting discrete behaviour. Although acceptable for replicating some track effects, continuous supports cannot capture higher frequency results accurately (e.g. pin-pin frequency). To address this limitation and simulate the discrete support effect, periodic conditions can be integrated into BOEF formulations. In this, periodicity is accounted for via the support arrangement, which repeats n times along the train passage direction with a constant spacing d – see for instance **Eq.** (2-12). Despite the improvement in the support definition, BOEF often defines railpad

components via springs and dampers [156,221]. These elements are described by minimal parameters (stiffness and damping only), ignoring the actual dimensions of the components and assuming small and rigid point supports spaced by length d (in the case of discrete supports) – see **Figure 2-27**(a). Instead, FEM employs elements defined by several material (stiffness, damping, Poisson's, density, etc.) and geometrical parameters (length, height, width), thus providing a more realistic representation of the railway system's behaviour [222] – as shown in **Figure 2-27**(b). In this, a ballasted track is simulated via solid Finite Elements, which allows for actual railpad dimensions with effective support spacing (from end to end) d differing from the support spacing (from mid- to mid-point) d^*.

- *Track components.* BOEF can consider various track components via multi-layer models. However, it typically combines several layers (e.g. ballast and sub-ballast) into equivalent parameters and disregards some of their mechanical behaviour and real dimensions – **Figure 2-27**(a) shows lower track components combined into the single layer 'foundation'. In contrast, FEM complexity facilitates several track components' mechanical behaviour representation [14,136] – as illustrated in **Figure 2-27**(b), in which ballast and sub-ballast layers are simulated separately.

- *Subgrade conditions.* BOEF employs springs-in-series elements to simulate the soil behaviour, thus, it is unable to reproduce the wave propagation within the soil and leads to an inaccurate dynamic track-ground response – see **Figure 2-27**(a). Alternatively, FEM allows for a more accurate mechanical representation of the supporting soil, considering their actual material properties, a closer geometrical domain, and its wave propagation effect [15,212] – see **Figure 2-27**(c).

2.6 Conclusions

This Chapter presents a state-of-the-art technical review of Beam on Elastic Foundation theory. It is shown that at a basic level, the use of a single continuous beam resting on a springs-in-series support is straightforward to implement and computationally efficient. Various BOEF modelling strategies and solution methods employed for the computation of track behaviour are reviewed.

Additional complexity is integrated into the fundamental BOEF formulation to accommodate discrete supports and multi-layered characteristics. While offering greater flexibility and potentially increased accuracy compared to continuous and single-layer models, these BOEF formulations have various limitations. For instance, a degree of periodicity must be introduced to address the discrete effect of the track

– see **Eq.** (2-12). In addition, simplifications in the support representation using springs, dashpots, and masses (all basic or primary elements) cannot accurately replicate their intricate geometries and mechanical behaviour. Similarly, multi-layered models also employ primary elements to integrate additional excitation mechanisms to simulate both track types and often combine different track components into equivalent layers, thus constraining the track approximation.
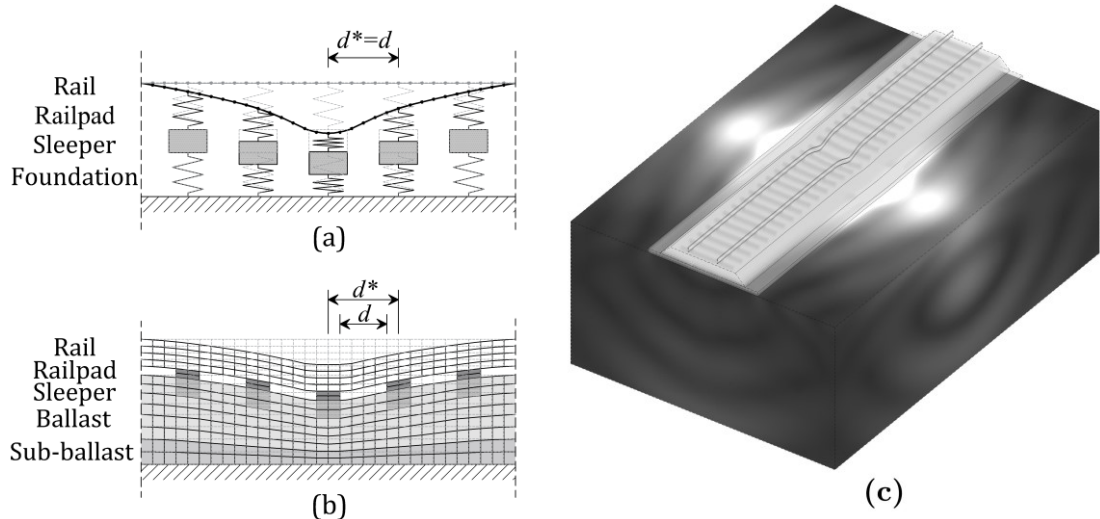
Figure 2-27. Track simulation comparison: (a) track on rigid support – BOEF model, (b) track on rigid support – FE model, and (c) track on flexible support – wave propagation effect (mesh omitted for visibility)

Considerations for extending BOEF approaches to approximate train-track and track-ground interactions are also discussed. Different vehicle and ground models were introduced in both cases, and the solution method involved coupling them with the track. It is observed that the springs-in-series layer in the basic BOEF, intended to mimic soil behaviour, fails to simulate wave propagation effects and requires additional and more complex methodologies for this purpose.

Overall, the majority of BOEF limitations outlined in this Chapter can be addressed through FEM. This approach can incorporate complex geometries and additional mechanical properties into the representation of track and ground behaviour. Despite offering strong modelling flexibility, FEM demands computationally intensive simulations, especially when analysing larger structures. To overcome this, approaches exploiting the periodic nature of track structures offer a promising alternative. These methods have the potential to reduce the computational effort while preserving accuracy.

Chapter 3

Periodic Approaches for Railway Track Simulation

3.1 Introduction

Railway engineering problems have been studied via analytical, semi-analytical and numerical approaches. Some methods, such as Beam on Elastic Foundation (BOEF) formulations, struggle to fully capture 3D wave propagation effects. Attempting to address this limitation, semi-analytical approaches can incorporate a more accurate representation of the ground. However, analytical and semi-analytical strategies rely on simplified approximations of the railway system components. To address this, Finite Element (FE) methods have been implemented. Although numerical methods potentially provide more flexibility to model the true geometry of a railway track compared to analytical and semi-analytical methods, they are computationally demanding. To reduce the computational effort while still delivering accurate approximations of the structure's behaviour, periodic strategies are a promising solution.

This Chapter introduces the framework of periodic approaches. Firstly, Section 3.2 describes various solutions for periodic track structures, including considerations for semi-periodic structures. Following this, Section 3.4 presents examples of applications for two common railway problems using periodic approaches. Section 3.5 outlines the challenges associated with the fundamental periodic approach. Then, in Section 3.6, the studied periodic approaches are compared against the analytical and semi-analytical techniques introduced in Chapter 2, and the solution techniques are classified and ranked according to their suitability for the study of railway engineering problems. Finally, conclusions are highlighted in Section 3.7.

3.2 Solutions for Periodic Track Structures

Periodicity implies the presence of repetitive features, such as geometrical or material properties. Periodic structures can be found in both ballast and slab tracks, for which repetitive parameters (such as material properties and track dimensions) are present in the train passage direction. In ballasted tracks, periodicity arises from the repeated pattern provided by the sleepers [223,224] as shown in **Figure 3-1**(a). Similarly, slab tracks have a periodic nature due to either the discrete rail-seats [225,226], or repeating slab units [36,98,227,228]. **Figure 3-1**(b) and (c) show examples of 3D FE meshes of slab track periodicity in terms of rail-seats and slab panels respectively.

Periodicity in the track can be studied using a fully-periodic or semi-periodic approach. In the former, the entire and infinitely extending track is assumed to have invariant material and geometric properties. In contrast, the periodicity of semi-periodic structures is restricted to specific sections that are discretised according to their parameters (i.e. discrete patterns or discrete periodicity) which are later combined through compatibility conditions. **Figure 3-2**(a) shows a fully-periodic, Ω, BOEF model with restricted domains $\widetilde{\Omega}$ of length d, while **Figure 3-2**(b) presents a semi-periodic BOEF model comprised of four periodic domains or sections (Ω_A, Ω_B, Ω_C and Ω_D) coupled to each other.

To study longer structures (e.g. infinitely long tracks) and still provide accurate results with minimal computational effort, the periodic nature of the track (i.e. invariant geometrical and material properties) is exploited during modelling and analysis. With this method, the response of the complete periodic domain Ω (i.e. the total invariant structure), is obtained by restricting the study domain to only a portion $\widetilde{\Omega}$ of the structure (also known as the restricted, generic, or unit cell, as shown in **Figure 3-2**), which is later used to retrieve the total response via compatibility conditions at the boundaries of $\widetilde{\Omega}$.

3.2.1 Discrete Supports

Despite often being used to provide an approximation of discrete track response, continuously supported track models are unable to fully capture the discrete character of such structures. This discrete behaviour is generated for example by the sleepers (parametric excitation), which are periodically spaced and give rise to a change in dynamic stiffness, which includes the 'pinned-pinned' resonance frequency [8,10,45,51].
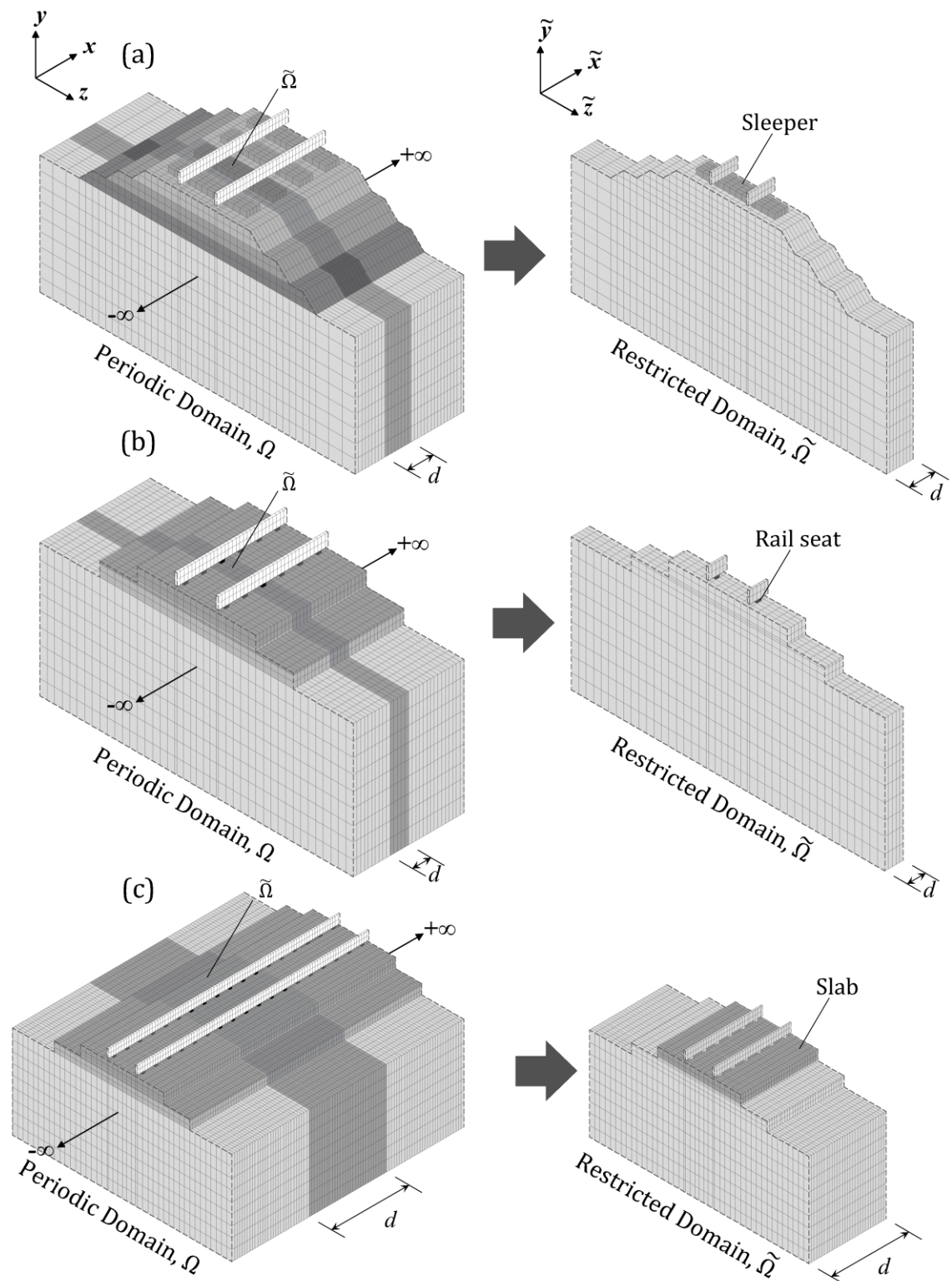
Figure 3-1. Overview of 3D periodic and restricted domains:
(a) ballasted track – periodicity due to sleeper placement, (b) slab track – periodicity due
to rail-seats, and (c) slab track – periodicity due to the discontinuous slabs

3.2.1.1 Point Source Method

In the analytical point-source method described by Heckl [229], the discrete nature of railway track supports is modelled in the form of reaction forces, which are proportional to the displacements generated at the support points. Heckl assumes the track is subject to an external stationary vertical point-force modelled as a free (i.e. infinitely long) Timoshenko beam discretely supported by a spring-mass-spring element representing the railpad, the sleeper, and the ballast, as shown in **Figure 3-3**.

(a)

(b)
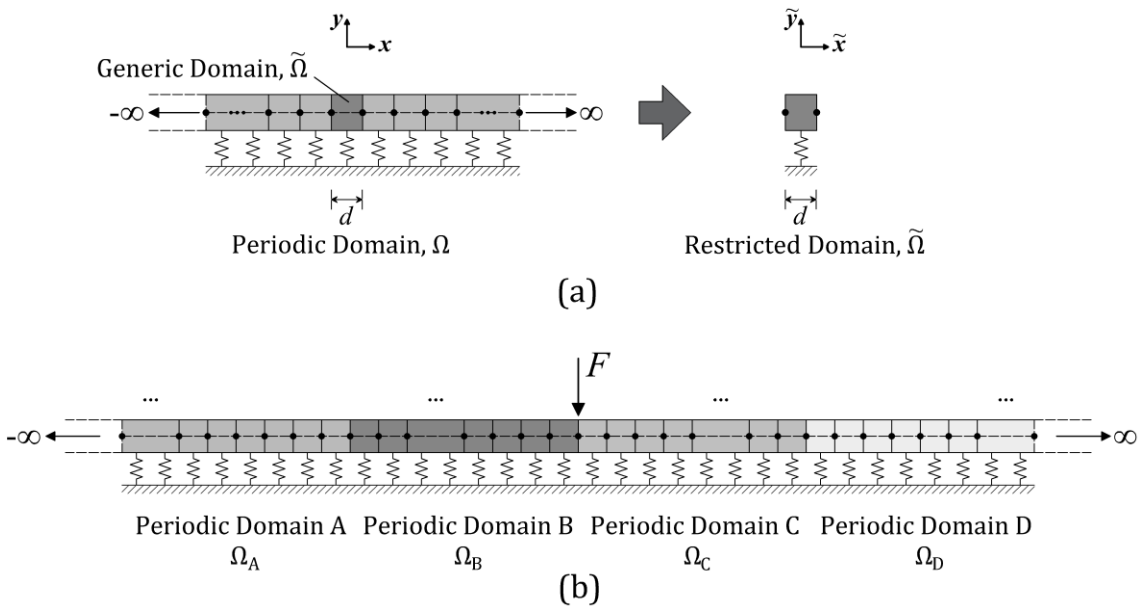
Figure 3-2. BOEF model with: (a) fully-periodic domain, and (b) four semi-periodic domains
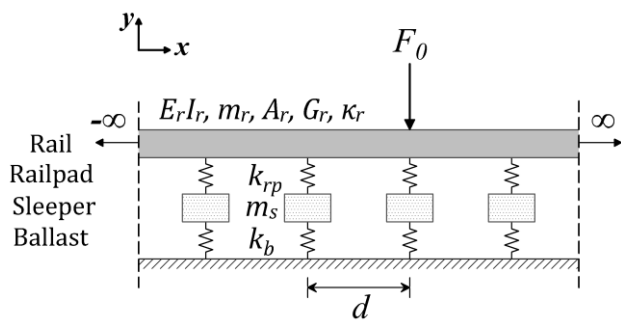
Figure 3-3. Discretely supported track model [229]

The track response is computed using superposition, considering both the effect of the wheel force and the point force at the structure's multiple discrete supports. Based on this, the receptance response $\alpha(x, x_F)$ at any point x of the beam due to a unit point force $F = 1$ applied at x_F, is first determined by [10,229]:

$$\alpha(x, x_F) = u_p e^{-i\beta_p|x-x_0|} + u_e e^{-i\beta_e|x-x_0|} \tag{3-1}$$

$$u_{p,e} = \frac{i}{G_r A_r \kappa_r}\left(\frac{\beta_{p,e}^2 + A_1}{4\beta_{p,e}^3 + 2\beta_{p,e}A_2}\right), \quad \beta_{p,e}^2 = -\frac{1}{2}A_2 \pm \frac{1}{2}\sqrt{A_2^2 - 4A_3}$$

$$A_1 = \frac{G_r A_r \kappa_r}{E_r I_r} - \frac{\rho_r I_r \omega^2}{E_r I_r}, \qquad A_2 = -\left(\frac{m_r \omega^2}{G_r A_r \kappa}\right) - \left(\frac{\rho_r I_r \omega^2}{E_r I_r}\right), \tag{3-2}$$

$$A_3 = \left(\frac{m_r \omega^2}{E_r I_r}\right)\left(\frac{\rho_r I_r \omega^2}{G_r A_r \kappa_r} - 1\right)$$

where u_p and u_e are the amplitude of the propagating bending wave, and the peak value of the bending wave in the near-field respectively; the wavenumbers β_p and β_e correspond to the solution close to the positive real and negative imaginary axes respectively – see **Eq.** (3-2). Constants A_1, A_2 and A_3 relate the various Timoshenko beam parameters, where A_r is the cross-sectional area, ρ_r is the density, m_r is the rail mass, E_r is the Young's modulus, G_r is the shear modulus, and κ_r is the shear coefficient.

Note that Timoshenko's theory [49] – see Section 2.3.1, includes the shear deformation and rotational inertial contribution in its formulation. Thus, the model presented in **Figure 3-3** accounts for both vertical deflections and rotations. However, since the response is obtained via free wave solutions in the frequency-domain, the solution is expressed in terms of complex amplitudes and the various Timoshenko parameters, as shown in **Eq.** (3-2). For more information, please refer to [10].

To compute the response of a discretely supported periodic track, consider an infinitely long Timoshenko beam with n equally spaced supports at positions $x_n = nd$. Furthermore, at positions x far from the excitation point x_0 (i.e. $x \gg x_0$), the response is negligible so can be ignored; thus, it is only required to consider a large, but not infinite, number of supports: $n = -N, \dots, N$. In general, the method assumes that each support exerts a point force $F_n = -Du(x_n)$ at each x_n in the beam, where D is the dynamic stiffness of the support. Next, using the superposition principle, the track response $u(x)$ can be defined [10,51,229]:

$$u(x) = F_0 \alpha(x, x_0) + \sum_{n=-N}^{n=+N} F_n \alpha(x, x_n) \tag{3-3}$$

where both receptance values $\alpha(x, x_F = x_0)$ and $\alpha(x, x_F = x_n)$ are computed from **Eq.** (3-2). Notice that the left term in **Eq.** (3-3) corresponds to the response due to the external wheel force $F = F_0$, in which the position $x_F = x_0$ is in the range $0 \leq x_0 \leq L$. The right hand term refers to the response due to the point forces $F = F_n$, arising from the supports at positions $x_F = x_n$. For the track model depicted in **Figure 3-3**, the dynamic stiffness D of the support includes the effect of the railpad, sleeper and the ballast, such that [10,230,231]:

$$D = \frac{m_s \omega^2 k_{rp} - k_{rp} k_b}{m_s \omega^2 - \left(k_{rp} + k_b\right)} \tag{3-4}$$

where m_s is the mass of the sleeper, and k_{rp} and k_b refer to the stiffness of the railpad and ballast, respectively. Note that **Eq. (3-4)** refers to a discrete support, thus, $\mathrm{m_s}$ is given in [kg] and $\mathrm{k_{rp,b}}$ in [N/m]. Next, **Eq. (3-3)** is evaluated at a particular support at position $x = x_m$ – resulting in **Eq. (3-5)**, which allows the formulation of **Eq. (3-6)**, that can be inverted to obtain the response $u(x_n)$ [10,229]:

$$u(x = x_m) = F_0 \alpha(x_m, x_0) - D \sum_{n=-N}^{n=+N} u(x_n)\alpha(x_m, x_n) \tag{3-5}$$

$$([I] + D[\alpha(x_m, x_n)])\{u(x_n)\} = F_0\{\alpha(x_m, x_0)\} \tag{3-6}$$

In **Eq. (3-6)**, both the identity matrix $[I]$ and the receptance matrix at all support points $[\alpha(x_m, x_n)]$ have size $(2N + 1 \times 2N + 1)$, both the vector of transfer receptance for point x_0 $\{\alpha(x_m, x_0)\}$ and the vector of displacements $\{u(x_n)\}$, have size $(2N + 1 \times 1)$. Once $u(x_n)$ is obtained through **Eq. (3-6)**, this is inserted in **Eq. (3-3)** and the displacement of the track $u(x)$ at a general point is computed [10,51].

When a unit force is considered ($F_0 = 1$), **Eq. (3-5)** describes the point receptance of the discrete system in the frequency-domain, i.e. $u(x = x_m) = \alpha(\omega)$. This allows for the definition of the decay rate of vibration Δ, a parameter which describes the noise radiated from the track structure [230,232,233]:

$$\Delta \approx \frac{4.343|Y(x = 0)|^2}{\sum_{x_n=0}^{x_{max}}|Y(x_n)|^2 \, \Delta x_n} \tag{3-7}$$

in which the mobility function, defined by $Y = \alpha(\omega) \, \omega$, is computed at different measurement points x_n, including the first point in the grid $x = 0$ and the last or maximum measurement point x_{max}, and Δx_n is the distance between the mid-points of the intervals of the grid.

3.2.1.2 Dirac Comb Approach

The Dirac Comb approach, is an analytical method that describes the discrete support effect through a Dirac Delta function $\delta(x - nd)$ in which the response is non-zero at the support position $x = nd$. Thus, considering an infinitely long track structure with n support points, its solution requires the inclusion of all the supports by means of a Dirac Comb function $\Pi(x)$ [90–93], as shown in **Eq. (3-8)**:

$$\Pi(x) = \sum_{n=-\infty}^{n=+\infty} \delta(x - nd) \tag{3-8}$$

Combining **Eq.** (3-8) with the differential equation of motion for a Euler-Bernoulli beam subject to a load $F(x,t)$:

$$E_r I_r \frac{\partial^4 u(x,t)}{\partial x^4} + m_r \frac{\partial^2 u(x,t)}{\partial t^2} + \Pi(x) \left[k_{rp} u(x,t) + c_{rp} \frac{\partial u(x,t)}{\partial t} \right]$$
$$= F(x,t) \tag{3-9}$$

The first two terms in **Eq.** (3-9) are related to the continuous rail, where $E_r I_r$ and m_r are the flexural bending and mass of the rail, respectively. On the contrary, the terms in brackets of **Eq.** (3-9), correspond to the discrete supports with the stiffness k_{rp} and damping c_{rp}. **Eq.** (3-9) in the space-time-domain (x,t) is analytically transformed, through the inverse Fourier, into the wavenumber-frequency-domain (β, ω):

$$E_r I_r \beta^4 \tilde{u}(\beta, \omega) - \omega^2 m_r \tilde{u}(\beta, \omega) + \left[i\omega c_f + k_f \right] \sum_{n=-\infty}^{n=+\infty} \hat{u}(nd, \omega) e^{-ind\beta}$$
$$= \tilde{F}(\beta, \omega) \tag{3-10}$$

Since the supports n are equally spaced by length d, the structure is periodic with period d. This allows the track response $\hat{u}(nd, \omega)$ in **Eq.** (3-10) to be rewritten according to Floquet's theorem [36,86,92,93]:

$$\hat{u}(x + nd, \omega) = \hat{u}(x, \omega) e^{ng} \tag{3-11}$$

Where g is a complex coefficient of propagation. Thus, with $x = 0$, **Eq.** (3-11) can be combined with **Eq.** (3-10), yielding:

$$E_r I_r \beta^4 \tilde{u}(\beta, \omega) - \omega^2 m_r \tilde{u}(\beta, \omega)$$
$$+ \left[i\omega c_{rp} + k_{rp} \right] \hat{u}(0, \omega) \sum_{n=-\infty}^{n=+\infty} e^{ng} e^{-ind\beta} = \tilde{F}(\beta, \omega) \tag{3-12}$$

It should be noted that solutions computed through **Eq.** (3-11) are valid for the entire structure [92]. This allows the problem to be simplified, requiring only the computation of $\hat{u}(x = 0, \omega)$ in **Eq.** (3-11) to retrieve the response anywhere in the domain.

3.2.1.3 Time-Domain Green's Function Approach

A common BOEF modelling strategy is to compute the Green's function for a BOEF system in the frequency-wavenumber-domain and combine it directly with a frequency-wavenumber defined load [84,92]. However, if non-linear train-track interaction is of interest, a space-time-domain Greens' approach for the track can be useful, because then the train-track interaction is not restricted to being a linear system. To achieve this, in the semi-analytical Green's function approach [81,82,179], the frequency-wavenumber Green's function is transformed into the space-time-domain, before combining with a load defined in terms of time.

The space-frequency-domain Green's function can be computed either in a fixed [81] or moving reference frame [82,179]. In the former, the load speed v is disregarded and the Green's function is stationary, i.e. the track receptance is computed. Alternatively, in the latter case, the speed is directly accounted for inside the Green's function formulation. Considering a moving reference frame, the Green's function G for a track resting on n discretely supported sleepers equally spaced by a length d – see **Figure 3-3**, can be defined in the space-frequency-domain through **Eq.** (3-13) [53,179]:

$$\hat{G}(x', x_0 = a + vt, \omega) = \sum_{n=-\infty}^{n=+\infty} \hat{G}_n(x', \omega)\, e^{-i2\pi n(x=a+vt+x')/d} \qquad (3\text{-}13)$$

Where $\hat{G}$ is the track response at the observation point: $x = a + vt + x'$, due to a unit impulse applied at, $x_0 = a + vt$. The initial position of the force is: $x_0 = a$ (at $t = 0$ s), where x' is the space coordinate measured from the load position, and ω is the angular frequency. Once $\hat{G}$ is determined, an inverse Fourier transformation is employed – see **Eq.** (2-34), to obtain the time-domain moving Green function, as a function of time τ:

$$G(x', x_0, \tau) = \frac{1}{2\pi} \int_{-\infty}^{+\infty} \hat{G}(x', x_0, \omega)\, e^{i\omega\tau} \mathrm{d}\omega \qquad (3\text{-}14)$$

where the moving Green's function G can be interpreted as the track response computed at the observation point $x = a + v(\tau - t) + x' = v\tau = a + vt + x'$ at the time instant τ, due to a unit impulse force at $x_0 + v(\tau - t)$ at $\tau = 0$ – see [179]. Finally, the total track response is computed through a Duhamel's or convolution integral [112,234,235] which combines both the response due to a unit impulse (i.e. the Green's function) and the external force F [82,179]:

$$u_r(x', a, t) = \frac{1}{2\pi} \int_{-\infty}^{+\infty} \hat{G}(x', a + vt, \omega)\hat{F}(\omega)e^{i\omega t}\,\mathrm{d}\omega$$
$$= \int_{-\infty}^{+\infty} G(x', a + vt, t - \tau)F(\tau)\,\mathrm{d}\tau$$

(3-15)

where $\hat{F}$ and F are the external force in the frequency and time-domain, respectively; and u_r is the rail deflection in the space-time-domain.

Overall, the integral in **Eq.** (3-15) allows for the computation of the track response in the time-domain and gives the framework for the study of complex problems, e.g. the train-track interaction dynamics via iterative time-stepping integration procedures – see for instance [81,82,179], for which G must be computed at different track and loading positions.

Note that this project's focus is on methodologies solved in the transformed domain, specifically the wavenumber-frequency-domain. Therefore, excluding the time-domain Green's function approach described in this section, several time-domain methods using modal superposition techniques are not covered in this review.

3.2.2 2.5D Method

The 2.5D Finite Element, also known as the wavenumber FE, is a periodic approach widely applied for railway track simulations [21–25,184]. This method requires simplifying the structure into a 2D slice. Then, by assuming this slice repeats along the longitudinal or train passage direction x, a fully 3D response is recovered via Fourier transformations. Thus, the method fails to capture discrete rail support effects. **Figure 3-4** shows the 3D continuous periodic domain Ω and its 2D slice or restricted domain $\tilde{\Omega}$ employed in the 2.5D FEM simulation.

The 2.5D FEM considers the 3D linear-elastic FE structure is periodic along x. Then, by performing a double transformation – see **Eqs.** (2-33) and (2-35), the equation of motion can be defined in wavenumber-frequency-domain as described in **Eq.** (3-16)

$$[\tilde{D}]\{\tilde{u}(\beta_x, \omega)\} = \{\tilde{F}(\beta_x, \omega)\}$$

(3-16)

$$[\tilde{D}] = [\tilde{K}] + i\omega[\tilde{C}] - \omega^2[\tilde{M}]$$

(3-17)

where $[\tilde{D}]$ is the Dynamic Stiffness Matrix (DSM) – see **Eq.** (3-17). Note that the vertical and transversal space coordinates, $y - z$, (dropped for visibility) are employed for the definition of the 2D slice mesh, thus, they are not transformed to the corresponding wavenumber-domain.
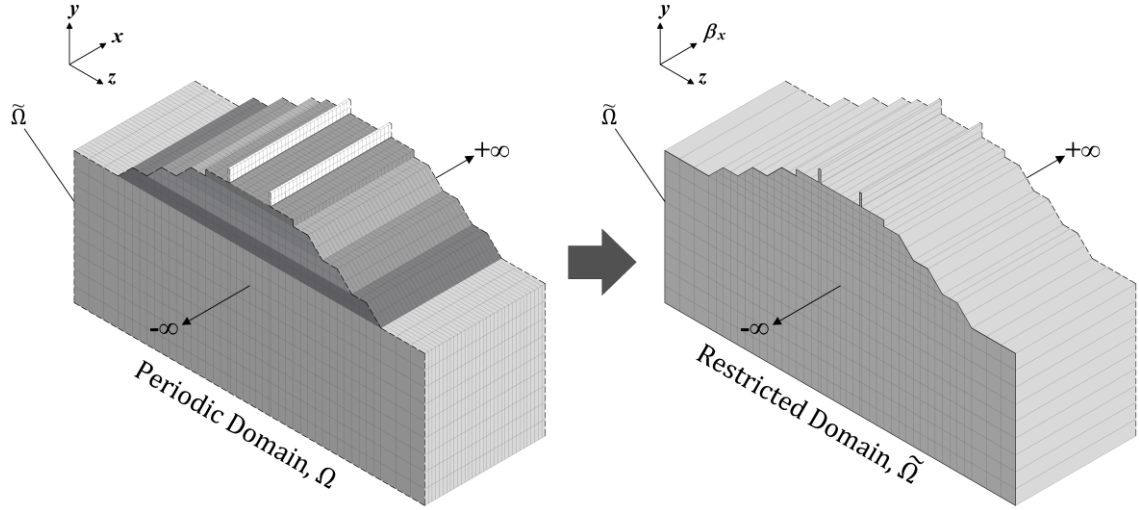
Figure 3-4. 2.5D Periodic and restricted domain in the longitudinal direction

Using classical FE definitions, the stiffness and mass matrices can be defined by **Eqs.** (3-18) and (3-19), respectively [23]:

$$\left[\widetilde{K}(\beta_x)\right] = \int_y \int_z [B(-\beta_x)]^T [D][B(\beta_x)]\mathrm{d}y\mathrm{d}z \tag{3-18}$$

$$\left[\widetilde{M}(\beta_x)\right] = \int_y \int_z [N]^T \rho[N]\mathrm{d}y\mathrm{d}z \tag{3-19}$$

in which $[B] = [L][N]$ is the matrix of partial derivatives $[L]$ – see **Eq.** (3-20), of the shape functions $[N]$, and ρ is the material density.

$$[L] = [\tilde{L}(\beta_x)] = \begin{bmatrix} i\beta_x & 0 & 0 & \partial/\partial y & 0 & \partial/\partial z \\ 0 & \partial/\partial y & 0 & i\beta_x & \partial/\partial z & 0 \\ 0 & 0 & \partial/\partial z & 0 & \partial/\partial y & i\beta_x \end{bmatrix} \tag{3-20}$$

Since only the longitudinal space coordinate is transformed to wavenumber, **Eq.** (3-18) can be decomposed into **Eq.** (3-21):

$$\left[\widetilde{K}(\beta_x)\right] = [K_1] + i\beta_x[K_2] + \beta_x^2[K_3] + \beta_x^4[K_4] \tag{3-21}$$

Eq. (3-16) can be inverted to obtain displacements $\tilde{u}(\beta_x, \omega)$ in the wavenumber-frequency-domain. Finally, results can be transformed back to space-time results via Inverse Fourier transformations – see **Eqs.** (2-34) and (2-36). Note that despite providing computational benefits, the 2.5D only meshes the cross-section of the structure, i.e. a 2D mesh. Thus, the methods assumes a homogeneous behaviour in its longitudinal direction, which restricts the definition of discrete support conditions.

3.2.3 Transfer Matrix Method

The dynamic behaviour of repetitive track structures can be studied by taking advantage of their periodic features and their characteristics of wave propagation [125,236–238]. The Transfer Matrix Method (TMM), also known as the Repeating-Unit-Method [228], is an analytical method that makes use of a constant of propagation λ, to relate the displacements and forces at the boundaries of the same unit and periodic element, or cell, whose cross-sectional properties are considered to be uniform in a particular direction:

$$\{\hat{u}^R\} = \lambda\,\{\hat{u}^L\}\ ,\quad \{\hat{F}^R\} = -\lambda\,\{\hat{F}^L\} \tag{3-22}$$

where $\hat{u}^{R,L}$ and $\hat{F}^{R,L}$ are the vectors of displacements and forces, respectively, at the right–hand R (or front face) and left-hand L (or back face) boundary – see **Figure 3-5**. Bearing in mind **Eq.** (3-22), the response in each periodic element can be computed by employing the Transfer matrix $[T]$ to relate vectors $\{\hat{u}\}$ and $\{\hat{F}\}$ according their position in the cell (i.e. right- and left-hand side).

Matrix $[T]$ is computed from the Dynamic Stiffness Matrix (DSM), $[\hat{D}]$. The latter is based on the discrete dynamic equation of a cell obtained from a Finite Element model at a frequency ω – see **Eq.** (2-28), however, only relating the boundaries (i.e. external or active nodes) of the unit element [125,236,239]:

$$[\hat{D}] = [K] + i\omega[C] - \omega^2[M] \tag{3-23}$$

$$\{\hat{F}\} = \begin{Bmatrix} \hat{F}_L \\ \hat{F}_R \end{Bmatrix} = \begin{bmatrix} \hat{D}_{LL} & \hat{D}_{LR} \\ \hat{D}_{RL} & \hat{D}_{RR} \end{bmatrix} \begin{Bmatrix} \hat{u}_L \\ \hat{u}_R \end{Bmatrix} = [\hat{D}]\{\hat{u}\} \tag{3-24}$$

where $[\hat{D}_{lm}]$ $(l, m = L, R)$ represents a submatrix of the partitioned matrix $[\hat{D}]$. Next, $[T]$ can be obtained through matrix manipulation and enforcement of compatibility conditions at the boundaries [125,240]:

$$\{S^R\} = \begin{Bmatrix} \hat{u}_R \\ -\hat{F}_R \end{Bmatrix} = [T] \begin{Bmatrix} \hat{u}_L \\ \hat{F}_L \end{Bmatrix} = [T]\{S^L\}$$
$$[T] = \begin{bmatrix} -\hat{D}_{LR}^{-1}\hat{D}_{LL} & \hat{D}_{LR}^{-1} \\ -\hat{D}_{RL} + \hat{D}_{RR}\hat{D}_{LR}^{-1}\hat{D}_{LL} & -\hat{D}_{RR}\hat{D}_{LR}^{-1} \end{bmatrix} \tag{3-25}$$

and where $\{S^R\}$ and $\{S^L\}$ define the state vectors (i.e. vectors containing displacements and forces) at the right- and left-hand sides, respectively. Combining **Eq.** (3-25) and **Eq.** (3-22), and expressing the new relation in terms of the unit cell number n, it is possible to state the following eigenvalue problem:

$$\{S_{n+1}^L\} = [T]\{S_n^L\} \quad \Rightarrow \quad \{S_{n+1}^L\} = \lambda\{S_n^L\} \tag{3-26}$$

$$\hat{F}^L_{n=2} = -\hat{F}^R_{n=1} \qquad\qquad \hat{F}^L_{n_{end}} = -\hat{F}^R_{n_{end}-1}$$

$$\hat{F}^L_{n=1} = \hat{F}_{s=0} \qquad \hat{F}^L_{n=2} = \lambda\,\hat{F}^L_{n=1} \qquad\qquad \hat{F}^L_{n_{end}} = \lambda_{n_{end}-1}\,\hat{F}^L_{n=1}$$

$$\hat{F}^R_{n_{end}} = -\lambda\,\hat{F}^L_{n_{end}-1}$$

$$\hat{F}^R_{n=1} = -\lambda\,\hat{F}^L_{n=1} \qquad \hat{F}^R_{n=2} = -\lambda\,\hat{F}^L_{n=2} \qquad \hat{F}^R_{n_{end}} = \lambda_{n_{end}}\,\hat{F}^L_{n=1}$$

$s=0$ •$n=1$• $s=1$ $s=1$ •$n=2$• $s=2$ ••• $s=s_{end}-1$ •n_{end}• $s=s_{end}=n_{end}$

$$\hat{u}^R_{n=1} = \lambda\,\hat{u}^L_{n=1} \qquad \hat{u}^R_{n=2} = \lambda\,\hat{u}^L_{n=2} \qquad \hat{u}^R_{n_{end}} = \lambda\,\hat{u}^L_{n_{end}-1}$$

$$\hat{u}^R_{n_{end}} = \lambda_{n_{end}}\,\hat{u}^L_{n=1}$$

$$\hat{u}^L_{n=1} = \hat{u}_{s=0} \qquad \hat{u}^L_{n=2} = \hat{u}^R_{n=1} \qquad \hat{u}^L_{n_{end}} = \lambda\,\hat{u}^R_{n_{end}-1}$$

$$\hat{u}^L_{n=2} = \lambda\,\hat{u}^L_{n=1} \qquad \hat{u}^L_{n_{end}} = \lambda_{n_{end}-1}\,\hat{u}^L_{n=1}$$
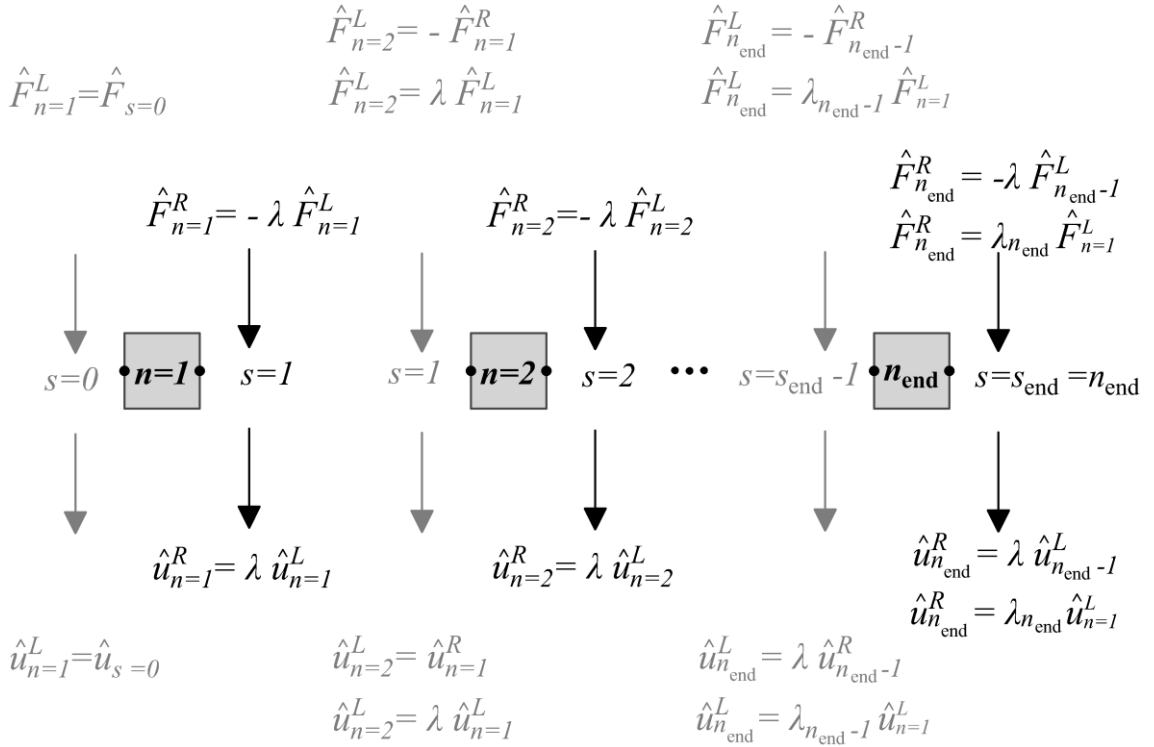
Figure 3-5. Displacements and forces on multiple unit elements, where *s* is the node number [27]

In order to solve the eigenvalue problem in **Eq.** (3-26), its eigenvectors $\{S^L_n\}$ and eigenvalues λ are determined by solving the equivalent problem:

$$[T]\{S^L_n\} = \lambda\{S^L_n\} \quad\Rightarrow\quad \big[[T] - \lambda[I]\big]\{S^L_n\} = \{0\} \tag{3-27}$$

where $[I]$ is the identity matrix, and $\{0\}$ is the vector of zeros. Solution of **Eq.** (3-27) implies that $\{S^L_n\}$ must have non-zero values. Thus, $\big[[T] - \lambda[I]\big]$ should be zero and the problem can be easily solved by computing its determinant:

$$\det\big[[T] - \lambda[I]\big] = \{0\} \tag{3-28}$$

Note that **Eq.** (3-28) omits the term $\{S^L_n\}$ in its solution, implying a free vibration response that considers the structure's stiffness, damping and mass (via [T]). Considering that $[T]$ is a $2j_{end} \times 2j_{end}$ matrix (j_{end} being the total number of degrees-of-freedom), **Eq.** (3-28) will result in $2j_{end}$ eigenvalues $2j_{end} \times 1$ eigenvectors, as shown in:

$$\{\lambda_j\} = \big[\lambda_1, \lambda_2, \dots, \lambda_{2j_{end}}\big] \tag{3-29}$$

$$\{S^L_{n,j}\} = \big[\{S^L_{n,1}\}, \{S^L_{n,2}\}, \dots, \{S^L_{n,2j_{end}}\}\big]^T \tag{3-30}$$

Note that λ_j are complex values. Next, **Eq.** (3-26) can be rewritten as:

$$\{S^L_{n+1,j}\} = [T]\{S^L_{n,j}\} = \lambda_j\{S^L_{n,j}\} \tag{3-31}$$

Following this methodology, it is assumed that the state vectors propagate along the structure without amplitude and phase changes. Thus, the wave propagation 'pattern' is obtained using the eigenvalues λ and eigenvectors $\{S_n^L\}$ of the Transfer matrix $[T]$. In other words, the response vector can be determined by combining, via a scalar multiplication, each eigenvector and its associated eigenvalue with a constant C– a process known as the linear combination of eigenvectors [241]. However, only those values corresponding to decaying solutions (i.e. $|\lambda| < 1$) are used to compute the response throughout the entire structure. This is described mathematically as:

$$\{S_{n+1}^L\} = \sum_{j=1}^{J=j_{\text{end}}} C_j \lambda_j \{S_{n,j}^L\} \tag{3-32}$$

where λ_j and $\{S_{n,j}^L\}$ are the eigenvalues and eigenvectors corresponding to the decaying solutions, respectively. C_j represents the constant factors of propagation determined through the boundary conditions, and j_{end} is the number of degrees-of-freedom at each boundary. Since the unit element is the same along the entire structure, its eigenvalues and eigenvectors do not change. Further, waves propagate along the structure unchanged, except for amplitude and phase, which are given by the C coefficients. Thus, the only values that must be updated in **Eq.** (3-32) are the coefficients C_j.

$[T]$ relates the state vectors at one point in a 'structural chain' (i.e. overall structure made of several periodic elements) to those at another point. Also, this matrix is computed for each part of the structure until boundary conditions can be enforced, so that one cell can be related to another [238]. Based on this 'chain' analogy, $[T]$ has also been employed in alternative implementations such as the 'layer transfer matrix' to study track-soil interaction, for which soil is considered to be composed of several layers, all of them related via the transfer matrix $[T]$ [66,70,242,243].

3.2.4 Floquet method

The Floquet transform [244], is an analytical method which exploits a track structure's periodic nature by studying a subdomain only [26,245–247]. The method defines Ω as a three-dimensional periodic domain in the Cartesian reference system: e_x, e_y, e_z, as shown in **Figure 3-2**. This domain is formed from the repetition of $\widetilde{\Omega}$, which is the unit, generic or reference element defined by $\widetilde{\Omega} = \{X \in \Omega| - d/2 < X \cdot e_x < +d/2\}$, with the position vector of any point in Ω given by $\{X\} = \{xe_x + ye_y + ze_z\}$ [26,226,246,248].

d is the length period (i.e. length of $\widetilde{\Omega}$ in e_x) and $\widetilde{\Omega}$ is invariant in any translation at position nde_x, where n is an integer defining the number of the generic element. Thus, the function $\tilde{g}$ in $\widetilde{\Omega} \times [-\pi/d, \pi/d]$ is defined as the Floquet transform of any function g in Ω, as shown in **Eq.** (3-33) [226,248,249]:

$$\tilde{g}(\tilde{X}, \beta_x^*) = \sum_{n=-\infty}^{n=+\infty} g(\tilde{X} + nde_x)e^{(ind\beta_x^*)} \tag{3-33}$$

where the wavenumber of $\widetilde{\Omega}$ is defined by $\beta_x^* \in [-\pi/d, \pi/d]$, and the position vector in $\widetilde{\Omega}$ is $\{\tilde{X}\} = \{\tilde{x}e_x + \tilde{y}e_y + \tilde{z}e_z\}$, with $\tilde{x} = x - nd$, $\tilde{y} = y$, $\tilde{z} = z$. Furthermore, the function $\tilde{g}(\tilde{X}, \beta_x^*)$ defined on Ω is periodic of the first and the second kind [225,245,249]:

- Periodicity of the first kind with respect to β_x^* and with a period $2\pi/d$, as shown in **Eq.** (3-34).
- Periodicity of the second kind in $\tilde{X}$ with a period d in in space , as described in **Eq.** (3-35).

$$\tilde{g}\left(\tilde{X}, \beta^* + \frac{2\pi}{d}\right) = \tilde{g}(\tilde{X}, \beta^*) \tag{3-34}$$

$$g(\tilde{X} + de_x, \beta^*) = e^{-(ind\beta^*)}\tilde{g}(\tilde{X}, \beta^*) \tag{3-35}$$

Moreover, for any location in Ω ($X = \tilde{X} + nde_x$), function g can be recovered from $\tilde{g}$ through the Inverse Floquet transform [226,247,249]:

$$g(X = \tilde{X} + nde_x) = \frac{d}{2\pi}\int_{-\pi/d}^{+\pi/d} g(\tilde{X}, \beta^*)e^{(-ind\beta^*)}\mathrm{d}\beta^* \tag{3-36}$$

In general, the Floquet approach – **Eq.** (3-35), computes the response throughout a restricted domain $\widetilde{\Omega}$. Then, once the dynamic formulation is solved and the track response is obtained for $\widetilde{\Omega}$ in the wavenumber-frequency-domain, the solution at the other points in the structure (i.e. outside the restricted domain) is retrieved through the inverse Floquet transformation in **Eq.** (3-36), which transforms from the wavenumber to the spatial longitudinal coordinate x. Despite being computationally efficient, it is challenging to use the Floquet method to consider variations in the periodic longitudinal direction x [27] as discussed in the next section. This is because of the restricted domain $\widetilde{\Omega}$ and the periodicity conditions in **Eqs.** (3-34) and (3-35) used for the definition of its formulation.

3.2.5 Direct Periodic Method

The Direct Periodic Method, DPM, employs the Floquet's theorem introduced in Section 3.2.4, to reduce and solve the periodic problem [226,244,248,249]. The DPM computes the response of the total periodic domain Ω by studying a discretized domain $\widetilde{\Omega}$ known as reference or unit cell $n = 0$. For this, the equations of motion of the reference cell are first defined in the space-domain and then modified via the enforcement of periodic conditions applied at the borders of $n = 0$, as shown in **Eq.** (3-37):

$$\tilde{u}_{n=0}^{R}(\tilde{x} = d, \beta_x, \omega) = \tilde{u}_{n=0}^{L}(\tilde{x} = 0, \beta_x, \omega)e^{id\beta_x} \qquad (3\text{-}37)$$

where $\tilde{u}_{n=0}^{L,R}$ are the displacements at the right–hand R (or front face) and left-hand L (or back face) boundary of the reference cell $n = 0$ with periodic length d. Once periodic conditions have been applied and reference cell displacements are computed via inversion of the modified system of equations of motion, Floquet theory is exploited to obtain the response at both sides of $n = 0$. **Eq.** (3-38) shows the displacement of cell $n \neq 0$:

$$\tilde{u}_{n}(x, \beta_x, \omega) = \tilde{u}_{n=0}(\tilde{x}, \beta_x, \omega)e^{ind\beta_x} \qquad (3\text{-}38)$$

Once obtained $\tilde{u}_n$, the β_x domain response for all n^{th} cells, it can be transformed back to space-domain x through the Fourier transform depicted in **Eq**. (3-39):

$$\hat{u}(x, \omega) = \frac{1}{2\pi} \int_{-\infty}^{+\infty} \tilde{u}_{n}(x, \beta_x, \omega)e^{ix\beta_x} \mathrm{d}\beta_x \qquad (3\text{-}39)$$

where $\hat{u}$ is the displacement of the total domain in the space-frequency-domain (x, ω), as described by the hat notation '^'. Note that although defined for non-moving excitations, the DPM can easily incorporate moving contributions by considering that the angular frequency is related to speed: $\omega = \varpi - \beta_x v$, in which ϖ is the driving oscillating frequency.

Overall, the DPM proves to be a straightforward periodic solution that only requires: (1) modification of the equations of motion of the reference cell via periodic conditions, (2) computation of the reference cell response via inversion of the modified system, and (3) enforcement of periodic conditions as a function of the $n = 0$ response to obtain the response at $n \neq 0$.

3.3 Solutions for Semi-Periodic Structures

Fully periodic methods exploit a structure's repetitive character and compute the global response by studying only a restricted domain rather than the entire track. A shortcoming of this is that only free-wave propagation problems can be studied, i.e. no changes in the periodic track parameters (in the direction of train passage). This makes it challenging for modelling cases such as transition zones. To overcome this drawback and allow for the inclusion of varying track properties, semi-periodic solutions can be used.

3.3.1.1 Multi-Coupled Periodic Method

Similar to the TMM, the Multi-Coupled Periodic Method (MCM) is an analytical method based upon a wave propagation approach. The method analyses the free-wave propagation due to a force applied on a unit element, to retrieve the response throughout the entire track structure, via the solution of an eigenvalue problem and an enforcement of boundary conditions.

To obtain the response of a periodic structure, the MCM expresses the constant of propagation in exponential format (i.e. $\lambda = e^{\mu}$) and exploits the Dynamic Stiffness Matrix $[\widehat{D}]$ rather than the Transfer Matrix $[T]$ [250–253]. **Eq.** (3-40) depicts the displacement $\{\hat{u}^{R,L}\}$ and force $\{\hat{F}^{R,L}\}$ vector relationship at the right-hand R and left-hand L boundary of the same unit element n:

$$\{\hat{u}_n^R\} = \{\hat{u}_{n+1}^L\} = e^{\mu}\{\hat{u}_n^L\}$$
$$\{\hat{F}_n^R\} = -\{\hat{F}_{n+1}^L\} = -e^{\mu}\{\hat{F}_n^L\} \tag{3-40}$$

Next, the combination of **Eq.** (3-23) and **Eq.** (3-40) define the generalised linear eigenvalue problem in **Eq.** (3-41), which is employed to compute the eigenvalues λ and eigenvectors $\{\theta\}$:

$$[A + \lambda B]\{\theta\} = \{0\}$$
$$A = \begin{bmatrix} \widehat{D}_{RL} & \widehat{D}_{RR} \\ 0 & I \end{bmatrix}, \quad B = \begin{bmatrix} \widehat{D}_{LL} & \widehat{D}_{LR} \\ -I & 0 \end{bmatrix}, \quad \{\theta\} = \begin{Bmatrix} \hat{u}_L \\ \hat{u}_r \end{Bmatrix}, \quad \lambda = e^{\mu} \tag{3-41}$$

where $\{0\}$ is the null or zero vector; and $[\widehat{D}_{lm}]$ $(l,m = L,R)$ are submatrices of $[\widehat{D}]$. Note that **Eq.** (3-41) is solved in a similar manner to Eq. (3-28) in Section 3.2.3. In general, the eigenvalues are used to retrieve the constants of propagation $(\mu = \log \lambda)$, whereas the eigenvectors provide the generalised displacements or shapes.

The eigenvalue problem in **Eq.** (3-41) has a dimension of $2j_{\text{end}}$ (j_{end} degrees-of-freedom per node), which gives $2j_{\text{end}}$ eigenvalues and $2j_{\text{end}} \times 1$ eigenvectors. This

solution occurs in pairs, and j_{end} waves propagate symmetrically in each direction. Waves propagating to the right-hand side of the symmetric structure, i.e. positive-travelling waves, have negative real or purely imaginary constants of propagations ($\mu^+ = \{\mu \mid \text{Re} < 0 \parallel \text{Re} = 0\}$). Alternatively, waves propagating to the left-hand side, i.e. negative-travelling waves, have positive real or purely positive imaginary constants of propagation ($\mu^- = \{\mu \mid \text{Re} > 0 \parallel \text{Re} = 0 , \text{Im} > 0\}$) [252].

Furthermore, each μ is related to a generalised vector of displacements $\{\theta\}$ and a generalised vector of forces $\{\phi\}$. Thus, by exploiting the symmetric character of the problem, one can differentiate the multiple components of the problem according to the direction of propagation of the wave and then, through **Eqs.** (3-40)-(3-41), compute $\{\phi^+\}_j$ and $\{\phi^-\}_j$ for each degree-of-freedom $j = 1, \dots, j_{\text{end}}$. Finally, reapplying **Eq.** (3-40), the total response at node s is computed according the direction of propagation of the wave, such that:

$$
\begin{aligned}
\{\hat{u}^\pm\}_s &= \sum_{j=1}^{j=j_{\text{end}}} e^{s\mu_j^\pm} \{\theta^\pm\}_j \ \psi^\pm{}_j = [\Theta^\pm]\left[E^{s\mu_j^\pm}\right]\{\Psi^\pm\} \\
\{\hat{F}^\pm\}_s &= \sum_{j=1}^{j=j_{\text{end}}} e^{s\mu_j^\pm} \{\phi^\pm\}_j \ \psi^\pm{}_j = [\Phi^\pm]\left[E^{s\mu_j^\pm}\right]\{\Psi^\pm\}
\end{aligned}
\tag{3-42}
$$

where $[\Theta^\pm]$, $[\Phi^\pm]$ and $\left[E^{s\mu_j^\pm}\right]$ are $j_{\text{end}} \times j_{\text{end}}$ matrices containing the generalised displacements $\{\theta^\pm\}_j$, the generalised forces $\{\phi^\pm\}_j$, and the exponential terms $e^{s\mu_j^\pm}$, respectively. Furthermore, the vector $\{\Psi^\pm\}$ contains the generalised coordinates $\psi_j^\pm$, which are obtained by enforcing the initial boundary conditions at $s = 0$. Once the response is obtained at $s = 0$, $\{\Psi^\pm\}$ is used to retrieve the response at the remaining nodes ($s > 0$).

Eq. (3-42) is similar to that defined by the TMM in **Eq.** (3-32) because both equations add only the wave component contributions associated with their response. Thus, the first step is to decompose the wave and select those components acting on the structure. The next step is to use these components to compute the result. Since only waves decaying/propagating away from the source occur in infinitely extending structures, the problem can be analysed by exploiting symmetry and bounding the track at one side only. Thus, a semi-infinite structure can be composed from 2 distinct sub-structures [252]:

- A finite-infinite structure, which is bounded at its left-side boundary and infinitely extending to its right. Thus, only positive-travelling waves occur.
- An infinite-finite structure, which is bounded at its right-side boundary and infinitely extending to its left. Thus, only negative-travelling waves occur.

Eqs. (3-32) and (3-42) assume periodicity or no change in the unit element properties, meaning waves do not reflect back to the source. However, this reflective nature can be included by considering that the track is bounded at both of its boundaries, i.e. a finite-finite structure. Therefore, all waves must be accounted for in the response [27,252]:

$$\{u^R\}_s = \{\hat{u}^L\}_s = [\Theta^-]\big[E^{(s_{\text{end}}-s)\mu^-}\big]\{\Psi^-\} + [\Theta^+]\big[E^{s\mu^+}\big]\{\Psi^+\}$$
$$\{\hat{F}^R\}_s = -\{\hat{F}^L\}_s = [\Phi^-]\big[E^{(s_{\text{end}}-s)\mu^-}\big]\{\Psi^-\} - [\Phi^+]\big[E^{s\mu^+}\big]\{\Psi^+\} \qquad (3\text{-}43)$$

where s_{end} is the total number of nodes, which coincide with the total number of elements (the first node is zero). Results are first determined at both boundaries $s = 0$ and $s = s_{\text{end}}$, which provide the values required to compute $\{\Psi^\pm\}$ that are then inserted into **Eq.** (3-43) to determine the response at the remaining nodes $s = 1, \dots, s_{\text{end}} - 1$.

Considering **Eqs.** (3-42) and (3-43) describe the responses for semi-infinite and finite-finite structures, a track with varying properties (i.e. non-periodic domain with changes in material parameters, geometry, etc.) can be analysed by discretising the total structure into different sections with periodic domains. Thus, periodicity is enforced at discrete sections, which are later coupled to each other and analysed as a global structure which is semi-periodic. **Figure 3-6** shows a semi-periodic structure of four sections or periodic domains. The solution of the global/assembled dynamic system of equations for a semi-periodic structure is [27,252,254]:

$$[K_{\text{All}}]\{\hat{u}_{\text{All}}\} = \{\hat{F}_{\text{All}}\} \qquad (3\text{-}44)$$

where $[K_{\text{All}}]$ is the global stiffness matrix, $\{\hat{u}_{\text{All}}\}$ is the global displacement vector, and $\{\hat{F}_{\text{All}}\}$ is the assembled or global force vector, all of which relate the multiple sections of the track. In general, by solving **Eq.** (3-44) through the application of boundary conditions, the responses at the boundaries of each section are obtained. Next, $\{\Psi^\pm\}$ is computed for each section, and responses of the remaining nodes are retrieved.
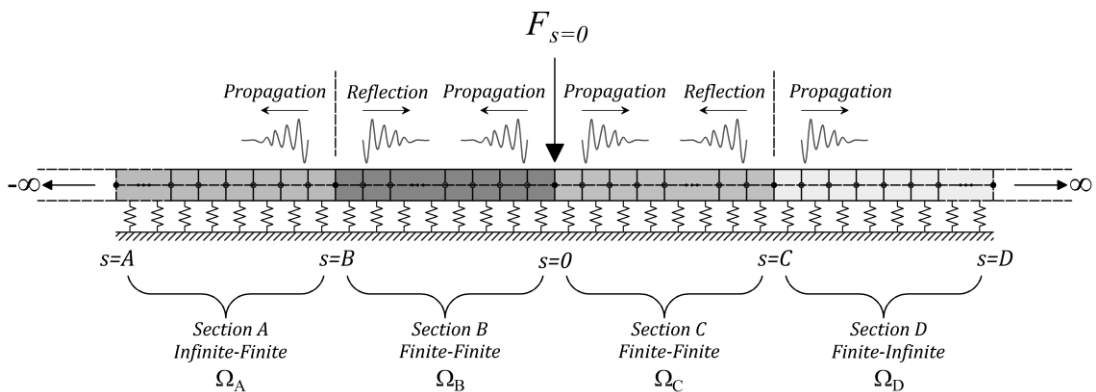
Figure 3-6. Coupled system with bounded nodes B, 0 and C; and free nodes A and D

3.4 Example Application of Solution Methods

Periodic approaches can be used to study a wide range of railway engineering problems. Following the example applications presented in Section 2.4, this Section uses a variety of the methods discussed previously in this Chapter to address two common applications:

1. *Airborne noise generation* – the noise resulting from wheel-rail contact is analysed, considering both continuous and discrete track support conditions. Track receptance and decay rates are computed.
2. *Track-ground dynamics* - the effect of train speed on track deflection is analysed. Ballast and slab track models are considered.

Table 3-1 summarises the solution methods used for each application and the results shown.

No.	Application	Results	Solution Methods
1	Noise	Receptance Noise decay rate	1. Analytical Continuous 2. Discrete point source method
2	Track Dynamics	Track deflection	1. Fourier analytical continuous 2. Dirac comb method

Table 3-1. Results and solution methods used in each application

3.4.1 Application no. 1: Noise

Point receptance and track decay rates are computed using the combination of the fundamental BOEF formulation and the discrete point source periodic method. The results are then compared against the basic continuous BOEF formulation. The effect of varying layers, beam definition, and damping models are also studied. **Table 3-2** presents the various track parameters employed for this application. For this, material and geometrical values were taken based on examples depicted by [10,51,75,170,212].

Note that for the 1-layered model, equivalent properties are required. For the computation of the equivalent support stiffness k_1, **Eq.** (3-4) is modified, as shown in **Eq.** (3-45):

$$k_1 = \frac{m_s \omega_{co}^2 k_{rp} - k_{rp} k_b}{m_s \omega_{co}^2 - \left(k_{rp} + k_b\right)}$$

(3-45)

where ω_{co} corresponds to the second cut-on frequency of the 2-layered BOEF model. $k_{rp,b}$ is the stiffness per unit length of the railpad 'rp' and ballast 'b', and m_s is the mass per unit length of the sleeper 's'. For comparison purposes, discrete support values will be denoted using a prime symbol ('). Thus, in the case of discrete supports, the discrete railpad stiffness k'_{rp} is obtained by multiplying the continuous railpad stiffness k_{rp} by the sleeper spacing d, i.e. $k'_{rp} = k_{rp}d$. Similarly, the discrete mass of the sleeper m'_s can be defined by $m'_s = m_s d$.

Once k_1 is obtained, the equivalent viscous damping coefficient c_1 can be computed via **Eq.** (2-22), as recalled in **Eq.** (3-46):

$$c_1 = \frac{k_1 \eta_1}{\omega_{co}}$$
(3-46)

in which η_1 is the hysteretic or damping loss factor of the equivalent support of the 1-layered model.

Component	Parameter		Units	Value
(One) Rail	$E_r I_r$	Bending moment	[MNm^2]	6.38
	$\rho_r I_r$	Rotational inertia	[kg m]	0.24
	$G_r A_r$	Shear stiffness	[MN]	591
	m_r	Mass per unit length	[kg/m]	60.23
	κ_r	Shear parameter	[−]	0.4
Railpad	k_{rp}	Stiffness per unit length	[MN/m^2]	350
	η_{rp}	Damping loss factor (hysteretic)	[−]	0.15
	c_{rp}	Damping (viscous)	[Ns/m]	1.92E+04
(Half) Sleeper	m_s	Mass per unit length of rail	[kg/m]	245
	d	Sleeper spacing	[m]	0.6
Ballast	k_b	Stiffness per unit length	[MN/m^2]	180
	η_b	Damping loss factor (hysteretic)	[−]	1
	c_b	Damping (viscous)	[Ns/m]	2.34E+05
Other (1 layer model)	k_1	Stiffness per unit length	[MN/m^2]	450
	η_1	Damping loss factor (hysteretic)	[−]	0.2
	c_1	Damping (viscous)	[Ns/m]	3.29E+04

Table 3-2. Noise application parameters

In the case of continuous single- and two-layered Euler-Bernoulli BOEF models, the point receptance $\alpha(\omega)$ is computed from the equation of motion in the wavenumber-frequency-domain (β, ω) in **Eq.** (2-38). This is described mathematically in **Eq.** (3-47) [10]:

$$\alpha(\omega) = \frac{-(1+i)}{4E_r I_r \beta_j^3} \tag{3-47}$$

where β_j, computed through **Eq.** (2-46), is the complex wavenumber root with positive real and negative imaginary component, i.e. $\beta = \{\beta_j \mid \text{Re} > 0, \text{Im} < 0\}$.

Alternatively, for the Timoshenko beam formulation, a new set of equations of motion in wavenumber-frequency-domain must be defined to compute its point receptance. **Eq.** (3-48) shows the dynamic equation of motion for a Timoshenko beam derived after transforming the set of equations of motion in space-time-domain – see **Eq.** (2-16). **Eq.** (3-49) describes its receptance, and **Eq.** (3-50) defines the corresponding wavenumber roots β_j and constants A.

$$\beta^4 + A_2(\omega)\,\beta^2 + A_3(\omega) = 0 \tag{3-48}$$

$$\alpha(\omega) = i \sum_{\substack{j \text{ with} \\ \text{Im}(\beta_j)<0}} \frac{1}{G_r A_r \kappa_r}\left(\frac{\beta_j^2 + A_1}{4\beta_j^3 + 2\beta_j A_2}\right) \tag{3-49}$$

$$\beta_j^2 = -\frac{1}{2}A_2 \pm \frac{1}{2}\sqrt{A_2^2 - 4A_3}, \quad A_1 = \frac{G_r A_r \kappa_r}{E_r I_r} - \frac{\rho_r I_r \omega^2}{E_r I_r},$$
$$A_2 = \left(\frac{k^* - m_r \omega^2}{G_r A_r \kappa_r}\right) - \left(\frac{\rho_r I_r \omega^2}{E_r I_r}\right), \quad A_3 = \left(\frac{k^* - m_r \omega^2}{E_r I_r}\right)\left(1 - \frac{\rho_r I_r \omega^2}{G_r A_r \kappa_r}\right) \tag{3-50}$$

where constants A_1, A_2 and A_3 relate the various Timoshenko beam and track support parameters, β_j is the new set of wavenumber roots defined after inversion of **Eq.** (3-48), A_r is the cross-sectional area, ρ_r is the density, m_r is the rail mass, E_r is the Young's modulus, G_r is the shear modulus, κ_r is the shear coefficient, and k^* is the viscous or hysteretic complex stiffness of the support (see **Eq.** (2-19) and **Eq.** (2-23), respectively). Instead, for discrete BOEF models, $\alpha(\omega)$ is defined by **Eq.** (3-1).

Figure 3-7 shows (a) the receptance and (b) mobility curves for multiple BOEF models with hysteretic damping. It is seen that an increased number of degrees-of-freedom better reveal the resonance modes of the structure. This is particularly evidenced in the single layered model, in which only the resonance of the rail mass on the support can be captured. This behaviour occurs at 435 Hz and coincides with the second cut-on frequency relating the rail mass and the stiffness of the foundation. On the contrary, both the continuous and discontinuous 2-layered models are able to capture the resonance of the rail and sleeper on the ballast (at 122 Hz, the first cut-on-frequency) and the anti-resonance of the sleepers on the ballast and railpads (at 234 Hz).

Regarding the beam theory, **Figure 3-7**(a) shows that although the receptance is similar for both the Timoshenko (T) and Euler-Bernoulli (EB) beams at low frequencies, divergence occurs at frequencies higher than 435 Hz, i.e. above the rail resonance. It is evident that continuous models are unable to simulate the discrete behaviour of the track support. This results in inaccurate results at higher frequencies and the inability to simulate the pinned-pinned resonance. Instead, this behaviour is better simulated using two-layered discrete models, which are able to capture the first- and second-order pinned-pinned resonance frequencies at around 1100 Hz and 2800 Hz, respectively. Note that when the force is applied at mid-span, there are upward peaks corresponding to resonance frequencies. However, when the impulse is applied above the sleeper, these frequencies are anti-resonances, and the peaks are downward. Similar results are shown in the mobility curves in **Figure 3-7**(b).

The decay rate of vibration Δ along the track is highly influenced by the damping of its supporting components (e.g. railpads and ballast) [10]. This allows for the determination of the noise radiated from the track, which increases with larger vibrations. For the discretely supported Timoshenko BOEF model, Δ is defined by **Eq.** (3-7). Instead, for continuously supported Euler-Bernoulli and Timoshenko BOEF models, Δ is described by [10,232]:

$$\Delta = -20 \log_{10}\left(e^{\mathrm{Im}(\beta_j)}\right) = -8.686 \, \mathrm{Im}(\beta_j) \qquad (3\text{-}51)$$

Decay rate curves for hysteretic and viscous damping models are presented in **Figure 3-8**. Again, the effect of the degrees of freedom is evident, particularly at lower frequencies. For the 1-layered BOEF model – see **Figure 3-8**(a), damping has a negligible effect below the second cut-on frequency. However, for the 2-layered models, a slight dip occurs above the first cut-on-frequency corresponding to the effect of the rail and sleeper on the ballast.

After the pronounced peak, above 435 Hz, the damping effect is significant and decay rates decrease rapidly with frequency. In addition, above this frequency, the response due to discrete models clearly diverges from that of the continuous models, again showing the limitations of the latter as they are unable to capture the pinned-pinned frequencies at around 1100 Hz and 2800 Hz.

Although similar results are obtained at lower frequencies for Euler-Bernoulli and Timoshenko beams, at higher frequencies the differences between models becomes more pronounced, as shown in **Figure 3-8**(a).

Figure 3-8(b) presents the effect of different damping implementations on both continuous and discrete two-layered tracks. Viscous damping parameters were selected so that the cut-on-frequencies coincide with the response provided by the

corresponding hysteretic models. Results show that, as expected, there is no significant change at frequencies below the second cut-on-frequencies. However, above this frequency, viscous damping models result in lower decay rates than the hysteretic cases. This is because viscous damping parameters c vary with frequency whereas hysteretic models parameters (loss factor) η are constant.
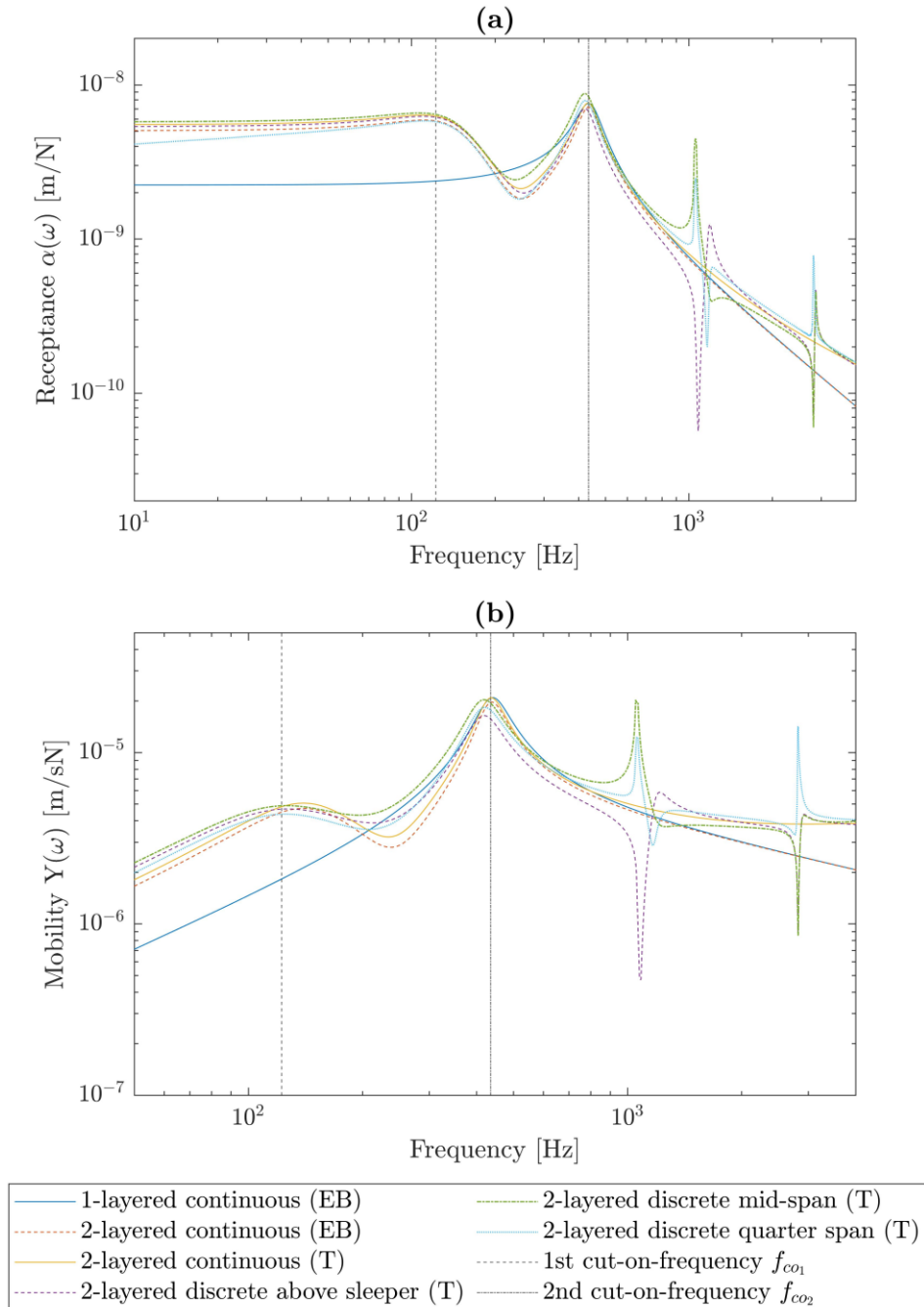
Figure 3-7. BOEF models with hysteretic damping, Euler-Bernoulli (EB) and Timoshenko (T) beam theory: (a) Receptance, and (b) Mobility

3.4.2 Application no. 2: Track Dynamics

To study track dynamics for discrete and continuous problems, the response due to a moving point load on the rail is analysed. Single-layer continuous and discrete BOEF models are employed – see Section 2.2.2. In both models, railpad damping is simulated using a viscous approach – see **Eq.** (2-19). Analytical formulations in the frequency-domain with Fourier transformations in **Eqs.** (2-33) to (2-36) are employed in both simulations. For the discrete response, the Dirac comb approach is used – see **Eq.** (3-8). **Table 3-2** shows the track parameters employed for the single layer BOEF simulation, which includes the rail and the railpad (note that symmetry is not exploited so track parameters must be doubled).
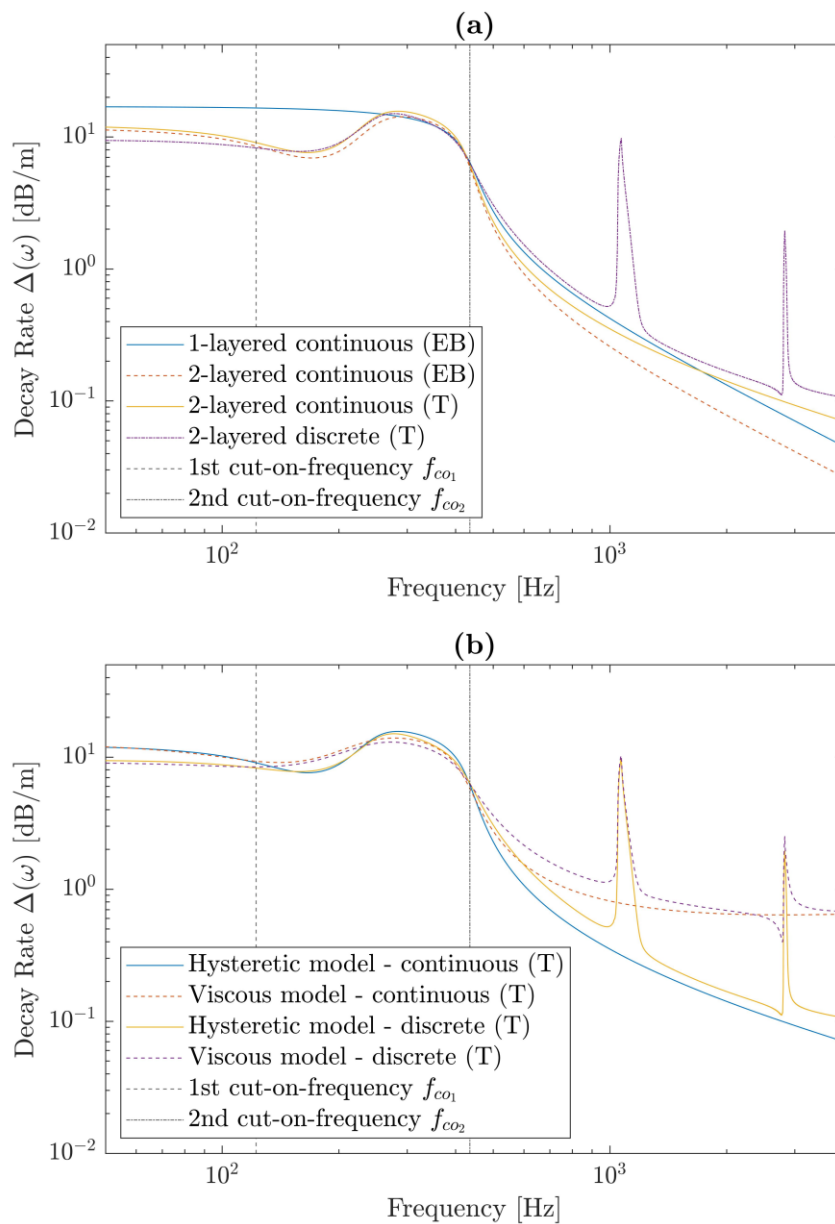
Figure 3-8. Decay rates: (a) 1 and 2-layered continuous and discrete models with hysteretic damping, (b) discrete two-layered models with hysteretic and viscous damping models

Figure 3-9 presents the discrete and continuous track response at $x = 0$ m due to a load $F = 150$ kN moving at 40 km/h with two different riding frequencies $\bar{f}_1 = 0$ Hz and $\bar{f}_2 = 50$ Hz. It can be seen that in all cases the maximum deflection occurs near these frequencies. The results highlight the limitations of the continuous model which, despite giving similar results close to $\bar{f}_{1,2}$, is unable to capture the rail deflection at certain frequencies – this result is consistent with the findings of [255].
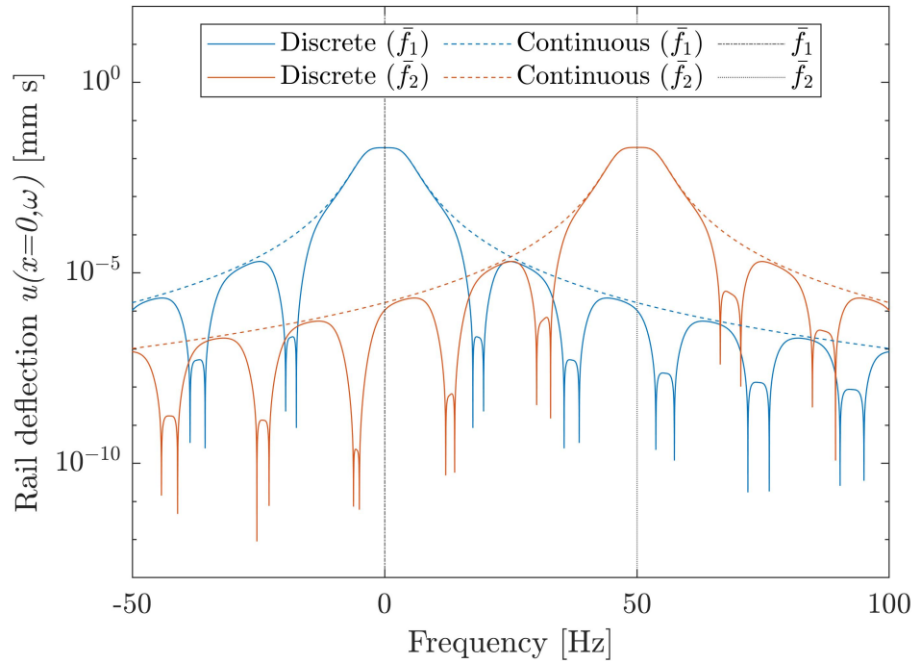
Figure 3-9. Continuous vs discrete track response due to a moving load

3.5 Challenges Associated to Periodic Approaches

At a fundamental level, periodic approaches exploit the repetitive nature of railway track structures, allowing for a reduction of the study domain to a single slice and enhancing computational efficiency. These characteristics make periodic approaches valuable as supplementary techniques, facilitating the optimization of traditional methods such as BOEF and FEM. When coupled with BOEF formulations, periodic techniques enable the inclusion of discrete support conditions and reduce the analysis domain. Similarly, when integrated with FEM, periodic approaches simplify complex geometrical domains into a slice, offering highly accurate and computationally efficient simulations. Despite these advantages, periodic approaches also present several challenges associated with their basic formulation:

- *Constant behaviour.* The fundamental periodic approach assumes repetitive track behaviour. Thus, their geometrical and material parameters are always constant. This definition confines the study domain to a constant structure

unable to replicate non-linear conditions and changes in other track parameters, i.e. the structure is fully-periodic. Although variable conditions (e.g. transition zones) cannot be simulated with the fundamental periodic approach, additional considerations in its formulation may address these limitations – see Section 3.3.

- *Numerical considerations.* Typical periodic formulations are based on modal decomposition methods, i.e., they require solving Eigenvalue problems and extracting the corresponding Eigen modes. When considering several degrees of freedom, this process may lead to an ill-conditioning problem [236], and requires additional strategies to optimise it, such as a model reduction [254].

- *Force conditions.* Although they can replicate stationary forces, Periodic approaches struggle to simulate moving contributions. To include the latter, the fundamental periodic approach is often coupled with superposition methods. This adds complexity to the simulation as these methods are usually defined in the time – see [27], different to the frequency-domain employed in the Periodic formulation.

3.6 Identifying Suitable Solution Approaches

When choosing a solution technique, careful consideration should be made depending upon the problem requirements. Some considerations include:

1. *Problem type.* For example, modelling noise generation for a tramway requires a different strategy to dynamic track amplification for a high-speed line. This is because noise problems require the study of a higher/wider range of frequencies compared to problems such as ground-borne vibration. Further, it should be considered whether the problem requires a stationary force, or a moving load.

2. *Track type.* Is the track ballasted or non-ballasted, does the problem require the simulation of pinned-pinned resonances, and should non-linearity be simulated.

3. *Coupling.* Will the BOEF model need coupling to a multi-body vehicle model and/or foundation model. Discretely supported and periodic approaches require additional consideration when performing such coupling, compared to continuously supported approaches.

4. *Computational effort.* Does the model require execution many times (e.g. for a sensitivity analysis, or for quantifying uncertainty), meaning computational effort per simulation should be minimised. Continuously supported tracks in the frequency-domain can take advantage of the speed-

wavenumber-frequency relationship thus requiring only wavenumber sampling in the response computation. Further, for noise generation, response symmetry in the wavenumber-frequency-domain means mirroring can often be used for to greatly reduce the number of computations required.

Table 3-3 compares the different solution approaches that have been detailed in the previous and present Chapter, with each method scored from 1 (poor) to 4 (excellent) stars ('*'). Scoring is performed against the ability of the approach to model track dynamics problems (e.g. receptance and dynamic amplification), and noise generation problems.

Regarding track dynamics problems, most frequency-domain approaches, regardless of whether they consider a continuously or discretely supported track, are attractive and computationally efficient. However, although methods such as the boundary value, point source, and periodic are well suited for computing the response due to non-moving sources, they require additional considerations when modelling moving loads (e.g. convolution integrals). Alternatively, the commonly used analytical time-space method is restricted to the use of a simplified track support (e.g. typically a spring with constant stiffness). Finally, the FEM is capable of studying complex track geometries, however requires larger domains, potentially leading to computationally demanding simulations.

Regarding noise generation, discretely supported methods score highest, due to their efficiency and ability to capture pined-pined resonances. Alternatively, periodic methods are computationally efficient due to their simplified domains, however enforce restrictions on domain complexity. Although their repetitive nature is unable to simulate complex track geometries and the pined-pined resonance, improvement in the response can be achieved by combining with FE methods. FEM models by themselves can also capture the pined-pined resonance, however due to the wide frequency range needed to study noise problems, their computational expense is high. Alternatively, continuously supported models in both frequency- and time-domains score lowly due to their inability to capture the pined-pined resonance.

Computation approach	Track dynamics	Noise generation	Comments
Continuously supported-Time-domain			
Analytical time-space	***	**	Simplified modelling of track support. Unable to capture pinned-pinned resonance
Continuously supported-Frequency-domain			
Fourier	****	***	Track support can be simulated with moderate accuracy. Unable to capture the pinned-pinned resonance.
Filon quadrature	****	***	
Contour integration	***	***	
Boundary value^	**	***	
FEM	***	***	Large domains resulting in computational demanding simulations. Flexibility in geometry and material properties.
Discrete support			
Point source^	**	****	Can capture pinned-pinned resonance. Additional consideration required to couple to a detailed track support.
Dirac comb	****	****	
Green's function	****	****	
2.5D	****	**	Track supports are simulated with moderate accuracy. Unable to capture the pinned-pinned resonance as they cannot replicate the discrete support conditions.
Periodic-Eigenvalues^			
Floquet	**	***	Can account for semi-periodic conditions. Eigenvalue problems may lead to ill-conditioning issues. Track supports can be simulated with high accuracy.
Transfer matrix	**	***	
Multi-coupled periodic	**	***	
Direct Periodic	****	****	Can account for semi-periodic conditions. Straightforward solution. Track supports can be simulated with high accuracy.

^Moving loads require additional consideration

Table 3-3. Comparison of reviewed solution approaches

3.7 Conclusions

This Chapter presents a technical review of Periodic approaches. First, it presents the generalities associated with its formulation and how it can be introduced to railway track structures. Next, various solution approaches for fully periodic structures are introduced, ranging from the simplest BOEF periodic formulations with discrete support conditions, to more complex periodic approaches that can be coupled with FEM. Solutions for semi-periodic approaches are then introduced. These approaches allow changes in track geometry and material parameters to be considered, thus allowing for the analysis of more complex structures such as transition zones.

This Chapter complements the example applications presented in Chapter 2, and studies two common railway engineering problems via traditional continuous BOEF and discrete periodic approaches. Results demonstrate the limitation of continuous simulations when capturing the accurate track response at certain frequencies.

Challenges associated to periodic approaches are highlighted. Overall, it is shown that the fundamental periodic formulation presents several limitations, including: (1) confinement to fully-periodic structures, (2) potential numerical issues due to the size of the problem, and (3) restriction to non-moving excitations.

Finally, the various solution approaches presented in this and previous Chapter are compared and ranked depending on their ability to simulate two common railway engineering problems. It is seen that the Direct Periodic is a straightforward solution that can consider both moving and non-moving excitations, simulate the track support with high accuracy, and potentially account for semi-periodic conditions.

Chapter 4

Development of a Periodic Track Model

4.1 Introduction

This Chapter describes the development of a track-ground model based on the Direct Periodic Method (DPM). This computationally efficient approach exploits the inherent periodic behaviour of railway tracks to study large structural domains (e.g. infinitely extending tracks) via a single slice. The method is combined with 3D FE and PML techniques (3D DPM-FE-PML), thus allowing the inclusion of complex geometries, additional track components' mechanical behaviour, and wave propagation effects.

Section 4.2 outlines the Direct Periodic Method, including: (1) a step-by-step solution process for calculating the total railway track using FE methods, and (2) its combination with perfectly matching layer techniques for the soil behaviour representation. Finally, some conclusions are provided in Section 4.3.

4.2 Model Overview

The Direct Periodic Method (DPM) proposed by [256], is a technique that exploits the repetitive or invariant nature of railway structures to study large domains (e.g. infinitely extending tracks). In railway systems, periodicity is found by considering both material and geometrical properties repeat themselves at a regular interval, known as the periodic length d– see **Figure 3-1**.

Since the properties repeat themselves every length d, only a portion $\widetilde{\Omega}$ of the total structure Ω is required in the simulation. Then, the total response of the latter is

retrieved by enforcing compatibility conditions at the boundaries of the former. This restricted domain is often known as the generic or unit cell, and it is assumed to be infinitely repeated, forming the entire structure or total domain [11]. Due to the simplification in the study domain, the periodic approach allows for computing accurate results with minimal computational effort and shorter simulation times compared to fully 3D modelling techniques. Procedure for calculating the total track response via the Direct Periodic Method comprises three steps – **Figure 4-1**:

(a) Computation of the reference cell response in the wavenumber-frequency-domain – see **Figure 4-1**(a). Firstly, the system of equations of motion of the restricted domain is defined in the wavenumber and frequency-domain. Then, periodic boundary conditions at the restricted domain's back and front face are enforced, modifying the equilibrium equations and allowing for its response computation.

(b) Response of all cells in the wavenumber-frequency-domain – see **Figure 4-1**(b). Once the reference cell response is obtained, periodic conditions are again imposed, and the response of the remaining cells in the wavenumber-frequency-domain is computed.

(c) Total structure response in the space-frequency-domain – see **Figure 4-1**(c). Fourier transformation is used to transform the total structure response in the wavenumber-domain back to space.

4.2.1 Solution Process

The DPM method allows for the computation of the entire periodic structure Ω by simply studying the behaviour of a discretised domain $\widetilde{\Omega}$, i.e. the reference cell response $\tilde{u}_{n=0}$. Next, via enforcement of a periodic condition – defined by Floquet theory [226,244,248,249], the total domain response at all cells $\tilde{u}_n$ is obtained, as shown in **Eq**. (3-38):

$$\tilde{u}_n(x, y, z, \beta_x, \omega) = \tilde{u}_{n=0}(\tilde{x}, \tilde{y}, \tilde{z}, \beta_x, \omega)e^{ind\beta_x} \qquad (4-1)$$

Where $s = \{x, y, z\}$ and $\tilde{s} = \{\tilde{x}, \tilde{y}, \tilde{z}\}$ are the space vectors defining Ω and $\widetilde{\Omega}$, respectively. Similarly, $\tilde{u}_n$ and $\tilde{u}_{n=0}$ are the displacements of the total Ω and discretised $\widetilde{\Omega}$ domain, respectively. The tilde notation '$\sim$' in $\tilde{u}_n$, is employed to represent the wavenumber-frequency-domain (β_x, ω), and the number of the cell is defined by n, being $n = 0$ the reference cell, and $n \neq 0$ the remaining structure; and d is the thickness of the reference cell in the periodic direction – x axis or longitudinal direction. Since periodicity is assumed only in the longitudinal direction, the wavenumber response is presented solely around this direction and $\tilde{x} \neq x$. Similarly, the vectors corresponding to the vertical and transversal

coordinates remain constant, i.e. $y = \tilde{y}, z = \tilde{z}$, and their corresponding wavenumber response, β_y and β_z, are not considered in **Eq**. (3-38).
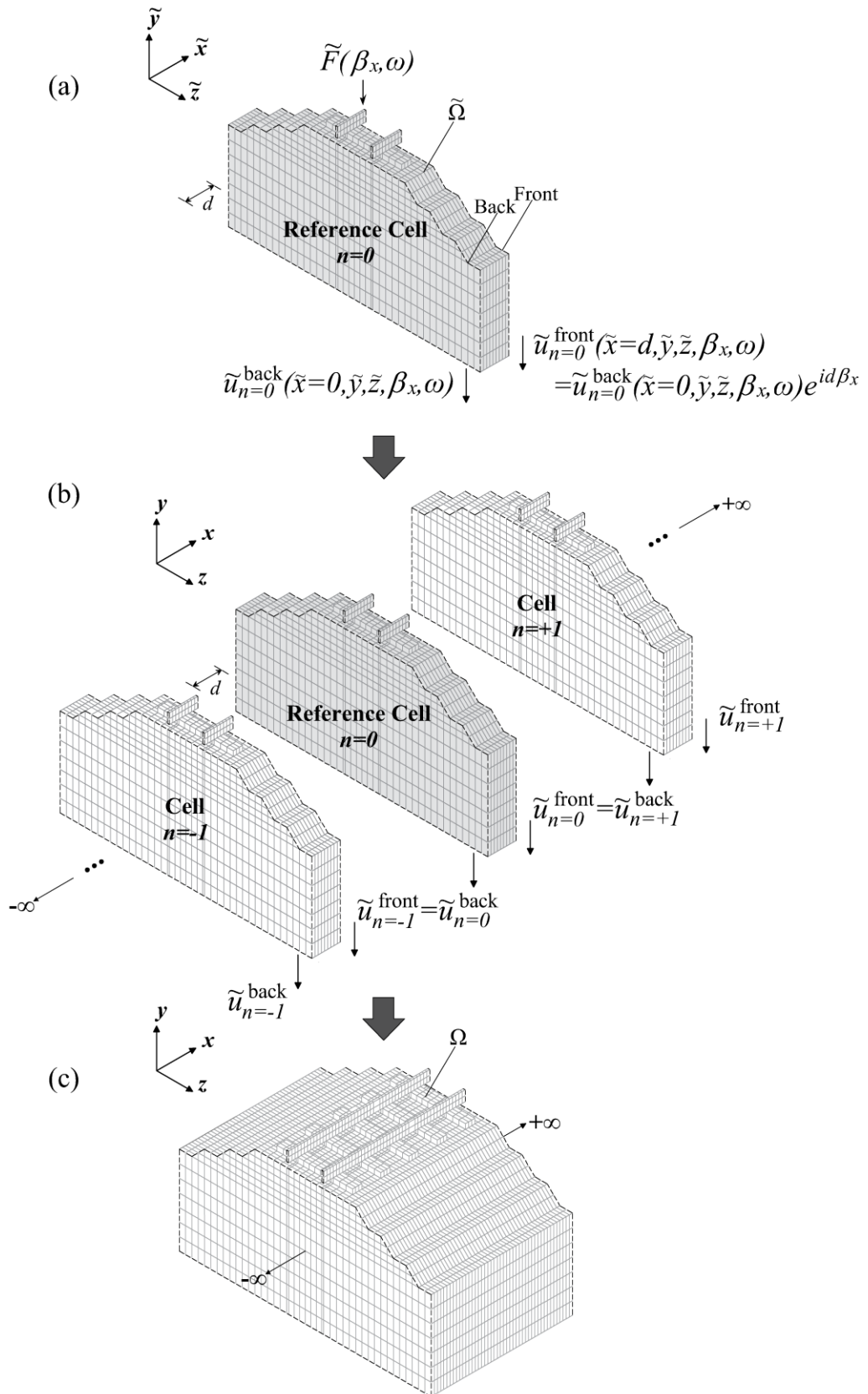
Figure 4-1. Direct Periodic Method overview: (a) reference cell response in wavenumber-frequency-domain, (b) all cells' response in wavenumber-frequency-domain, and (c) total response in space-frequency-domain

In order to properly enforce the periodic condition described in **Eq**. (3-38), the displacements at the front face of the reference cell must be formulated according to those at the back and the periodic condition $e^{id\beta_x}$, see **Eq**. (3-37):

$$\tilde{u}_{n=0}^{\text{front}}(\tilde{x} = d, y = \tilde{y}, z = \tilde{z}, \beta_x, \omega)$$
$$= \tilde{u}_{n=0}^{\text{back}}(\tilde{x} = 0, y = \tilde{y}, z = \tilde{z}, \beta_x, \omega)e^{id\beta_x} \tag{4-2}$$

where $\tilde{u}_{n=0}^{\text{front}}$ and $\tilde{u}_{n=0}^{\text{back}}$ refer to the front (or right-hand side) and back (or left-hand side) border displacements of the reference cell, respectively.

Enforcement of the periodic conditions described in **Eqs**. (3-37)-(3-38), ensures the continuity of the displacements at the boundaries of each cell, allowing for the displacements of the back and front faces of the nth cell to be continuous at the front of the $n^{th} - 1$ cell and back of the $n^{th} + 1$ cell, respectively – see **Figure 4-1**(b) and **Eq**. (4-3):

$$\tilde{u}_n^{\text{back}} = \tilde{u}_{n-1}^{\text{front}}$$
$$\tilde{u}_n^{\text{front}} = \tilde{u}_{n+1}^{\text{back}} \tag{4-3}$$

Once obtained the β_x domain response for all n cells, $\tilde{u}_n$ – see **Eq**. (3-38), it can be transformed back to space-domain x through the Fourier transform in **Eq**. (3-39):

$$\hat{u}(x, y, z, \omega) = \frac{1}{2\pi} \int_{-\infty}^{+\infty} \tilde{u}_n(x, y, z, \beta_x, \omega)e^{ix\beta_x}d\beta_x \tag{4-4}$$

where $\hat{u}$ is the displacement of the total domain in the space-frequency-domain (x, ω), as described by the hat notation '^'.

4.2.1.1 Reference Cell Definition and Response

Firstly, the reference cell response $\tilde{u}_{n=0}$ must be computed in order to retrieve the total structural response $\hat{u}$. To do so, the system of equations of motion of the restricted domain must be formulated and solved in the wavenumber-frequency-domain. **Eq.** (4-5) shows the set of equilibrium equations of the reference cell $n = 0$, in matrix format:

$$[\widetilde{D}_{n=0}]\{\tilde{u}_{n=0}\} = \{\tilde{F}_{n=0}\} \tag{4-5}$$

where $\{\tilde{F}_{n=0}\}$ and $\{\tilde{u}_{n=0}\}$ are the vectors of the moving external force and displacements of the reference cell, respectively; and $[\widetilde{D}_{n=0}]$ is the Dynamic Stiffness Matrix (DSM) of the reference cell.

4.2.1.1.1 Dynamic Stiffness Matrix Definition

$[\widetilde{D}_{n=0}]$ is computed by combining its stiffness k, damping c and mass m parameters, in the frequency-domain ω, as shown in **Eq.**(4-6):

$$[\widetilde{D}_{n=0}] = [K_{n=0}] - \omega^2[M_{n=0}]$$

(4-6)

in which $[K_{n=0}]$ and $[M_{n=0}]$ are the complex stiffness and mass matrices of the cell $n = 0$. The damping formulation is accounted within $[K_{n=0}]$ via the hysteretic model [11] in **Eq.** (4-7):

$$[K_{n=0}] = [K](1 + i\eta)$$

(4-7)

where $[K]$ is the real stiffness matrix and η is the loss factor of the material. Note that η depends on the individual track component, and so is $[K_{n=0}]$.

The stiffness and mass matrices are computed via Finite Element approaches with **Eqs.** (3-18) and (3-19):

$$[K_{n=0}(\tilde{x}, \tilde{y}, \tilde{z})] = \int_{\tilde{x}} \int_{\tilde{y}} \int_{\tilde{z}} [B(\tilde{x}, \tilde{y}, \tilde{z})]^T [D][B(\tilde{x}, \tilde{y}, \tilde{z})] d\tilde{x} d\tilde{y} d\tilde{z}$$

(4-8)

$$[M_{n=0}(\tilde{x}, \tilde{y}, \tilde{z})] = \int_{\tilde{x}} \int_{\tilde{y}} \int_{\tilde{z}} [N(\tilde{x}, \tilde{y}, \tilde{z})]^T \rho [N(\tilde{x}, \tilde{y}, \tilde{z})] d\tilde{x} d\tilde{y} d\tilde{z}$$

(4-9)

where $[D]$ is the elasticity or material matrix, $[B] = [L][N]$ is the strain–displacement transformation matrix or matrix of partial derivatives $[L]$ of the shape functions $[N]$, and ρ is the material density. Note that when considering a moving force contribution (i.e. $v \neq 0$), the angular frequency ω is a function of the driving oscillating frequency ϖ, the wavenumber β_x, and the speed v: $\omega = \varpi - \beta_x v$.

4.2.1.1.2 Force Vector Definition

Regarding the force vector $\{\tilde{F}_{n=0}\}$, a point load is defined by considering a combination of multiple plane waves [23]. **Figure 4-2**(a) shows the plane wave combination, and their shapes, related to each value of the wavenumber sampling (only the limits and the jth component of β_x are shown). In contrast, **Figure 4-2**(b) presents the resulting point load in the wavenumber-domain $\tilde{F}(\beta_x)$ obtained after combining the plane waves associated to all wavenumber values. The schematic representation of the point load can be defined via **Eq.** (4-10):

$$\tilde{F}(\beta_x) = P e^{i\tilde{x}\beta_x}$$

(4-10)

where P is the magnitude of the force, the exponential term $e^{i\tilde{x}\beta_x}$ defines the plane waves, and $\tilde{x}$ is the space coordinate, in the longitudinal direction, of the nodes where the plane waves are distributedly applied in the reference cell. Note that **Eq**. (4-10) is similar to the format used when accounting for multiple axles, derived from the Fourier transform of the force in the space-domain depicted in **Eq**. (4-11):

$$F(x) = P\delta(\tilde{x} - \tilde{x}_o)e^{i\varpi t} \tag{4-11}$$

where $\delta(\cdot)$ is a Dirac delta function defining an impulse, ϖ is the oscillating frequency of the excitation, and $\tilde{x}_o$ is the observation point related to the position a of the lth axle. **Eqs.** (4-12) and (4-13) show the observation point definition for moving and non-moving force case, respectively:

$$\tilde{x}_o = vt + a_l \tag{4-12}$$

$$\tilde{x}_o = a_l \tag{4-13}$$

Fourier transformation of the force (from space to wavenumber), results in the removal of the exponential term $e^{i\varpi t}$:

$$\begin{aligned}\tilde{F}(\beta_x) &= \int_{-\infty}^{+\infty} F(\tilde{x})e^{-i\tilde{x}\beta_x}\mathrm{d}x = \int_{-\infty}^{+\infty} P\delta(\tilde{x} - \tilde{x}_o)e^{i\varpi t}e^{-i\tilde{x}\beta_x}\mathrm{d}x \\ &= Pe^{-i\tilde{x}_o\beta_x}\end{aligned} \tag{4-14}$$

In the case of moving and non-moving force, **Eqs.** (4-15) and (4-16) are obtained, respectively:

$$\tilde{F}_l(\beta_x) = P_l e^{-i(vt+a_l)\beta_x} \tag{4-15}$$

$$\tilde{F}_l(\beta_x) = P_l e^{-i(a_l)\beta_x} \tag{4-16}$$

Thus, by combining **Eqs**. (4-10) and (4-14), it is possible to define the total force contribution, in the wavenumber-domain:

$$\tilde{F}_l(\beta_x) = P_l e^{i(\tilde{x}-a_l)\beta_x} \tag{4-17}$$

$$\tilde{F}_{\text{tot}}(\beta_x) = \sum_{l=1}^{l=l_{\text{tot}}} \tilde{F}_l(\tilde{x}, \beta_x) \tag{4-18}$$

where $\tilde{F}_l$ is the force vector related to axle l, and $\tilde{F}_{\text{tot}}$ is the total force vector computed by superimposing the single axle contribution.

Overall, it is important to consider that the plane waves are distributed forces – as shown in **Figure 4-2**. Thus, its equivalent nodal forces are required to define the force vector in the Finite Element problem.
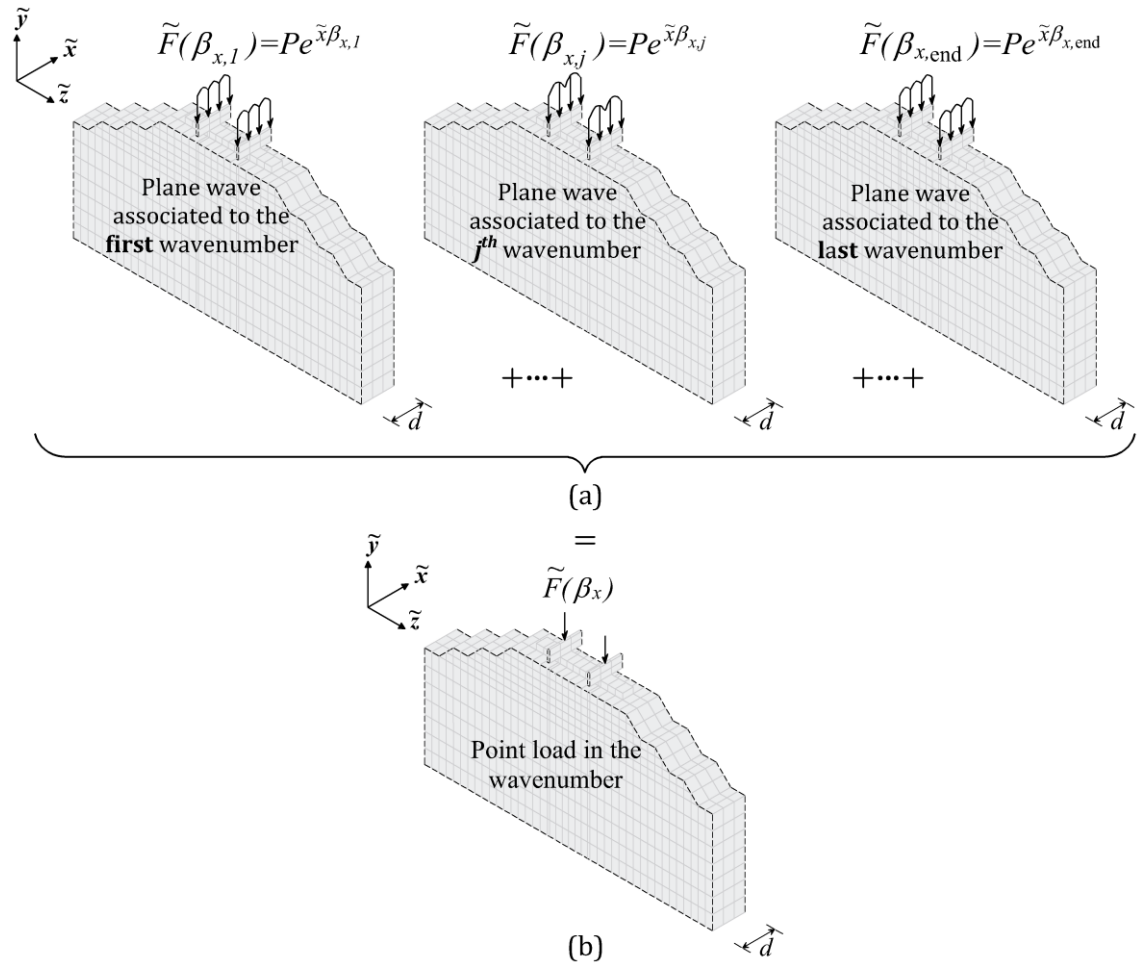
Figure 4-2. Reference cell subject to a point load decomposed into plane waves: (a) plane wave shapes, and (b) point load in β_x domain

4.2.1.2 Boundary Conditions and Response

Before solving the system in **Eq.** (4-5), periodic boundary conditions at the restricted domain's back and front face are enforced, rearranging the equilibrium equations and allowing for its response computation. This rearrangement can be seen as a compatibilisation procedure, since periodic conditions are enforced at the back ($\tilde{x} = 0$) and front ($\tilde{x} = d$) faces of the reference cell – see **Figure 4-1**. **Eq.** (4-19) recalls the periodic condition to be imposed within $n = 0$:

$$\{\tilde{u}_{n=0}^{\text{front}}\} = \{\tilde{u}_{n=0}^{\text{back}}\}e^{id\beta_x} \tag{4-19}$$

To allow for continuity in the complete domain, it is necessary to avoid double counting the front contribution of each cell in the total response. This is achieved by taking the contribution of the front nodes of the reference cell to the corresponding

back nodes in the Dynamic Stiffness Matrix and the vectors of displacements and forces. **Eqs**. (4-20) and (4-21) show the compatible system and its inversion to obtain the response of the reference cell in terms of displacements, respectively.

$$\left[\widetilde{D}_{n=0}^{*}(\beta_x, \omega)\right]\{\tilde{u}_{n=0}^{*}(\beta_x, \omega)\} = \{\tilde{F}_{n=0}^{*}(\beta_x)\} \tag{4-20}$$

$$\{\tilde{u}_{n=0}^{*}(\beta_x, \omega)\} = \left[\widetilde{D}_{n=0}^{*}(\beta_x, \omega)\right]^{-1}\{\tilde{F}_{n=0}^{*}(\beta_x)\} \tag{4-21}$$

where '*' indicates the compatibilisation condition imposed in the vectors and the matrix (dropped in the following computations for visibility). For more information regarding the applied compatibilisation procedure, please refer to Appendix B.

4.2.1.3 Total Structural Response

Assuming a periodic behaviour, the track can be thought as a combination of multiple reference cells connected to each other at their ends via enforcement of periodic conditions – see **Figure 4-1**(b). **Eq**. (4-22) shows the track response $\tilde{u}$ in the wavenumber-frequency-domain:

$$\begin{aligned}
\tilde{u}(x, y, z, \beta_x, \omega) &= \tilde{u}_n(x = \tilde{x} + nd, y = \tilde{y}, z = \tilde{z}, \beta_x, \omega) \\
&= \tilde{u}_{n=0}(\tilde{x}, \tilde{y}, \tilde{z}, \beta_x, \omega)e^{ind\beta_x}
\end{aligned} \tag{4-22}$$

where $\tilde{u}_n$ is the displacement of all nodes of the nth cell, which is computed from the combination of the reference cell displacement $\tilde{u}_{n=0}$ and the exponential term $e^{ind\beta_x}$ defining the periodic condition.

The space vectors describing the reference cell in the longitudinal, transversal and vertical directions are $\{\tilde{s}\} = \{\tilde{x}, \tilde{y}, \tilde{z}\}$, respectively. Alternatively, the space vectors defining the total track response are $\{s\} = \{x, y, z\}$. Note that although the response is computed in the (β_x, ω) domain, $\{\tilde{s}\}$ and $\{s\}$ are used in the definition of the reference cell and the track response in terms of the nth cell – as shown in **Eq**. (4-22). Also, since periodicity is assumed only in the longitudinal direction, the wavenumber response is presented solely around the x direction, and the space vector related to this coordinate depends upon the number of cell n and its length d, i.e. β_x and $x = \tilde{x} + nd$, respectively. Thus, the vectors corresponding to the transversal and vertical coordinates remain unchanged, i.e. $y = \tilde{y}$, $z = \tilde{z}$, and no wavenumber samplings are required along these directions.

Once the response in the (β_x, ω) is obtained at all cells, the inverse Fourier transform – see **Eqs**. (2-36) and (4-23), is employed to convert the wavenumber result $\tilde{\mathcal{F}}(\beta_x)$ back to space-domain $\mathcal{F}(x)$, as described in **Eq**. (4-24):

$$\mathcal{F}(x) = \frac{1}{2\pi} \int_{-\infty}^{+\infty} \tilde{\mathcal{F}}(\beta_x) e^{ix\beta_x} d\beta_x \tag{4-23}$$

$$\begin{aligned}
\hat{u}(x, y, z, \omega) &= \frac{1}{2\pi} \int_{-\infty}^{+\infty} \tilde{u}_n(x = \tilde{x} + nd, y, z, \beta_x, \omega) \, d\beta_x \\
&= \frac{1}{2\pi} \int_{-\infty}^{+\infty} \left[\tilde{u}_{n=0}(\tilde{x}, \tilde{y}, \tilde{z}, \beta_x, \omega) e^{ind\beta_x} \right] d\beta_x
\end{aligned} \tag{4-24}$$

where $\hat{u}$ is the total domain response in the space-domain. By expanding **Eq**. (4-24), it can be seen that the exponential value $e^{ind\beta_x}$ is analogous to the exponential $e^{ix\beta_x}$ in the inverse Fourier transformation shown in **Eq**. (4-23).

4.2.1.4 Dynamic Train-Track Interaction

The structural response due to a dynamic excitation is computed through a compliance procedure in the frequency-domain. This procedure requires the formulation of equations of motion for the vehicle and the track in the frequency-domain, and the enforcement of compatibility conditions at the contact point between the wheel and the rail (i.e. continuity of displacements). For this, a wheel-rail perfect contact is assumed and can be described by **Eq**. (4-25):

$$u_r(x, t) = u_c(x, t) + r(x, t) \tag{4-25}$$

where u_r and u_c are the vertical displacements of the rail and the contact point, respectively, and r is the irregularity of the rail (i.e. roughness or unevenness).

4.2.1.4.1 Definition of Track Irregularities

First, consider a train moving at a constant speed v on a track with a rough rail. This track unevenness is defined as a random function in the space-domain and is based on a statistical form of Power Spectral Density (PSD) $S_l(\phi)$ in spatial-frequency-domain ϕ (i.e. the number of cycles per unit of length, $\phi = 1/\lambda$) or $S_l(\beta_x)$ in wavenumber-domain – in both cases S_l is related to the lth axle. Among the various PSD functions defined in the literature [13,199,201,202], the formulated by the Federal Railway Administration (FRA) is often employed [217]. This formulation divides the track profile into 8 classes, from 1 (poor quality) to 8 (very good quality). **Eq**. (4-26) shows the PSD function defined by the FRA:

$$\tilde{S}_l(\beta_x) = \frac{A\rho_3^2(\beta_x^2 + \rho_2^2)}{\beta_x^4(\beta_x^2 + \rho_3^2)} \tag{4-26}$$

where ρ_2 and ρ_3 are the break spatial frequencies, and A is the roughness constant [13]. Computation of the PSD allows for the definition of the amplitude of unevenness $\tilde{r}$, as shown in **Eq.** (4-27):

$$\tilde{r}_l\left(\beta_{x_j}\right) = \left(\sqrt{2\tilde{S}_l(\beta_x)\Delta\beta_x}\right)e^{i(\beta_x a_l - \theta_j)} \tag{4-27}$$

where $\tilde{r}_l$ is the unevenness function in the wavenumber-domain for the lth axle at position a_l, $\Delta\beta_x$ is the resolution retained for the spatial frequency, and θ is the phase angle taken as a random variable with uniform distribution in the range 0 to 2π. Note that the number or amplitude values r depend upon the jth wavenumber value β_{x_j} – which at the same time depends on the jth wavelength value $\lambda_j = 2\pi/\beta_{x_j}$, and allows for the definition of the jth excitation frequency $\varpi_j = 2\pi v/\lambda_j$. Once defined $\hat{r}$, its space transform r can be computed by summing up all j^{th} contributions, often known as harmonics – see **Eq.** (4-28)

$$r_l(x,t) = \sum_{j=1}^{j=j_{\text{end}}} \tilde{r}_l\left(\beta_{x_j}\right)e^{i\beta_{x_j}x} = \sum_{j=1}^{j=j_{\text{end}}} \tilde{r}_l\left(\beta_{x_j}\right)e^{i\frac{2\pi}{\lambda_j}x} \tag{4-28}$$

Eq. (4-28) shows that the roughness can be interpreted as a sum of all j^{th} harmonics. This allows us to separate the total irregularity value into harmonic profiles ϖ_j described by wavelengths λ_j, as shown in **Figure 4-3** for a single axle.

Considering $x = a_l + vt$, in which a is the lth axis location, **Eq.** (4-28) can be expressed in terms of wavenumber-frequency-domain [167]:

$$r_l(x,t) = \sum_{j=1}^{j=j_{\text{end}}} \tilde{r}_l\left(\beta_{x_j}\right)e^{i\frac{2\pi}{\lambda_j}(a_l+vt)} = \sum_{j=1}^{j=j_{\text{end}}} \tilde{r}_l\left(\beta_{x_j}\right)e^{i\frac{2\pi}{\lambda_j}a_l}e^{i\varpi_j t}$$
$$= \sum_{j=1}^{j=j_{\text{end}}} \hat{r}_l\left(x,\varpi_j\right)e^{i\varpi_j t} \tag{4-29}$$

$$\hat{r}_l\left(x,\varpi_j\right) = \hat{r}_l\left(\beta_{x_j}\right)e^{i\frac{2\pi}{\lambda_j}a_l} \tag{4-30}$$

Note that since track irregularities are stochastic (i.e. they are random), relying on a single profile may not capture the full range of potential impacts on track dynamics. Therefore, the analysis should include multiple profiles and incorporate statistical methods for a better representation of the track dynamics response.
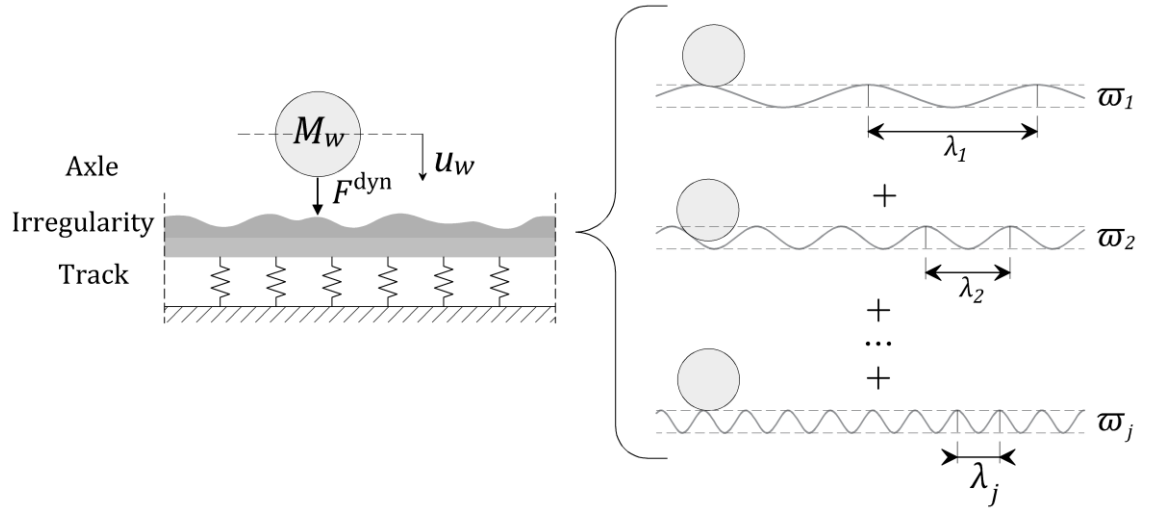
Figure 4-3. Irregularity decomposition. 1 DOF multi-body vehicle system

4.2.1.4.2 Computation of Dynamic Interaction Forces

Let us consider a single unsprung system described by a wheel of mass M_w and a Hertzian spring K_{HZ} in contact with the roughness r (as highlighted in **Figure 2-17**). The equations of motion in time and frequency-domain of this wheel-rail contact interaction model is defined in **Eqs**. (4-31) and (4-32), respectively.

$$M_w \ddot{u}_w(t) + K_{Hz}[u_w(t) - u_r(t)] = 0$$
$$K_{HZ}[u_r(t) - u_w(t)] = -F^{\text{dyn}}(t)$$

$$(4\text{-}31)$$

$$-\varpi M_w \hat{u}_w(\varpi_j) + K_{Hz}\left(\hat{u}_w(\varpi_j) - \hat{u}_r(\varpi_j)\right) = 0$$
$$K_{HZ}[\hat{u}_r(\varpi_j) - \hat{u}_w(\varpi_j)] = -\hat{F}^{\text{dyn}}(\varpi_j)$$

$$(4\text{-}32)$$

where u_r is the rail deflection, u_w and $\ddot{u}_w$ are the displacement and the acceleration of the wheel respectively; and F^{dyn} is the dynamic force. The hat '^' notation is employed to represent the riding frequency-domain $\varpi_j = 2\pi v/\lambda_j$. Inversion of **Eq**. (4-32) allows for the definition of the vertical rail deflection in terms of the compliance of the vehicle $\hat{C}^V$:

$$\hat{u}_{r,n=0}(\varpi_j) = -\hat{C}^V(\varpi_j)\,\tilde{F}_l^{\text{dyn}}(\varpi_j)$$

$$(4\text{-}33)$$

$$\hat{C}^V(\varpi_j) = \left(\frac{K_{Hz}\,\varpi_j^2\,M_w}{\varpi_j^2\,M_w\,+\,K_{Hz}}\right)^{-1}$$

$$(4\text{-}34)$$

Since the dynamic response is computed via the Direct Periodic Method, the rail deflection is computed at the reference cell level, i.e. $\hat{u}_r = \hat{u}_{r,n=0}$.

$\tilde{F}_l^{\text{dyn}}$ is the magnitude of the lth dynamic force for the jth harmonic located at $x = a_l$ at $t = 0$ s. When multiple axles are considered, the total force $\tilde{F}_{\text{tot}}^{\text{dyn}}$, in the

wavenumber-frequency-domain, can be computed by summing every l^{th} contribution, as described in **Eq**. (4-35):

$$\tilde{F}_{\text{tot}}^{\text{dyn}}(\beta_x, \varpi_j) = \sum_{l=1}^{l=l_{\text{tot}}} \hat{F}_l^{\text{dyn}}(\varpi_j)\, e^{-i(x=a_l)\beta_x} = \sum_{l=1}^{l=l_{\text{tot}}} \tilde{F}_l^{\text{dyn}}(\beta_x, \varpi_j) \qquad (4\text{-}35)$$

Alternatively, the track response is obtained through the Green's function of the vertical displacement at the contact point, $\tilde{u}_{c,n=0}^{\text{Green}}$, i.e. the rail response of the reference cell due to a unit force at the corresponding frequency $\omega = \varpi_j - \beta_x v$. Considering a linear model, the track response at the contact point can be obtained by multiplying its unit response by the force in the wavenumber-frequency-domain $\tilde{F}_l^{\text{dyn}}(\beta_x, \varpi_j)$, as defined in **Eq**. (4-36).

$$\tilde{u}_{c,l,n=0}^{\text{dyn}}(\beta_x, \varpi_j) = \tilde{u}_{c,n=0}^{\text{Green}}(\beta_x, \omega = \varpi_j - \beta_x v)\, \tilde{F}_l^{\text{dyn}}(\beta_x, \varpi_j) \qquad (4\text{-}36)$$

where $\tilde{u}_{c,l,n=0}^{\text{dyn}}$ is the dynamic contact deflection of the reference cell $(n = 0)$ in the wavenumber-frequency-domain (β_x, ϖ_j) related to axle l. $\tilde{u}_{c,n=0}^{\text{dyn}}$ in **Eq**. (4-36) can be transformed back to space through the inverse Fourier transformation – see **Eq**. (2-36), as described in **Eq**. (4-37):

$$\begin{aligned}
\hat{u}_{c,l,n=0}^{\text{dyn}}(x, \varpi_j) &= \frac{1}{2\pi} \int_{-\infty}^{+\infty} \tilde{u}_{c,n=0}^{\text{Green}}(\beta_x, \varpi_j)\, e^{ia_l\beta_x}\, \mathrm{d}\beta_x \\
&= \frac{1}{2\pi} \int_{-\infty}^{+\infty} \left(\tilde{u}_{c,n=0}^{\text{Green}}(\beta_x, \omega)\, \hat{F}_l^{\text{dyn}}(\beta_x, \varpi_j) \right) e^{ia_l\beta_x}\, \mathrm{d}\beta_x \qquad (4\text{-}37)\\
&= \frac{1}{2\pi} \int_{-\infty}^{+\infty} \left(\tilde{u}_{c,n=0}^{\text{Green}}(\beta_x, \omega) \hat{F}_l^{\text{dyn}}(\varpi_j)\, e^{-ia_l\beta_x} \right) e^{ia_l\beta_x}\, \mathrm{d}\beta_x
\end{aligned}$$

where $\hat{u}_{c,l,n=0}^{\text{dyna}}$ is the dynamic contact force of the reference cell, corresponding to axle l, in the space-frequency-domain. Note that vertical and transversal axis (y, z) have been dropped in the following computations for visibility, and only longitudinal (x) and periodic axis is shown.

Rearrangement of **Eq**. (4-37) allows for the definition of the track compliance $\hat{C}^T$:

$$\begin{aligned}
&\hat{u}_{c,l,n=0}(\tilde{x}, \varpi_j) \\
&= \left[\frac{1}{2\pi} \int_{-\infty}^{+\infty} \tilde{u}_{c,n=0}^{\text{Green}}(\beta_x, \omega)\, e^{-i(a_{l=m} - a_{l=k})\beta_x} \mathrm{d}\beta_x \right] \hat{F}_l^{\text{dyn}}(\tilde{x}, \varpi_j) \qquad (4\text{-}38)\\
&= \left[\hat{C}_{m,k}^T(\tilde{x}, \varpi_j) \right] \hat{F}_l^{\text{dyn}}(\tilde{x}, \varpi_j)
\end{aligned}$$

$$\hat{C}_{m,k}^T(\tilde{x}, \varpi_j) = \frac{1}{2\pi} \int_{-\infty}^{+\infty} \tilde{u}_{c,n=0}^{\text{Green}}(\beta_x, \omega = \varpi_j - \beta_x v) e^{-i(a_m - a_k)\beta_x}\, \mathrm{d}\beta_x \qquad (4\text{-}39)$$

where the track compliance $\hat{C}_{m,k}^T$ relates the deflections of the track at the position of the kth axle due to the unit load at the mth axle [83].

Finally, **Eqs**. (4-33) and (4-38) can be combined in **Eq**. (4-40) to retrieve the dynamic interaction force $\hat{F}^{\text{dyn}}(\tilde{x}, \varpi_j)$ – sub indices relate to l^{th} axis are dropped for clarity.

$$\hat{u}_r = \hat{u}_c + \hat{r}$$
$$\Rightarrow \left[-\hat{C}^V(\tilde{x}, \varpi_j)\, \hat{F}^{\text{dyn}}(\tilde{x}, \varpi_j)\right] = \left[\hat{C}^T(\tilde{x}, \varpi_j)\, \hat{F}^{\text{dyn}}(\tilde{x}, \varpi_j)\right] + \hat{r}(\tilde{x}, \varpi_j)$$
$$\Rightarrow -\left[\hat{C}^T(\tilde{x}, \varpi_j) + \hat{C}^V(\tilde{x}, \varpi_j)\right] \hat{F}^{\text{dyn}}(\tilde{x}, \varpi_j) = \hat{r}(\tilde{x}, \varpi_j) \tag{4-40}$$

$$\hat{F}^{\text{dyn}}(\tilde{x}, \varpi_j) = -\left[\hat{C}^T(\tilde{x}, \varpi_j) + \hat{C}^V(\tilde{x}, \varpi_j)\right]^{-1} \hat{r}(\tilde{x}, \varpi_j) \tag{4-41}$$

Note that $\hat{F}^{\text{dyn}}$ is obtained for each position $\tilde{x}$ in the reference cell, however, response is only taken at the back node contribution, i.e. at $\tilde{x} = 0$. This is due to the compatibilisation required in the computation of the cell response (Section 4.2.1.2), in which the Dynamic Stiffness Matrix and force vector are rearranged in order to avoid double counting the contribution from nodes at the boundaries, and front ($\tilde{x} = d$) contributions are placed in the back ($\tilde{x} = 0$). Thus, the dynamic force is computed following **Eq**. (4-42):

$$\hat{F}^{\text{dyn}}(\varpi_j) = \hat{F}^{\text{dyn}}(\tilde{x} = 0, \varpi_j)$$
$$= -\left[\hat{C}^T(\tilde{x} = 0, \varpi_j) + \hat{C}^V(\tilde{x} = 0, \varpi_j)\right]^{-1} \hat{r}(\tilde{x} = 0, \varpi_j) \tag{4-42}$$

Note that by considering only the contributions at $\tilde{x} = 0$, periodicity is enforced. Thus leading to the assumption of a periodic rail irregularity.

Once the dynamic magnitude of the force $\hat{F}^{\text{dyn}}$ is obtained, this can be described in the wavenumber-domain $\tilde{F}^{\text{dyn}}$, via **Eq**. (4-35). Next, the track deflection of the reference cell, $\tilde{u}_{n=0}^{\text{dyn}}(\beta_x, \varpi_j)$, can be computed by multiplying the corresponding Green's function (i.e. unit force response) by the dynamic force in the wavenumber-frequency-domain, as presented in **Eq.** (4-43):

$$\tilde{u}_{n=0}^{\text{dyn}}(\tilde{x}, \beta_x, \varpi_j) = \tilde{u}_{n=0}^{\text{Green}}(\tilde{x}, \beta_x, \omega = \varpi_j - \beta_x v)\, \tilde{F}^{\text{dyn}}(\beta_x, \varpi_j) \tag{4-43}$$

Finally, the dynamic track response is retrieved through enforcement of the periodic condition in **Eq.** (4-44):

$$\tilde{u}_n^{\text{dyn}}(x = \tilde{x} + nd, \beta_x, \varpi_j) = \tilde{u}_{n=0}^{\text{dyn}}(\tilde{x}, \beta_x, \varpi_j)\, e^{ind\beta_x} \tag{4-44}$$

For further information regarding time-domain transformation, please refer to Appendix C. Additionally, although this section focuses on a single wheel-mass model, Section 2.2.3.2 demonstrates the significance of full-vehicle models. Additional information on the full vehicle model can be found in Appendix D.

4.2.2 Soil Domain

Vibrations induced by the train passage have two excitation components: quasi-static and dynamic. Although the former, resulting from the vehicle weight, plays an important role at lower frequencies in the near-field, the dynamic excitation caused by train-track interaction dominates the ground vibration levels [11,23,215,216]. To study the wave propagation within the ground, half-space foundation models are useful. However, these models are complex and computationally demanding since they often require large domain simulations and/or absorbing boundaries.

By itself, the Finite Element Method (FEM) can be employed to model the foundation soil. Nevertheless, FEM computational efficiency is highly reduced due to the large number of elements required to provide an accurate soil representation – particularly when employing three-dimensional formulations. Thus, soil simulations via FE tend to restrict its number of elements and soil domain, and requires the inclusion of additional techniques to prevent wave reflection effect on its boundaries [27]. The Perfectly Matched Layers (PML) provide a solution for this problem by simulating the absorbing domain and preventing wave's reflection at the boundaries of the model [257]. Therefore, the combination of both the FEM and the PML allow for the wave propagation behaviour representation and improves the computational efficiency.

Following this approach, the FEM-PML method can be combined with periodic strategies (i.e. DPM-FEM-PML) to further increase the efficiency of studying the ground-borne response. **Figure 4-4** shows a 3D reference cell, of domain $\widetilde{\Omega}$ and thickness d, with the railway track and ground components defined by the elastic domain $\widetilde{\Omega}_{\mathrm{FEM}}$ and bounded by the PML domain $\widetilde{\Omega}_{\mathrm{PML}}$ (i.e. $\widetilde{\Omega}=\widetilde{\Omega}_{\mathrm{FEM}}\cup\widetilde{\Omega}_{\mathrm{PML}}$).

4.2.2.1 PML Stretching Functions

The PML is a layer of elements with material properties similar to the elastic medium they bound or truncate. In addition, they can perfectly match the truncated medium by absorbing and attenuating outgoing waves from it [258]. The outgoing wave, travelling in the s direction, is attenuated at a finite distance $\widetilde{H}_s$ within the PML domain $\widetilde{\Omega}_{\mathrm{PML}}$ and is minimally reflected back toward the truncated domain $\widetilde{\Omega}_{\mathrm{FEM}}$ from the outer fixed PML limit $\tilde{s}_t$ – see **Figure 4-5**. Since the reflection of the wave is not significant, the PML is able to simulate unbounded domain [258,259].
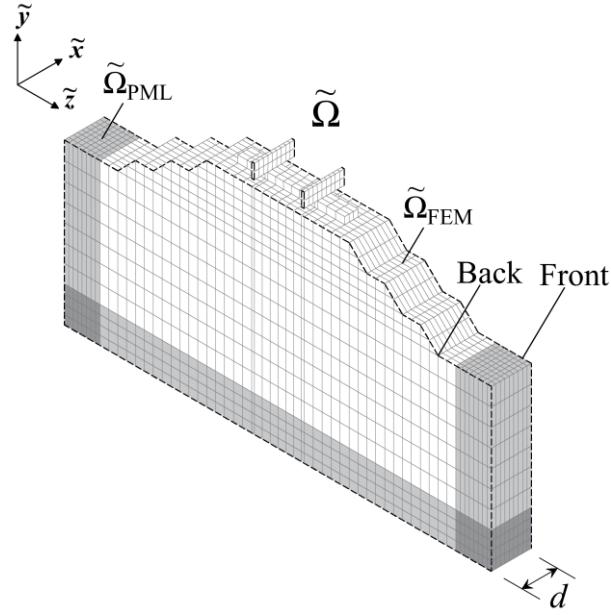
Figure 4-4. 3D FE reference cell $\widetilde{\Omega}_{\text{FEM}}$ bounded by PML layers $\widetilde{\Omega}_{\text{PML}}$. Back and front boundaries in dashed lines
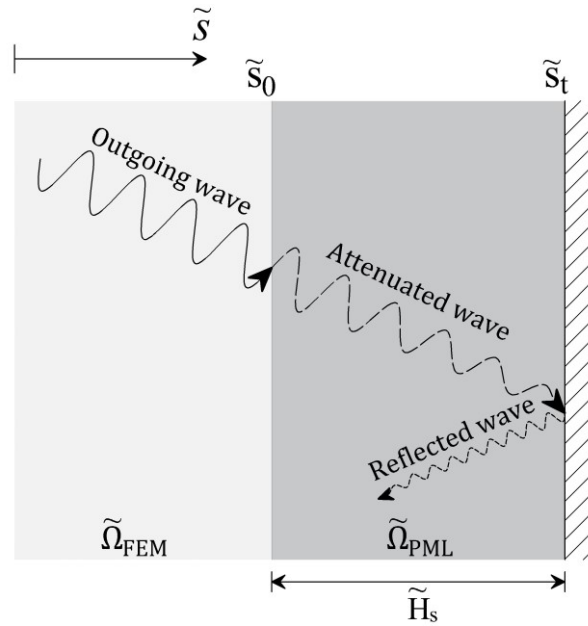
Figure 4-5. PML domain $\widetilde{\Omega}_{\text{PML}}$ of thickness $\widetilde{H}_s$, adjacent to a bounded FEM domain $\widetilde{\Omega}_{\text{FEM}}$, attenuating and reflecting back an outgoing wave

The absorbing domain is defined through complex stretching coordinates š, which allow for the artificial increment of the propagating wave attenuation [260]. **Eq**. (4-45) shows the stretching or new coordinate š, derived from the stretching function $\tilde{\lambda}$, corresponding to each Cartesian coordinate within the reference cell domain $\tilde{s}$:

$$\check{s} = \int_0^{\tilde{s}} \tilde{\lambda}(\tilde{s})\mathrm{d}\tilde{s} = \tilde{s}_0 + \int_{\tilde{s}_0}^{\tilde{s}_t} \tilde{\lambda}(\tilde{s})\mathrm{d}\tilde{s}, \quad \begin{cases} \tilde{s} = \tilde{x}, \tilde{y}, \tilde{z} \\ \check{s} = \check{x}, \check{y}, \check{z} \end{cases} \tag{4-45}$$

where $\tilde{s}_0$ and $\tilde{s}_t$ are the origin and end limits of the PML. Note that throughout $\widetilde{\Omega}$, only $\widetilde{\Omega}_{\text{PML}}$ is stretched and $\widetilde{\Omega}_{\text{FEM}}$ remains unchanged – see **Figure 4-5** and **Figure 4-6**. In addition, since the structure is assumed to be periodic in the longitudinal domain $\tilde{x}$, only $\{\tilde{s}\} = \{\tilde{y}, \tilde{z}\}$ are stretched, as depicted in **Eq.** (4-46):

$$\check{s} = \begin{cases} \check{x} = \tilde{x} \\ \check{y} = \displaystyle\int_0^s \tilde{\lambda}(\tilde{y})\mathrm{d}\tilde{y} \\ \check{z} = \displaystyle\int_0^s \tilde{\lambda}(\tilde{z})\mathrm{d}\tilde{z} \end{cases} \tag{4-46}$$

Enforcement of $\widetilde{\Omega}_{\text{PML}}$ is achieved through the same set of equations of motion defined for $\widetilde{\Omega}_{\text{FEM}}$ – see **Eq.** (4-19). However, stretching coordinates $\{\check{s}\}$ are used instead of the reference cell Cartesian coordinates $\{\tilde{s}\}$. Although different $\tilde{\lambda}$ formulations have been defined in the literature – see for instance [27,259–262], most stretching functions follow the formulation presented in **Eq.** (4-47):

$$\tilde{\lambda}(\tilde{s}) = f_{\tilde{s}}^e(\tilde{s}) - i\frac{f_{\tilde{s}}^p(\tilde{s})}{a_0} \tag{4-47}$$

where $f_{\tilde{s}}^e$ and $f_{\tilde{s}}^p$ are the polynomial functions that attenuate the evanescent and propagating waves inside the PML, respectively; and a_0 is a frequency dependent parameter related to the stretching function definition. This study employs the stretching function proposed by [260], which defines the attenuation functions in terms of linear and quadratic polynomials with unit or zero values when computed within the FEM domain, as shown in **Eq.** (4-48)-(4-49):

$$f_{\tilde{s}}^e(\tilde{s}) = \begin{cases} f_{\tilde{s}_0}^e \dfrac{\bar{s}}{H_{\tilde{s}}} & ; \widetilde{\Omega}_{\text{PML}} = \{\tilde{s}_0 < \tilde{s} \le \tilde{s}_t\} \\ 1 & ; \widetilde{\Omega}_{\text{FEM}} = \{\tilde{s} \le \tilde{s}_0\} \end{cases}$$

$$f_{\tilde{s}}^p(\tilde{s}) = \begin{cases} f_{\tilde{s}_0}^p \left(\dfrac{\bar{s}}{H_{\tilde{s}}}\right)^2 & ; \widetilde{\Omega}_{\text{PML}} = \{\tilde{s}_0 < \tilde{s} \le \tilde{s}_t\} \\ 0 & ; \widetilde{\Omega}_{\text{FEM}} = \{\tilde{s} \le \tilde{s}_0\} \end{cases} \tag{4-48}$$

$$a_0 = k(\beta_x, \omega) = \sqrt{\beta_s^2 - \beta_x^2} \tag{4-49}$$

where $f_{\tilde{s}_0}^p = 2\pi/|k|$ and $f_{\tilde{s}0}^e = 20$ are the parameters employed to adjust the amount of attenuation; $H_{\tilde{s}}$ and $\bar{s} = |\tilde{s} - \tilde{s}_0|$ are the layer thickness and the local Cartesian coordinates within $\widetilde{\Omega}_{\text{PML}}$, respectively. In addition, a_0 or k are the effective wavenumber for waves propagating along the cross-Section – see **Eq.** (4-49). Note that to avoid mathematical problems, when $\beta_s^2 = \beta_x^2$, the wavenumber is modified to $\beta_x = 0.999\beta_x$. Similarly, $\beta_s = \omega/C_s$, is the variable depending on the angular frequency ω and the velocity of the shear wave C_s. Combining **Eqs.** (4-48) and (4-49) into **Eq.** (4-50), the latter becomes:

$$\tilde{\lambda}(\tilde{s}) = \frac{2\pi}{|k|}\left(\frac{\bar{s}}{H_{\tilde{s}}}\right) - i\frac{20}{k}\left(\frac{\bar{s}}{H_{\tilde{s}}}\right)^2 \qquad (4\text{-}50)$$

Depending on the PML region, the direction of the propagating waves varies – see **Figure 4-6**:

- $\tilde{\lambda}(\tilde{x}) = 1$, $\tilde{\lambda}(\tilde{y}) \neq 1$, $\tilde{\lambda}(\tilde{z}) = 1$; stretching coordinates in the $\tilde{y}$ direction only (i.e. bottom region).
- $\tilde{\lambda}(\tilde{x}) = 1$, $\tilde{\lambda}(\tilde{y}) = 1$, $\tilde{\lambda}(\tilde{z}) \neq 1$; stretching coordinates in the $\tilde{z}$ direction only (i.e. side regions).
- $\tilde{\lambda}(\tilde{x}) = 1$, $\tilde{\lambda}(\tilde{y}) \neq 1$, $\tilde{\lambda}(\tilde{z}) \neq 1$; stretching coordinates in t*he $\tilde{y}$ and $\tilde{z}$* directions (i.e. corner regions).
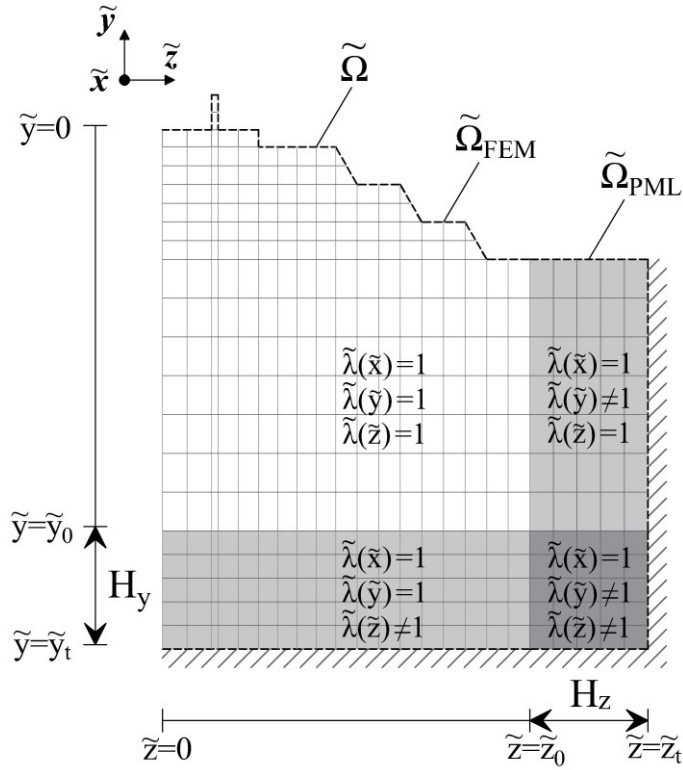
Figure 4-6. Back face of reference cell $\widetilde{\Omega}$ composed by linear $\widetilde{\Omega}_{\text{FEM}}$ and PML $\widetilde{\Omega}_{\text{PML}}$ domain. Limits and stretching functions $\tilde{\lambda}$ highlighted

4.2.2.2 Equilibrium Equations of Motion

In the $\widetilde{\Omega}_{\text{PML}}$, the partial derivatives with respect to the stretching coordinates (**Eq. (4-51)**) allows for the definition of the PML matrix of partial derivatives L_{PML} (**Eq. (4-52)**):

$$\frac{\partial}{\partial \tilde{s}} = \frac{1}{\tilde{\lambda}(\tilde{s})}\frac{\partial}{\partial \tilde{s}}; \ \{s\} = \{x, y, z\} \qquad (4\text{-}51)$$

$$[L_{\text{PML}}] = [\check{L}(\check{x},\check{y},\check{z})] = \begin{bmatrix} \partial/\partial\check{x} & 0 & 0 \\ 0 & \partial/\partial\check{y} & 0 \\ 0 & 0 & \partial/\partial\check{z} \\ 0 & \partial/\partial\check{z} & \partial/\partial\check{y} \\ \partial/\partial\check{z} & 0 & \partial/\partial\check{x} \\ \partial/\partial\check{y} & \partial/\partial\check{x} & 0 \end{bmatrix} \tag{4-52}$$

Note that in the direct periodic problem, the stretching coordinates are only present in the vertical $\tilde{y}$ and transversal $\tilde{z}$ direction; therefore, the partial derivatives with respect to the longitudinal axis $\tilde{x}$ remain unchanged in $[L_{\text{PML}}]$, i.e. $\tilde{\lambda}(\tilde{x}) = 1$ and $\partial/\partial\check{x} = \partial / \partial\tilde{x}$. Similar to the FEM case, the PML approach satisfies the differential system of equations – see **Eqs.** (3-18) and (3-19). Thus, the reference cell stiffness and mass matrices in $\widetilde{\Omega}_{\text{PML}}$, can be computed through **Eqs.** (4-53) and (4-54), respectively:

$$\begin{aligned}
&[K_{n=0}^{\text{PML}}(\tilde{x},\tilde{\lambda}_{\tilde{y}},\tilde{\lambda}_{\tilde{z}})] \\
&= \int_{\tilde{x}}\int_{\tilde{y}}\int_{\tilde{z}} \tilde{\lambda}_{\tilde{y}}\tilde{\lambda}_{\tilde{z}} [\check{B}(\tilde{x},\tilde{\lambda}_{\tilde{y}},\tilde{\lambda}_{\tilde{z}})]^T [D] [\check{B}(\tilde{x},\tilde{\lambda}_{\tilde{y}},\tilde{\lambda}_{\tilde{z}})] \, \mathrm{d}\tilde{x}\mathrm{d}\tilde{y}\mathrm{d}\tilde{z}
\end{aligned} \tag{4-53}$$

$$\begin{aligned}
&[M_{n=0}^{\text{PML}}(\tilde{x},\tilde{\lambda}_{\tilde{y}},\tilde{\lambda}_{\tilde{z}})] \\
&= \int_{\tilde{x}}\int_{\tilde{y}}\int_{\tilde{z}} \tilde{\lambda}_{\tilde{y}}\tilde{\lambda}_{\tilde{z}} [\tilde{N}(\tilde{x},\tilde{\lambda}_{\tilde{y}},\tilde{\lambda}_{\tilde{z}})]^T \rho \, [\tilde{N}(\tilde{x},\tilde{\lambda}_{\tilde{y}},\tilde{\lambda}_{\tilde{z}})] \, \mathrm{d}\tilde{x}\mathrm{d}\tilde{y}\mathrm{d}\tilde{z}
\end{aligned} \tag{4-54}$$

where $[K_{n=0}^{\text{PML}}]$ and $[M_{n=0}^{\text{PML}}]$ are the PML stiffness and mass matrices, respectively; and $[\check{B}] = [\check{L}][\tilde{N}]$ is the matrix of partial derivatives $[\check{L}]$ of the shape functions $[\tilde{N}]$. Since the PML domain is defined through complex stretching coordinates, all matrices in **Eqs.** (4-53) and (4-54) are also complex. Thus, $[\check{B}]^T$ and $[\tilde{N}]^T$ require the non-conjugate transpose instead of their conjugate transpose. Although in both cases, rows and columns are interchanged, in the former, the sign of the imaginary part remains unchanged, whereas, in the latter, they are the opposite. For instance, **Eq.** (4-55) shows the non-conjugate and conjugate transpose of matrix $[A]$, $[A]^T$ and $[A]^{*T}$, respectively.

$$[A] = \begin{bmatrix} a_1 + ib_1 \\ a_2 + ib_2 \end{bmatrix} \Longrightarrow [A]^T = \begin{cases} [A]^T = [a_1 + ib_1 & a_2 + ib_2] \\ [A]^{*T} = [a_1 - ib_1 & a_2 - ib_2] \end{cases} \tag{4-55}$$

Eq. (4-56) describes the system of equations of motion in the total reference cell domain, in which the total Dynamic Stiffness Matrix $[\widetilde{D}_{n=0}^{\text{FEM+PML}}]$ is computed by properly assembling the matrices in both $\widetilde{\Omega}_{\text{FEM}}$ and $\widetilde{\Omega}_{\text{PML}}$ domains, as shown in **Eqs.** (4-57) and (4-58):

$$[\widetilde{D}_{n=0}^{\text{FEM+PML}}]\{\tilde{u}_{n=0}^{\text{FEM+PML}}\} = \{\tilde{F}_{n=0}^{\text{FEM+PML}}\} \tag{4-56}$$

$$[\widetilde{D}_{n=0}^{\text{FEM+PML}}] = [\widetilde{D}_{n=0}^{\text{FEM}}] + [\widetilde{D}_{n=0}^{\text{PML}}] \tag{4-57}$$

$$\left[\widetilde{D}_{n=0}^{\text{FEM}}(\tilde{x}, \tilde{y}, \tilde{z}, \beta_x, \omega)\right] = \left[K_{n=0}^{\text{FEM}}(\tilde{x}, \tilde{y}, \tilde{z})\right] - \omega^2\left[M_{n=0}^{\text{FEM}}(\tilde{x}, \tilde{y}, \tilde{z})\right]$$
$$\left[\widetilde{D}_{n=0}^{\text{PML}}(\tilde{x}, \breve{y}, \breve{z}, \beta_x, \omega)\right] = \left[K_{n=0}^{\text{PML}}(\tilde{x}, \breve{y}, \breve{z})\right] - \omega^2\left[M_{n=0}^{\text{PML}}(\tilde{x}, \breve{y}, \breve{z})\right]$$

(4-58)

where $\left[K_{n=0}^{\text{FEM,PML}}\right]$ are complex stiffness matrices accounting for the hysteretic damping model.

4.3 Conclusions

This Chapter introduces the Direct Periodic Method (DPM), a technique able to simulate the intricate track-ground behaviour. This approach exploits the inherent periodic behaviour of railway tracks, which allows for the computation of the total railway structural system via the analysis of a single 3D slice. This reduction in the domain of study improves the computational efficiency of the simulation while still providing accurate results.

The 3D slice, also referred to as reference or unit cell, is defined by considering the material and complex geometrical properties of the structure repeats by a distance d along the train passage direction. Then, by enforcing periodic-boundary conditions defined in the Floquet's framework, and performing a direct inversion of a modified system of equations of motion, the unit cell response is obtained. Finally, assuming the reference cell repeats infinitely, periodic conditions are again applied and the total response is obtained. Note that by combining DPM techniques with FEM (FE-DPM), the unit cell can account for complex geometries such as discrete support conditions and definition of a track components mechanical behaviour.

Additionally, the DPM allows considering both moving and non-moving excitations. For the latter, the frequency-wavenumber-speed relationship is exploited in the computation of the reference cell response; thus, no additional techniques (e.g. superposition approaches) are required.

Regarding the subgrade representation, the DPM-FE is combined with PML (DPM-FE-PML) to include its wave propagation behaviour. Since the PML only requires a layer of elements to represent the absorbing domain rather than simulating larger soil domains, its inclusion further enhances the computational efficiency of the overall simulation.

Chapter 5
DPM Model Verification

5.1 Introduction

This Chapter describes validations of the 3D DPM track model introduced in Chapter 4. This assessment is crucial as it enables the evaluation of the method's capability to replicate the railway track behaviour under various excitation conditions and the propagation effects of waves within the subgrade component.

For this purpose, four numerical verifications are presented. First, Section 5.2 evaluates the track model under non-moving excitations. Subsequently, in Section 5.3, the model is validated under moving excitations. Similarly, Section 5.4 assesses the model considering both moving dynamic and multiple-axle contributions. Section 5.5 then verifies the effect of ground vibrations. Finally, Section 5.6 summarises the main conclusions.

5.2 Verification Case 1:

Track Dynamics – Non-Moving Excitation

Case 1 allows to demonstrate the accuracy of the periodic formulation and its ability to approximate the dynamic response of a rigidly supported track excited by a non-moving harmonic excitation. The periodic response is computed by combining the DPM with 3D FEM (i.e. 3D DPM-FEM). Next, results are compared to the 2.5D approach and 3D FEM simulation conducted using ABAQUS.

Figure 5-1 shows the study track which consists of a rail resting on a continuous railpad, supported by two continuous track layers lying on a rigid foundation – see Appendix E for further details on track material and geometrical parameters. Also,

all models are subject to a stationary harmonic force of magnitude $P = 1$ N applied at the top of the rail ($x = y = z = 0$ m) and symmetry of the structure is exploited, therefore only half of the domain is modelled.

Figure 5-1(a) displays the 3D DPM reference cell of thickness $d = 8 \times \Delta x$, where Δx is the size element in the periodic direction x, employed in the periodic method formulation. The reference cell is defined by linear brick elements, 2640 elements with 3438 nodes in total, described by hysteretic damping in the frequency-domain. Alternatively, the 2.5D method – see **Figure 5-1**(b), uses a continuous Euler-Bernoulli beam, springs-in-series and cubic solid elements representing the rail, railpad and track layers 1 and 2, respectively, with 567 nodes in total. Excluding the railpad, which uses viscous damping, all track components are defined by hysteretic damping models in the frequency-domain. In the case of the 3D FEM – see **Figure 5-1**(c), all track components are simulated using finite cubic solid elements bounded by infinite Elements defining the far-filed behaviour. Note that to replicate the far-field effect, ABAQUS employs infinite Elements, rather than PML. The complete structure, comprised of 15023 elements and 74874 nodes, is defined by viscous damping models, and the solution is computed via time-integration procedures.

Figure 5-2 compares the rail receptance (i.e. the absolute rail deflection in the frequency-domain at the point of force application), computed via: the 3D DPM, 2.5D approach and 3D FEM (ABAQUS). At 0 Hz, the 3D DPM and 2.5D provide similar results. However, the 3D FEM result is slightly more rigid than in previous cases. This difference can be attributed to the periodic conditions in the 3D DPM and 2.5D approaches: both methods employ reduced domains, thus resulting in a stiffer response at 0 Hz, compared to the fully 3D FEM, which considers a longer domain. Despite the difference in amplitude, all models capture the full-track resonance $f_{\text{full-track}}$ and the sleeper f_{sleeper} resonance at around 132 Hz and 153 Hz. Again, slight differences between the 3D and the periodic and 2.5D approaches at these frequencies are related to the different damping models. Above these frequencies, 2.5D and 3D FEM results converge at around the railpad frequency of resonance, $f_{\text{railpad}} = 239$ Hz. Alternatively, 3D periodic finds this frequency at around 242 Hz. Similarly, differences are attributed to the damping models, in this case viscous damping for 2.5D and 3D FEM, and hysteretic for the 3D DPM.

Lastly, it is important to highlight that since the material and geometrical properties of the track are continuous along the periodic direction (longitudinal axis x), the thickness of the reference cell in the DPM can be reduced from $d = 8 \times \Delta x$ to a single value $d = \Delta x$, i.e. from a 2640 to 330 node structure. This domain reduction produces similar results to the obtained in **Figure 5-2** and allows for further optimisation of the periodic simulation.
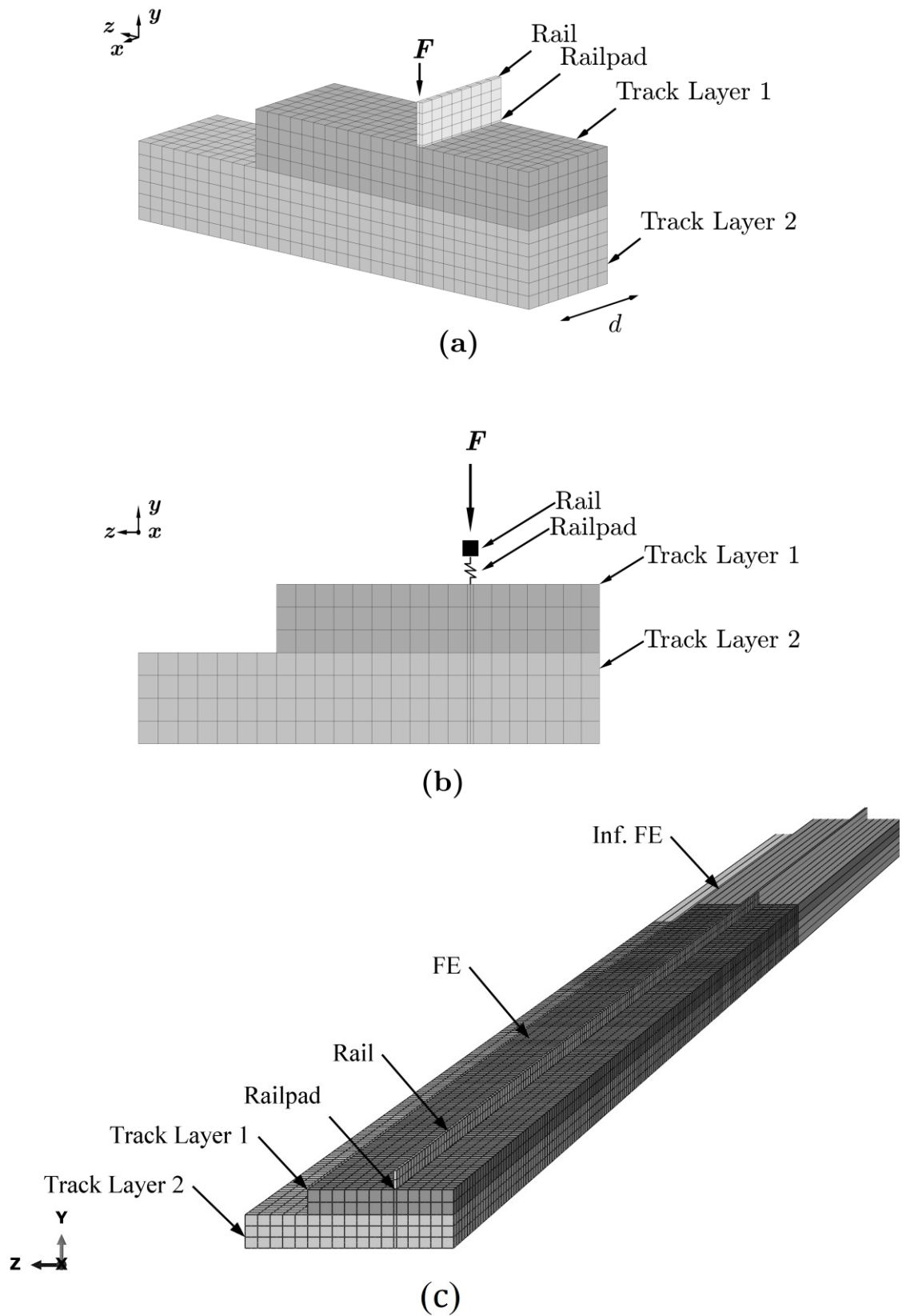
Figure 5-1. Track mesh validation problem: (a) 3D DPM reference cell, (b) 2.5D, and (c) 3D FEM
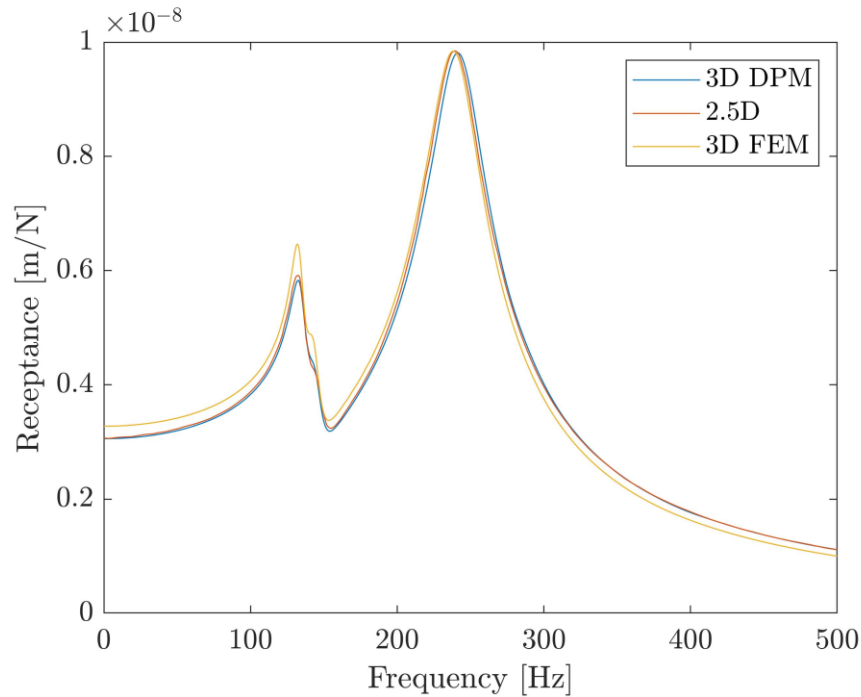
Figure 5-2. Receptance computed via different approaches: 3D DPM, 2.5D, and 3D FEM

5.3 Verification Case 2:

Track Dynamics – Moving Excitation

Case 2 provides the validation for the dynamic track response due to a moving excitation. Similar track geometry and material properties as those defined in Case 1 are employed – see Appendix E for further details. For this, the track response is computed using the DPM and then compared against results obtained via 2.5D. Regarding the force, the rigid track is subject to a force of magnitude $P = 90$ kN moving at $v = 60$ m/s with a driving frequency $\varpi = 0$ rad/s, applied at the top of the rail ($x = y = z = 0$ m).

Figure 5-3 shows the rail deflection at the same point of the force application, computed via (a) the 3D DPM, and (b) 2.5D approach. Both methods yield their maximum deflections, with similar magnitudes, at x $= 0$ m, which is the location of the force application. However, deflections at rail locations $\neq 0$ m differ in magnitude. This occurs due to damping model difference in the railpad definition: hysteretic for the DPM, and viscous damping for the 2.5D. Note that due to the presence of damping, the response is not symmetric around $t = 0$ s. This asymmetry is particularly evidenced in materials with hysteretic damping models, as demonstrated by the 3D DPM results.
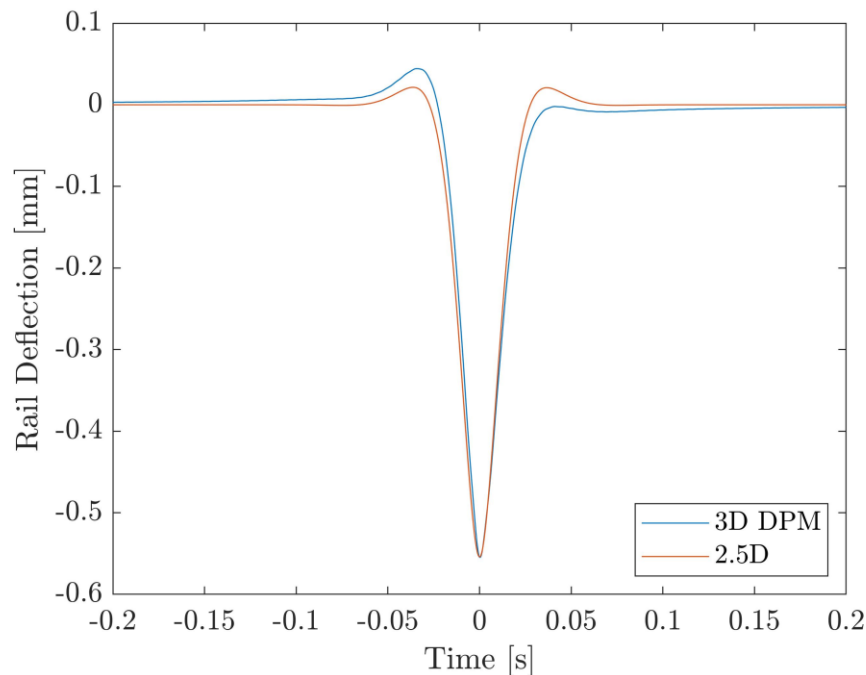
Figure 5-3. Vertical rail deflection, due to a force moving at 60 m/s, computed via different approaches: 3D DPM, and 2.5D

5.4 Verification Case 3: Dynamic Excitation Contribution

Case 3 presents the verification of the dynamic contribution of the moving excitation. For this, the track is modelled as a single-layer beam supported by an elastic foundation, representing the rail and the railpad, respectively. The DPM model, simulated as a combination of 3D solid elements for the rail and a single viscous-elastic element for the railpad (i.e. 3D FE-BOEF-DPM discrete support – see **Figure 5-4**), is compared against the analytical continuous BOEF – as described in Chapter 2.
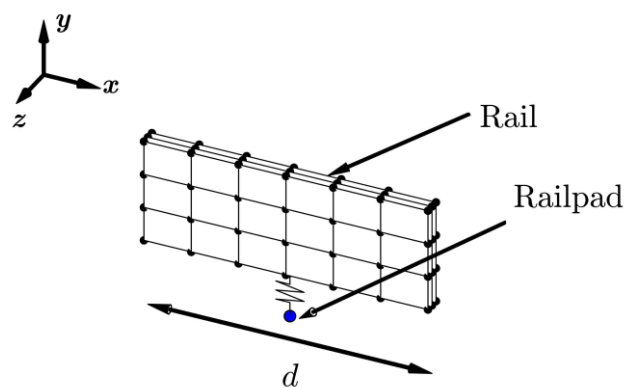
Figure 5-4. 3D discrete FE-BOEF-DPM reference cell. Single-layer

Regarding the excitation, the effect of multiple axles was studied. For this, The dynamic response was computed for an Alfa Pendular train – see **Figure 5-5**, moving at a constant speed $v = 100$ m/s on an uneven track profile of class 6, defined according to the FRA [217]. In contrast, the wavelength range employed in the analysis is $\lambda = [3 - 25]$m, corresponding to a settlement problem [78,167].

The vehicle behaviour was simulated using a 10-degrees-of-freedom multi-body system – see Chapter 2. Refer to 4.2.1.4 and Appendix D for further information regarding the dynamic-train interaction effect, and Appendix E for the track and train properties. Note that the complete multi-body model is used instead of the single wheel mass model for illustrative and practical purposes, as it provides a representation closer to reality.

Figure 5-6 shows the rail deflections due to (a) quasi-static and (b) dynamic contributions of the moving excitations. It can be seen that the DPM yield similar results to the analytical case, thus showing the capability of the former to capture moving excitation contributions. Additionally, **Figure 5-7** shows the various contributions of the response computed via the DPM: quasi-static, dynamic and total.
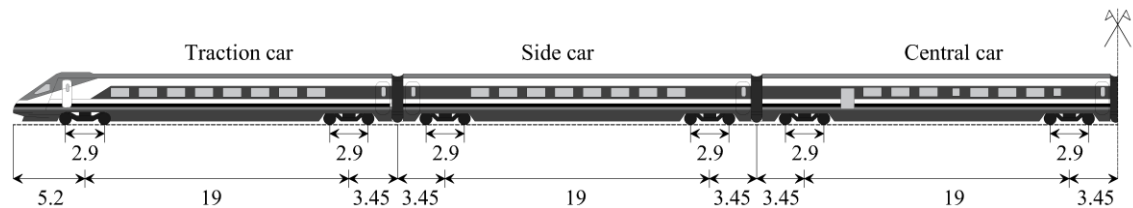
Figure 5-5. Alfa Pendular HST. Distances in [m]

5.5 Verification Case 4: Ground Vibration

Case 4 describes the validation for the ground behaviour. This is essential to confirm that the 3D DPM-FEM can be coupled with PML (i.e. 3D DPM-FEM-PML), thus allowing to replicate the ground response and its wave propagation effect. This verification considers the example described in [39], which uses the fully analytical solution proposed by Tadeu and Kausel [261].

Figure 5-8 shows the geometry of the 3D DPM reference cell: a 3m × 3m FEM mesh bounded by a PML layer of 1 m of width H in the vertical (y) and transversal (z) directions: $H_y = H_z = 10 \times \Delta y, z$, where $\Delta y = \Delta z = 0.1$ m is the size of the elements. Note that the dimensions and high discretisation of the PML employed in **Figure 4-6**, which is adapted from Tadeu and Kausel [261], ensure effective wave absorption and convergence in simulations. In fact, studies have shown that a 1 m thick PML consisting of 5 or 6 layers is generally sufficient to prevent spurious wave reflections from reaching the artificial boundaries – see [260,261].

Regarding the reference cell, this has a thickness of $d = 6 \times \Delta x$, where $\Delta x = 0.1$ m is the size element in the periodic direction x.
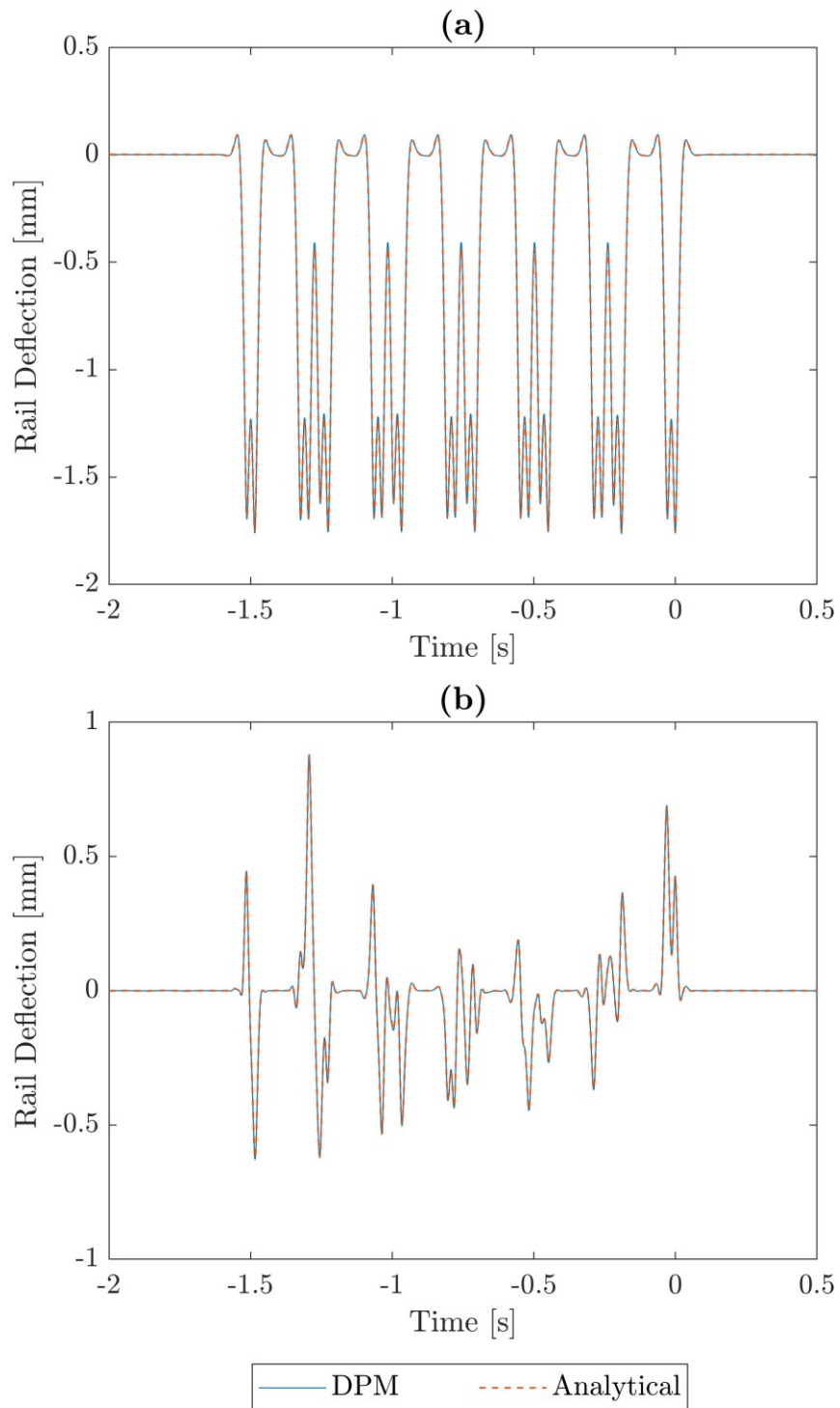
Figure 5-6. Rail deflections computed via DPM and Analytical approach: (a) quasi-static, and (b) dynamic contributions
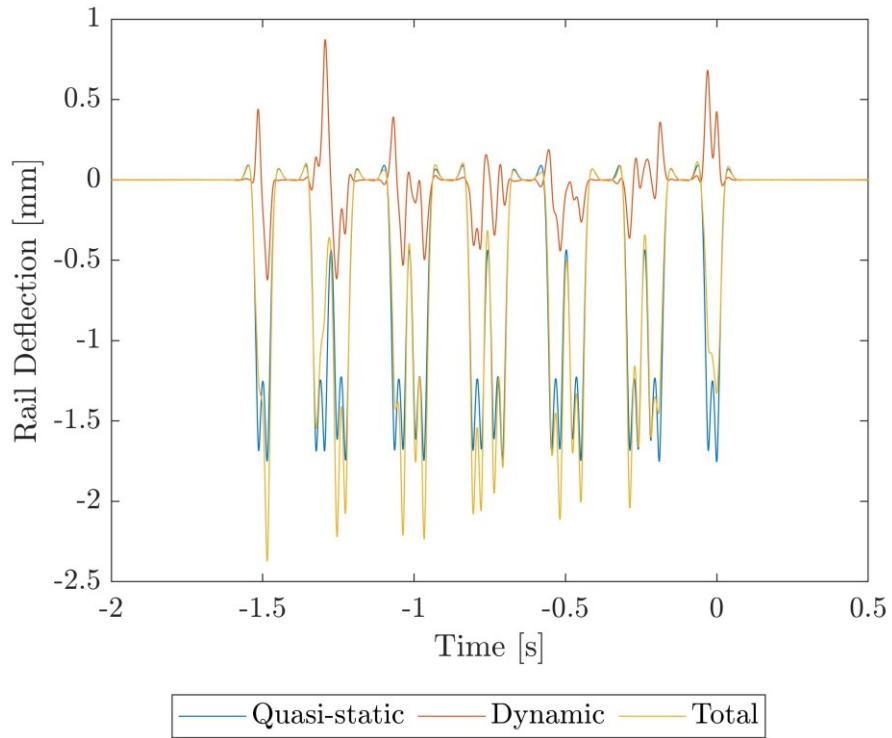
Figure 5-7. Rail deflections due to moving constant excitation: quasi-static, dynamic and total contribution
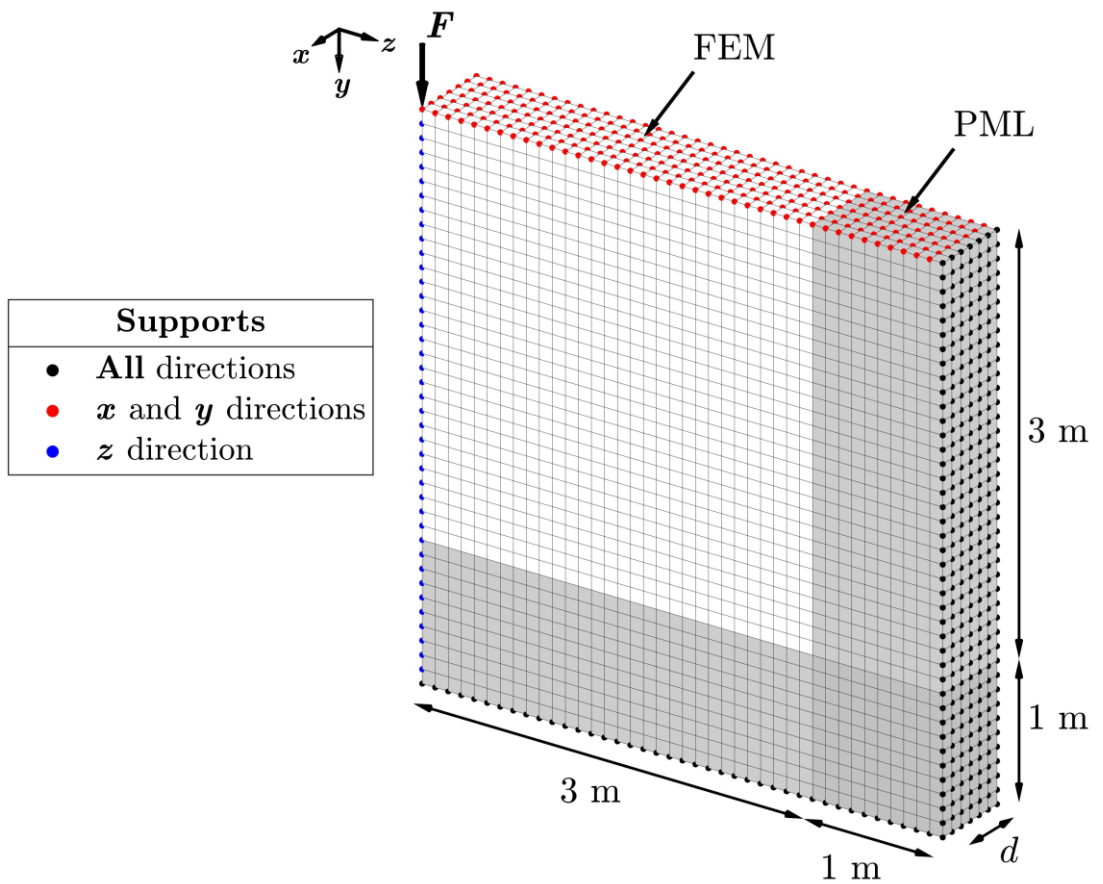
Figure 5-8. 3D DPM reference cell

Also, the reference cell is defined by linear brick elements, 9600 elements with 11767 nodes in total, described by hysteretic damping in the frequency-domain. The symmetry of the structure is exploited, therefore only half of the domain is modelled. Regarding the boundary conditions, constraints are applied at the ends of the PML domains (black markers) and the symmetry axis (blue markers). In addition, the ground domain is constrained longitudinally and transversally at the top (red markers), i.e. in the x and y direction, respectively.

This domain is subject to a stationary force $F = Pe^{i\varpi t}$ of magnitude $P = 0.25$ N applied at the axis origin ($x = y = z = 0$ m) and excited by two frequencies $\bar{f} = [10, 75]$ Hz, where the angular frequency is $\varpi = 2\pi\bar{f}$, and t is the time. Regarding the material properties, the soil has a Young's modulus $E = 80$ MPa; velocity of the shear and dilatational waves $C_s = 126.5$ m/s and $C_p = 219.1$ m/s, respectively; Poisson's coefficient $\nu = 0.25$; density $\rho = 2000$ kg/m^3; and loss factor $\eta = 0.002$.

The vertical surface displacements are computed along the transversal direction (i.e. $x = y = 0$ m) at three dimensionless wavenumbers $\bar{\beta}_x = [0.5, 1.0, 1.5]$, where the wavenumber is defined by $\beta_x = \bar{\beta}_x \varpi / C_s$. **Figure 5-9** compares the real and imaginary components of the response computed via the periodic and analytical solution at 10 Hz and 75 Hz. In both cases, the periodic model uses the stretching function $\tilde{\lambda}(\tilde{s})$ defined in Chapter 4 – see **Eq**. (4-50). It can be seen that periodic results yield a good approximation to the analytical solution for $\bar{\beta}_x = [0.5, 1.5]$. However, small discrepancies are evident at $\bar{\beta}_x = 1.0$ due to the numerical inaccuracy in the periodic method when $\beta_x = \varpi / C_s$. Overall, results confirms the accuracy of the DPM-FEM-PML when simulating the ground behaviour and its wave propagation effect.

Finally, it is important to highlight that since the material and geometrical properties of the structure are continuous along the periodic direction (longitudinal axis x), the thickness of the reference cell in the DPM can be reduced from $d = 6 \times \Delta x$ to a single value $d = \Delta x$, i.e. from 11767 to 3362 nodes. This domain reduction produces similar results to the obtained in **Figure 5-9** and allows for further optimisation of the periodic simulation.
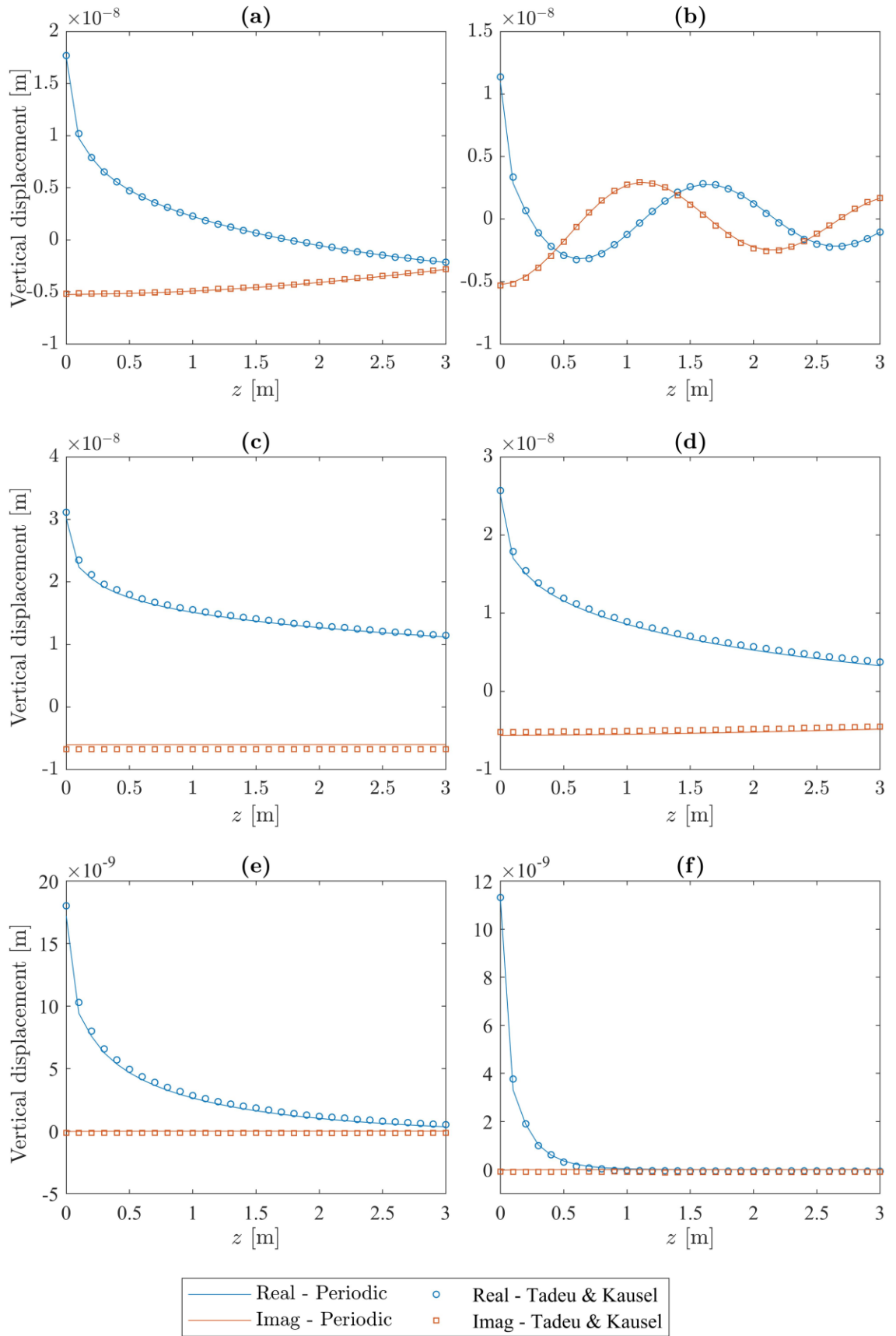
Figure 5-9. Vertical deflection at: (a) $\bar{f} = 10$ Hz, $\bar{\beta}_x = 0.5$, (b) $\bar{f} = 75$ Hz, $\bar{\beta}_x = 0.5$, (c) $\bar{f} = 10$ Hz, $\bar{\beta}_x = 1.0$, (d) $\bar{f} = 75$ Hz, $\bar{\beta}_x = 1.0$, (e) $\bar{f} = 10$ Hz, $\bar{\beta}_x = 1.5$, and (f) $\bar{f} = 75$ Hz, $\bar{\beta}_x = 1.5$

5.6 Conclusions

This Chapter demonstrates the accuracy of the periodic formulation and its ability to approximate the complex dynamic track and ground response. In the first Case, a numerical verification related to the track dynamic excited by a non-moving harmonic force is presented. This verification is constrained to the track response; thus, a rigid support is assumed. Then, rail receptance is computed, and the 3D DPM results are compared against 2.5D and 3D FEM approaches. Results show good agreement, highlighting the capability of the 3D DPM to capture the track response.

In the second verification, identical railway track geometrical and material properties are considered. However, in this Case, rail deflections are computed due to a moving excitation. Results obtained from the 3D DPM are compared against the 2.5D solution, demonstrating a good agreement at the location of the force. While rail deflections at positions other than the excitation source may differ between both techniques, this discrepancy is attributed to the railpad damping model definitions used in each approach: the 3D DPM employs a hysteretic damping model, whereas the 2.5D solution uses a viscous damping model.

The last verification focuses on the ground behaviour. For this Case, the analysis is strictly confined to the ground domain, thus no track structure is included in the model. Ground deflections resulting from a stationary harmonic force are computed using the 3D DPM and then compared to a fully analytical solution. Although minor discrepancies are observed between models at certain wavenumbers, the DPM produces results similar to those obtained via the analytical approach.

Chapter 6
Model Refinement for Receptance Applications

6.1 Introduction

Railway track dynamic stiffness is the relationship between track deflection and loading frequency. Its inverse, also known as receptance, is an important quantity that affects the track's dynamic response under moving trains and noise and vibration characteristics. This Chapter employs the computationally efficient periodic technique presented in Chapter 4 to study receptance on ballasted tracks. The model is refined by considering common track modelling assumptions, thus introducing a new numerical approach tailored to receptance calculation on ballasted tracks.

Section 6.2 introduces the theory of receptance, highlighting: (1) resonant frequencies and vibration modes definitions, and (2) typical receptance configurations used in-situ. Then, in Section 6.3, the 3D DPM-FE-PML is refined considering the effect of two common modelling assumptions on the calculation of track receptance: (1) track bed support, and (2) symmetry conditions. Finally, Section 6.4 provides some conclusions.

6.2 Receptance Concepts

Receptance is a Frequency Response Function (FRF) which allows for an understanding of the dynamic track behaviour in terms of deflection. The various vibration modes of the track are related to specific resonant frequencies and

strongly depend upon their various components' properties [10,16,37]. The conventional definition of receptance is described in **Eq.** (6-1):

$$\alpha^2(\omega) = \frac{S_{ww}(\omega)}{S_{FF}(\omega)} \tag{6-1}$$

where α is receptance or displacement amplitude resulting from the unit impulse excited with frequency ω; and S_{ww} and S_{FF} are the auto-spectrum of the displacement and the force, respectively [16]. In addition to receptance function, which expresses the response as displacements, two additional FRFs sometimes computed during in-situ testing are: mobility and accelerance, in terms of velocities and accelerations, respectively. See **Table 6-1** where all frequency functions are mutually related by the angular frequency ω. Note that although FRFs are inherently complex functions, the focus of this Chapter is on the absolute response of the track. Thus, **Eq.** (6-1) and **Table 6-1** depict auto-spectrum and absolute results, respectively (i.e. FRF complexity vanishes). Alternatively, if considering FRFs' complexity, derivations in **Table 6-1** should incorporate the imaginary component in terms of $i\omega$. Similarly, to describe the complexity in **Eq.** (6-1), the cross-spectrum between the displacement and the force S_{wF} can be included, resulting in $\alpha(\omega) = S_{wF}(\omega)/S_{FF}(\omega)$ – see [37].

	Receptance (or Compliance)	**Mobility (or Admittance)**	**Accelerance (or Inertance)**
Response definition	Displacement/Force	Velocity/Force	Acceleration/Force
Equation	$\alpha = \dfrac{Y}{\omega} = \dfrac{\chi}{\omega^2}$	$Y = \omega\alpha = \dfrac{\chi}{\omega}$	$\chi = \omega^2\alpha = \omega Y$
Unit	[m/N]	[m/Ns]	[m/Ns^2]
Inverse	Dynamic stiffness	Mechanical impedance	Apparent mass

Table 6-1. Frequency response definition and relationships [16]

6.2.1 Vibration Frequencies and Modes

The properties and position of the track components define the complete structural vibration. Based on this, three frequency ranges can be identified according to their main effect on the structural components [5]:

- Low frequencies, $f = [0\text{-}300]$ Hz, mostly influencing the track substructure.
- Mid frequencies, $f = [300\text{-}800]$ Hz, affecting all superstructure components except the rail.
- High frequencies, $f > 800$Hz, which mainly impact the rail behaviour.

The important track frequencies can be discretised into those below. The corresponding mode shapes are shown in **Figure 6-1** using simplified beam-on-elastic foundation visual representation to assist understanding. From low to high frequency:

(a) *Subgrade resonance* f_{subgrade}. Although mainly governing the low-frequency range, the subgrade properties also influence the response up to the mid-range [12]. At this frequency, the ballasted track has its maximum deformed shape, with all layers adopting a similar deformed shape to the subgrade, leading to a wide bending shape, as shown in **Figure 6-1**(a).

(b) *Full-track resonance* $f_{\text{full-track}}$. Often found at low- and lower mid-ranges, at this frequency, the rail and the sleeper mass move vertically in phase on the flexibility of the lower track layers (i.e. ballast and sub-ballast). The amplitude of receptance is well-damped at $f_{\text{full-track}}$, mainly due to the ballast, which makes its receptance peak flat [263]. The vibration mode generated at this frequency is similar to that displayed at f_{subgrade}, however its deflection is lower with reduced subgrade deflection – see **Figure 6-1**(b). Despite its characteristic deformed shape, due to the wave propagation effect of the subgrade, $f_{\text{full-track}}$ can be challenging to identify.

(c) *Rail frequency* f_{rail}. This receptance frequency occurs at frequencies above $f_{\text{full-track}}$, between the mid- and high-frequency ranges. At this frequency, the rail and the sleeper mass move in opposite directions (i.e. in antiphase) on the flexibility of the railpad [8,9] – as illustrated in **Figure 6-1**(c). Often, several peaks with similar mode shapes to f_{rail} can be found at different frequencies, resulting in multiple $f_{\text{rail},i}$. Lower frequency peaks $f_{\text{rail},1}$ are mostly related to the ballast properties. On the contrary, peaks located at higher ranges are related to a stiff railpad behaviour and the rail frequency can instead be defined as the railpad frequency, i.e. $f_{\text{rail},2} = f_{\text{railpad}}$. Note that for soft railpads, f_{railpad} value is low, likely combining into a single peak with $f_{\text{rail},1}$.

(d) *Sleeper anti-resonance* f_{sleeper} is a low magnitude region separating both consecutive resonant frequencies $f_{\text{full-track}}$ and f_{rail}. At this frequency, the amplitude of displacement drops, reaching a pronounced minimum. Due to this behaviour, which is analogous to the pronounced maxima found in $f_{\text{full-track}}$ and f_{rail}, this frequency is known as an anti-resonance. At this frequency, the rail displays minimal movement, while the sleeper moves

vertically in parallel to the railpad and the ballast [8,12] – as described in **Figure 6-1**(d).

(e) *Pin-pin resonant frequency* $f_{\text{pin-pin}}$. Similar to f_{rail}, at $f_{\text{pin-pin}}$ the rail is in antiphase with its discrete supports. However, at the pin-pin resonance, the bending shape of the rail is defined by the support spacing [8,12]. Due to the low damping provided by the rail, the receptance peak lies in a narrow frequency range [263]. **Figure 6-1**(e) shows the first order pin-pin frequency $f_{\text{pin-pin}}$.
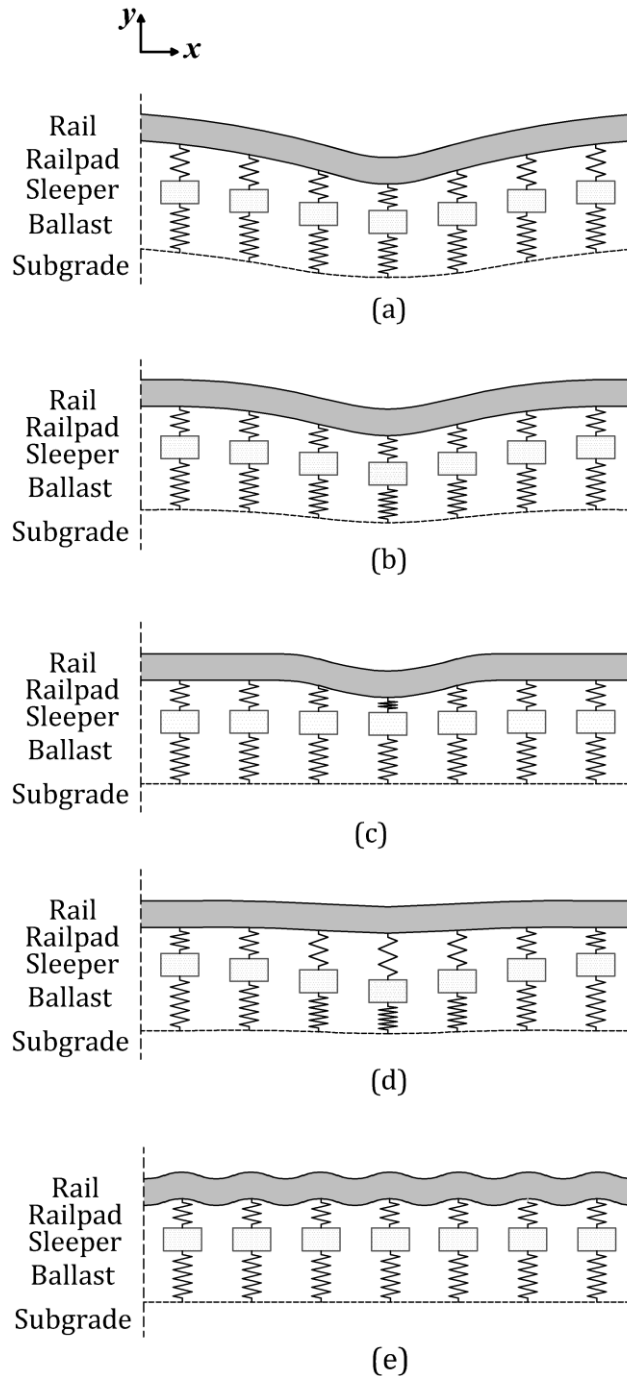
Figure 6-1. Generalised mode shapes of a track on a flexible foundation. Corresponding to: (a) subgrade resonance, (b) full-track resonance, (c) rail resonance, (d) sleeper anti-resonance, and (e) pin-pin resonant frequency

To illustrate the reading and interpretation of receptance curves, **Figure 6-2** highlights the main resonant frequencies of a ballasted track resting on a homogeneous half-pace. Receptance curves, computed at mid-span and on support of the rail, are displayed in different formats: (a) linear-linear, (b) linear-log (semi-log), and (c) log-log scale. Also, the effect of the railpad stiffness is shown at mid-span and above sleeper receptance curves: soft railpads result in a single f_{rail}, while stiff railpads leads to multiple $f_{rail,i}$. In addition, it is seen that the railpad does not significantly affect the $f_{pin-pin}$ value at mid-span of the rail, however, stiff railpads increase the amplitude of the response at this frequency. On the contrary, above the sleeper, $f_{pin-pin}$ and its amplitude are lower for the soft compared to stiff railpads. In the linear-linear case, results are scaled equally on both axes, meaning readability can be challenging if the stiffness changes significantly throughout the track-ground structure. For instance, when a stiff track rests on a much softer ground, the amplitude of the response at lower frequencies is larger than that at higher frequencies. Therefore, a linear-linear scale is usually most suitable for studying lower frequency energy.
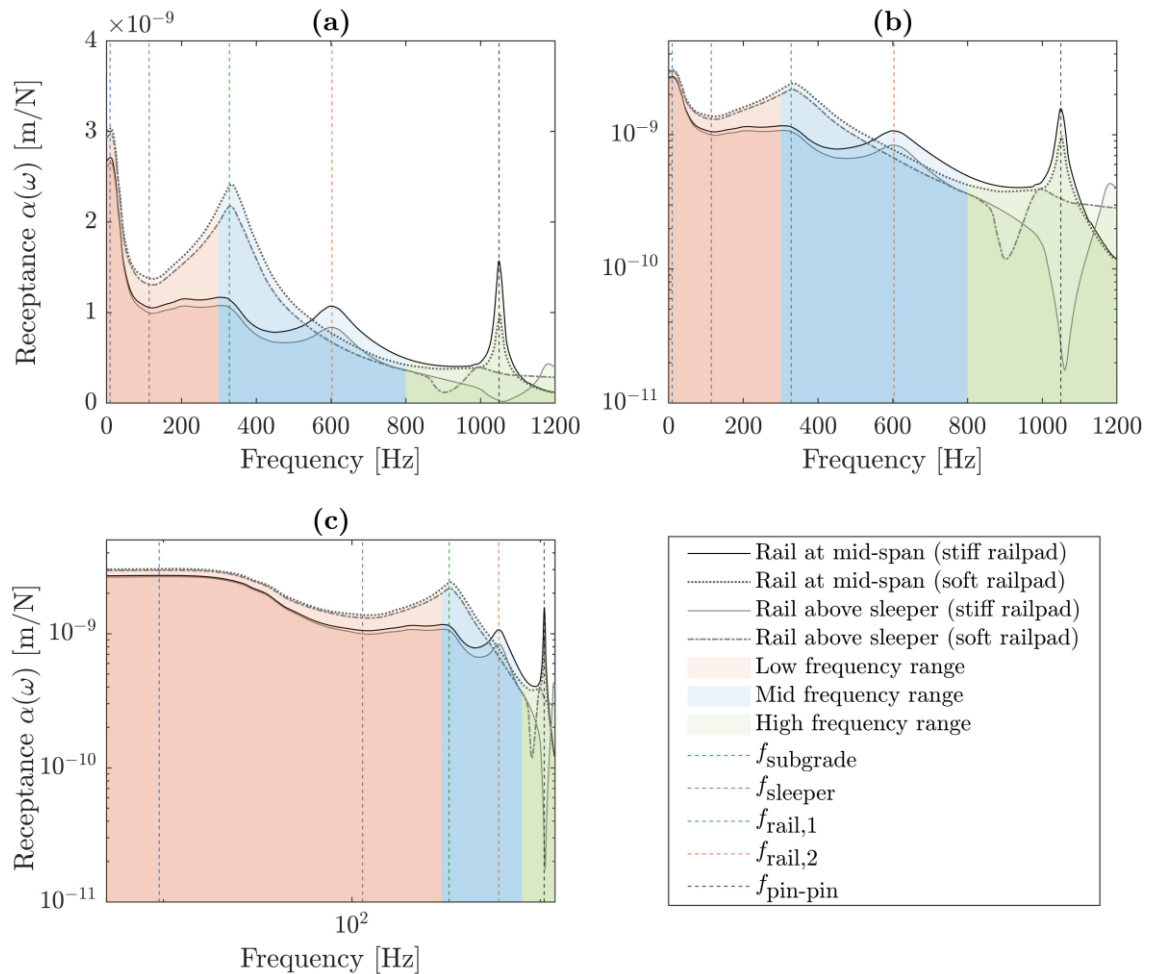
Figure 6-2. Ballasted track receptance curves with resonant frequencies highlighted: (a) linear scale, (b) semi-log scale, and (c) log-log scale

Alternatively, logarithmic formats can help improve the readability of receptance curves that oscillate over the wider amplitude (and frequency) ranges. In the linear-log scale, the horizontal axis (frequency) is linear, while the vertical (receptance amplitude) is in logarithmic format. This helps highlight changes in amplitude in the mid frequency range. Finally, a log-log format is useful for studying changes in the high frequency range because it amplifies oscillations at high frequency, which are small compared to the low frequency energy. Therefore, it is commonly used for noise analysis. Considering the focus of this thesis is on the effect of track components on receptance, the linear-linear scale is predominantly used hereafter.

6.2.2 Receptance Testing Configuration

Experimentally, receptance can be computed via an instrumented hammer test, which excites the track – either the rail or the sleeper. This results in time-history amplitudes recorded through accelerometers (or geophones) that, along with the time-domain excitation signal, are later processed to obtain the frequency-domain response and compute the receptance function [16,21,264,265]. However, when performing in-situ receptance testing, it is challenging to measure the response at the exact track position where the hammer excitation is applied. Thus, in contrast to the idealised receptance procedure performed in numerical models, in-situ transfer functions (also known as cross-receptance) require the sensor position to differ from the excitation. This results in lower deflection amplitudes in the latter case compared to the former.

Figure 6-3 shows some typical in-situ receptance test configurations, highlighting the excitation and sensor locations, including: rail above the sleeper (blue), rail at mid-span or between two sleepers (red), sleeper shoulder (yellow), and sleeper centre (green). The choice of excitation position plays a significant role in the receptance curve characteristics, particularly at high-frequency ranges. For example, when the excitation is applied at mid-span of the rail, the response at $f_{\text{pin-pin}}$ is high, resulting in an upper peak describing a large deflection and a resonant frequency. In contrast, when the force is on the rail above the support or directly on the sleeper, the pin-pin occurs at a lower peak, resulting in a stiff track and an anti-resonance [8,53,263] – see **Figure 6-2**.

Note that receptance tests with instrumented hammers measure the discrete track's response at standstill [3], thus requiring the application of a stationary loading. Alternatively, rolling receptance tests (e.g. VibTrain [2,3], Banverket [3,266], CARS [267], etc.) can measure the continuous track response under moving dynamic contributions, an assumption closer to real loading conditions. Despite the higher accuracy of the latter test, they require complex testing configurations, which can be

challenging to implement and simulate. Thus, due to its straightforward setup and simplicity in simulation, this research only studies standstill receptance.
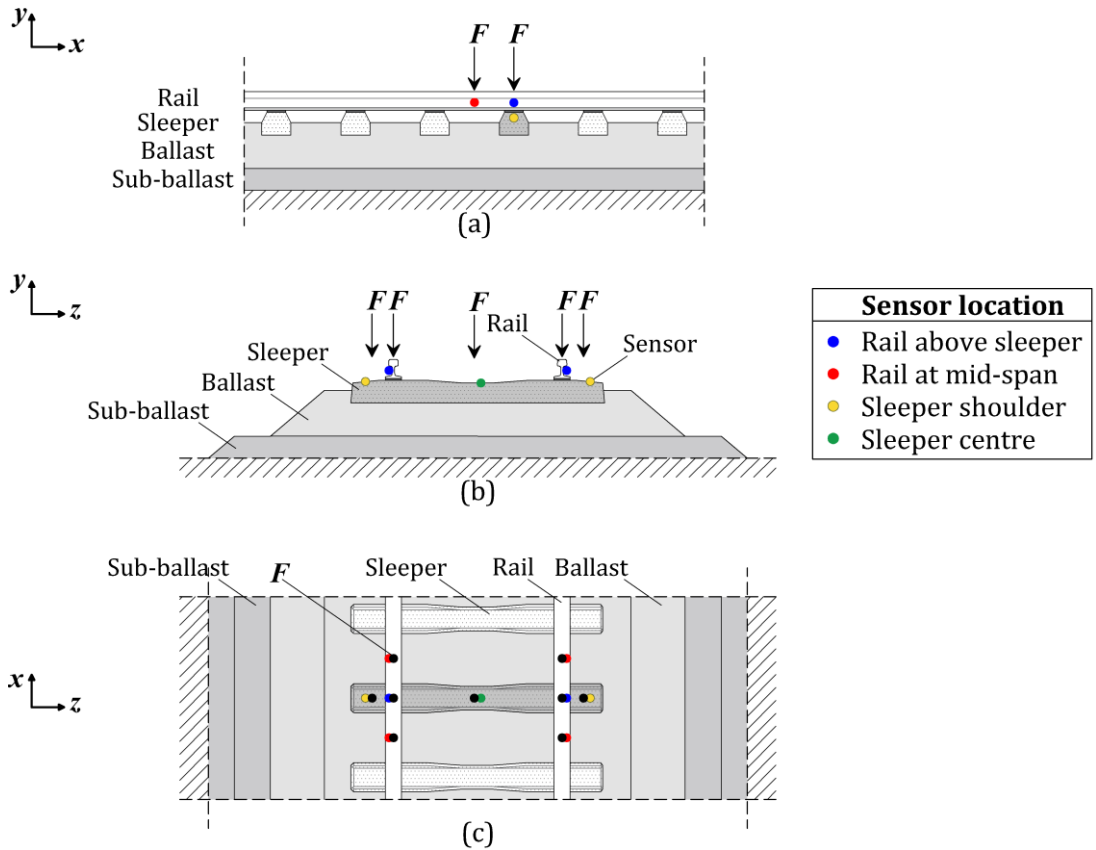
Figure 6-3. Typical receptance excitation and accelerometers positions:
(a) longitudinal view, (b) transversal view, and (c) birdseye view

6.3 Model Refinement

The receptance calculation models presented in the literature often make assumptions regarding the track to improve computational efficiency. One common assumption is the track support can be modelled as a rigid boundary condition rather than a flexible condition representative of the underlying earthworks. Another is that symmetry can be assumed along the track centreline, meaning both rails are excited rather than one, which is unlikely to be the case when field testing. This Section investigates the validity of these two assumptions. It is shown that large errors at frequencies up to 450 Hz are introduced if the track support conditions are not adequately considered. Similarly, errors are introduced up to approximately 800 Hz when comparing symmetrical and non-symmetrical loading.

6.3.1 Modelling Parameters

The DPM is used for all receptance calculations. **Table 6-2** shows the characteristic or base parameters, while Appendix F shows all additional properties. Note that the

selected base permutation corresponds to a stiff track supported by well-compacted earthworks, which is characteristic of a modern high-speed track. Also, under-sleeper pad (USP) and the presence of the embankment are ignored during model refinement.

All components are defined using linear brick elements (8-node solid elements) with hysteretic damping – as described in **Eq.** (4-7). **Figure 6-4** shows the 3D view of the reference cell mesh with thickness d, defined according to the sleeper spacing.

Component	Parameter		Units	Value
Track	l_0	Gauge	m	0.7175
Reference cell	d	Length	m	0.6
Rail	-	Section	-	CEN60/60E2
Railpad	E_{rp}	Young's modulus	MPa	200
Sleeper	-	Material		Concrete
USP	$l_{y,usp}$	Depth	m	0
Ballast	E_b	Young's modulus	MPa	220
	$l_{y,b}$	Depth	m	0.3
Sub-ballast	$l_{y,sb}$	Depth	m	0.2
Embankment	$l_{y,e}$	Depth	m	0
Subgrade	E_{sg}	Young's modulus	MPa	80

Table 6-2. Main track parameters. Base permutation

The reference cell is subject to a stationary force of magnitude $F = 1$ N excited at frequency ω, which is evenly applied on top of both rails above the sleeper support ($x = d/2$) – see **Eqs.** (4-10) and (4-11). The vertical deflection is computed at different track positions, initially in (β_x, ω) domain and later transformed back to (x, ω). **Figure 6-5** shows the position of the excitation F and the observation points where the response is obtained:

   (1) rail above sleeper – $u(x = d/2, y = y_{\text{rail}}, z = \pm z_{\text{rail}})$,
   (2) rail at mid-span – $u(x = 0, y = y_{\text{rail}}, z = \pm z_{\text{rail}})$,
   (3) sleeper shoulder – $u(x = d/2, y = y_{\text{sleeper}}, z = \pm z_{\text{sleeper},1})$, and
   (4) sleeper centre – $u(x = d/2, y = y_{\text{sleeper}}, z = \pm z_{\text{sleeper},0})$,

in which y_j and z_j are the vertical (top) and transversal coordinates of $j =$ rail, sleeper. Note that $z = z_{\text{sleeper},0}$ describes the centre of mid-span coordinate of the sleeper. In contrast, $z = z_{\text{sleeper},1}$ corresponds to the mid coordinate between

the sleeper end and the rail. Additionally, only in case (1) the response is a receptance – since the deflection is obtained at the same coordinate as the excitation. In contrast, in cases (2), (3) and (4), the result is a transfer function (or a cross-receptance) since both coordinates differ.
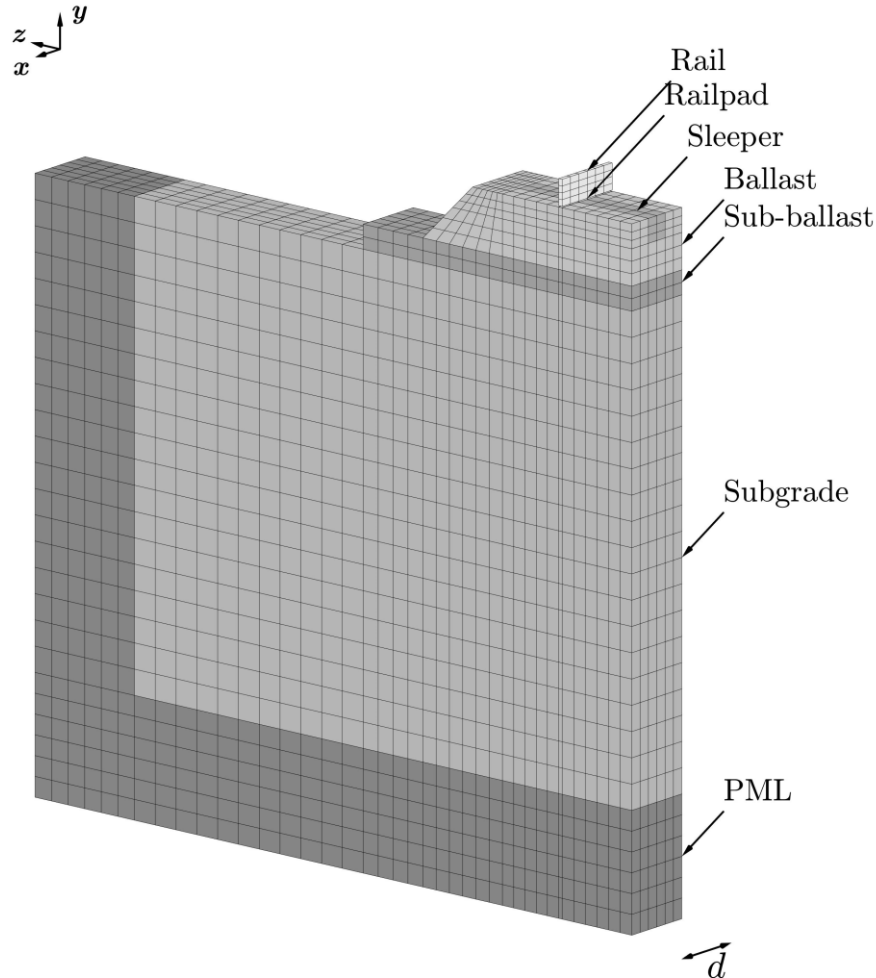
Figure 6-4. Base permutation reference cell mesh 3D view. Only half-track shown for visibility purposes

The frequency range of study is $f = [0\text{-}1000]$ Hz, while the wavenumber sampling is $\beta_x = \left[-\beta_{x,\text{max}}\!:\!\beta_{x,\text{max}}/2048\!:\!\beta_{x,\text{max}}\right]$, where $\beta_{x,\text{max}} = 20$ rad/m. This sampling is chosen because it is sufficient to capture the response from both the track and the ground. Note that the employed wavenumber sampling in this section is wider than the defined in previous applications – see **Eq.** (2-61). This is due to the complexity of the geometry included in the DPM compared to previous approaches. Regarding discretisation, element size is, $\Delta x = d/6$, where d is cell thickness.

6.3.1.1 Flexible vs Rigid Trackbed Support

To study the support conditions, the frequency responses of a track resting on a semi-infinite ground and on a rigid support are compared – see **Figure 6-6**. In both

cases, base parameters are employed and results are shown in terms of absolute vertical deflections at different points on the rail and the sleeper – see **Figure 6-5**.
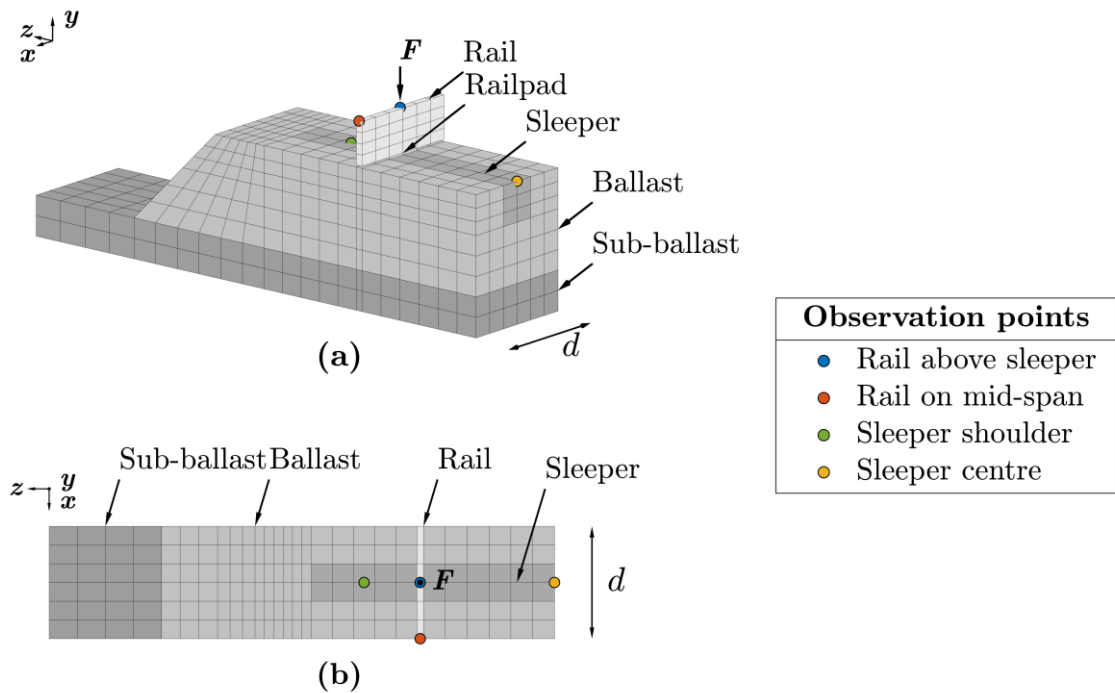
Figure 6-5. Excitation and observation point locations within the ballasted track model: (a) 3D view, and (b) birdseye view. Subgrade layer omitted and only half-track shown for visibility
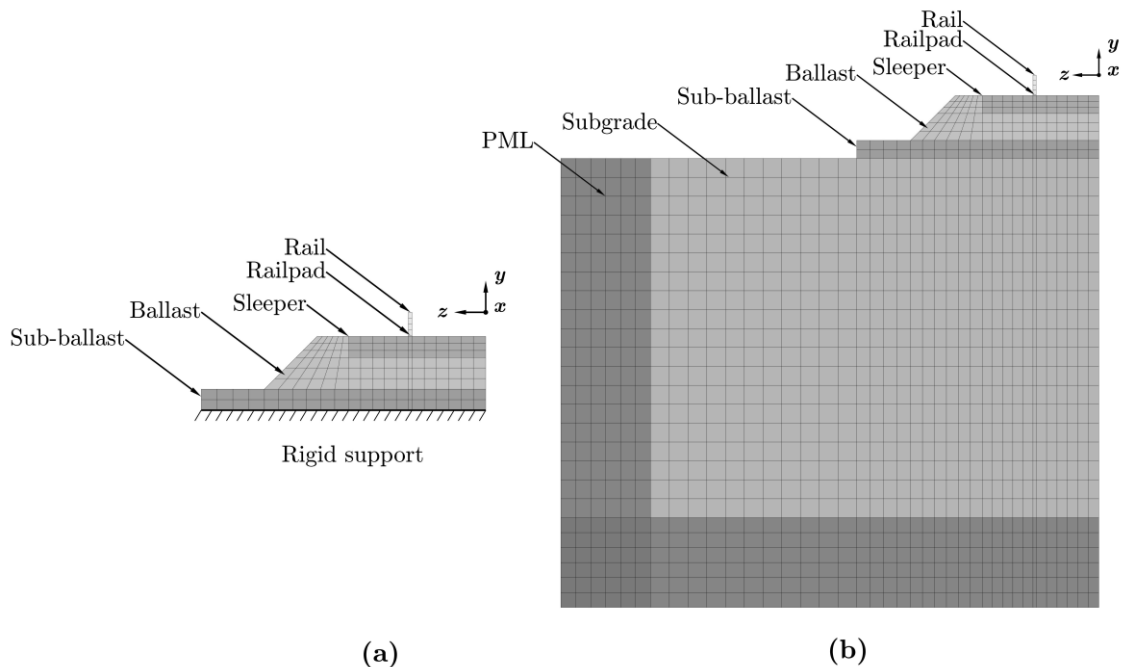
Figure 6-6. Ballasted track model support conditions: (a) rigid trackbed, and (b) flexible trackbed. Half-track transversal view shown for visibility

Figure 6-7 illustrates the absolute deflection computed in a track resting on a subgrade or flexible support (TS) and on a rigid support (TR). Similarly, Appendix G

presents the response in terms of velocity and acceleration. Results computed at the rail above sleeper and at mid-span – see **Figure 6-7**(a), show that the maximum deflection is obtained at low frequencies: at 0 to 50 Hz in TS and at 130 Hz in TR. This behaviour is attributed to soft lower components supporting much stiffer upper layers. In TS model, the maximum response corresponds to the subgrade f_{subgrade} ($\approx$ 6 Hz). This additional component leads to wave-propagation effect, magnifying the response below 50 Hz and making it challenging to identify $f_{\text{full-track}}$, the frequency of resonance related to the lower-track layers (i.e. ballast and sub-ballast), above this frequency. Alternatively, in TR model, the maximum occurs at $f_{\text{full-track}}$ and f_{subgrade} is not visible due to the absence of the subgrade.

Above these frequencies, the amplitude decays, reaching a low region between 50-180 Hz and 160-220 Hz in TS and TR, respectively. In the latter case, the minimum is observed at a lower sharp peak around 180 Hz and can be interpreted as f_{sleeper}. In contrast, this region is not clearly delineated in the former case, and its minimum is not prominent. This occurs because of the wave propagation effect, which makes it challenging to identify f_{sleeper}.

After this low region, the amplitude of the response increases in both models and two upper peaks are observed: at 250 Hz and 400 Hz for the rigid support, and 320 Hz and 440 Hz in the subgrade support model. Note that the second peaks are close to convergence, indicating that the subgrade impact has decreased. Then, above 440 Hz, both models overlap and the response is governed by upper track components. Similarly, new peak occurs at 730 Hz at both observation points. Although no evident difference between these peaks, they are all associated to f_{rail}. Note that both curves experience a rapid decay above 800 Hz. This behaviour is attributed to the frequency of resonance of the rail, $f_{\text{pin-pin}}$, which is not captured in the frequency range displayed in **Figure 6-7**.

Alternatively, **Figure 6-7**(b) shows the absolute deflection at the shoulder and centre of the sleeper. Again, the greatest response occurs at lower frequencies: at f_{subgrade} and $f_{\text{full-track}}$ in TS and TR, respectively. After these frequencies, all curves decay reaching their minimum between 50-250 Hz in TR and 200-350 Hz in TS. The low region is clearly defined in the latter. However, this range differs to the displayed at the rail observation points in **Figure 6-7**(a), and the minimum at the sleeper points occurs at a higher frequency that in the rail case. This behaviour is typical of the vibration mode related to f_{sleeper}, in which the sleeper's deflection is larger than the rail.

Regarding the subgrade case, its low region is not well defined due to the subgrade properties. This behaviour and range are consistent with results obtained at the rail observation points – see **Figure 6-7**(a), indicating that the sleeper follows a

behaviour close to that of the rail. This can be explained by a combination of factors, such as a soft supporting subgrade, a low sleeper mass, and a strong connection between the rail and the sleeper [16].

Next, an upper peak develops around 440 Hz where both models converge. Above this frequency, all curves decay, illustrating the reduced effect of the sleeper, and the rail and railpad track dominance. Regarding the observation point, both support models show that the sleeper at mid-span experiences a greater amplitude compared to that on support. This behaviour can be explained by the bending effect of the sleeper.

Figure 6-8 to **Figure 6-10** compare the vibration modes due to different support conditions according to the resonant frequencies identified in **Figure 6-7**. To improve visibility, only 11 track cells are illustrated (i.e. $n = -5:5$), and the railpad height and all deflection values have been magnified (by a percentage increment of 800% and a factor of 1E+03, respectively). **Figure 6-8** shows the absolute deformation of (a) a track resting on rigid support excited at 130 Hz, (b) a zoomed view of a track on a flexible support excited at 6 Hz, and (c) a full view of a track on a flexible support excited at 6 Hz. The first vibration mode in (a) corresponds to $f_{\text{full-track}}$, while the response at (b) and (c) is related to $f_{\text{sub-grade}}$. Although in all cases the track components move in phase with a broad bending wave-shape, the wave propagation effect of the subgrade magnifies the response, resulting in a larger deformation in (b) and (c) compared to (a).

Figure 6-9 presents the absolute deformation related to f_{sleeper}. **Figure 6-9**(a) shows the response at 180 Hz in the rigid-support case, in which the rail deflection is much lower than the sleeper. Since identifying f_{sleeper} in a track on subgrade model is challenging, deflections at two frequencies are plotted: 100 Hz and 130 Hz, as seen in **Figure 6-9**(b) and (c) respectively. These values lie within low frequency range described in **Figure 6-7**. At 100 Hz, the track components move in phase with both the rail and the sleeper experiencing a large deflection. In contrast, at 130 Hz, the sleeper displays minimal movement relative to the rail. Overall, (b) shows that the sleeper follows a behaviour similar to the rail. In contrast, (c) illustrates how the sleeper effect decreases with frequency.

Alternatively, **Figure 6-10** illustrates the track deflections at $f_{\text{rail,2}} = 730$ Hz, where the rail moves in anti-phase with the supporting track layers. Note that although $f_{\text{rail,2}}$ lies in the upper mid-range, the rail deflection and response propagation within the lower track layers are still visible at this frequency.
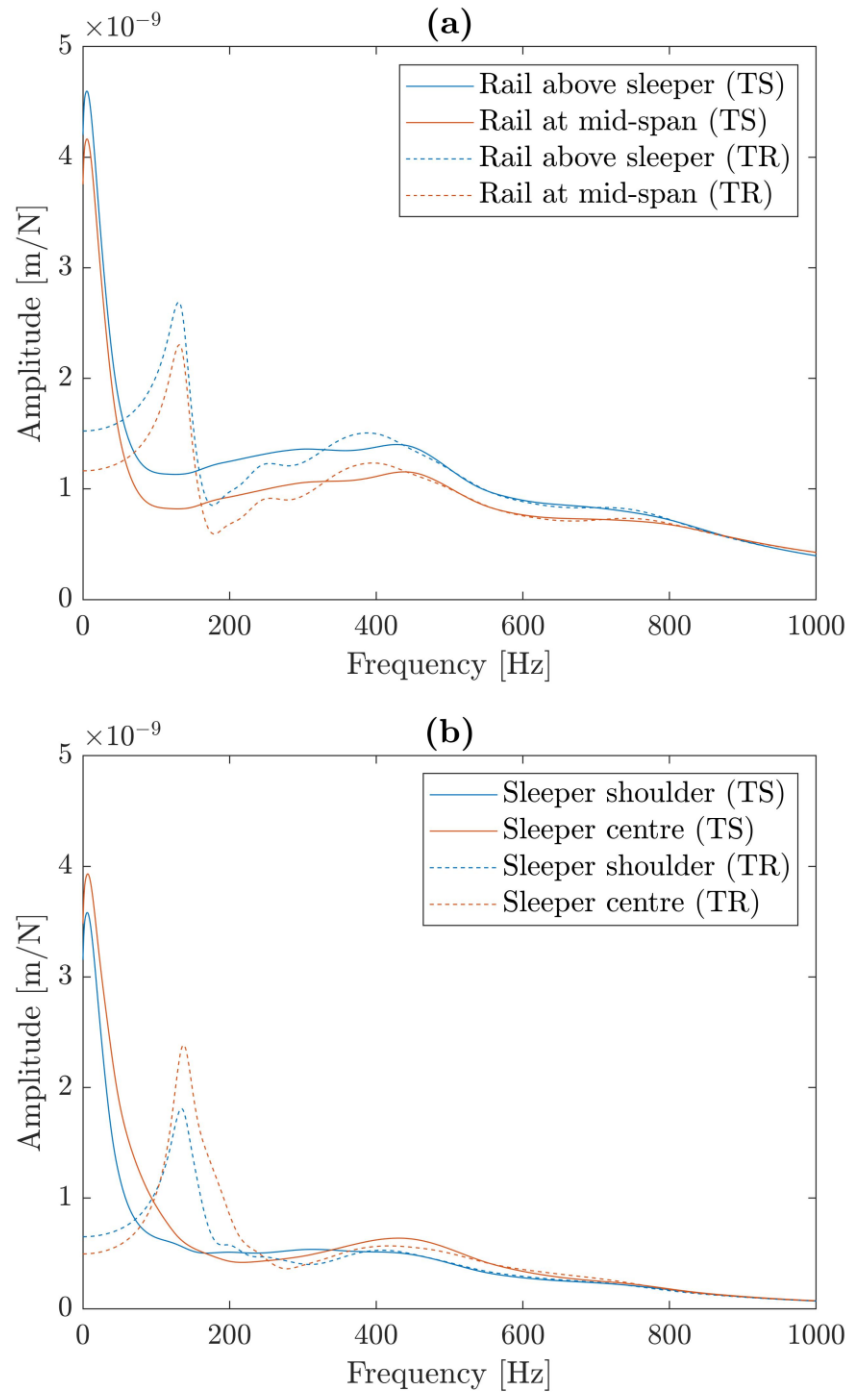
Figure 6-7. Deflections due to a track on subgrade (TS) and a track on rigid support (TR) at: (a) at rail above sleeper and rail at mid-span, and (b) sleeper shoulder and sleeper centre

Figure 6-11 compares the difference in amplitude between both support conditions at all observation points. Results show that the maximum difference is found at lower frequency ranges, within $f_{\text{sub-grade}}$ range, where an error of approximately 80% occurs at 0 Hz. This high error occurs due to the absence of f_{subgrade} under rigid support conditions. Similarly, the subgrade presence amplifies the response, making identifying $f_{\text{full-track}}$ and f_{sleeper} challenging. This behaviour explains the maximum error of 300% at around 130 Hz. The error rapidly decays with frequency, reaching

an average of 30% between 200-440 Hz. This range corresponds to the frequencies of resonance of the rail (f_{rail}) occurring in both models. Above 440 Hz, all observation points yield an error of approximately 10%. This low error is expected since both models converge at higher frequencies. Regarding the observation points, the maximum error is obtained at the sleeper. This occurs due to the subgrade properties, which greatly influence the lower-track layers, including the sleeper. In contrast, the overall minimum is observed at the rail on support, where the excitation is applied.

(a)

(b)

(c)
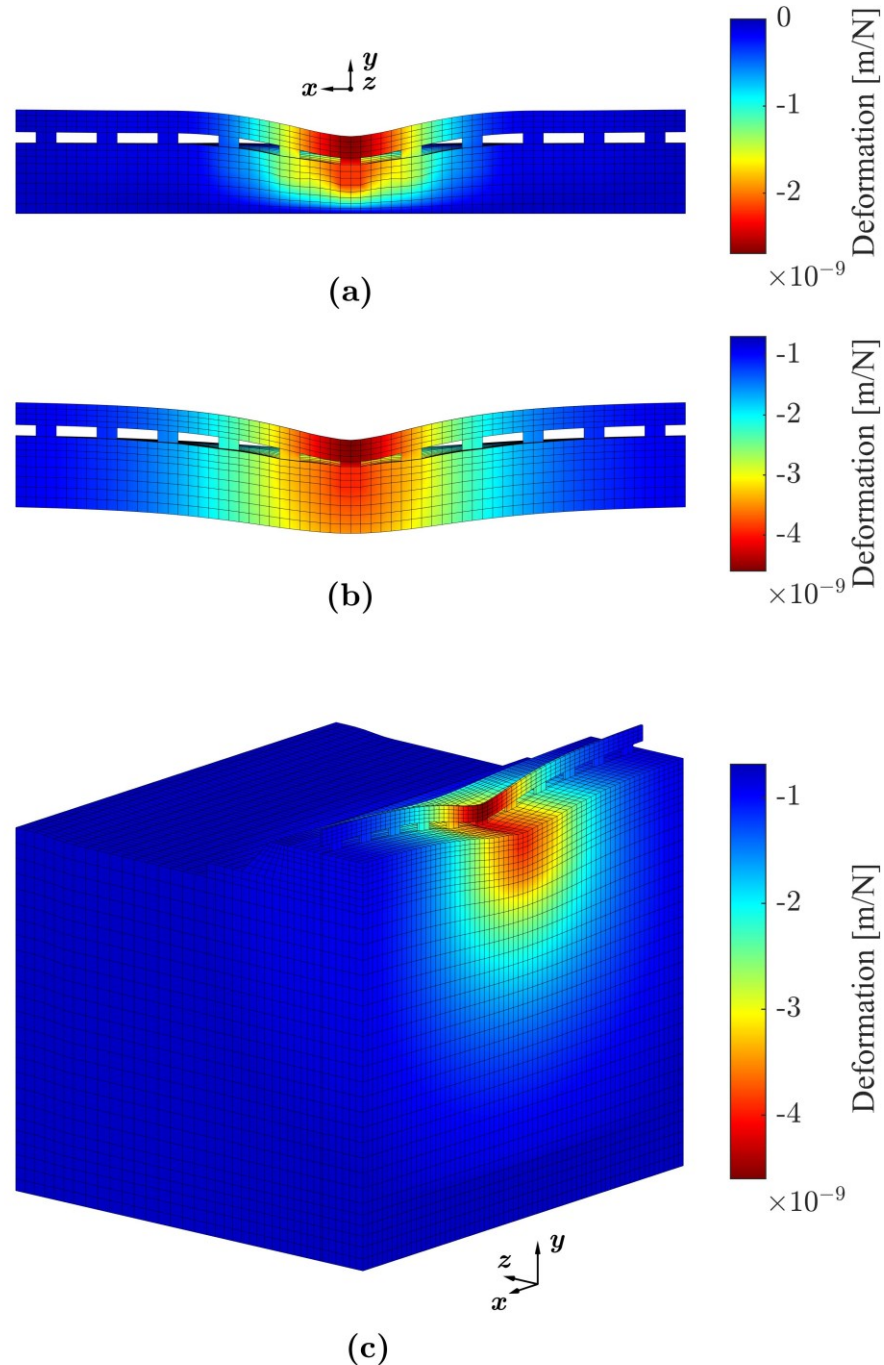
Figure 6-8. Vertical deflections of: (a) track on rigid support excited at 130 Hz – longitudinal view, (b) track on subgrade support excited at 6 Hz – zoomed longitudinal view, and (c) track on subgrade support excited at 6 Hz – 3D view
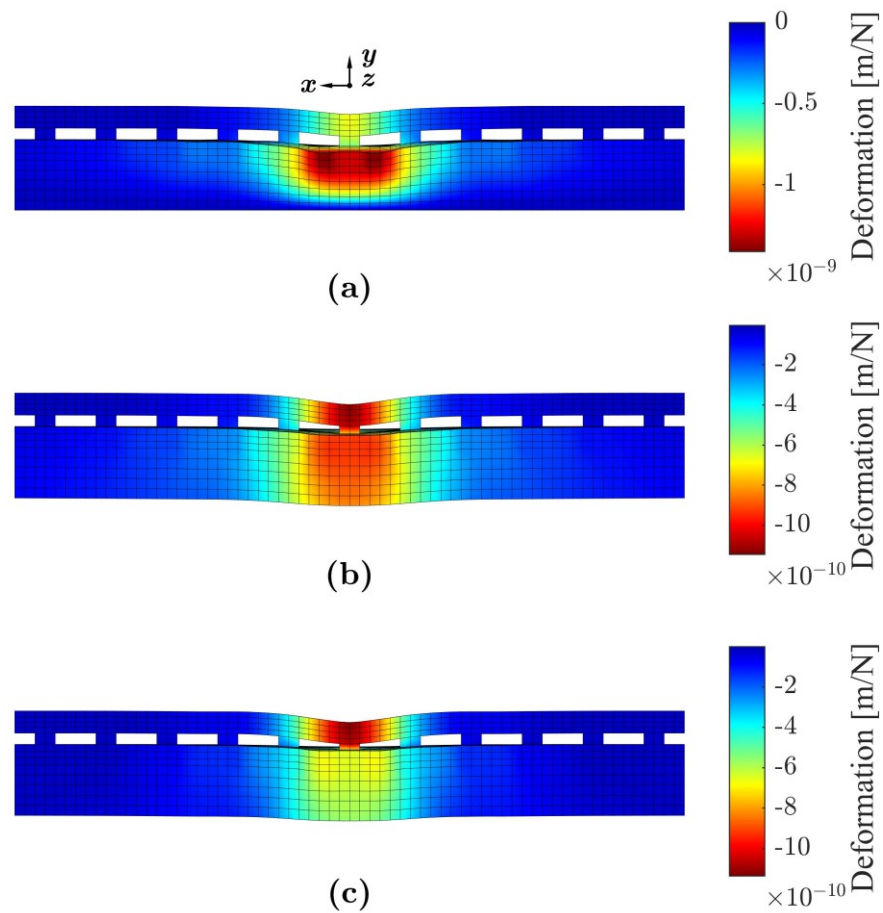
Figure 6-9. Vertical deflections of: (a) track on rigid support excited at 180 Hz, (b) track on subgrade support excited at 100 Hz – zoomed view, and (c) track on subgrade support excited at 130 Hz – zoomed view. Longitudinal views
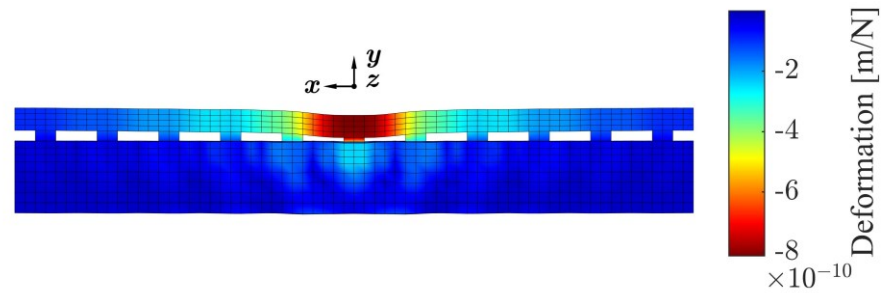
Figure 6-10. Vertical deflections due to an impulse excited at 730 Hz – zoomed view. Longitudinal view

6.3.1.2 Symmetry Boundary Conditions

Numerical simulations of track receptance typically assume the track can be modelled using a centreline symmetry condition. Although this reduces computation requirements, it means both rails must be excited in an identical manner. In contrast, in-situ receptance test configurations excite a single side of the structure, thus making the problem inherently non-symmetric. In order to study the

effect of this symmetry assumption and its effect on track bending modes, a full-track model is excited in two different ways:

(1) symmetric loading, where $F_1 = F_2 = 0.5$ N, and
(2) non-symmetric loading, where $F_1 = 0.5$ N and $F_2 = 0$ N.

In configuration (1), a full-width track is excited by identical forces on both sides of the track. This is the case of a track centreline symmetry condition, as commonly used in numerical simulations to approximate the response due to rolling stock excitation. In contrast, configuration (2) is used to excite only one side of the track, as commonly performed during receptance field-testing that excites a single side of the track. **Figure 6-12** illustrates the reference cell with the observation and excitation points arrangement used to study symmetry conditions. Note that for comparison purposes, configuration (2) sets $F_1 = 0.5$ N.
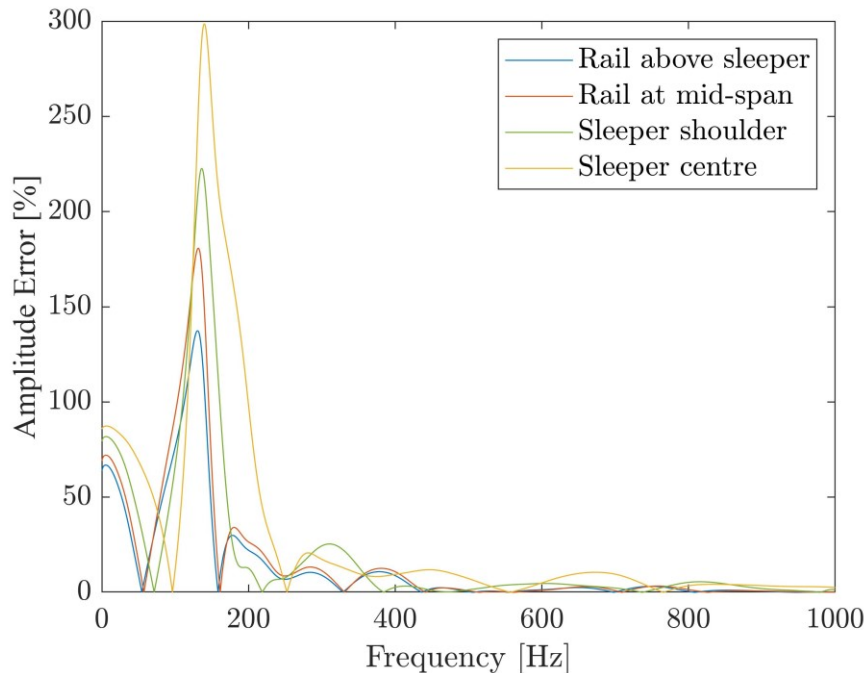
Figure 6-11. Amplitude error between track on subgrade and track on rigid support model at different observation points

However, for a closer approximation to in-situ receptance conditions, F_1 should be 1.0 N. Additionally, considering the geometrical symmetry of the structure (symmetric boundary conditions and linear material properties), it is possible to approximate case (2) by combining two symmetric models subject to:

(a) symmetric loading, where $F_1 = F_2 = 0.25$ N, and
(b) anti-symmetric loading, where $F_1 = 0.25$ N and $F_2 = -0.25$ N.

Figure 6-13 shows the absolute deflection at the rail (a) above the sleeper and (b) at mid-span, and at the shoulder and centre of the sleeper. In both cases, symmetric

(Symm) and non- symmetric (NSymm) excitation are compared. **Figure 6-13**(a) shows that in the case of symmetric conditions, the structure is equally loaded and provides similar results on both sides. Due to this behaviour, only a single side of the structure response is presented in Symm case. Alternatively, in NSymm case, the response at the loaded (Load) and unloaded (ULoad) sides differ, indicating non-symmetric deformations, with the maximum response obtained at Load-side.
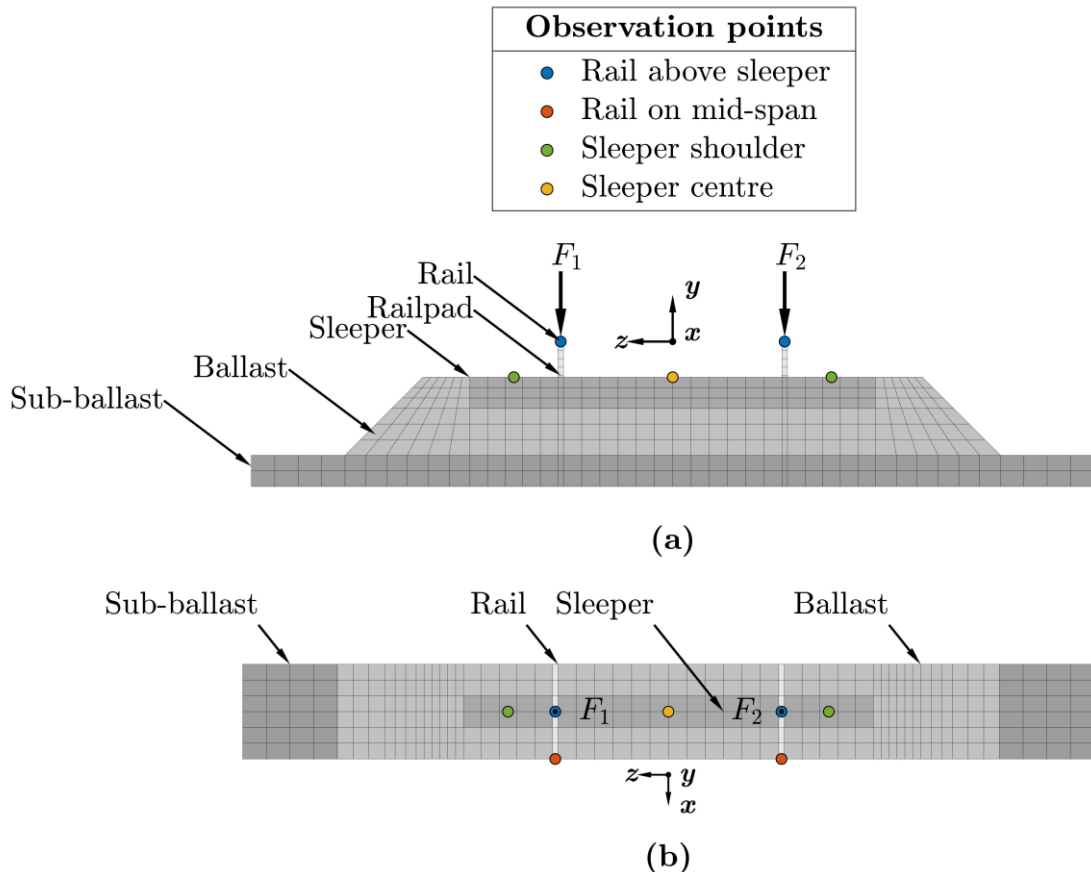
Figure 6-12. Excitation and observation point locations within the full-track model: (a) transversal view, and (b) birdseye view. Subgrade layer omitted for visibility

It can be seen that the overall maximum occurs when both sides of the track are equally excited. This difference is particularly evident between 0-50 Hz, i.e. around $f_{\text{sub-grade}}$. Between 50-180 Hz, results shift and the maximum is obtained in the NSymm case at both observation points. At this frequency range, the response of the sleeper (f_{sleeper}) is more rigid in NSymm than Symm.

Above 180 Hz, four main frequencies are identified: $f_{\text{rail,0}}$ = 320 Hz, $f_{\text{rail,1}}$ = 440 Hz, $f_{\text{rail,2}}$ = 600 Hz, and $f_{\text{rail,3}}$ = 730 Hz. Excluding the peak at $f_{\text{rail,0}}$, all frequencies of resonance at f > 180 Hz differ in both models and NSymm frequencies values are higher than those obtained in Symm. Also, although only the Load-side is excited, the response propagates to the opposite ULoad-side, resulting in small yet significant deformations on the latter. However, between 180-400 Hz and above

800 Hz, ULoad-side's contribution reaches its minimum, explaining the convergence of both models at these ranges.

Regarding the sleeper's results – see **Figure 6-13**(b), it is seen that as the sleeper centre is a unique point corresponding to the geometric centre of the track, a single curve is retrieved for this observation point in the NSymm-model. Thus, only for the sleeper shoulder, results are presented for both loaded (Load) and unloaded (ULoad) sides. Similar to the rail results – see **Figure 6-13**(a), sleeper's deflections obtained with Symm-model are symmetric, thus indicating symmetric bending modes. Alternatively, Load-side results differ from ULoad in NSymm, thus sleeper bending models are non-symmetric in this case.

It can be seen that, below 600 Hz, the overall maximum is found with Symm-model at both observation points. However, both models converge above this frequency at the sleeper shoulder, and after 1000 Hz at the sleeper centre. Again, both models converge when NSymm − ULoad contribution is minimum. However, as the result at sleeper centre is only provided by a single point, results converge at a higher frequency than the sleeper shoulder case.

Although the excitation is non-symmetric in NSymm, its structure (including its boundary conditions and geometrical and linear material properties) is fully-symmetric. Thus, combination of Load- and ULoad-side at each observation point in NSymm can approximate the fully symmetric model. **Figure 6-14** compares the total response due to the non-symmetric model (NSymm$_{tot}$) with the corresponding symmetric results (Symm). However, since the sleeper centre response at the non-symmetric model retrieves a single value, the corresponding NSymm$_{tot}$ result is obtained by doubling its response.

Figure 6-15 compares the difference in amplitude between symmetric and non-symmetric conditions models at all observation points. Results show that symmetric conditions induce moderate errors ($\approx 20\%$) at around 0-20 Hz, 60-100 Hz, 420-520 Hz and 570-700 Hz. These ranges correspond to the frequencies of resonance $f_{subgrade}$, $f_{sleeper}$, $f_{rail,1}$ and $f_{rail,2}$, respectively. In contrast, lower errors < 20%) are observed at the remaining frequencies, where both models converge. Note that as the sleeper centre response in the non-symmetric model is half the symmetric case, it will lead to a constant error of approximately 100%, thus, the error at this observation point is not included in **Figure 6-15**.
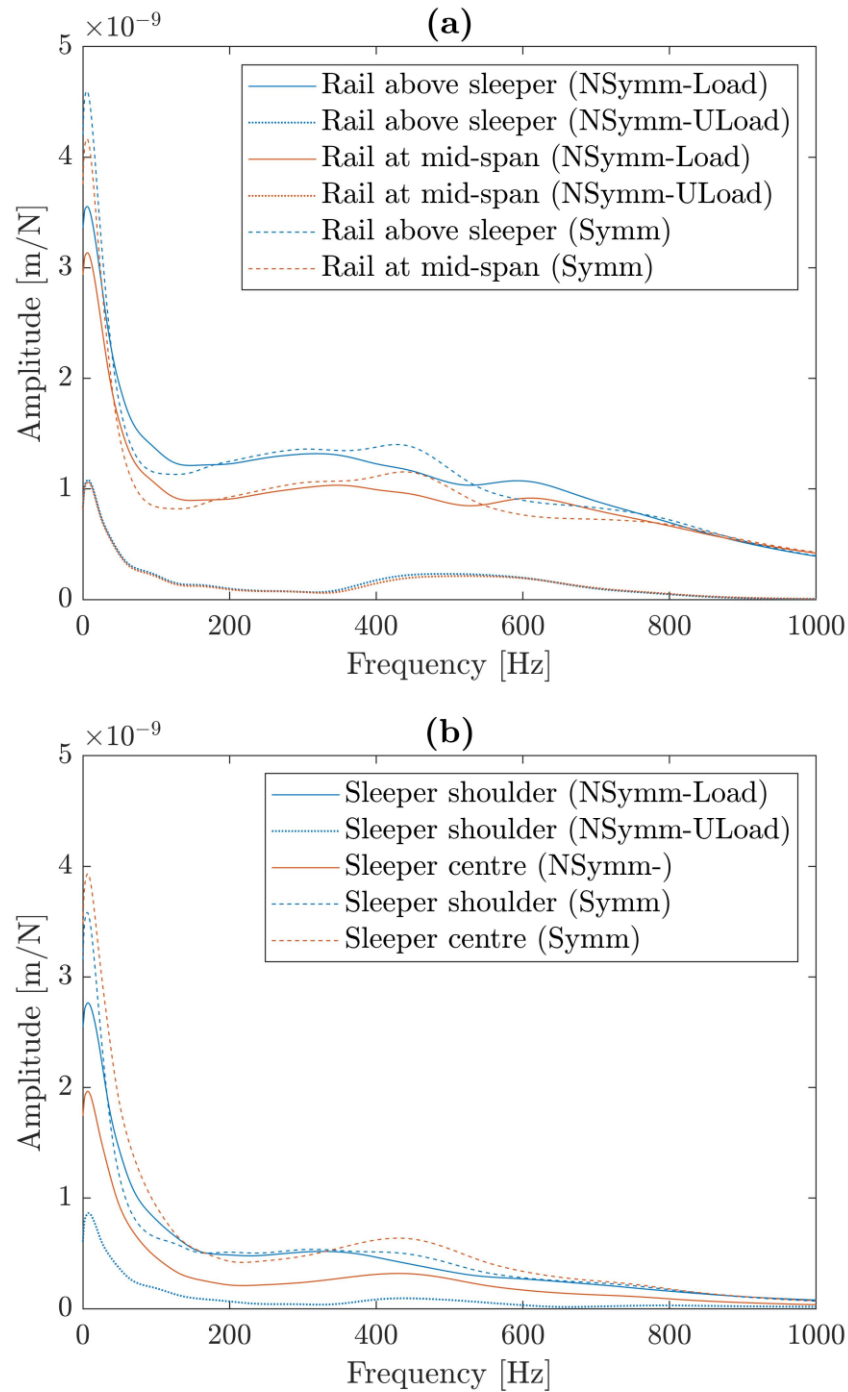
Figure 6-13. Deflections at: (a) rail above sleeper and at mid-span, and (b) sleeper shoulder and centre. Full-track model: non-symmetric loaded side (NSymm − Load), non-symmetric unloaded side (NSymm − ULoad), and fully-symmetric loaded (Symm)

Figure 6-16 to **Figure 6-19** compare the absolute track deflections caused by symmetric and non-symmetric loading, when excited at various frequencies. Three-dimensional and transverse views results are employed to highlight the transversal bending modes at the upper track layers. Firstly, **Figure 6-16** presents the track deformation at 6 Hz. At this frequency, the response is mainly affected by the subgrade properties and the symmetric model yields larger deflections than the non-symmetric case. The maximum deformation occurs at the rail, the point where

the force is applied, and its effect propagates in all directions within the track, with a considerable contribution in the sleeper below. In the symmetric case, the force is evenly distributed along the track, resulting in a symmetric bending mode. In contrast, the transversal bending mode of the track is non-symmetric in the non-symmetric case, and its loaded side experiences the greatest deflection. Overall, the large response in both cases is due to the magnification effect resulting for the wave propagation effect at low frequencies.

Figure 6-17 illustrates that at 130 Hz, the maximum is achieved with the non-symmetric configuration. Because the influence of the subgrade diminishes with frequency, the propagation of the response within the track is less significant at 130 Hz than at 6 Hz – see **Figure 6-16**.

Figure 6-18 shows the absolute deformation at 320 Hz. Both results present similar magnitudes, with the symmetric case displaying a slightly higher value. This similarity is responsible for the near-undeformed deformation on the unloaded side of the non-symmetric model. It can be observed that the propagation of the response within the lower-track layers is lower at 320 Hz than at 130 Hz – see **Figure 6-17**. This is because as frequency increases, the track component's effect on the response increases while the subgrade's effect decreases.

Alternatively, results computed at 440 Hz – see **Figure 6-19**, show that the symmetric model provides a greater deformation compared to the non-symmetric. The difference between both models is also presented on the unloaded side of the non-symmetric case, which is considerable and larger than the obtained in the quasi-undeformed result at 320 Hz – see **Figure 6-18**. Similarly, the deformation is concentrated on the upper-track layers, accounting for their relevance at higher frequencies.

Finally, it is evident that symmetry conditions have an effect on receptance results. In a symmetrical configuration, two forces of equal magnitude are applied on two opposite positions, resulting in a response that propagates evenly along the track to the ground support and symmetric transversal bending modes. In contrast, in a non-symmetrical configuration a single impulse leads to non-symmetric bending modes, where the maximum response, occurring at the loaded side, gradually decreases as it extends to the opposite and unloaded side. In addition, results show non-symmetric conditions lead to lower deflections and lower frequencies of resonance compared to the symmetric case. Thus, to realistically approximate receptance field tests, a full-track model with non-symmetric conditions (with $F_1 = 1$ N and $F_2 = 0$ N) is considered hereafter. Regarding the support conditions, the subgrade component is considered at low- and mid-frequency ranges while disregarded at higher-frequency, ranges for simplicity purposes.
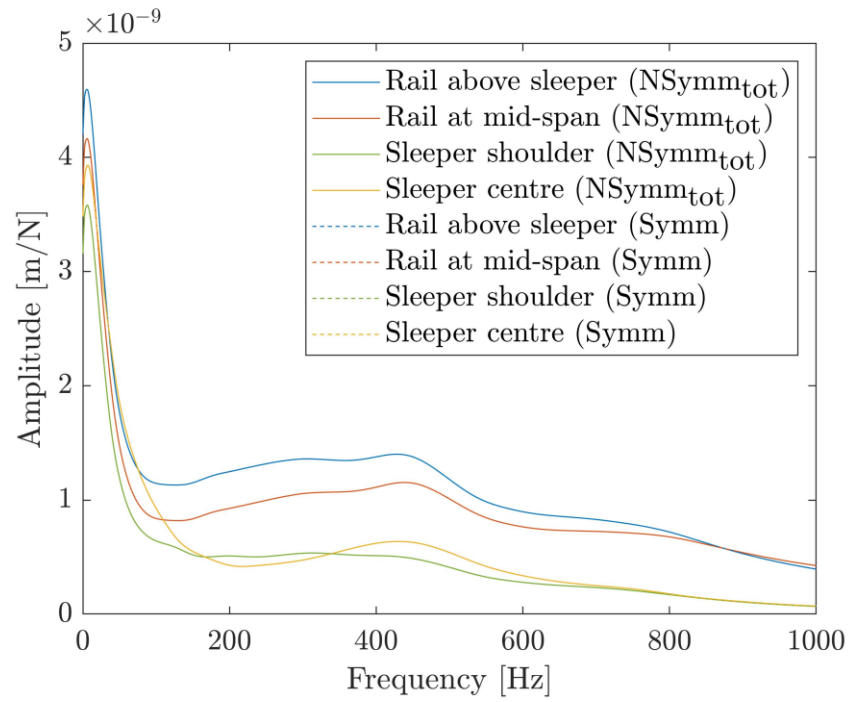
Figure 6-14. Deflections at different observation points of a full-track model: non-symmetric total (NSymm$_{tot}$), and fully-symmetric (Symm)
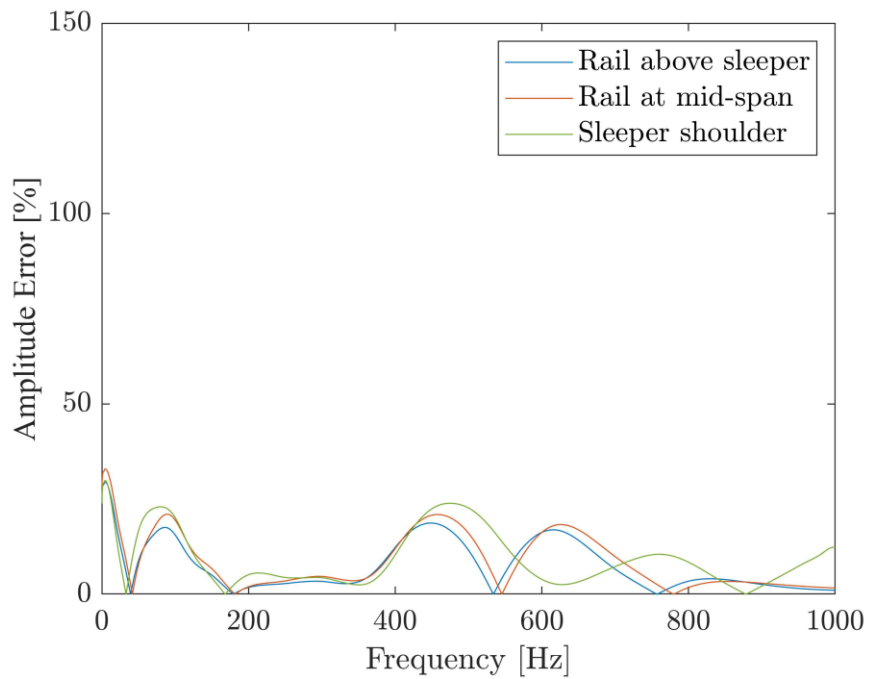
Figure 6-15. Amplitude error between symmetric and non-symmetric loaded model at different observation points – track on subgrade support
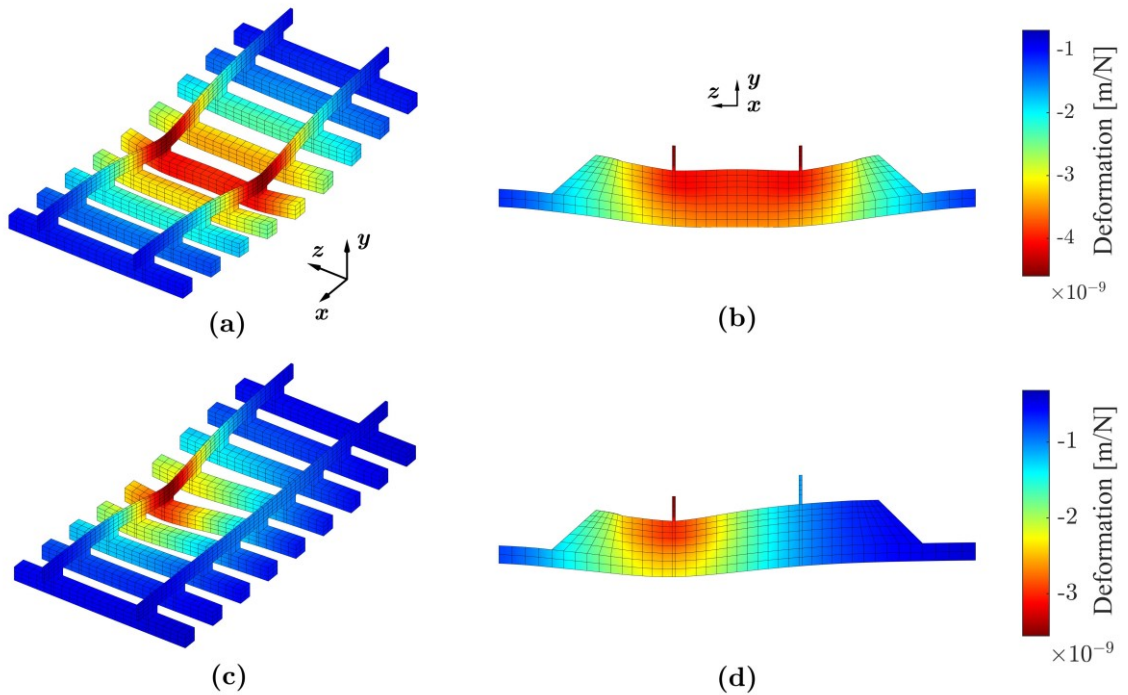
Figure 6-16. Absolute track deformation at 6 Hz: (a) symmetric force model 3D view, (b) symmetric force model transversal view, (c) non-symmetric force model 3D view, and (d) non-symmetric force model transversal view. Lower components removed for visibility
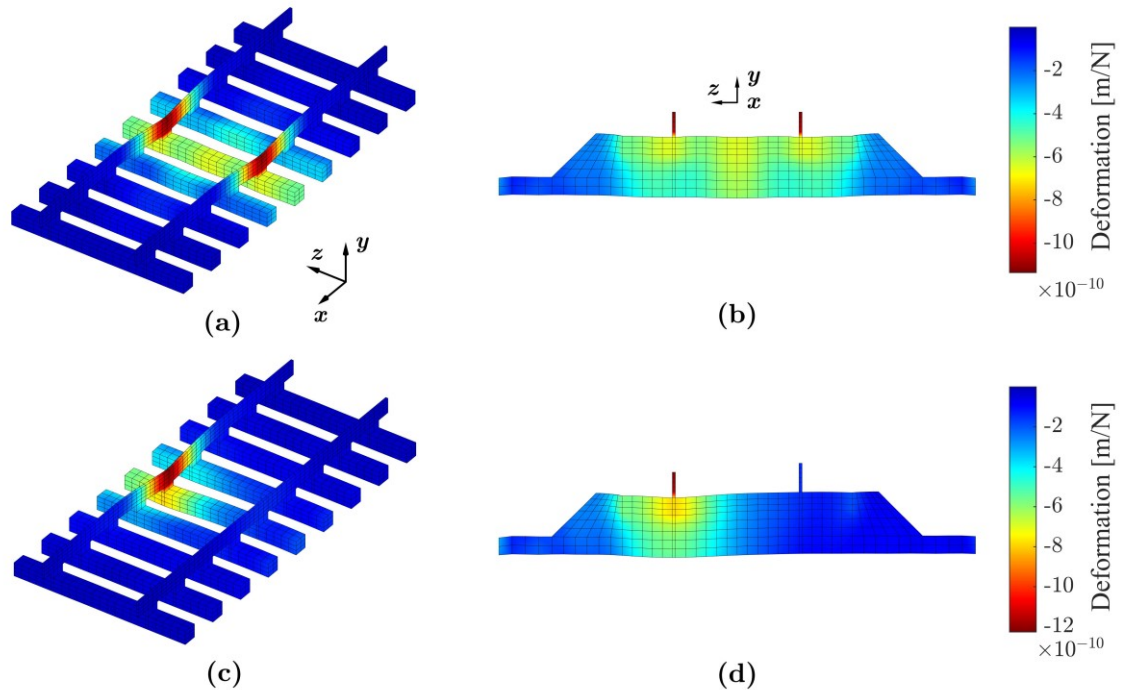
Figure 6-17. Absolute track deformation at 130 Hz: (a) symmetric force model 3D view, (b) symmetric force model transversal view, (c) non-symmetric force model 3D view, and (d) non-symmetric force model transversal view. Lower components removed for visibility
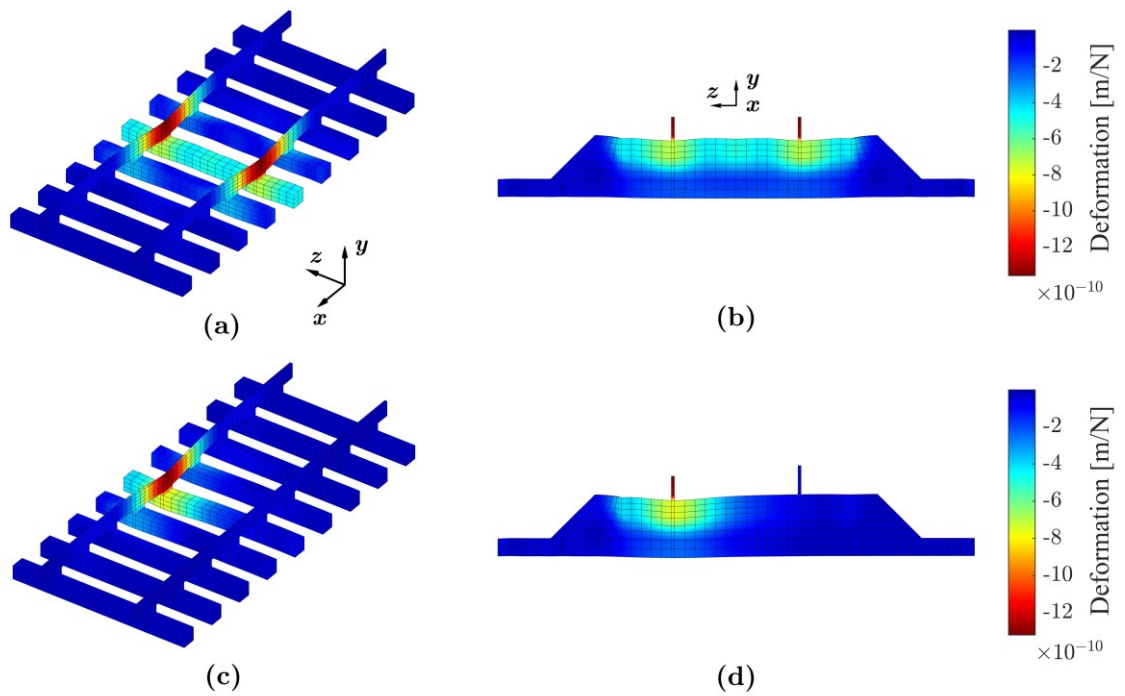
Figure 6-18. Absolute track deformation at 320 Hz: (a) symmetric force model 3D view, (b) symmetric force model transversal view, (c) non-symmetric force model 3D view, and (d) non-symmetric force model transversal view. Lower components removed for visibility
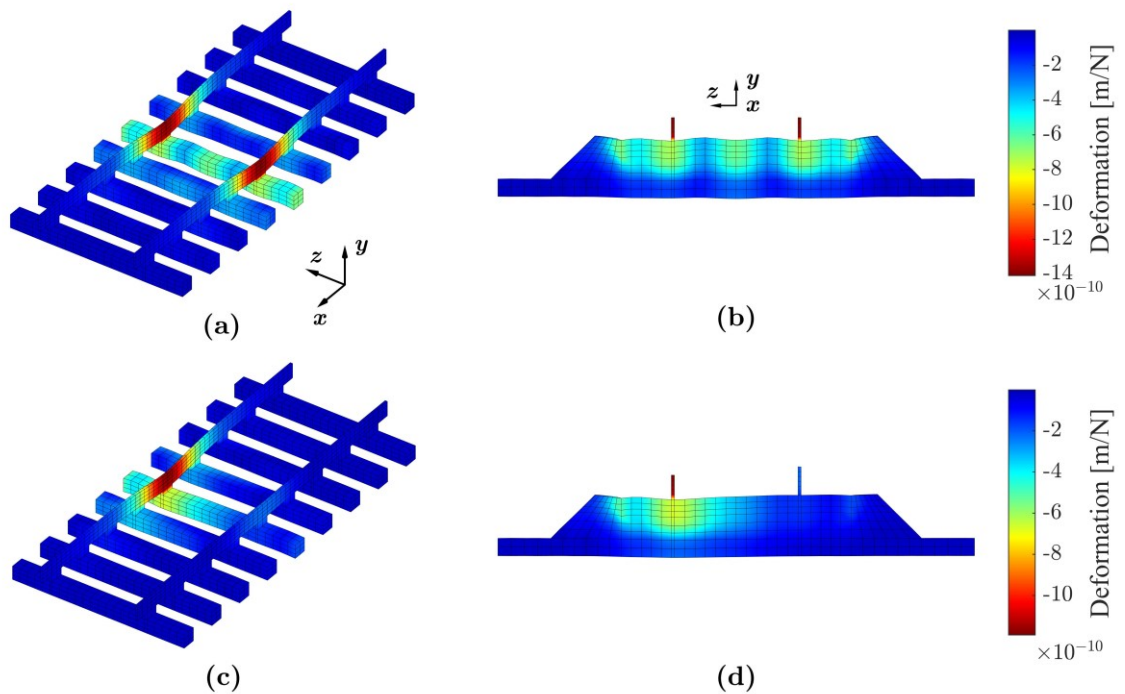
Figure 6-19. Absolute track deformation at 440 Hz: (a) symmetric force model 3D view, (b) symmetric force model transversal view, (c) non-symmetric force model 3D view, and (d) non-symmetric force model transversal view. Lower components removed for visibility

6.4 Conclusions

This Chapter presents a novel numerical approach well-suited for calculating receptance of ballasted railway tracks. The new approach uses the 3D DPM-FE-PML model introduced in Chapter 4, which can capture dynamic wave propagation within the complex geometries associated with each track component while using an efficiently sized domain. Then, the model is refined considering the effect of two common modelling assumptions (beam-on-elastic foundation and symmetry) on the calculation of track receptance.

Firstly, the model is improved by studying the supports conditions. For this, tracks resting on semi-infinite ground and on a rigid support are compared. It is shown that ignoring wave propagation in the subgrade-earthwork layers induces errors in the $\approx$ 80-300% range at frequencies below 200 Hz, and errors of $\approx$ 30% in the 200-440 Hz range. Therefore, subgrade conditions must not be disregarded in the simulation.

Lastly, the model is refined to approximate the loading configurations in in-situ receptance tests. This involved studying both symmetric and non-symmetric loading conditions and their impact on track bending modes. It is shown that the assumption of track centreline symmetry ignores some track bending modes and can also introduce errors ($\approx$ 20%) at frequencies up to 1000 Hz. Thus, non-symmetric conditions must be included in receptance simulations of ballasted tracks.

Chapter 7
Sensitivity Study

7.1 Introduction

This Chapter performs a sensitivity study on the most common high-speed railway ballasted track components. For this, the refined model tailored to receptance of ballasted tracks, presented in Chapter 6, is employed. This model is based on the 3D periodic method introduced in Chapter 4. Multiple permutations considered for the sensitivity analysis are compared against a base case described by stiff track properties, typical of modern high-speed track structures.

Section 7.2 describes the geometrical and material properties employed in the sensitivity analysis. These include the effect of: (1) rail sections, (2) railpad stiffness, (3) sleeper material, (4) Under-Sleeper Pads (USP) application, (5) ballast stiffness and thickness, (6) embankment simulation, and (7) subgrade stiffness. Then, using this information, new knowledge regarding the typical frequency ranges and stiffness ratios associated to each track component is presented in Section 7.3. Lastly, Section 7.4 outlines the main conclusions of the Chapter.

7.2 Case of Study

A sensitivity analysis is used to study the geometric and material properties of a high-speed ballasted track. Appendix F presents the properties of each track component while the track properties defined in **Table 6-2** are the base parameters, which correspond to a stiff track supported by well-compacted earthworks, characteristic of a modern high-speed track. **Table 7-1** highlights the base permutation and the 17 combinations grouped according to the characteristic parameters related to each component. **Figure 7-1** shows the 3D view of the reference cell mesh with all studied components. Note that the base simulation did

not include Under-Sleeper Pads (USP) or an embankment. Using the findings related to model design from Chapter 6, the full track width is modelled (i.e. no symmetry condition), supported by an infinitely deep soil medium.

Permutation		Case of Study
A3/B2/C3/D1/E2/F1/G1/H2	-	Base parameters
A123/B2/C3/D1/E2/F1/G1/H2	A	Rail: sections
A3/**B123**/C3/D1/E2/F1/G1/H2	B	Railpad: stiffness
A3/B2/**C123**/D1/E2/F1/G1/H2	C	Sleeper: material
A3/B2/C3/**D123**/E2/F1/G1/H2	D	USP: stiffness
A3/B2/C3/D1/**E12345**/F1/G1/H2	E	Ballast: stiffness and thickness
A3/B2/C3/D1/E2/**F1**/G1/H2	F	Sub-ballast: single case
A3/B2/C3/D1/E2/F1/**G123**/H2	G	Embankment: depth
A3/B2/C3/D1/E2/F1/G1/**H123**	H	Subgrade: stiffness

Table 7-1. Parametric simulation permutations
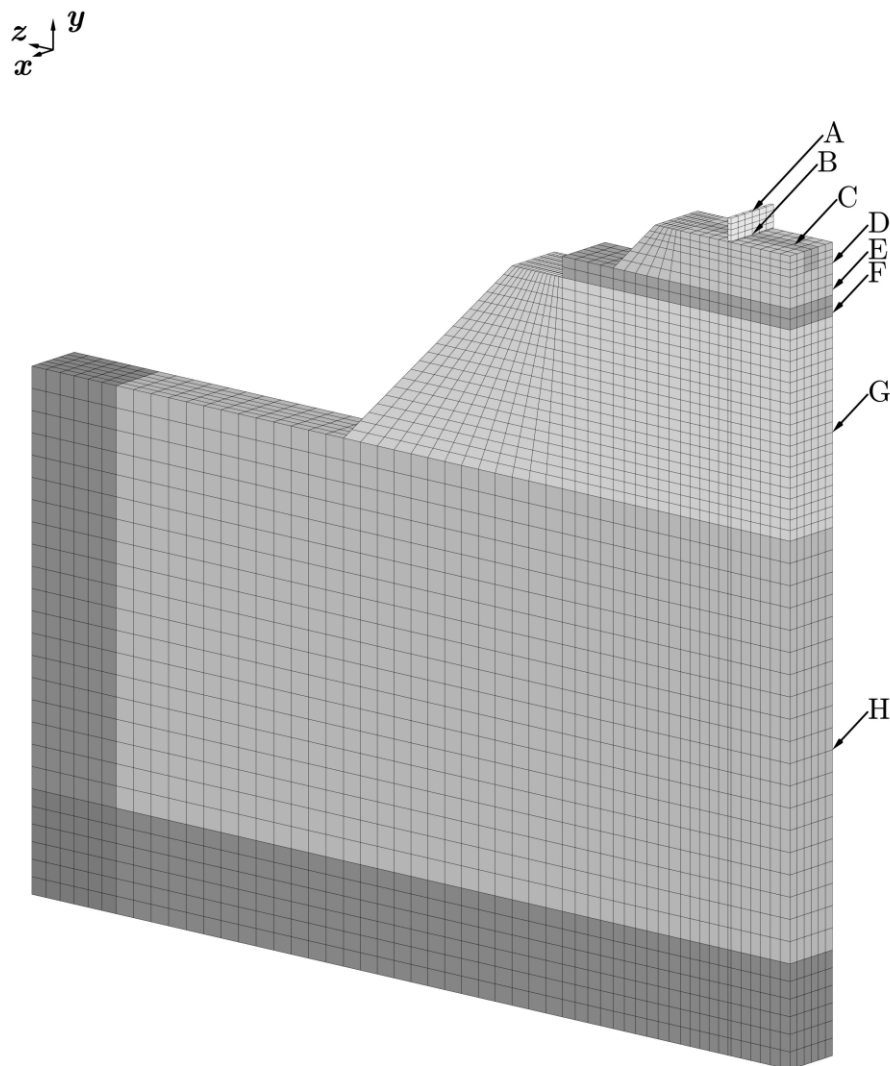
Figure 7-1. 3D view reference cell mesh with components in permutations highlighted. Only half-track shown for visibility purposes

Note that in this Chapter, standstill receptance is computed. Therefore, only harmonic stationary forces are considered, and moving contributions (quasi-static and dynamic components that include train-track effects) are disregarded.

7.2.1 Rail

Figure 7-2 presents the absolute deflection for three different rail sections: 49E1, 56E1 and 60E2 (base case). The rail properties primarily influence the response at higher frequencies ($f > 800$ Hz) and therefore the results are shown only at the rail above the sleeper, rather than at other observation points. Below 50 Hz, the curves have comparable gradients, with the heaviest rail exhibiting the lowest amplitude and the lightest rail displaying the highest amplitude. The rail section size induces a similar response at all frequencies up to approximately 800 Hz, where all curves rapidly decay.

7.2.2 Railpad

Figure 7-3 displays the response of the rail above the sleeper, computed with soft (B1), typical (base case, B2) and stiff railpads (B3). Similar to the rail behaviour, all railpad curves experience a comparable decay rate of amplitude below 50 Hz. Beyond this frequency, the difference between them becomes more pronounced, leading to diverging results where the maximum difference occurs between $300 - 600$ Hz, where the rail mass resonates over the railpad stiffness, i.e. at the railpad frequency of resonance f_{railpad}. Between these frequencies, soft and stiff railpads exhibit the highest and lowest amplitude, respectively. Note that typical and stiff railpads show multiple peaks at around 300 Hz and 600 Hz, corresponding to f_{rail} and f_{railpad}, respectively. In contrast, soft railpad response results in a low f_{railpad} overlapped by f_{rail}, thus making the former challenging to identify. Next, at $f > 600$ Hz, all curves experience a rapid decay.

7.2.3 Sleeper

The sleeper effect is investigated considering three scenarios: wooden (C1), plastic (C2), and concrete (base case, C3) sleepers. To do so, results are shown at the rail above sleeper (RS) and sleeper centre (SC) observation points – see **Figure 7-4**. All curves experience a similar and relatively constant gradient below 50 Hz, with identical and more flexible behaviour in C1 and C2, compared to C3. Note that the stiffness values of wooden and plastic sleepers are comparable (8.4 GPa and 8 GPa, respectively), thus explaining their similarities in the response. Above this frequency, the sleeper stiffness and density induce a change in the gradient and all

curves diverge reaching their maximum difference at around 320 Hz (f_{rail}). At this frequency, the response at the rail point (RS) yields the stiffest at C3 and the softest at C1. This behaviour is opposed to the sleeper observation point (SC), where C3 and C1 yield the stiffest and softest response, respectively. Regarding C1 and C2 cases, it can be seen that the lower density of the former induces a greater deflection.

7.2.4 Under-Sleeper Pads

The effect of Under-Sleeper Pads (USP) is explored in **Figure 7-5**. Results are shown at the rail above sleeper and at the sleeper centre observation points, considering three scenarios: no USP (base case, D1), soft USP (D2) and stiff USP (D3). Below 50 Hz, the gradients of all curves remain relatively stable. However, above this frequency, the gradient difference starts to increase slightly. In the $50 - 500$ Hz range, USP inclusion leads to a slight increase in the response amplitude. Conversely, for frequencies above 500 Hz, the USP scenarios generate the stiffest response, resulting in a slightly higher railpad resonance frequency ($f_{railpad}$) compared to the absent case.

7.2.5 Ballast

Figure 7-6 compares the effect of the ballast stiffness at the rail above sleeper and sleeper centre observation points. Below 50 Hz, the ballast stiffness impact the response in a similar manner, with the soft case (E1) producing the greatest amplitude, followed by the typical (base case, E2) and the stiff ballast (E3) – all curves with comparable gradients. This behaviour persists up to approximately 300 Hz, the rail resonance (f_{rail}), where the amplitude difference among all results reaches its maximum. Above 300 Hz, all curves decays, first by the soft ballast, followed by the typical and the stiff cases. Next, at around 600 Hz ($f_{railpad}$), all curves converge, indicating that the ballast does not affect the structure at high-frequency ranges.

In addition to the stiffness effect, ballast thickness is also investigated. Three cases are assessed: typical (E2), deep (E4) and deeper (E5) ballast. Results demonstrate the height does not significantly influence the resonant frequencies – see **Figure 7-7**. It is observed that the ballast height leads to similar amplitudes and gradients up to approximately 50 Hz. However, beyond this frequency, all curves intersect at around 100 Hz and 200 Hz and ultimately converge above 400 Hz.

7.2.6 Embankment

Figure 7-8 illustrates the effect of embankment height, considering a well compacted embankment with $E_e = 200$ MPa. Results are shown at the rail above sleeper point for three cases: at-grade (base case, G1), deep embankment (G2), and deeper embankment (G3). Results show the embankment implementation primarily affects the response at $f < 300$ Hz, reducing the structure deflection and broadening the response. This occurs because the embankment is stiffer than the supporting subgrade. This behaviour is accompanied by disturbances manifested as peaks between 0-200 Hz, representing the propagation of the response within the embankment. Also, it is observed that the embankment cases (G2 and G3) intersect the at-grade case at 50 Hz, 180 Hz and 300 Hz. Between the first two intersection points $(50 - 180$ Hz) all curves exhibit a similar gradient, with G2 and G3 displaying a higher deflection than G1. This behaviour is opposed to the second set of intersection points (180-300 Hz), where G2 and G3 display a stiffer response compared to G1. Overall, this behaviour likely indicates the frequency range in which the sub-ballast layer is most affected, as both the embankment and the sub-ballast has similar properties.

7.2.7 Subgrade

Finally, **Figure 7-9** compares the rail on support response for a soft (H1), typical (base case, H2) and stiff (H3) subgrade cases. Results show the subgrade mainly affects the response at frequencies below 300 Hz. Similar to the embankment effect, it can be seen that the typical and the stiff subgrade curves intersect the soft subgrade at approximately 50 Hz, 180 Hz and 300 Hz. At $f < 50$ Hz, the stiff subgrade has the lowest deflection, followed by the typical and soft subgrade. Between 50-180 Hz, all curves show similar behaviour, with the stiff subgrade having a slightly larger amplitude than the typical and soft cases. In contrast, at 180-300 Hz, the soft subgrade exhibits a slightly softer deflection compared to the other subgrade cases. Overall, it is observed that both the stiff subgrade and the inclusion of embankment – see **Figure 7-8**, greatly improves the response at lower frequency ranges. However, the latter is accompanied by additional disturbances, which do not develop when increasing the stiffness of the subgrade.
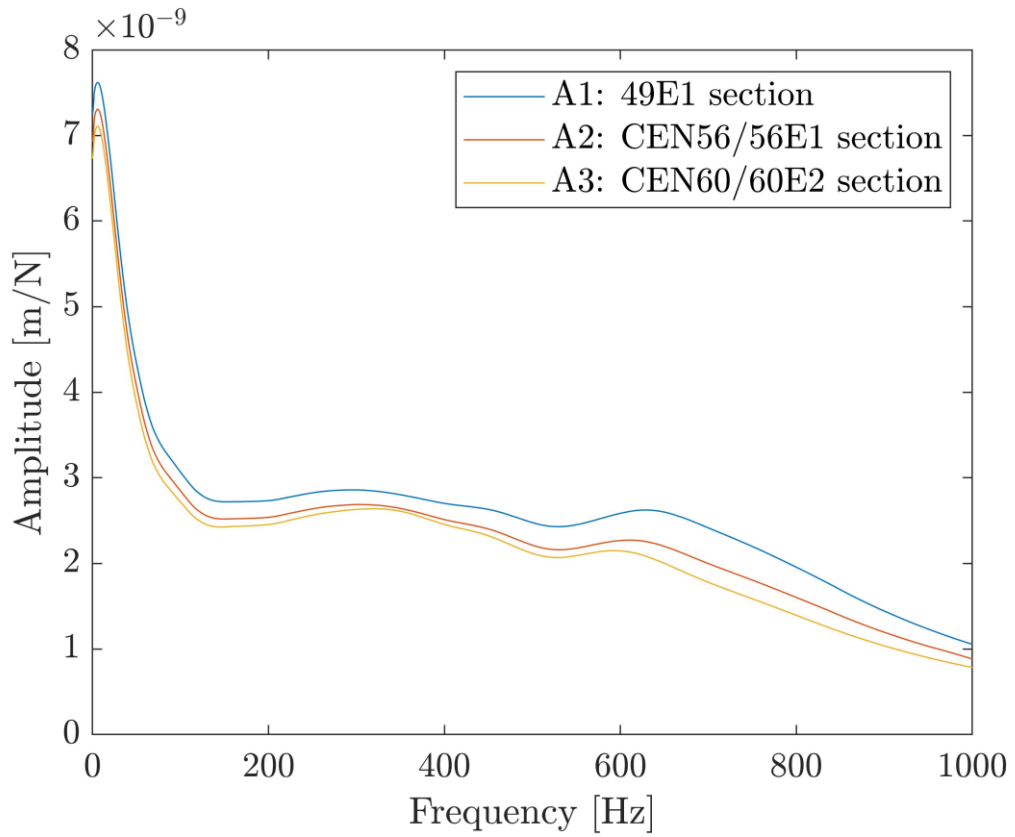
Figure 7-2. Rail receptance above sleeper. Rail section effect
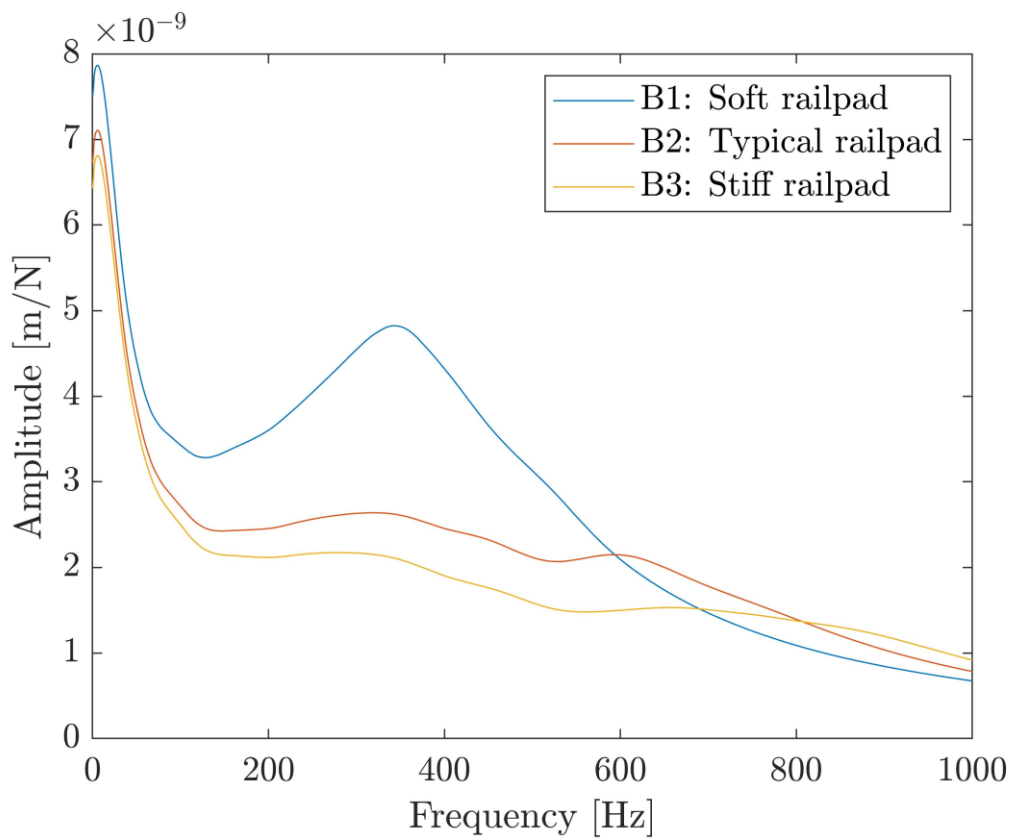
Figure 7-3. Rail receptance above sleeper. Railpad stiffness effect
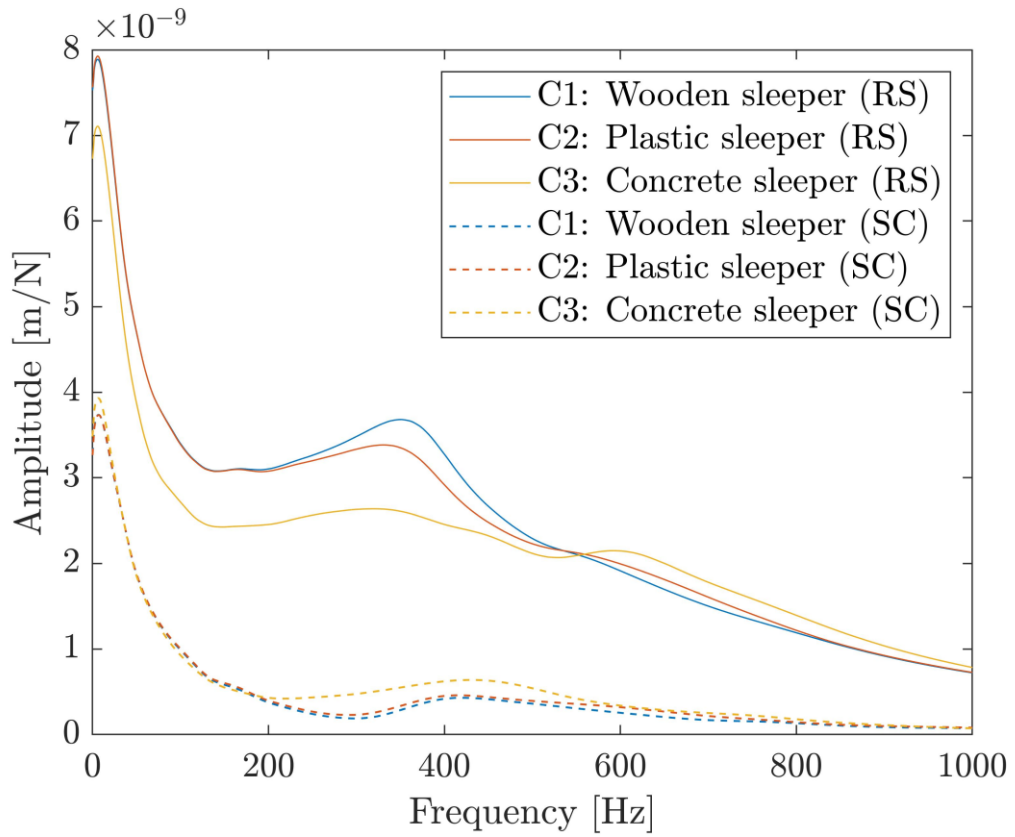
Figure 7-4. Frequency response at rail above sleeper (RS) and sleeper centre (SC).
Sleeper material effect
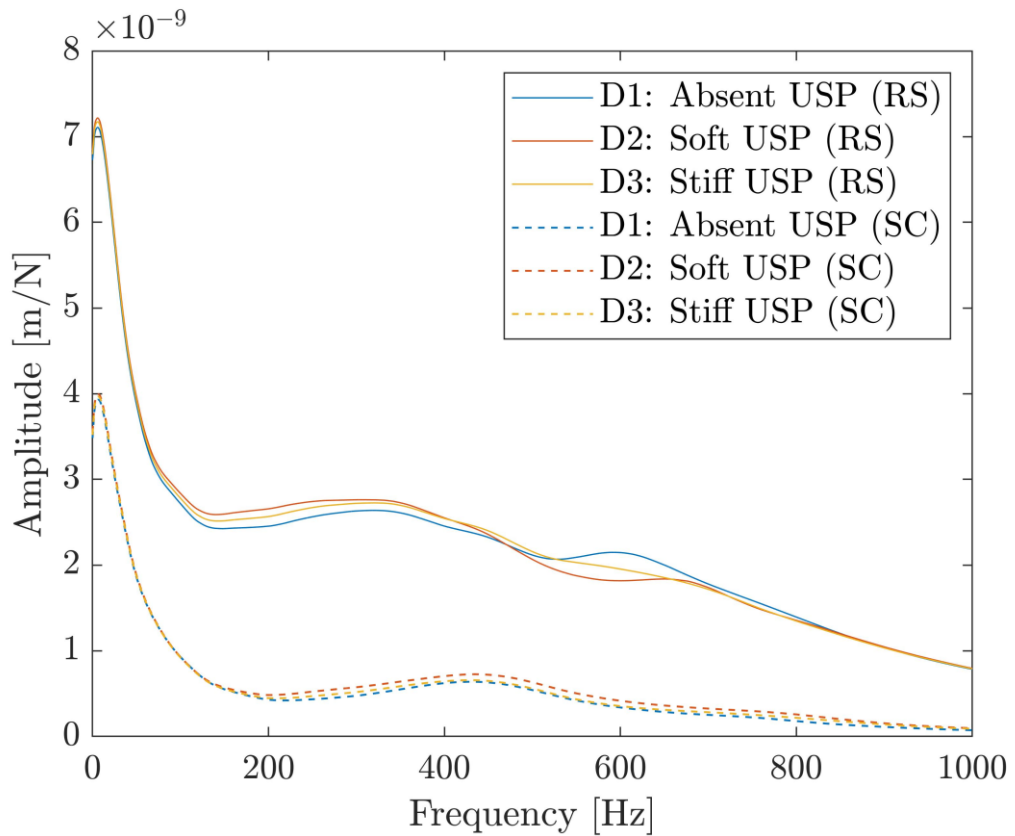
Figure 7-5. Frequency response at rail above sleeper (RS) and sleeper centre (SC).
USP effect
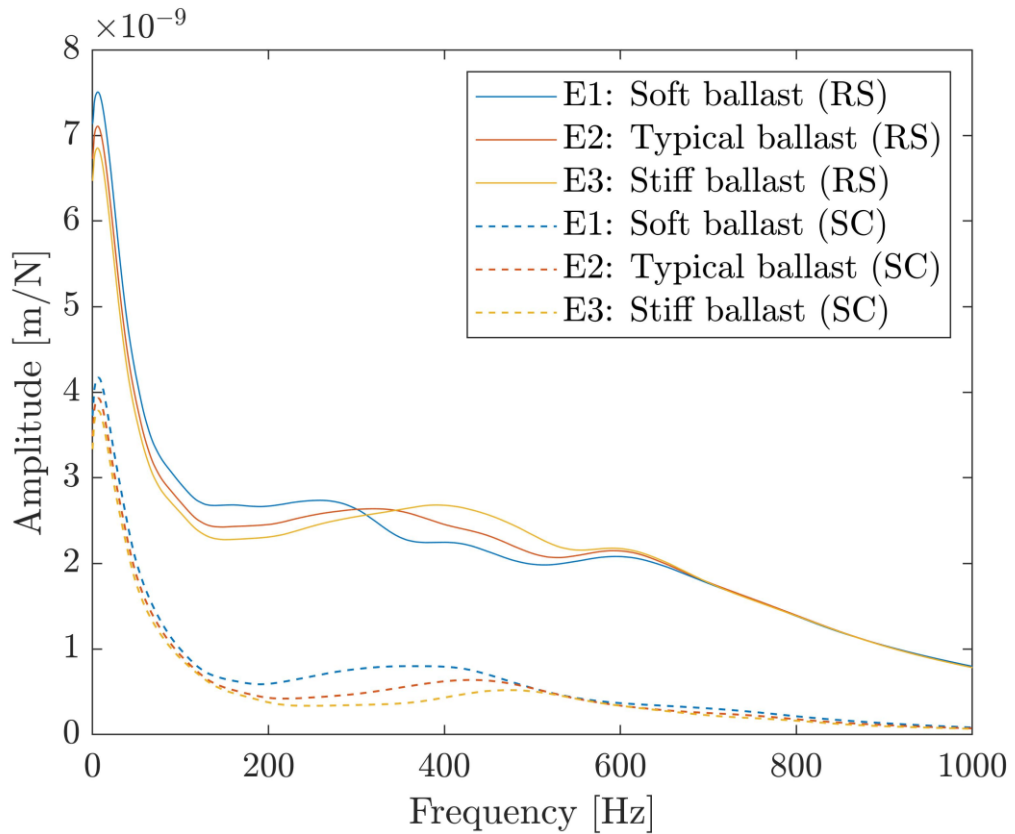
Figure 7-6. Frequency response at rail above sleeper (RS), rail at mid-span (RM), and sleeper centre (SC). Ballast stiffness effect
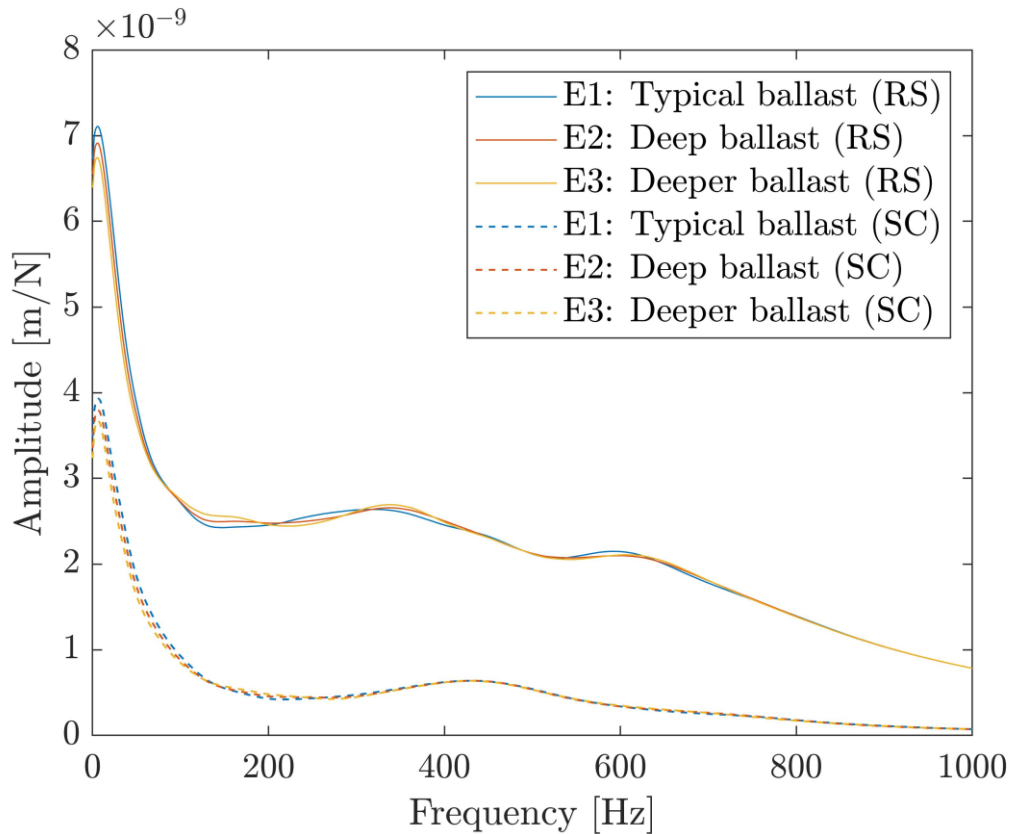
Figure 7-7. Frequency response at rail above sleeper (RS), rail at mid-span (RM), and sleeper centre (SC). Ballast thickness effect
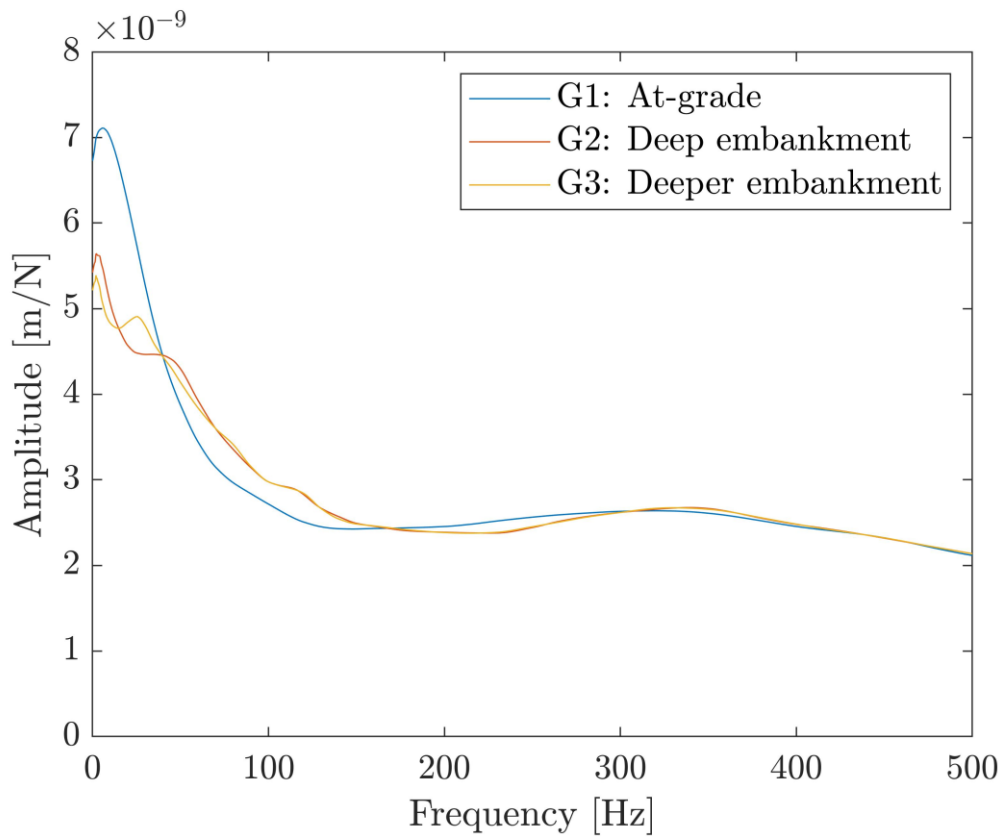
Figure 7-8. Rail receptance above sleeper. Embankment effect
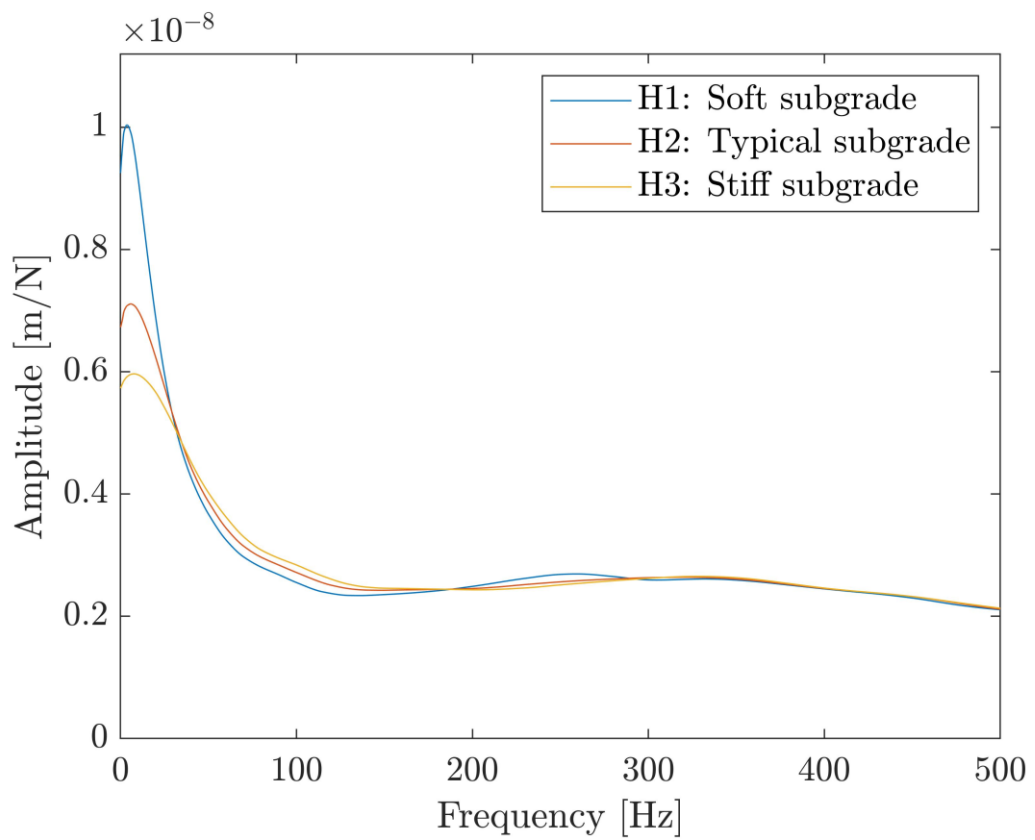
Figure 7-9. Rail receptance above sleeper. Subgrade stiffness effect

7.3 Discussion

This Chapter introduces new in-sights on receptance analysis and expands upon previous researches conducted in [9,12,16] by focusing on:

1. Implementing the DPM, a computationally efficient technique that allows replicating the total structural behaviour via a single slice,
2. Providing a closer approximation of both track (through complex support conditions and track's components representation) and ground dynamic behaviour via a combination of 3D FEM-PML techniques,
3. Investigating the effect of rigid foundations and symmetry conditions, and
4. Presenting an in-depth assessment of multiple track components' effect on the structure's response which allows for the definition of more detailed frequency ranges.

The related sensitivity study is used to identify the influence of specific track parameters on the entire structure. This allows for the definition of frequency ranges within which the response amplitude changes or remains constant. With this information, it is possible to identify and target particular railway issues by adjusting the track components' mechanical parameters and ultimately optimize railway system's design and maintenance operations, thus improving the total system response.

7.3.1 Frequency Ranges

Figure 7-10 displays the frequency ranges where each track component has a dominant effect on the track response. For each component the horizontal bar indicates the relevant frequency range, with the colour intensity indicating the dominance of each frequency within. It can be seen that the subgrade mainly impacts frequencies around 10 Hz however still has some influence up to 300 Hz. The embankment's effect is comparable to that of the subgrade albeit with a minimal shift to higher frequency. In contrast, the ballast energy is observed between 80-600 Hz, with its main impact at approximately 300 Hz. The sleeper's influence extends to the high-frequency range (> 800 Hz) however primarily affects frequencies around 350 Hz. Finally, the railpad and the rail affect the response above 250 Hz and 800 Hz, respectively. This behaviour is expected as they are the uppermost track components. However, the dominant effect of the railpad occurs around 600 Hz – a frequency close to the rail's lower limit, while the rail occurs at > 1000 Hz.

7.3.2 Stiffness Ratios

Transfer function results provide valuable information related to the stiffness of the overall railway system. At 0 Hz, the response is related to the global static stiffness. Alternatively, low-frequencies ($f < 300$ Hz) define the subgrade stiffness, and low- and mid-frequency ranges ($f < 800$ Hz) the track stiffness. **Figure 7-11** illustrates the amplitude ratios at different frequencies: (a) at 0 Hz, and (b) below 800 Hz. In both cases, relationships are compared against the base permutation and results are presented for 'low' and 'high' values (stiffness, height or mass parameters) of each track component. Note that in scenario (a), the ratio is calculated at a single frequency value (0 Hz). However, in scenario (b), it considers the relationship between the average amplitude below 800 Hz and the amplitude at 0 Hz, i.e. the track-static amplitude.
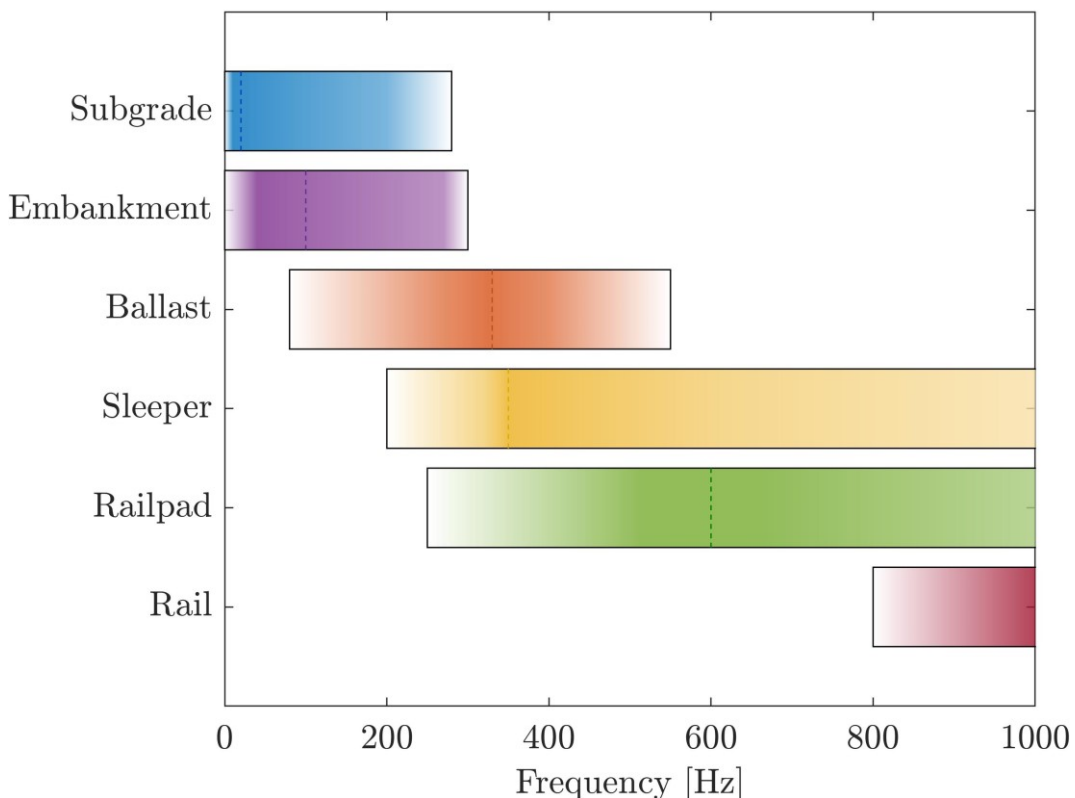
Figure 7-10. Frequency ranges effect of each track component.
Dominance within the range indicated in dashed lines

Figure 7-11(a) shows that the most significant changes in amplitude are associated with the lower track components, which dominate the response at low-frequency ($f < 300$ Hz) ranges. The first two maxima are found in the 'low' subgrade and embankment cases: 38% and 22%, respectively. These components are associated with low stiffness parameters, which result in flexible components with large

deflections. The following maxima are related to 'high' stiffness cases of these components, 20% for the embankment and 15% for the subgrade.

Both sleepers and low railpad components exhibit the following maxima of approximately 12%. Again, these results are attributed to low stiffness parameters which leads to increased deformations. Despite being an uppermost track component, a low railpad stiffness results in a combination of f_{rail} and f_{railpad} – see **Figure 7-11**, which leads to the response magnification at around these resonance frequencies ($f \approx 300$ Hz) and its static response ($f = 0$ Hz).

Note that despite being a sub-structure track component, the ballast stiffness impact on the static response is comparable to that of the rail. Low components of the ballast and rail give a similar static change in amplitude of around 7%. In contrast, high cases of railpad, ballast and rail provide a small variation in the static amplitude of 4%. Lastly, USP components exhibit the smallest variation in amplitude: 2% and 1% in its low and high cases, respectively, indicating its negligible effect in the static response.

Alternatively, the ratio between average track and static amplitude in **Figure 7-11**(b) shows that, 'low' upper-track components result in greater ratios than their 'high' cases. For instance, the low railpad stiffness case provides a ratio of 48%, higher than the 30% of its 'high' case. A similar phenomenon is observed in the rail and sleeper components. Overall, the difference between the track and static amplitudes can explain this behaviour: 'low' upper-track properties result in softer tracks with larger amplitudes than 'high' cases. Thus, 'low' upper-track parameters reduce the amplitude differences, leading to high amplitude ratios.

Regarding the USP and ballast components, the ratio of track to static amplitude remains approximately constant ($\approx 35\%$) in all cases. Consequently, the USP implementation and ballast stiffness condition have a similar impact on both the track and the static response, leading to minor changes in the ratio.

In contrast, components below the ballast have the opposite effect. It is clear that including a high embankment and increasing the subgrade stiffness significantly affect the amplitude ratios. For these components, 'high' cases result in greater ratios compared to 'low' cases. Again, this can be explained by the difference between the track and static amplitude values, which decreases with the static amplitude when stiff subgrades and high embankments ('high' parameters) are employed.

(a)

(b)
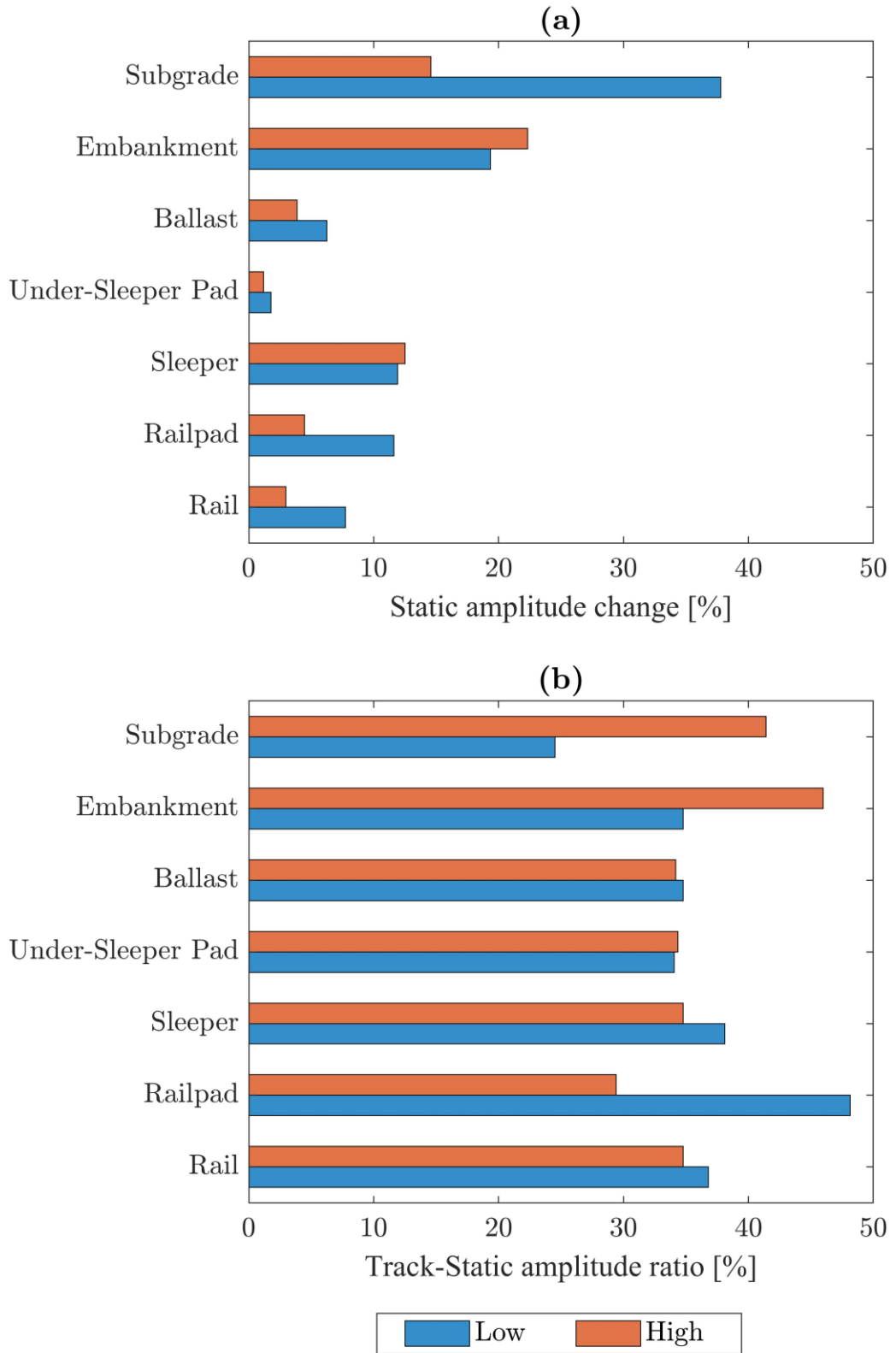
Figure 7-11. Amplitude of the response due to different track components:
(a) static, and (b) track-static

7.4 Conclusions

This Chapter employs the refined periodic model tailored to receptance computation – see Chapter 6, to perform a parametric study on different ballasted track components. The study includes the effect of rail sections, railpad stiffness, sleeper material, ballast stiffness and thickness, embankment depth, and subgrade stiffness. The various permutations were compared to a base case described by a stiff track supported by well-compacted earthworks, typical of a modern high-speed track.

This comprehensive study facilitates the identification of the key frequencies associated with different track components. It is shown that lower track components dominate lower frequency ranges. Alternatively, upper track components govern the track response at higher ranges. Additionally, the results obtained offer insights into track stiffness: flexible track components exhibit larger amplitudes, while stiffer components yield lower magnitudes.

Overall, with this information, it is possible to pinpoint and address particular railway issues through adjustments to the mechanical parameters of track components. This, ultimately, allows for optimising the design and maintenance operations of the railway system, leading to an improved overall system response.

Chapter 8
Definition of Receptance Relationships

8.1 Introduction

This Chapter presents a three-step approach for formulating new empirical equations tailored for receptance applications. Section 8.2 introduces this procedure, which involves: (1) defining initial relationships using power regression methods, (2) identifying the pivotal parameters influencing the response, and (3) formulating the final empirical equations through optimization techniques. The primary algorithm employed for this process is then detailed in Section 8.3. Using this method, Section 8.4 presents new empirical equations for resonance frequencies and receptance amplitudes. Section 8.5 compared these equations with results obtained via sensitivity analysis in Chapter 7. Lastly, Section 8.6 summarises the key conclusions.

8.2 Main Procedure

This Section employs the sensitivity results from Chapter 7 to define new empirical equations for estimating resonance frequencies and amplitudes. For their formulation, the following procedure is employed – see **Figure 8-1**:

(a) *Definition of initial relationships.* In this step, power regression analysis is performed for each jth component in the sensitivity study, and equations of the form $y = C_j x_j^{b_j}$ are derived. Where y is the resonance frequency or amplitude, x is the mechanical parameter of the component, and C_j and b_j are regression constants – see **Figure 8-1**(a).

(b) *Selection of important parameters*. The influence of each parameter in the frequency of resonance or static amplitude is evaluated via constant b_j. If the absolute value of this constant is lower than 0.1 (i.e. $|b_j| < 0.1$), then the parameter x is not sufficiently important and is disregarded – see **Figure 8-1**(b).

(c) *Definition of final equations*. Remaining relationships are combined and new equations of the form $y = C_{\text{base}}x_m^{d_m} \dots x_{m_{\text{end}}}^{d_{m_{\text{end}}}}$ (where $m = 1,2, \dots m_{\text{end}}$) are derived via optimisation techniques. In this step, all values C_j are replaced by a single constant C_{base} corresponding to the frequencies of resonance and amplitude of the base permutation ($C_{\text{base}} = f_{\text{base}}$ or $C_{\text{base}} = A_{\text{base}}$). Then exponentials d_m are computed using multiple-objective optimisation [268]. Note that d constants increase or decrease at this step; therefore, condition of step (b) is ignored, i.e. $|d_m| < 0.1$ are allowed – see **Figure 8-1**(c).
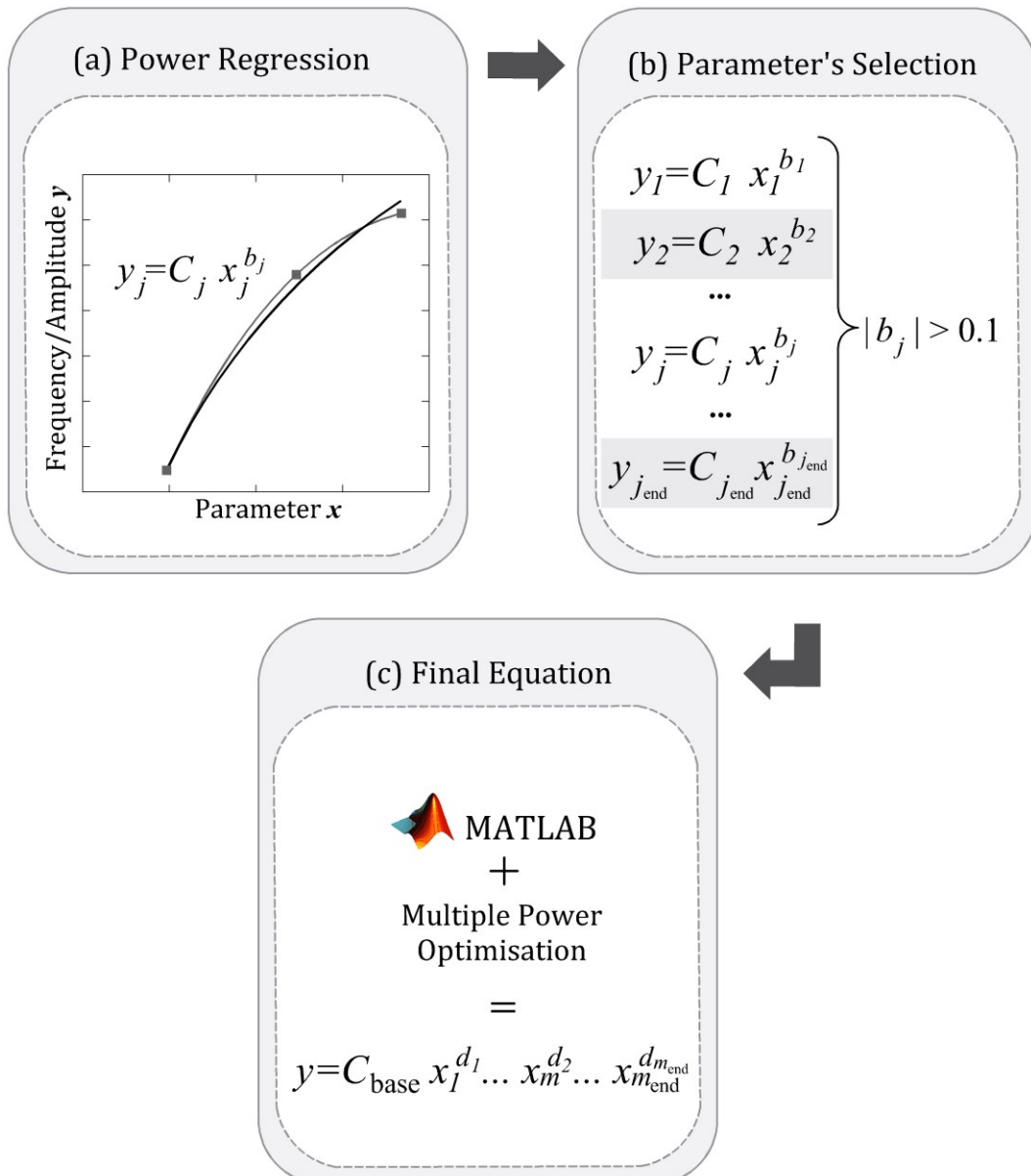
Figure 8-1. Empirical equations procedure

Algorithm 174

Excluding step (c), the procedure presented in this Chapter is similar to the described in [17] – where individual power equations of step (b) are combined via multiple power approximations to find a single constant C while exponentials b remain unchanged. In this, the remaining individual power equations in step (b) are fit together via multiple power approximations, an approach in which all constants C_j are weighted into a single value C, while exponentials b_j remain unchanged, thus resulting in empirical equations of the form $y = Cx_j^{b_j} \dots x_{j_{\text{end}}}^{b_{j_{\text{end}}}}$.

8.3 Algorithm

Once the important track parameters have been selected – see step (b) in Section 8.2, it is possible to define the final empirical equation via the multiple-objective optimisation toolbox of MATLAB. This step can be divided into 7 sub-steps – as shown in **Table 8-1**:

1. *Definition of initial equality expression.* Equations of the form $y_k = C_{\text{base}} x_{k,m}^{d_m} \dots x_{k,m_{\text{end}}}^{d_{m_{\text{end}}}}$ are defined by combining the important parameters $x_{k,m}$ in each kth permutation. In this step, exponential terms are unknown and constant in all permutations. In order to simplify each equation, these are inverted $(0 = C_{\text{base}} x_{k,m}^{d_m} \dots x_{k,m_{\text{end}}}^{d_{m_{\text{end}}}} - y_k)$, and then defined in MATLAB as functions handle.

2. *Definition of anonymous functions.* Equations are further simplified by turning each ith equation into anonymous functions, function of a simple variable d.

3. *Combination of equations.* All k^{th} anonymous functions are combined into a single function associated to a single variable d.

4. *Set an initial estimation.* The software performs an iterative process for which it requires initial values d_0. Although they can be set to zero, it is recommended to set values equal or similar to the initial exponents obtained in the power regression of step (b) in Section 8.2.

5. *Set optimisation functions.* In this step, it is necessary to define the optimisation options via 'optimoptions'. These include the type of optimisation function to be used, and additional options to refine the solution. Fort this case, the problem will be solved via the minimax constraint function 'fminimax', a function that seeks a point that minimises the maximum of a set of objective functions. The number of elements to be minimise is included via 'AbsoluteMaxObjectiveCount' and it is set to the total number of functions k. At this point, the problem solution can be refined by modifying the tolerance conditions such as 'OptimalityTolerance' and

'ConstraintTolerance' (these options are not shown in **Table 8-1** for visibility).

6. *Set constraints.* Constraints options are employed to refine the problem. These include linear inequality constraints A and b, linear equality constraints A_{eq} and b_{eq}, lower bounds l_b, upper bounds u_b, and nonlinear constraints nonlcon – see [268] for more information. However, for this particular case none constraints are set as the problem depends on the defined functions, the initial estimation, and the optimisation options.

7. *Problem solution.* Once all functions and options have been defined, exponents d can be computed via 'fminimax'.

```
1   % 1) Define equations as an optimisation equality expression:
2   % Equation 1:
3   eq1 = @(d1,…,dm)(Cbase*(X11^d1)*…*(X1m^dm)) – C1;
4   ⋮
5   % Equation k:
6   eqk = @(d1,…,dm)(Cbase*(Xk1^d1)*…*(Xkm^dm)) – Ck;
7
8   % 2) Define anonymous functions
9   Eq1 = @(d)eq1(d(1),…,d(k));
10  ⋮
11  Eqk = @(d)eq2(d(1),…,d(k));
12
13  % 3) Combine All equations
14  fun = @(d)[eq1(d(1),…,d(m));…;eqk(d(1),…,d(m))];
15
16  % 4) Initial estimation
17  d0 = [d01,…,d0m];
18
19  % 5) Set optimisation options
20  options = optimoptions('fminimax' ,' AbsoluteMaxObjectiveCount',k);
21
22  % 6) Set Constraints
23  A = [];     b = [];     Aeq = [];     beq = [];     lb = []     ub = []     nonlcon = [];
24
25  % 7) Problem solution
26  [d]= fminimax(fun,d0,A,b,Aeq,beq,lb,ub,nonlcon,options);
```

Table 8-1. General optimisation algorithm. MATLAB

8.4 Empirical Equations

Eqs. (8-1) and (8-2) show the proposed empirical equations for the frequencies of resonance of the rail (f_{rail}) and railpad (f_{railpad}). Similarly, **Eqs.** (8-3) and (8-4) present the relationships for the static amplitude A_{static}, and mid-frequencies (or track) amplitude $A_{\text{mid-freq}}$, respectively:

$$f_{\text{rail}} = f_1 E_{sg}^{0.087} E_b^{0.3} E_s^{-0.17} E_{rp}^{-0.17} \tag{8-1}$$

$$f_{\text{railpad}} = f_2 E_{rp}^{0.17} (E_r I_r)^{-0.14} m_r^{-0.26} \tag{8-2}$$

$$A_{\text{static}} = P E_{sg}^{-0.45} E_{rp}^{-0.31} (E_r I_r)^{-0.30} \tag{8-3}$$

$$A_{\text{mid-freq}} = P E_s^{-0.18} E_{rp}^{-0.59} (E_r I_r)^{-0.27} \tag{8-4}$$

where $f_1 = 320$ Hz and $f_2 = 600$ Hz are to the rail and railpad frequencies of resonance corresponding to the base permutation. Similarly, $P = 1.0$ N is the unit force magnitude; E is the Young's modulus, EI is the bending moment, and m describes the mass per unit length. Also, 'r', 'rp', 's', 'b' and 'sg', refers to the rail, railpad, sleeper, ballast and subgrade components, respectively. Note that **Eq.** (8-4) describes the average amplitude at mid-frequency ranges.

Additionally, the proposed empirical equations are strongly related to the track conditions under consideration: stiff ballasted track type excited at the rail above the sleeper, with 0.6 m support spacing, resting on a semi-infinite medium. Thus, different conditions may require further analyses.

8.5 Discussion

Figure 8-2 compares the resonance frequencies obtained through periodic simulations with those estimated values using empirical equations. Again, 'low' components refer to mechanical parameters with lower stiffness, mass and density; and 'high' to parameters with higher values. **Figure 8-2**(a) shows the error related to the frequency of resonance of the rail ($f_{\text{rail}} = f_{\text{rail},1}$). It can be seen that the minimum error (1%) is associated with the rail, the upper most track component. Alternatively, the largest errors (3-14%) is found for the remaining components, mainly those included in **Eq.** (8-1). Overall, this behaviour is expected as f_{rail} is located at low-mid frequencies (< 800 Hz), and therefore is mainly affected by lower- and mid-track layers.

Regarding the frequency of resonance of the railpad ($f_{\text{railpad}} = f_{\text{rail},2}$) – see **Figure 8-2**(b), it can be seen that the lowest error ($< 1\%$) occurs in the subgrade, embankment and ballast. These are the lower-most track layers that primarily affect low frequency ranges (< 300 Hz) and have a negligible effect at mid-frequencies ($300 - 800$ Hz), where f_{railpad} occurs. Similarly, the USP is negligible at these frequency range, yielding an error of $\approx 1\%$. Alternatively, the highest errors ($3 - 8\%$) are related to the upper-track layers: sleeper, railpad and rail, upper-track components primarily influencing mid-high frequency ranges (> 300 Hz).
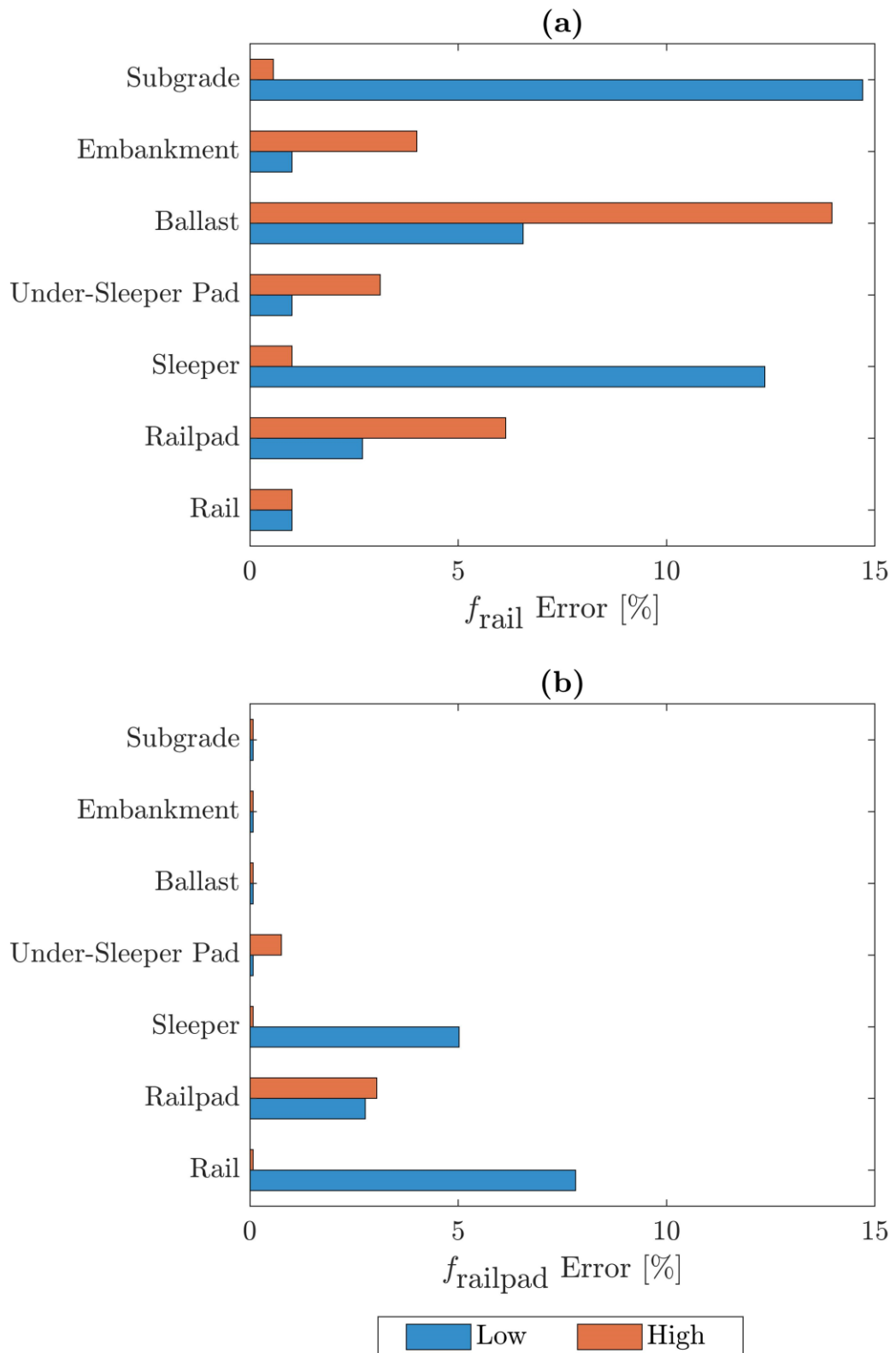
Figure 8-2. Frequencies of resonance error: (a) rail, and (b) railpad

Figure 8-3 illustrates the amplitude errors corresponding to (a) the static case ($f = 0\,Hz$) calculated from **Eq.** (8-3), and (b) the track case obtained with **Eq.** (8-4). In the first case, results show that the maximum error, of approximately 30%, corresponds to the high embankment parameter. Although the embankment layer's primary influence occurs at low frequencies ($< 300\,Hz$), its effect is not sufficient to be

included in **Eq.** (8-3) and its error remains relatively high. Excluding this value, the obtained errors are relatively low, around 1% to 12%, in the remaining components. Alternatively, **Figure 8-3**(b) shows **Eq.** (8-4) can approximate $A_\text{mid-freq}$ with a low error of approximately 1 to 5%.
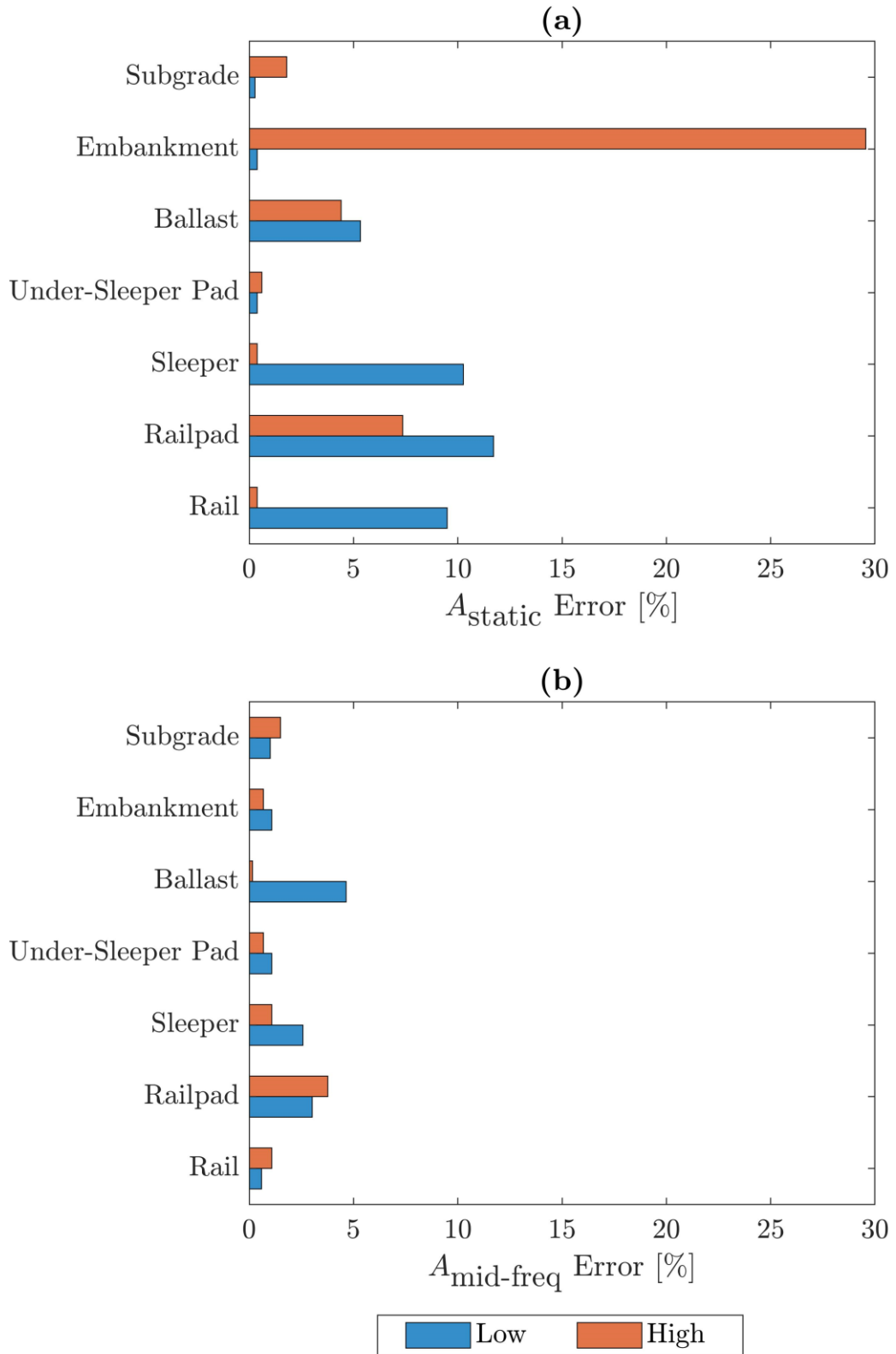
Figure 8-3. Amplitude error: (a) static, and (b) mid-frequencies

8.6 Conclusions

This Chapter introduces a three-step procedure for formulating new empirical equations for receptance applications. This procedure requires (1) the definition of initial relationships via power regression methods, (2) a selection of the most important parameters influencing the response, and (3) the formulation of the final empirical equations via optimisation techniques.

The last step is explained in detail, including the algorithm employed, which uses the multiple-objective optimisation MATLAB toolbox. Using this procedure, empirical equations for frequencies of resonance and receptance amplitudes are proposed. Then, they are compared against the values obtained via sensitivity analysis in Chapter 7, and errors are computed.

Results show that the largest errors (3-14%) related to the frequencies of resonances occur in track components with a greater impact at that frequency range. For instance, the highest errors in the railpad frequency of resonance are related to the upper-track layers: sleeper, railpad and rail, upper-track components primarily impacting mid-high frequency ranges (> 300 Hz). Alternatively, the largest error in static receptance amplitudes are associated with the embankment, a component of major importance in lower frequency ranges which is not included in the emprirical equation. .

Chapter 9

Conclusions and Future Research

9.1 Introduction

This Chapter summarises the main conclusions of the research (Section 9.2), outlines the scope and limitations (Section 9.3), and offers recommendations for future work (Section 9.4).

9.2 Conclusions

This research aims to *develop a computational tool to calculate the dynamic performance of ballasted periodic railway track structures*. To achieve this, four objectives were proposed, each leading to specific conclusions.

(1) *Conduct a review of literature of the different railway modelling strategies for continuous and periodic beams on Elastic Foundations:*
A technical review of BOEF and periodic approaches was conducted in Chapter 2 and Chapter 3, respectively. First, it is seen that the fundamental BOEF formulation, involving a continuous beam on springs-in-series, is straightforward and computationally efficient. Although BOEF can be expanded to include complex conditions like discrete supports and multi-layers, it struggles to replicate the intricate geometries of track components, mechanical behaviour, and soil wave propagation. These limitations can be overcome with FEM, a flexible numerical approach that accurately represents track-ground behaviour. However, FEM requires large domain definitions, making simulations computationally intensive. To address this,

periodic approaches exploit the repetitive nature of track structures, offering a promising alternative. Chapter 3 explores various periodic methods and highlights the fundamental periodic formulation's limitations, including: (1) restriction to fully-periodic structures, (2) potential ill-conditioning due to Eigenvalue problem definitions, and (3) limitation to non-moving excitations and the need for additional methods to address moving excitations. Among the periodic approaches reviewed, DPM can overcome all these limitations. This method has the potential to account for semi-periodic conditions, avoids Eigenvalue problems by using direct inversion, and accommodates both moving and non-moving excitations without additional techniques. Finally, the review in Chapter 2 and Chapter 3 provide insights into BOEF and periodic approaches, identifying DPM as the most suitable for railway track simulations.

(2) *Develop a 3D periodic numerical model of railway track structures subjected to static, quasi-static and dynamic excitations.*

The intricate track-ground behaviour was simulated using the DPM, as detailed in Chapter 4. This computationally efficient approach exploits the inherent periodic behaviour of railway tracks to study large structural domains via a single 3D slice. This restrained domain, also known as a reference or unit cell, was defined by considering that the material and geometrical properties of the structure are repeated by a distance d along the train passage direction. Then, the unit cell response was obtained by enforcing periodic boundary conditions defined in the Floquet's framework and performing a direct inversion of a modified system of equations of motion. Next, by assuming the cell repeats infinitely, the total response was retrieved. By combining the DPM with 3D FE techniques (3D DPM-FE), the model was able to include complex track geometries such as discrete supports and additional track components. Similarly, the model incorporated the soil's wave propagation effect via PML (3D DPM-FE-PML), further enhancing the overall simulation's computational efficiency. Regarding the excitation conditions, the DPM allowed considering both moving and non-moving excitations. For the latter, the frequency-wavenumber-speed relationship was exploited in the computation of the reference cell response; thus, no additional techniques (e.g. superposition approaches) were required. In addition, the approach could effectively replicate both, quasi-static and dynamic effects. Lastly, Chapter 5 demonstrated the accuracy of the DPM and its ability to approximate the complex dynamic track and ground response.

(3) *Optimise the new 3D periodic numerical approach for receptance calculation*

The 3D DPM-FE-PML track-ground model introduced in Chapter 4 was refined for receptance applications in Chapter 6. Two common track modelling assumptions were considered: (1) track-bed support, and (2) symmetry conditions. In the former, it was shown that the BOEF assumption ignores the wave propagation effect in the subgrade and induced errors of $\approx$ 80-300% below 200 Hz, and $\approx$ 30% between 200-440 Hz. This proved the need to include a flexible support in receptance computations. For the second assumption, it was found that the track centreline symmetry could not accurately replicate receptance testing conditions, as it ignored some track bending modes, resulting in errors of $\approx$ 20% below 1000 Hz. Similarly, this demonstrated the necessity to include non-symmetric loading conditions in receptance simulations of ballasted tracks.

(4) *Analyse the receptance characteristics of high-speed ballasted tracks.*

Using the refined track-ground model defined in Chapter 6, a sensitivity analysis of common high-speed railway ballasted track components was performed. This provided new insights into typical frequency ranges and amplitudes (Chapter 7), and a new methodology for formulating empirical equations for receptance applications (Chapter 8). This parametric study examined the effect of rail sections, railpad stiffness, sleeper material, ballast stiffness and thickness, embankment depth, and subgrade stiffness. Results show that while some track layers' influence extends into the mid-frequency range ($300 - 800$ Hz), the lower track components dominate the lower frequencies (< 300 Hz), and the upper track components dominate the higher frequencies (> 800 Hz). Similarly, the sensitivity study evidenced that flexible track components exhibit larger amplitudes while stiffer components yield lower magnitudes. Additionally, the tree-step procedure proposed to derive empirical equations proved to be effective, with a maximum error of 3-14% for resonance frequencies and 30% for receptance amplitudes. . Overall, this information enables the identification and resolution of specific railway issues by adjusting the mechanical parameters of track components. Ultimately, it allows for the optimisation of the design and maintenance operations of the railway system, leading to an improved overall system response.

9.3 Scope and limitations of the thesis

The following are the limitations identified in this thesis:

(1) *Periodic behaviour*. Although the selected periodic approach can potentially incorporate semi-periodic conditions, this research only considers a track-ground model with constant behaviour (material and geometrical properties) along the periodic direction, i.e. a fully-periodic track structure.

(2) *Mechanical properties*. The selected track properties employed in the main analysis correspond to a stiff track supported by well-compacted earthworks, characteristic of a modern high-speed track. Additionally, the mechanical properties for each track component defined in the periodic formulation are the same in all directions, i.e. isotropic material.

(3) *Railway track type*. The 3D periodic approach can easily replicate both ballasted and slab track types. However, this research only addresses the analysis of the former case.

(4) *Subgrade conditions*. A multi-layer subgrade domain can be included in the periodic model; however, this thesis limits the track-bed support to a homogeneous half-space medium only.

9.4 Recommendations for future work

The following recommendations aim to improve the development of the computational tool for calculating the dynamic performance of periodic railway track structures:

(1) *Modelling techniques.* Investigate advanced modelling techniques to incorporate semi-periodic material and geometrical properties, allowing for the consideration of transition zone conditions.

(2) *Mechanical parameters.* Expand the range of mechanical parameters studied to capture more diverse track behaviour under different conditions. For instance, incorporate anisotropic and non-linear material conditions. This could potentially allow for the incorporation of environmental factors, such as temperature variations and moisture content.

(3) *Railway track type.* The dynamic performance of slab tracks can be studied via the proposed periodic model. This can be easily achieved due to the simulation flexibility provided by the FEM coupled to the DPM.

(4) *Subgrade conditions.* Similarly, multi-layered subgrade domains can be incorporated into the simulation, providing a more realistic representation of the track-bed support behaviour.

(5) *Further analysis.* Although this thesis aims to compute dynamic performance via receptance applications, this assessment can be expanded by studying other railway engineering issues, such as long-term deformations, i.e. settlement. This broader approach allows for more accurate predictions of maintenance needs and the structure's lifespan.

Appendix A

BOEF Models

Figure A-1 shows the ballasted and slab track models employed in applications no.1 and no. 2 presented in Chapter 2.

(a)

(b)
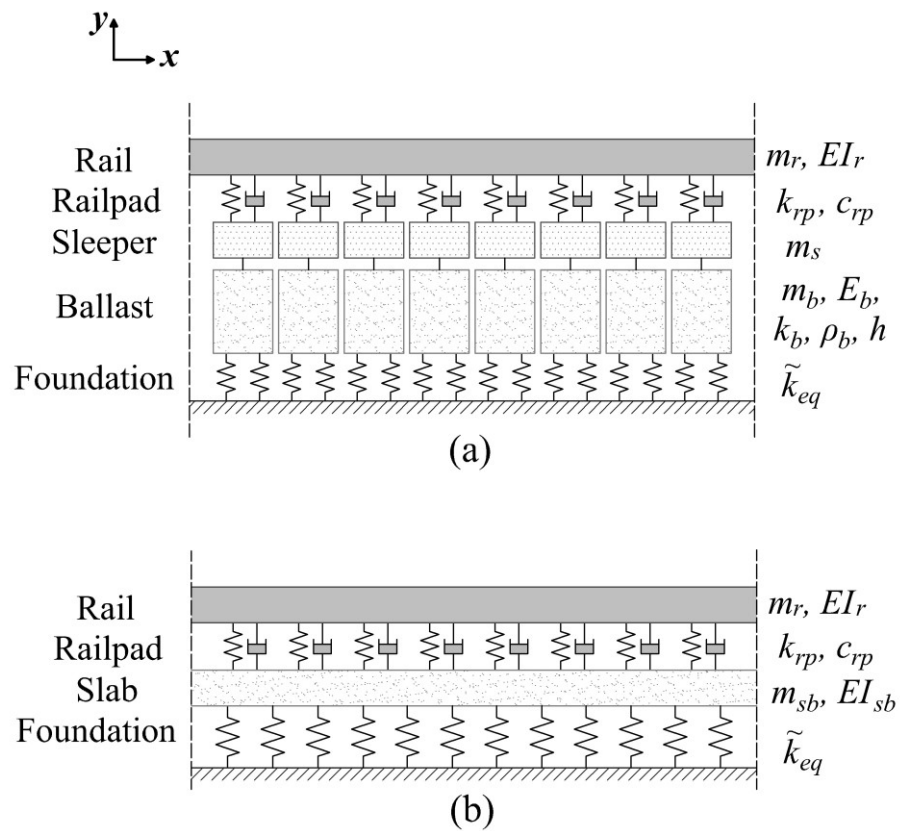
Figure A-1. BOEF models: (a) ballasted track models, and (b) slab track models

Eq. (A-1) describes the dynamic equation of motion in wavenumber-frequency-domain defined in all track models, where $[D]$ is the Dynamic Stiffness Matrix (DSM), $\{\tilde{u}\}$ is the vector of displacements, and $\{\tilde{F}\}$ is the vector of applied forces.

$$[\tilde{D}]\{\tilde{u}\} = \{\tilde{F}\} \tag{A-1}$$

In the case of ballasted tracks, DSM is depicted by **Eq.** (A-2):

$$
[\widetilde{D}]_{\text{Ballast}}^{\text{Model}}
= \begin{bmatrix}
E_r I_r \beta_x^4 - \omega m_r + k_{rp}^* & -k_{rp}^* & 0 \\
-k_{rp}^* & k_{rp}^* + k_{b,1}^{\text{Model}} - \omega^2 m_s & -k_{b,2}^{\text{Model}} \\
0 & -k_{b,2}^{\text{Model}} & k_{b,2}^{\text{Model}} + \tilde{k}_{eq}
\end{bmatrix}
\tag{A-2}
$$

where $k_{b,j}^{\text{Model}}$ are the stiffness components ($j = 1,2$) related to the ballast model defined by Alves Costa (Model=AC) or Sheng (Model=Sh), as shown in **Eqs.** (A-3) and (A-4), respectively:

$$
k_{b,1}^{\text{AC}} = \frac{2\omega E_b d\alpha}{\tan\left(\frac{\omega}{C_b} h_b\right) C_b}, \qquad
k_{b,2}^{\text{AC}} = \frac{2\omega E_b d\alpha}{\sin\left(\frac{\omega}{C_b} h_b\right) C_b}
\tag{A-3}
$$

$$
k_{b,1}^{\text{Sh}} = k_b - \omega^2 \frac{m_b}{3}, \qquad
k_{b,2}^{\text{Sh}} = k_b + \omega^2 \frac{m_b}{6}
\tag{A-4}
$$

Alternatively, the DSM for the slab track model is presented in **Eq.** (A-5):

$$
[\widetilde{D}]_{\text{Slab}}
= \begin{bmatrix}
E_r I_r \beta_x^4 - \omega m_r + k_{rp}^* & -k_{rp}^* \\
-k_{rp}^* & E_{sb} I_{sb} \beta_x^4 - \omega m_{sb} + k_p^* + \tilde{k}_{eq}
\end{bmatrix}
\tag{A-5}
$$

Appendix B

DPM Compatibilisation Example

This Section presents an example aiming to clarify the compatibilisation procedure required in the DPM. For this, the three-node BOEF reference cell of thickness d shown in **Figure B-1** is considered. **Eq.** (B-1) depicts the space vector of the reference cell in the longitudinal or periodic direction $\tilde{x}$:

$$\tilde{x} = [\tilde{x}_1, \tilde{x}_2, \tilde{x}_3]^T = [0, d/2, d]^T \tag{B-1}$$
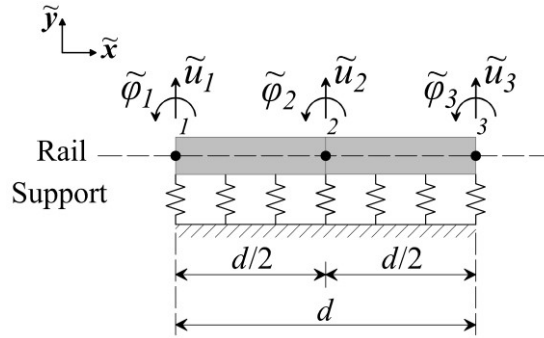
Figure B-1. Three-node reference cell of length d

where $\tilde{u}_j$ and $\tilde{\varphi}_j$ are the displacements and rotations at node $j = 1,2,3$. Next, the initial equation of motion system is defined and expanded:

$$\begin{bmatrix} \widetilde{D}_{1,1} & \widetilde{D}_{1,2} & \widetilde{D}_{1,3} & \widetilde{D}_{1,4} & \widetilde{D}_{1,5} & \widetilde{D}_{1,6} \\ \widetilde{D}_{2,1} & \widetilde{D}_{2,2} & \widetilde{D}_{2,3} & \widetilde{D}_{2,4} & \widetilde{D}_{2,5} & \widetilde{D}_{2,6} \\ \widetilde{D}_{3,1} & \widetilde{D}_{3,2} & \widetilde{D}_{3,3} & \widetilde{D}_{3,4} & \widetilde{D}_{3,5} & \widetilde{D}_{3,6} \\ \widetilde{D}_{4,1} & \widetilde{D}_{4,2} & \widetilde{D}_{4,3} & \widetilde{D}_{4,4} & \widetilde{D}_{4,5} & \widetilde{D}_{4,6} \\ \widetilde{D}_{5,1} & \widetilde{D}_{5,2} & \widetilde{D}_{5,3} & \widetilde{D}_{5,4} & \widetilde{D}_{5,5} & \widetilde{D}_{5,6} \\ \widetilde{D}_{6,1} & \widetilde{D}_{6,2} & \widetilde{D}_{6,3} & \widetilde{D}_{6,4} & \widetilde{D}_{6,5} & \widetilde{D}_{6,4} \end{bmatrix} \begin{Bmatrix} \tilde{u}_1 \\ \tilde{\varphi}_1 \\ \tilde{u}_2 \\ \tilde{\varphi}_2 \\ \tilde{u}_3 \\ \tilde{\varphi}_3 \end{Bmatrix} = \begin{Bmatrix} \tilde{F}_1 \\ \widetilde{M}_1 \\ \tilde{F}_2 \\ \widetilde{M}_2 \\ \tilde{F}_3 \\ \widetilde{M}_3 \end{Bmatrix} \tag{B-2}$$

where $\tilde{F}_j$ and $\widetilde{M}_j$ are the forces and moments at node j. Similarly, $\widetilde{D}_{k,l}$ are the components of the Dynamic Stiffness Matrix (DSM), with degrees-of-freedom $k = l = 1,2, \dots ,6$.

Compatibilisation procedure requires the identification of the back, front and internal nodes. For this example, the back node is the number 1 (with degrees-of-freedom 1 and 2), and the front node is the number 3 (with degrees-of-freedom 5 and 6). Alternatively, node number 2 is the internal node (degrees-of-freedom 3 and 4). Once the nodes are identified, DSM is rearranged as shown in **Eq**. (B-3):

$$
[\widetilde{D}^*] =
\begin{bmatrix}
\widetilde{D}^*_{1,1} & \widetilde{D}^*_{1,2} & \widetilde{D}^*_{1,3} & \widetilde{D}^*_{1,4} & \widetilde{D}^*_{1,5} & \widetilde{D}^*_{1,6} \\
\widetilde{D}^*_{2,1} & \widetilde{D}^*_{2,2} & \widetilde{D}^*_{2,3} & \widetilde{D}^*_{2,4} & \widetilde{D}^*_{2,5} & \widetilde{D}^*_{2,6} \\
\widetilde{D}_{3,1} & \widetilde{D}_{3,2} & \widetilde{D}_{3,3} & \widetilde{D}_{3,4} & \widetilde{D}_{3,5} & \widetilde{D}_{3,6} \\
\widetilde{D}_{4,1} & \widetilde{D}_{4,2} & \widetilde{D}_{4,3} & \widetilde{D}_{4,4} & \widetilde{D}_{4,5} & \widetilde{D}_{4,6} \\
\widetilde{D}_{5,1} & \widetilde{D}_{5,2} & \widetilde{D}_{5,3} & \widetilde{D}_{5,4} & \widetilde{D}_{5,5} & \widetilde{D}_{5,6} \\
\widetilde{D}_{6,1} & \widetilde{D}_{6,2} & \widetilde{D}_{6,3} & \widetilde{D}_{6,4} & \widetilde{D}_{6,5} & \widetilde{D}_{6,4}
\end{bmatrix}
\tag{B-3}
$$

where the upper script '*' correspond to the modified components. **Eq.** (B-4) shows the modification related to the first row in **Eq.** (B-3):

$$\widetilde{D}^*_{1,1} = \widetilde{D}_{1,1} + \widetilde{D}_{5,1}e^{-id\beta_x}$$

$$\widetilde{D}^*_{1,2} = \widetilde{D}_{1,2} + \widetilde{D}_{5,2}e^{-id\beta_x}$$

$$\widetilde{D}^*_{1,3} = \widetilde{D}_{1,3} + \widetilde{D}_{5,3}e^{-id\beta_x}$$

$$\widetilde{D}^*_{1,4} = \widetilde{D}_{1,4} + \widetilde{D}_{5,4}e^{-id\beta_x} \tag{B-4}$$

$$\widetilde{D}^*_{1,5} = \widetilde{D}_{1,5} + \widetilde{D}_{5,5}e^{-id\beta_x}$$

$$\widetilde{D}^*_{1,6} = \widetilde{D}_{1,6} + \widetilde{D}_{5,6}e^{-id\beta_x}$$

Note that **Eq.** (B-4) can be expressed via **Eq.** (B-5):

$$
D^*_{L,k} = \widetilde{D}_{L,k} + \widetilde{D}_{R,k}e^{-id\beta_x},
\begin{cases}
L = 1,2 \\
R = 5,6 \\
k = 1,2,3,4,5,6
\end{cases}
\tag{B-5}
$$

where sub indices L and R are the degrees-of-freedom related to the back (or left-side) and front (or right-side) nodes, respectively; and k indicates all degrees-of-freedom. Next, periodic conditions – see **Eq**. (4-2), are enforced and the DSM is again modified, as described in **Eq.** (B-6):

$$
[\widetilde{D}^{**}] =
\begin{bmatrix}
\widetilde{D}^*_{11} & \widetilde{D}^*_{12} & \widetilde{D}^*_{13} & \widetilde{D}^*_{14} & \widetilde{D}^*_{15} & \widetilde{D}^*_{16} \\
\widetilde{D}^*_{21} & \widetilde{D}^*_{22} & \widetilde{D}^*_{23} & \widetilde{D}^*_{24} & \widetilde{D}^*_{25} & \widetilde{D}^*_{26} \\
\widetilde{D}_{31} & \widetilde{D}_{32} & \widetilde{D}_{33} & \widetilde{D}_{34} & \widetilde{D}_{35} & \widetilde{D}_{36} \\
\widetilde{D}_{41} & \widetilde{D}_{42} & \widetilde{D}_{43} & \widetilde{D}_{44} & \widetilde{D}_{45} & \widetilde{D}_{46} \\
-e^{ik_1d} & 0 & 0 & 0 & 1 & 0 \\
0 & -e^{ik_1d} & 0 & 0 & 0 & 1
\end{bmatrix}
\tag{B-6}
$$

Similarly, the force vector is rearranged according to **Eq.** (B-7):

$$\{\tilde{F}^*\} = \begin{Bmatrix} \tilde{F}_1 + \tilde{F}_3 \\ \tilde{M}_1 + \tilde{M}_3 \\ \tilde{F}_2 \\ \tilde{M}_2 \\ 0 \\ 0 \end{Bmatrix} \approx \begin{Bmatrix} 2\tilde{F}_1 \\ 2\tilde{M}_1 \\ \tilde{F}_2 \\ \tilde{M}_2 \\ 0 \\ 0 \end{Bmatrix} \tag{B-7}$$

Finally, the rearranged set of equilibrium equations can be defined through **Eq**. (B-8):

$$\left[\tilde{D}^{**}_{n=0}(\beta_x, \omega)\right]\{\tilde{u}_{n=0}(\beta_x, \omega)\} = \{\tilde{F}^*(\beta_x)\}$$

$$\left[\tilde{D}^{**}_{n=0}(\beta_x, \omega)\right] = \begin{bmatrix} \tilde{D}^*_{11} & \tilde{D}^*_{12} & \tilde{D}^*_{13} & \tilde{D}^*_{14} & \tilde{D}^*_{15} & \tilde{D}^*_{16} \\ \tilde{D}^*_{21} & \tilde{D}^*_{22} & \tilde{D}^*_{23} & \tilde{D}^*_{24} & \tilde{D}^*_{25} & \tilde{D}^*_{26} \\ \tilde{D}_{31} & \tilde{D}_{32} & \tilde{D}_{33} & \tilde{D}_{34} & \tilde{D}_{35} & \tilde{D}_{36} \\ \tilde{D}_{41} & \tilde{D}_{42} & \tilde{D}_{43} & \tilde{D}_{44} & \tilde{D}_{45} & \tilde{D}_{46} \\ -e^{ik_1 d} & 0 & 0 & 0 & 1 & 0 \\ 0 & -e^{ik_1 d} & 0 & 0 & 0 & 1 \end{bmatrix},$$

$$\{\tilde{u}_{n=0}(\beta_x, \omega)\} = \begin{Bmatrix} \tilde{u}_1 \\ \tilde{\varphi}_1 \\ \tilde{u}_2 \\ \tilde{\varphi}_2 \\ \tilde{u}_3 \\ \tilde{\varphi}_3 \end{Bmatrix}, \quad \{\tilde{F}^*(\beta_x)\} = \begin{Bmatrix} 2\tilde{F}_1 \\ 2\tilde{M}_1 \\ \tilde{F}_2 \\ \tilde{M}_2 \\ 0 \\ 0 \end{Bmatrix} \tag{B-8}$$

Note that the last 2 rows of the problem shown in **Eq**. (B-8) gives the following two equilibrium equations:

$$-\tilde{u}_1 e^{id\beta_x} + 0\tilde{\varphi}_1 + 0\tilde{u}_2 + 0\tilde{\varphi}_2 + 1\tilde{u}_3 + 0\tilde{\varphi}_3 = 0$$
$$\Longrightarrow -e^{id\beta_x}\tilde{u}_1 + \tilde{u}_3 = 0 \tag{B-9}$$
$$\Longrightarrow u_3 = e^{id\beta_x}\tilde{u}_1$$

$$0\tilde{u}_1 - \tilde{\varphi}_1 e^{id\beta_x} + 0\tilde{u}_2 + 0\tilde{\varphi}_2 + 0\tilde{u}_3 + 1\tilde{\varphi}_3 = 0$$
$$\Longrightarrow -\tilde{\varphi}_1 e^{id\beta_x} + \tilde{\varphi}_3 = 0 \tag{B-10}$$
$$\Longrightarrow \tilde{\varphi}_3 = \tilde{\varphi}_1 e^{id\beta_x}$$

where the periodic conditions in **Eq**. (4-2) are enforced in **Eq**. (B-11):

$$\{\tilde{u}^{\text{front}}_{n=0}\} = \{\tilde{u}^{\text{back}}_{n=0}\}e^{id\beta_x} \tag{B-11}$$

in this case, displacements at the back and the front of the reference cell are $\{\tilde{u}^{\text{back}}_{n=0}\} = [\tilde{u}_1, \tilde{\varphi}_1]^T$ and $\{\tilde{u}^{\text{front}}_{n=0}\} = [\tilde{u}_3, \tilde{\varphi}_3]^T$, respectively.

Appendix C
DPM Steady-State Assumption

The track response follows the steady-state or forced (or non-transient) response assumption, in which the solution is obtained from a constant or periodic force [68,70,112]. This allows for the simplification of the response computation since the solution can be decomposed into a space-wavenumber and time-wavenumber components, as described in **Eq.** (C-1):

$$\bar{u}(x, \beta_x, t) = [\tilde{u}(x, \beta_x)]e^{i\omega t} \tag{C-1}$$

where $\bar{u}$ is the total structure's deflection in the wavenumber-time-domain.

By combining the steady-state assumption from **Eq.** (C-1) with the periodic response in **Eq.** (4-22), it is possible to express the total time-domain response in terms of **Eq.** (C-2):

$$\bar{u}(x, y, z, \beta_x, t) = [\tilde{u}(x, y, z, \beta_x)]e^{i\omega t} \tag{C-2}$$

where $\tilde{u}$ and $\bar{u}$ is the displacement of the total structure (i.e. $\tilde{u} = \tilde{u}_n$ and $\bar{u} = \bar{u}_n$) in the wavenumber-domain and the wavenumber-time-domain.

C.1 Moving Quasi-Static Contribution

Under moving force conditions, $\bar{u}$ is harmonic with frequency $\omega = \varpi - \beta_x v$. Thus, **Eq.** (C-2) can be expressed as:

$$
\begin{aligned}
\bar{u}(x &= \tilde{x} + nd, y = \tilde{y}, z = \tilde{z}, \beta_x, t) \\
&= [\tilde{u}_{n=0}(\tilde{x}, \tilde{y}, \tilde{z}, \beta_x)e^{ind\beta_x}]e^{i(\omega = \varpi - \beta_x v)t}
\end{aligned} \tag{C-3}
$$

Next, the total structure's response in **Eq.** (C-3) can be transformed back to the space-domain by means of the inverse Fourier transformation – see **Eq.** (4-24), as depicted in **Eq.** (C-4):

$$u(x, y, z, t) = \frac{1}{2\pi} \int_{-\infty}^{+\infty} \left[\tilde{u}_{n=0}(\tilde{x}, \tilde{y}, \tilde{z}, \beta_x)e^{ind\beta_x}\right]e^{i(\omega=\varpi-\beta_x v)t}\mathrm{d}\beta_x \qquad \text{(C-4)}$$

Rearrangement of **Eq**. (C-4) allows to take the exponential $e^{i\varpi t}$ out of the wavenumber-domain integral, as shown in **Eq.** (C-5):

$$\begin{aligned}
u(x, y, z, t) &= \frac{1}{2\pi} \int_{-\infty}^{+\infty} \left[\tilde{u}_{n=0}(\tilde{x}, \tilde{y}, \tilde{z}, \beta_x)e^{ind\beta_x}\right]e^{i(\varpi-\beta_x v)t}\mathrm{d}\beta_x \\
&= \frac{1}{2\pi} \int_{-\infty}^{+\infty} \tilde{u}_{n=0}(\tilde{x}, \tilde{y}, \tilde{z}, \beta_x)e^{i(nd-vt)\beta_x}e^{i\varpi t}\mathrm{d}\beta_x \qquad \text{(C-5)}\\
&= \left[\frac{1}{2\pi} \int_{-\infty}^{+\infty} \tilde{u}_{n=0}(\tilde{x}, \tilde{y}, \tilde{z}, \beta_x)e^{i(nd-vt)\beta_x}\,\mathrm{d}\beta_x\right]e^{i\varpi t}
\end{aligned}$$

Note that the term in brackets in **Eq.** (C-5) is the Fourier transform of $u(x, y, z, \beta_x)$. Then, by denoting this term as u^*, **Eq.** (C-5) can be simplified into **Eq.** (C-6):

$$u(x, y, z, t) = [u^*(nd - vt), y, z]e^{i\varpi t}$$

$$\Rightarrow u^*(nd - vt, y, z) = \frac{1}{2\pi} \int_{-\infty}^{+\infty} \tilde{u}_{n=0}(\tilde{x}, \tilde{x}, \tilde{y}, \tilde{z}, \beta_x)e^{i(nd-vt)\beta_x}\mathrm{d}\beta_x \qquad \text{(C-6)}$$

Note that the exponential component within the integral of **Eqs.** (C-5) and (C-6), is similar to the definition of the moving reference frame μ described in **Eq.** (C-7):

$$\mu = x_0 - vt \approx nd - vt = x^* - vt \qquad \text{(C-7)}$$

where $x^* = nd$, the length of the structure at the nth cell, is analogous to the observation point x_0. Thus, the total deflection in space-time-domain can be defined by **Eq**. (C-8):

$$u(x, y, z, t) = [u^*(\mu, y, z)]e^{i\varpi t} \qquad \text{(C-8)}$$

By combining the moving reference definition μ with the speed-space-time relationship in **Eq.** (C-9), it is possible to compute the response at a specific position of the structure x_0 or instant of time t_0, rather than computing the response at each space and time values – see **Eq.** (C-10). When computing at x_0, a time-domain response is obtained, i.e. $u(x = x_0, t)$, and $\mu = \mu_1$. Alternatively, in the case of a time instant t_0, the solution is computed in the space-domain, i.e. $u(x, t = t_0)$, and $\mu = \mu_2$. Thus, depending on the problem purpose, the total structure's deflection computation in space-time-domain can be further simplified.

$$t = \frac{x}{v} = \frac{\tilde{x} + nd}{v} = \frac{\tilde{x} + x^*}{v} \qquad \text{(C-9)}$$

$$\mu = \begin{cases} \mu_1 = x_0 - vt \\ \mu_2 = x - vt_0 \end{cases} \qquad \text{(C-10)}$$

However, since the response calculation is based on a periodic assumption which implies the use of the exponential $e^{ind\beta_x}$ to retrieve the results at the total structural level – see **Eq.** (4-16), this condition must strictly be followed. This implies that nd must be positive in the exponential and the moving reference frame μ; thus, **Eq.** (C-8) must be slightly modified. **Eq.** (C-11) shows the moving reference frame required in the periodic methodology, μ_{Periodic}, for the time and space-domain cases: μ_1 and μ_2, respectively:

$$\mu_{\text{Periodic}} = \begin{cases} \mu_1 = x_0 + vt^* = x_0 + v\dfrac{x^*}{v} = x_0 + v\dfrac{nd}{v} = x_0 + nd \\ \mu_2 = x^* - vt_0 = nd - vt_0 \end{cases} \tag{C-11}$$

where $t^* = x^*/v$ is the modified time value. Regarding the modification in the total response, when computing the result in the time-domain, i.e. $u(x_0, t)$, the time vector must be flipped – this is easily done by making negative the second exponential term. **Eqs.** (C-12) and (C-13) show the track response in time and space-domain, respectively.

$$u(x_0, t) = \left[\frac{1}{2\pi} \int_{-\infty}^{+\infty} \tilde{u}_{n=0}(\tilde{x}, \beta_x) e^{i(\mu_1)\beta_x} d\beta_x \right] e^{-i\varpi t} \tag{C-12}$$

$$u(x, t_0) = \left[\frac{1}{2\pi} \int_{-\infty}^{+\infty} \tilde{u}_{n=0}(\tilde{x}, \beta_x) e^{i(\mu_2)\beta_x} d\beta_x \right] e^{+i\varpi t} \tag{C-13}$$

C.2 Moving Dynamic Contribution

The steady-state definition can be extended to moving dynamic contributions. For this, the dynamic component of the deflection can be described by **Eq.** (C-14). Note that only periodic direction axis x is shown for visibility.

$$\begin{aligned} \bar{u}^{\text{dyn}}\left(x = \tilde{x} + nd, \beta_x, t, \varpi_j\right) \\ = \left[\tilde{u}^{\text{dyn}}\left(x = \tilde{x} + nd, \beta_x, \varpi_j\right) \right] e^{i(\omega = \varpi_j - \beta_x v)t} \end{aligned} \tag{C-14}$$

where $\bar{u}^{\text{dyn}}$ is the dynamic response of the track in the wavenumber-time-domain for the jth harmonic. Similarly to the quasi-static case, the space-time-domain response of the structure can be obtained at x_0 and t_0 with **Eqs.** (C-15) and (C-16), respectively:

$$u^{\text{dyn}}(x_0, t) = \sum_{\varpi_j = \varpi_1}^{\varpi_j = \varpi_{\text{end}}} \left[\left(\frac{1}{2\pi} \int_{-\infty}^{+\infty} \tilde{u}_{n=0}^{\text{dyn}}(\tilde{x}, \beta_x) e^{i\mu_1 \beta_x} d\beta_x \right) e^{-i\varpi_j t} \right] \tag{C-15}$$

$$u^{\text{dyn}}(x, t_0) = \sum_{\varpi_j=\varpi_1}^{\varpi_j=\varpi_{\text{end}}} \left[\left(\frac{1}{2\pi} \int_{-\infty}^{+\infty} \tilde{u}_{n=0}^{\text{dyn}}(\tilde{x}, \beta_x) e^{i\mu_2\beta_x} \, \mathrm{d}\beta_x \right) e^{+i\varpi_j t} \right] \qquad \text{(C-16)}$$

In both cases, the moving reference frame μ is defined in **Eq.** (C-11). Note that the total result is obtained by summing up the individual contribution of each harmonic ϖ_j.

Appendix D
Vehicle Matrices

When considering the ten-degree-of-freedom multi-body model – see **Figure 2-9**, the dynamic force in **Eq.** (4-43), can be computed via:

$$\{\hat{F}^{\mathrm{dyn}}(\varpi_j)\} = -\left[[V_H] + [\hat{C}^V(\varpi_j)] + [\hat{C}^T(\varpi_j)]\right]^{-1} \{\hat{r}(\varpi_j)\} \tag{D-1}$$

where $[V_H]$ is the contact flexibility matrix – see **Eq.** (D-2), $[\hat{C}^V(\varpi_j)]$ is the vehicle compliance matrix – see **Eq.** (D-3), and $[\hat{C}^T(\varpi_j)]$ is the compliance of the track – see **Eq.** (D-4).

$$[V_H] = \frac{1}{K_{Hz}} \begin{bmatrix} 1 & 1 & 1 & 1 & 1 \\ 1 & 1 & 1 & 1 & 1 \\ 1 & 1 & 1 & 1 & 1 \\ 1 & 1 & 1 & 1 & 1 \end{bmatrix} \tag{D-2}$$

$$[\hat{C}^V(\varpi_j)] = [Z]\left[[K^v] - \varpi_j^2 [M^v]\right]^{-1} [Z]^T \tag{D-3}$$

$$[\hat{C}_{m,k}^T(\varpi_j)] = \frac{1}{2\pi} \int_{-\infty}^{+\infty} \tilde{u}_c^{Green}(\beta_x, \omega = \varpi_j - \beta_x v) e^{-i(a_m - a_k)\beta_x} \, d\beta_x \tag{D-4}$$

in which the track compliance $[\hat{C}_{m,k}^T(\varpi_j)]$ is a $(m \times k)$ matrix, where m and k are the axle positions, as described in **Eq.** (4-41). $[Z]$ is the constant matrix with zeros and ones, $[M^v]$ is the mass matrix of the vehicle, and $[K^v]$ is the stiffness matrix of the vehicle, as shown in **Eqs.** (D-5)-(D-7), respectively:

$$[Z] = \begin{bmatrix} 0 & 0 & 0 & 0 & 0 & 0 & 1 & 0 & 0 & 0 \\ 0 & 0 & 0 & 0 & 0 & 0 & 0 & 1 & 0 & 0 \\ 0 & 0 & 0 & 0 & 0 & 0 & 0 & 0 & 1 & 0 \\ 0 & 0 & 0 & 0 & 0 & 0 & 0 & 0 & 0 & 1 \end{bmatrix} \tag{D-5}$$

$$[M^v] = \begin{bmatrix} M_{cb} & 0 & 0 & 0 & 0 & 0 & 0 & 0 & 0 & 0 \\ 0 & J_{cb} & 0 & 0 & 0 & 0 & 0 & 0 & 0 & 0 \\ 0 & 0 & M_b & 0 & 0 & 0 & 0 & 0 & 0 & 0 \\ 0 & 0 & 0 & J_b & 0 & 0 & 0 & 0 & 0 & 0 \\ 0 & 0 & 0 & 0 & M_b & 0 & 0 & 0 & 0 & 0 \\ 0 & 0 & 0 & 0 & 0 & J_b & 0 & 0 & 0 & 0 \\ 0 & 0 & 0 & 0 & 0 & 0 & M_w & 0 & 0 & 0 \\ 0 & 0 & 0 & 0 & 0 & 0 & 0 & M_w & 0 & 0 \\ 0 & 0 & 0 & 0 & 0 & 0 & 0 & 0 & M_w & 0 \\ 0 & 0 & 0 & 0 & 0 & 0 & 0 & 0 & 0 & M_w \end{bmatrix} \tag{D-6}$$

$$[K^v] =$$

$$
\begin{bmatrix}
2K_2 & 0 & -K_2 & 0 & -K_2 & 0 & 0 & 0 & 0 & 0 \\
0 & 2K_2 l_b^2 & -K_2 l_b & 0 & K_2 l_b & 0 & 0 & 0 & 0 & 0 \\
-K_2 & -K_2 l_b & K_2 + 2K_1 & 0 & 0 & 0 & -K_1 & -K_1 & 0 & 0 \\
0 & 0 & 0 & 2K_1 l_w^2 & 0 & 0 & -K_1 l_w & K_1 l_w & 0 & 0 \\
-K_2 & K_2 l_b & 0 & 0 & K_2 + 2K_1 & 0 & 0 & 0 & -K_1 & -K_1 \\
0 & 0 & 0 & 0 & 0 & 2K_1 l_w^2 & 0 & 0 & -K_1 l_w & K_1 l_w \\
0 & 0 & -K_1 & -K_1 l_w & 0 & 0 & K_1 & 0 & 0 & 0 \\
0 & 0 & -K_1 & K_1 l_w & 0 & 0 & 0 & K_1 & 0 & 0 \\
0 & 0 & 0 & 0 & -K_1 & -K_1 l_w & 0 & 0 & K_1 & 0 \\
0 & 0 & 0 & 0 & -K_1 & K_1 l_w & 0 & 0 & 0 & K_1
\end{bmatrix}
\quad \text{(D-7)}
$$

where M_{cb}, M_b and M_w are the masses of the car body, bogie, and wheelset, respectively; J_{cb} is the rotational inertia of the car body, and J_b is the rotational inertia of the bogie. Similarly, K_1 and K_2 are the complex stiffness of the primary and secondary suspension system, respectively; l_b is half the distance between the centres of gravity of bogies, and l_w is half the wheelbase sharing the same bogie. Note that K_1 and K_2 are complex stiffness defined via the stiffness $k_{1,2}$ and damping $c_{1,2}$ values of their primary and secondary suspension, as defined in **Eq.** (D-8):

$$c_{1,2} = k_{1,2} + i\varpi c_{1,2} \qquad \text{(D-8)}$$

Appendix E
DPM Verifications

This Section describes the material and geometrical properties employed in the verification cases presented in Chapter 5. **Table E-1** and **Table E-2** show the track properties and mesh information related to case 1 and 2. Similarly, **Table E-3** and **Table E-4** describe the track and train properties for case 3, respectively.

Component	Parameter		Unit	3D Periodic	2.5D	3D FEM
Track (Half)	Gauge (half)	l_0	m	0.7	0.7	0.7
	Length	d		0.6	-	27
Rail[1] (Single)	Element type	-	-	Linear solid	Beam	Cubic solid
	Height	$l_{r,y}$	m	0.218	0.218	0.218
	Width	$l_{r,z}$	m	0.035	0.035	0.035
	Second moment of Inertia	I_r	m^4	3.022E-05	3.022E-05	3.022E-05
	Density	ρ_r	kg/m^3	7850	7850	7850
	Loss factor	η_r		0	0	-
	Rayleigh damping	α_r	-	-	-	0.00197
		β_r	-	-	-	2.97E-4
	Young's modulus	E_r	N/m^2	2.1E11	2.1E11	2.1E11
	Poisson's ratio	ν_r	-	0.3	0.3	0.3
Railpad[2] (Single)	Element type	-	-	Linear solid	Spring	Cubic solid
	Height	$l_{rp,x}$	m	0.01	-	0.01
	Width (half)	$l_{rp,y}$	m	0.035	-	0.035
	Density	ρ_{rp}	kg/m^3	1000	-	1000
	Loss factor	η_{rp}	-	0.17	-	-
	Viscous damping	c_{rp}	Ns^2/m	-	15E3	-
	Rayleigh damping	α_{rp}	-	-	-	0.0825
		β_{rp}	-	-	-	1.1E-4
	Young's modulus	E_{rp}	N/m^2	3.81E7	-	3.81E7
	Stiffness per unit length	k_{rp}	N/m^2	-	133.33E6	-
	Poisson's ratio	ν_{rp}	-	0	-	0
Track Layer 1[3] (Half)	Element type	-	-	Linear solid	Cubic solid	Cubic solid
	Height	$l_{1,y}$	m	0.3	0.3	0.3
	Width	$l_{1,z}$	m	1.75	1.75	1.75
	Density	ρ_1	kg/m^3	2400	2400	2400
	Loss factor	η_1	-	0.01	0.01	-

	Rayleigh damping	α_1	-	-	-	0.0025
		β_1	-	-	-	1E-5
	Young's modulus	E_1	N/m^2	3E10	3E10	3E10
	Poisson's ratio	ν_1	-	0.2	0.2	0.2
Track Layer 2[4] (Half)	Element type	-	-	Linear solid	Cubic solid	Cubic solid
	Height	$l_{2,y}$	m	0.4	0.4	0.4
	Width	$l_{2,z}$	m	2.5	2.5	2.5
	Density	ρ_2	kg/m^3	2000	2000	2000
	Loss factor	η_2	-	0.08	0.08	-
	Rayleigh damping	α_2	-	-	-	0.462
		β_2	-	-	-	8E-5
	Young's modulus	E_2	N/m^2	2E8	2E8	2E8
	Poisson's ratio	ν_2	-	0.35	0.35	0.35

Track parameters obtained or derived from: [1][269], [2][265,270–274], [3][23,222,275], [4][12,29,136,271,276]

Table E-1. Track properties. Validation case 1 and 2: Track dynamics

Note that in the case of the railpad, the Poisson's ratio ν_{rp} significantly increases its stiffness in the vertical direction [18,29]. Thus, the equivalent vertical Young's modulus depends can be derived according:

$$E_{rp} = \frac{k_{rp}l_{rp,y}\left(1 + \nu_{rp}\right)\left(1 - 2\nu_{rp}\right)}{l_{rp,x}l_{rp,z}\left(1 - \nu_{rp}\right)} \tag{E-1}$$

However, in order to facilitate the comparison between models (springs and dampers in 2.5D and soil elements in the Periodic and 3D FE simulations), ν_{rp} is assumed zero. Additionally, for this particular verification, the track supports are assumed continuous, therefore, k_{rp} corresponds to a continuous stiffness per unit length $l_{rp,z} = 1$. Thus, **Eq.** (E-1) can be simplified into:

$$E_{rp} = \frac{k_{rp}l_{rp,y}}{l_{rp,x}} \tag{E-2}$$

Component	3D Periodic	2.5D	3D FEM
Rail	8-nodes element 0.075m×0.0545m×0.0175m	Beam element	20-nodes element 0.15m×0.109m×0.035m
Railpad	8-nodes element 0.075m×0.010m×0.0175m	Spring element	20-nodes element 0.15m×0.109m×0.035m
Track Layer 1	Centre of track width to rail: 8-nodes element 0.075m×0.075m×0.06825m	Centre of track width to rail: 8-nodes element 0.1m×0.0975m	Centre of track width to rail: 20-nodes element 0.15m×0.15m×0.1365m
	At rail: 8-nodes element 0.075m×0.075m×0.0175m	At rail: 8-nodes element 0.1m×0.0175m	At rail: 20-nodes element 0.15m×0.15m×0.035m
	Rail to track layer edge: 8-nodes element 0.075m×0.075m×0.07375m	Rail to track layer edge: 8-nodes element 0.15m×0.10325m	Rail to track layer edge: 20-nodes element 0.15m×0.15m×0.1475m

Track Layer 2	Track centre to rail: 8-nodes element 0.075m×0.066m×0.06825m	Track centre to rail: 8-nodes element 0.1m×0.0975m	Track centre to rail: 20-nodes element 0.15m×0.15m×0.1365m
	At rail: 8-nodes element 0.075m×0.066m×0.0175m	At rail: 8-nodes element 0.1m×0.0175m	At rail: 20-nodes element 0.15m×0.133m×0.035m
	Rail to track layer edge: 8-nodes element 0.075m×0.066m×0.07375m	Rail to track layer edge: 8-nodes element 0.1m×0.10325m	Rail to track layer edge: 20-nodes element 0.15m×0.133m×0.1475m

Table E-2. Mesh information. Validation case 1 and 2: Track dynamics

Component	Parameter		Unit	Periodic	Analytical
Track (Half)	Gauge (half) Length	l_0 d	m	0.7 0.6	0.7 -
Rail[1] (Single)	Element type Height Width Second moment of Inertia Density Young's modulus Poisson's ratio	 $l_{r,y}$ $l_{r,z}$ I_r ρ_r E_r v_r	- m m m^4 kg/m^3 N/m^2 -	Linear solid 0.218 0.035 3.022E-05 7850 2.1E11 0.3	Beam - - 3.022E-05 7850 2.1E11 0.3
Railpad[2] (Single)	Element type Viscous damping Stiffness	 c_{rp} k_{rp}	- Ns^2/m N/m^2	Spring - 15E6	Spring 19.2E3 15E6

Track parameters obtained or derived from: [1][269], [2][265,270–274]

Table E-3. Track properties. Validation case 3: Dynamic excitation contribution

Component	Parameter		Units	Value
Traction car	Car body mass Car body inertia Bogie frame mass Bogie frame inertia Wheelset mass Primary suspension stiffness Primary suspension damping Secondary suspension stiffness Secondary suspension damping Hertzian stiffness	M_{cb} I_{cb} M_b I_b M_w k_1 c_1 k_2 c_2 K_{HZ}	kg kg m^2 kg kg m^2 kg MN/m kNs/m MN/m kNs/m kN/m	32901 2.08E06 4932 5.15E03 1538 3.42 36 1.32 36 1.1753E06
Side car	Car body mass Car body inertia Bogie frame mass Bogie frame inertia Wheelset mass Primary suspension stiffness Primary suspension damping Secondary suspension stiffness Secondary suspension damping Hertzian stiffness	M_{cb} I_{cb} M_b I_b M_w k_1 c_1 k_2 c_2 K_{HZ}	kg kg m^2 kg kg m^2 kg MN/m kNs/m MN/m kNs/m kN/m	32910 2.08E03 4823 5.09E03 1538 3.42 36 1.32 36 1.1736E06

Central car	Car body mass	M_{cb}	kg	33124
	Car body inertia	I_{cb}	kg m^2	2.08E03
	Bogie frame mass	M_b	kg	4712
	Bogie frame inertia	I_b	kg m^2	5.00E03
	Wheelset mass	M_w	kg	1538
	Primary suspension stiffness	k_1	MN/m	3.42
	Primary suspension damping	c_1	kNs/m	36
	Secondary suspension stiffness	k_2	MN/m	1.32
	Secondary suspension damping	c_2	kNs/m	36
	Hertzian stiffness	K_{HZ}	kN/m	1.1734E06

Table E-4. Dynamic properties of Alfa pendular HST [13]

	Car body mass	M_{cb}	kg	33124
	Car body inertia	I_{cb}	kg m^2	2.08E03
	Bogie frame mass	M_b	kg	4712
	Bogie frame inertia	I_b	kg m^2	5.00E03

Appendix F
Sensitivity Analysis Properties

Table F-1 shows the material and geometrical properties of each track component considered in the sensitivity analysis of Chapter 7, including the corresponding references from which these parameters were obtained and/or derived.

Component	Parameter		Units	Case 1	2	3	4	5
Track	Gauge	l_0	m	0.7175	-	-	-	-
Cell	Length	d	m	0.6	-	-	-	-
A Rail[1]	Layer type	-	-	49E1	CEN56/56E1	CEN60/60E2*	-	-
	Height	$l_{r,y}$	m	0.190	0.210	0.218	-	-
	Width	$l_{r,z}$	m	0.033	0.034	0.035	-	-
	Loss factor	η_r	-	0.01	0.01	0.01	-	-
	Density	ρ_r	kg/m^3	7850	7850	7850	-	-
	Mass	m_r	kg/m	49	56	60	-	-
	Poisson ratio	v_r	-	0.3	0.3	0.3	-	-
	Young's modulus	E_r	GPa	210	210	210	-	-
B Railpad[2]	Layer type	-	-	Soft	Typical*	Typical*	-	-
	Length	$l_{rp,x}$	m	0.2	0.2	0.2	-	-
	Thickness	$l_{rp,y}$	m	0.01	0.01	0.01	-	-
	Width	$l_{rp,z}$	m	0.035	0.035	0.035	-	-
	Loss factor	η_{rp}	-	0.15	0.15	0.15	-	-
	Density	ρ_{rp}	kg/m^3	1000	1000	1000	-	-
	Poisson ratio	v_{rp}	-	0.45	0.45	0.45	-	-
	Young's modulus	E_{rp}	MPa	100	200	300	-	-
C Sleeper[3]	Layer type	-	-	Wood	Plastic	Concrete*	-	-
	Length	$l_{s,x}$	m	0.2	0.2	0.2	-	-
	Thickness	$l_{s,y}$	m	0.2	0.2	0.2	-	-
	Width (half)	$l_{s,z}$	m	1.3	1.3	1.3	-	-
	Spacing	d_0	m	0.6	0.6	0.6	-	-
	Loss factor	η_s	-	0.01	0.01	0.01	-	-
	Density	ρ_s	kg/m^3	1096	1800	2500	-	-
	Poisson ratio	v_s	-	0.2	0.4	0.2	-	-
	Young's modulus	E_s	GPa	8.4	8	31	-	-
D USP[4]	Layer type	-	-	Absent*	Soft	Stiff	-	-
	Length	$l_{usp,x}$	m	-	0.2	0.2	-	-

Parameter	Symbol	Units					
Thickness	$l_{usp,y}$	m	0	0.01	0.005	-	-
Width	$l_{usp,z}$	m	-	1.3	1.3	-	-
Loss factor	η_{usp}	-	-	0.08	0.1	-	-
Density	ρ_{usp}	kg/m³	-	800	800	-	-
Poisson ratio	ν_{usp}	-	-	0.35	0.45	-	-
Young's modulus	E_{sup}	MPa	-	1.5	2	-	-
E Ballast[5]	Layer type	-	-	Soft	Typical*	Stiff	Deep	Deeper
	Shoulder width	w_b	m	0.3	0.3	0.3	0.3	0.3
	Length	$l_{b,x}$	m	0.6	0.6	0.6	0.6	0.6
	Thickness	$l_{b,y}$	m	0.3	0.3	0.3	0.4	0.5
	Width - Top	$l_{b,z1}$	m	1.6	1.6	1.6	1.6	1.6
	Width - Bottom	$l_{b,z2}$	m	2.1	2.2	2.3	2.2	2.2
	Loss factor	η_b	-	0.4	0.4	0.4	0.4	0.4
	Density	ρ_b	kg/m³	1700	1700	1700	1700	1700
	Poisson ratio	ν_b	-	0.3	0.3	0.3	0.3	0.3
	Young's modulus	E_b	MPa	150	220	290	220	220
F Sub-ballast[6]	Layer type	-	-	Typical*	-	-	-	-
	Shoulder width	w_{sb}	m	0.4	-	-	-	-
	Length	$l_{sb,x}$	m	0.6	-	-	-	-
	Thickness	$l_{sb,y}$	m	0.2	-	-	-	-
	Width - Top	$l_{sb,z1}$	m	2.7	-	-	-	-
	Width - Bottom	$l_{sb,z2}$	m	2.7	-	-	-	-
	Loss factor	η_{sb}	-	0.1	-	-	-	-
	Density	ρ_{sb}	kg/m³	1900	-	-	-	-
	Poisson ratio	ν_{sb}	-	0.3	-	-	-	-
	Young's modulus	E_{sb}	MPa	200	-	-	-	-
G Embankment[7]	Layer type	-	-	At-grade*	Deep	Deeper	-	-
	Length	$l_{e,x}$	m	-	0.6	0.6	-	-
	Height	$l_{e,y}$	m	0	2	4	-	-
	Width - Top	$l_{e,z1}$	m	-	3.3	3.3	-	-
	Width - Bottom	$l_{e,z2}$	m	-	5.3	7.3	-	-
	Loss factor	η_e	-	-	0.1	0.1	-	-
	Density	ρ_e	kg/m³	-	2000	2000	-	-
	Poisson ratio	ν_e	-	-	0.3	0.3	-	-
	Young's modulus	E_e	MPa	-	200	200	-	-
H Subgrade[8]	Layer type	-	-	Soft	Typical*	Stiff	-	-
	Depth	$l_{sg,y}$	m	∞	∞	∞	-	-
	Loss factor	η_{sg}	-	0.1	0.1	0.1	-	-
	Density	ρ_{sg}	kg/m³	1800	1800	1800	-	-
	Poisson ratio	ν_{sg}	-	0.35	0.35	0.35	-	-
	Young's modulus	E_{sg}	MPa	40	80	120	-	-

* Base parameters

Track parameters obtained or derived from: [1][269], [2][18,277–279], [3][23,280,281], [4][222,270,282–284], [5][12,20,23,29,126,212,270,271,285], [6][28,126,184,222,276,285], [7][28,184,256,286], [8][12,28,126,136,222,256,270,285]

Table F-1. Track properties. Model refinement and sensitivity analysis

Note that in the case of the railpad, the equivalent vertical Young's modulus is derived according to [18,29], as shown in **Eq.** (E-1). However, for this particular case, the discrete stiffness ($k'_{rp} = k_{rp}d$) must be considered. For comparison purposes, discrete support values will be denoted using a prime symbol ('). Thus, the equivalent vertical Young's modulus is:

$$E_{rp} = \frac{k'_{rp}l_{rp,y}\left(1 + \nu_{rp}\right)\left(1 - 2\nu_{rp}\right)}{l_{rp,x}l_{rp,z}\left(1 - \nu_{rp}\right)} \qquad \text{(F-1)}$$

Appendix G
Frequency Response Functions

In addition to vertical displacement, the track's response due to a harmonic impulse can be expressed in terms of velocity and acceleration. When measuring the response at the same point as the application of the force, point receptance, mobility, or accelerance can be determined, depending on whether displacements, velocities, or accelerations are being computed, respectively. On the contrary, when the measuring point differs from the force, the frequency responses are all transfer functions, i.e. transfer receptance, transfer mobility, or a transfer accelerance.

Figure G-1 compares the frequency response at different rail positions, taking into account the support and symmetric loading effect. In the first case, **Figure G-1**(a), results are presented in terms of velocity. Alternatively, **Figure G-1**(b) illustrates the acceleration of the structure. Overall, the resonant frequencies identified in the displacement response – see Chapter 6, are also displayed in the velocity and acceleration results. Despite this, the minimum amplitude is found at lower frequencies in the velocity and acceleration response, and on higher frequencies in the displacement case. This is because the response is divided by the frequency and the square of the frequency in the velocity and accelerance case respectively, resulting in suppression of the amplitude at lower frequencies and amplification at higher frequencies.
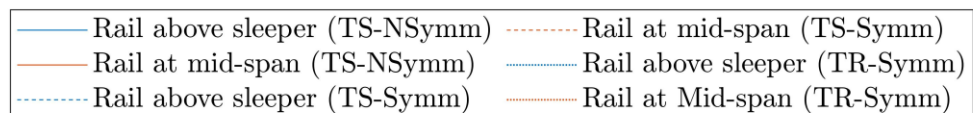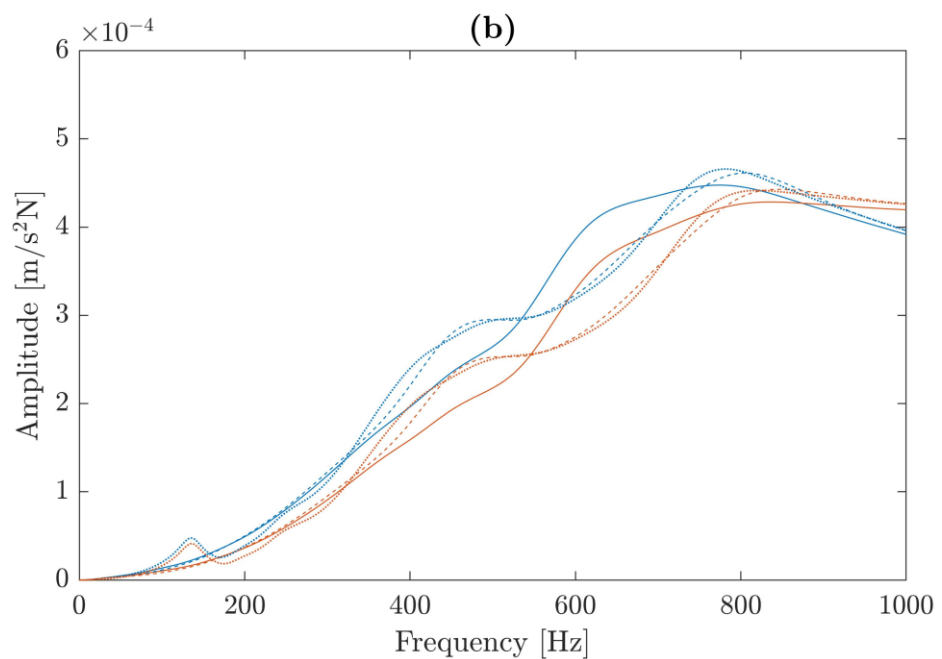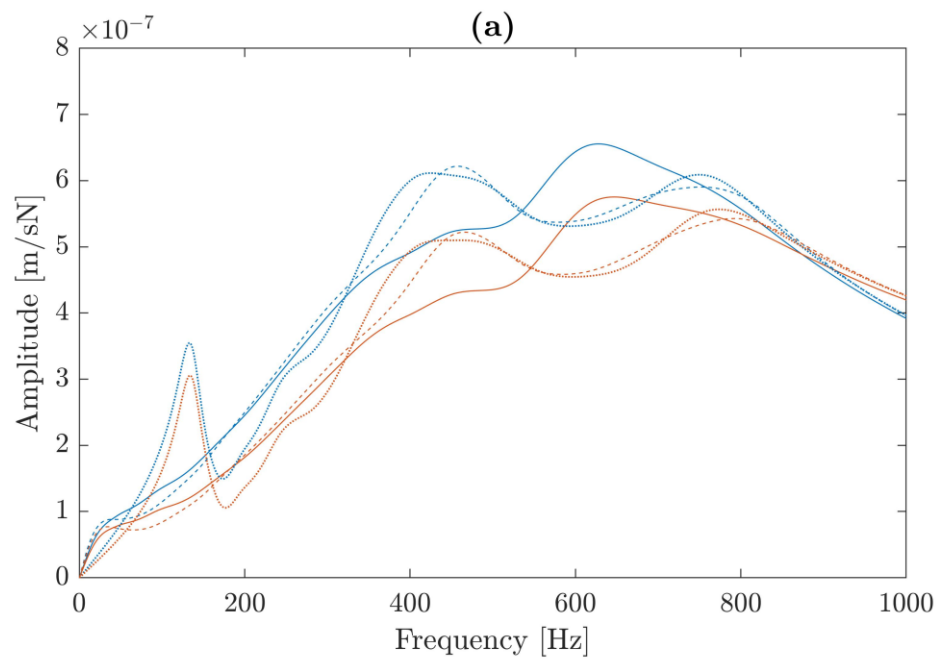
Figure G-1. Track response: (a) velocities and (b) accelerations. Track on subgrade support – non-symmetric loading (TS − NSymm), track on subgrade support – symmetric loading (TS − Symm), and track on rigid support – symmetric loading (TR − Symm)

References

[1]   Berggren EG, Jahlénius Å, Bengtsson B-E, Berg M. Simulation, development and field testing of a track stiffness measurement vehicle. Proc. 8th Int. Heavy Haul Conf., Rio de Janeiro: 2005, p. 763–72.

[2]   Berggren EG, Kaynia AM, Dehlbom B. Identification of substructure properties of railway tracks by dynamic stiffness measurements and simulations. J Sound Vib 2010;329:3999–4016. https://doi.org/10.1016/j.jsv.2010.04.015.

[3]   Berggren EG. Railway track stiffness : dynamic measurements and evaluation for efficient maintenance. Skolan för teknikvetenskap, farkost och flyg, Kungliga Tekniska högskolan, 2009.

[4]   Wang P, Wang L, Chen R, Xu J, Xu J, Gao M. Overview and outlook on railway track stiffness measurement. J Mod Transp 2016;24:89–102. https://doi.org/10.1007/s40534-016-0104-8.

[5]   Morais J, Fortunato E, Ribeiro D, Calçada R, Mendes J. Railway track support condition assessment — Methodology validation using numerical simulations. Eng Fail Anal 2023;152:107483. https://doi.org/10.1016/j.engfailanal.2023.107483.

[6]   Zhang X, Thompson D, Jeong H, Toward M, Herron D, Jones C, et al. Measurements of the high frequency dynamic stiffness of railway ballast and subgrade. J Sound Vib 2020;468:115081. https://doi.org/10.1016/j.jsv.2019.115081.

[7]   Ferreira PAAD. Modelling and prediction of the dynamic behaviour of railway infrastructures at very high speeds. Universidade Técnica de Lisboa, Instituto Superior Técnico, 2010.

[8]   Grassie SL, Gregory RW, Harrison D, Johnson KL. The Dynamic Response of Railway Track to High Frequency Vertical Excitation. J Mech Eng Sci 1982;24:77–90. https://doi.org/10.1243/JMES_JOUR_1982_024_016_02.

[9]   Knothe KL, Grassie SL. Modelling of Railway Track and Vehicle/Track Interaction at High Frequencies. Veh Syst Dyn 1993;22:209–62. https://doi.org/10.1080/00423119308969027.

[10]   Thompson D. Railway Noise and Vibration. Elsevier; 2009. https://doi.org/10.1016/B978-0-08-045147-3.X0023-0.

[11]   Lamprea-Pineda AC, Connolly DP, Hussein MFM. Beams on elastic foundations – A review of railway applications and solutions. Transp Geotech 2022;33:100696. https://doi.org/10.1016/j.trgeo.2021.100696.

[12] Knothe KL, Wu Y. Receptance behaviour of railway track and subgrade. Arch Appl Mech (Ingenieur Arch 1998;68:457–70. https://doi.org/10.1007/s004190050179.

[13] Kouroussis G, Connolly DP, Verlinden O. Railway-induced ground vibrations – a review of vehicle effects. Int J Rail Transp 2014;2:69–110. https://doi.org/10.1080/23248378.2014.897791.

[14] Chumyen P, Connolly DP, Woodward PK, Markine V. A comparison of earthwork designs for railway transition zones. Constr Build Mater 2023;395:132295. https://doi.org/10.1016/j.conbuildmat.2023.132295.

[15] Connolly DP, Giannopoulos A, Forde MC. Numerical modelling of ground borne vibrations from high speed rail lines on embankments. Soil Dyn Earthq Eng 2013;46:13–9. https://doi.org/10.1016/j.soildyn.2012.12.003.

[16] de Man AP. DYNTRACK, A survey of dynamic railway track properties and their qualities. Technische Universietit Delft, 2002.

[17] de Man AP. Pin-pin resonance as a reference in determining ballasted railway track vibration behaviour. HERON 2000;45:35–51.

[18] Oregui M, Li Z, Dollevoet R. An investigation into the modeling of railway fastening. Int J Mech Sci 2015;92:1–11. https://doi.org/10.1016/j.ijmecsci.2014.11.019.

[19] Oregui M, Núñez A, Dollevoet R, Li Z. Sensitivity Analysis of Railpad Parameters on Vertical Railway Track Dynamics. J Eng Mech 2017;143. https://doi.org/10.1061/(ASCE)EM.1943-7889.0001207.

[20] Shen C, Deng X, Wei Z, Dollevoet R, Zoeteman A, Li Z. Comparisons between beam and continuum models for modelling wheel-rail impact at a singular rail surface defect. Int J Mech Sci 2021;198:106400. https://doi.org/10.1016/j.ijmecsci.2021.106400.

[21] Alves Costa P, Calçada R, Silva Cardoso A. Track–ground vibrations induced by railway traffic: In-situ measurements and validation of a 2.5D FEM-BEM model. Soil Dyn Earthq Eng 2012;32:111–28. https://doi.org/https://doi.org/10.1016/j.soildyn.2011.09.002.

[22] François S, Schevenels M, Galvín P, Lombaert G, Degrande G. A 2.5D coupled FE–BE methodology for the dynamic interaction between longitudinally invariant structures and a layered halfspace. Comput Methods Appl Mech Eng 2010;199:1536–48.
https://doi.org/https://doi.org/10.1016/j.cma.2010.01.001.

[23] Charoenwong C, Connolly DP, Woodward PK, Galvín P, Alves Costa P. Analytical forecasting of long-term railway track settlement. Comput Geotech 2022;143:104601. https://doi.org/10.1016/j.compgeo.2021.104601.

[24] Charoenwong C, Connolly DP, Odolinski K, Alves Costa P, Galvín P, Smith A. The effect of rolling stock characteristics on differential railway track settlement: An engineering-economic model. Transp Geotech 2022;37:100845. https://doi.org/10.1016/j.trgeo.2022.100845.

[25] Charoenwong C, Connolly DP, Colaço A, Alves Costa P, Woodward PK, Romero A, et al. Railway slab vs ballasted track: a comparison of track geometry degradation. Constr Build Mater 2023.

[26] Chebli H, Clouteau D, Schmitt L. Dynamic response of high-speed ballasted railway tracks: 3D periodic model and in situ measurements. Soil Dyn Earthq Eng 2008;28:118–31. https://doi.org/10.1016/j.soildyn.2007.05.007.

[27] Germonpré M, Degrande G, Lombaert G. A track model for railway-induced ground vibration resulting from a transition zone. Proc Inst Mech Eng Part F J Rail Rapid Transit 2018;232:1703–17. https://doi.org/10.1177/0954409717745202.

[28] Arlaud E, D'Aguiar S, Balmes E. Validation of a reduced model of railway track allowing long 3D dynamic calculation of train-track interaction. Comput. Methods Recent Adv. Geomech., CRC Press; 2014, p. 1193–8. https://doi.org/10.1201/b17435-209.

[29] Arlaud E, Costa D'Aguiar S, Balmes E. Receptance of railway tracks at low frequency: Numerical and experimental approaches. Transp Geotech 2016;9:1–16. https://doi.org/10.1016/j.trgeo.2016.06.003.

[30] Winkler E. Die Lehre von Elastizität und Festigkeit (on Elasticity and Fixity). Dominicus, Prague: 1867.

[31] Frýba L. Vibration of solids and structures under moving loads. Dordrecht: Springer Netherlands; 1972. https://doi.org/10.1007/978-94-011-9685-7.

[32] Indraratna B, Babar Sajjad M, Ngo T, Gomes Correia A, Kelly R. Improved performance of ballasted tracks at transition zones: A review of experimental and modelling approaches. Transp Geotech 2019;21:100260. https://doi.org/10.1016/j.trgeo.2019.100260.

[33] Blanco-Lorenzo J, Santamaria J, Vadillo EG, Oyarzabal O. Dynamic comparison of different types of slab track and ballasted track using a flexible track model. Proc Inst Mech Eng Part F J Rail Rapid Transit 2011;225:574–92. https://doi.org/10.1177/0954409711401516.

[34] Hunt GA. Dynamic analysis of railway vehicle/track interaction forces. Loughborough University of Technology, 1986.

[35] Bian X, Jiang H, Cheng C, Chen Y, Chen R, Jiang J. Full-scale model testing on a ballastless high-speed railway under simulated train moving loads. Soil Dyn Earthq Eng 2014;66:368–84. https://doi.org/10.1016/j.soildyn.2014.08.003.

[36] Hussein MFM, Hunt HEM. Modelling of Floating-Slab Track with Discontinuous Slab: Part 1: Response to Oscillating Moving Loads. J Low Freq Noise, Vib Act Control 2006;25:23–39. https://doi.org/10.1260/026309206777637339.

[37] Esveld C. Modern Railway Track. Second Edi. 2001.

[38] Hetényi M. Beams On Elastic Foundation Theory With Applications In The Fields Of Civil And Mechanical Engineering. Ann Arbor: University of Michigan; 1946.

[39] Doyle NF. Railway track design: a review of current practice. Canbrerra, Australia: C.J. Thompson, Commonwealth Government Printer, Canberra; 1980.

[40] Frýba L, Nakagiri S, Yoshikawa N. Stochastic Finite Elements for a Beam on a Random Foundation with Uncertain Damping Under a Moving Force. J Sound Vib 1993;163:31–45. https://doi.org/10.1006/jsvi.1993.1146.

[41]   García-Palacios J, Samartín A, Melis M. Analysis of the railway track as a spatially periodic structure. Proc Inst Mech Eng Part F J Rail Rapid Transit 2012;226:113–23. https://doi.org/10.1177/0954409711411609.

[42]   Li MXD, Berggren EG. A Study of the Effect of Global Track Stiffness and its Variations on Track Performance: Simulation and Measurement. Proc Inst Mech Eng Part F J Rail Rapid Transit 2010;224:375–82. https://doi.org/10.1243/09544097JRRT361.

[43]   Wehbi M, Musgrave P. Optimisation of Track Stiffness on the UK Railways. Perm W Inst J 2017;135:24–31.

[44]   Ahlbeck DR, Meacham HC, Prause RH. The Development of Analytical Models for Railroad Track Dynamics. Railr. Track Mech. Technol., Elsevier; 1975, p. 239–63. https://doi.org/10.1016/B978-0-08-021923-3.50017-6.

[45]   Grassie SL. Dynamic models of the track and their uses. Rail Qual. Maint. Mod. Railw. Oper., Dordrecht: Springer Netherlands; 1993, p. 165–83. https://doi.org/10.1007/978-94-015-8151-6_14.

[46]   Zhai WM, Sun X. A Detailed Model for Investigating Vertical Interaction between Railway Vehicle and Track. Veh Syst Dyn 1994;23:603–15. https://doi.org/10.1080/00423119308969544.

[47]   Zhai WM, Wang KY, Lin JH. Modelling and experiment of railway ballast vibrations. J Sound Vib 2004;270:673–83. https://doi.org/10.1016/S0022-460X(03)00186-X.

[48]   OBrien EJ, Bowe CJ, Quirke P, Cantero D. Drive-by inference of railway track longitudinal profile using accelerometer readings taken by in-service vehicles. Civ. Eng. Res. Irel. 2016 (CERI), NUI Galw., 2016.

[49]   Timoshenko SP. On the transverse vibrations of bars of uniform cross-section. London, Edinburgh, Dublin Philos Mag J Sci 1922;43:125–31. https://doi.org/10.1080/14786442208633855.

[50]   Blanco B, Alonso A, Kari L, Gil-Negrete N, Giménez JG. Implementation of Timoshenko element local deflection for vertical track modelling. Veh Syst Dyn 2019;57:1421–44. https://doi.org/10.1080/00423114.2018.1513538.

[51]   Croft BE. The Development of Rail-Head Acoustic Roughness. University of Southampton, 2009.

[52]   Connolly DP, Kouroussis G, Laghrouche O, Ho CL, Forde MC. Benchmarking railway vibrations – Track, vehicle, ground and building effects. Constr Build Mater 2015;92:64–81. https://doi.org/10.1016/j.conbuildmat.2014.07.042.

[53]   Sheng X, Jones CJC, Thompson DJ. Responses of infinite periodic structures to moving or stationary harmonic loads. J Sound Vib 2005;282:125–49. https://doi.org/10.1016/j.jsv.2004.02.050.

[54]   Patil SP. Natural Frequencies of a Railroad Track. J Appl Mech 1987;54:299–304. https://doi.org/10.1115/1.3173011.

[55]   Younesian D, Hosseinkhani A, Askari H, Esmailzadeh E. Elastic and viscoelastic foundations: a review on linear and nonlinear vibration modeling and applications. Nonlinear Dyn 2019;97:853–95. https://doi.org/10.1007/s11071-019-04977-9.

[56]   Kerr AD. Elastic and Viscoelastic Foundation Models. J Appl Mech

1964;31:491–8. https://doi.org/10.1115/1.3629667.

[57] Singh H, Jha JN. Constitutive models for sustainable design of foundation systems. UKIERI Concr. Congr. - Innov. Concr. Constr., 2013.

[58] Madhira M, S.V. A, K. R. Modelling ground-foundation interactions. Int. Conf. Innov. Struct. Eng., 2015, p. 91–106.

[59] Filonenko-Borodich MM. Some approximate theories of elastic foundation. Uchenyie Zapiski Moskovkogo Gosudarstuennogo Universiteta Mekhanika, Moscow 1940:3–18.

[60] Henrot A. Extremum Problems for Eigenvalues of Elliptic Operators. Basel: Birkhäuser Basel; 2006. https://doi.org/10.1007/3-7643-7706-2.

[61] Slaughter WS. The Linearized Theory of Elasticity. Boston, MA: Birkhäuser Boston; 2002. https://doi.org/10.1007/978-1-4612-0093-2.

[62] Pasternak PL. On a new Method of Analysis of an Elastic Foundation by Means of Two Foundation Constants. Gosuderevstvennae Izdatlesva Literaturi po Stroitelstvu i Arkihitekture, Moscow, USSR 1954.

[63] Kerr AD. A study of a new foundation model. Acta Mech 1965;1:135–47. https://doi.org/10.1007/BF01174308.

[64] Creus GJ. Rheological Models; Differential Representation. Viscoelasticity — Basic Theory Appl. to Concr. Struct., Springer, Berlin, Heidelberg; 1986, p. 18–37. https://doi.org/10.1007/978-3-642-82686-3_2.

[65] Lamb H. I. On the propagation of tremors over the surface of an elastic solid. Philos Trans R Soc London Ser A, Contain Pap a Math or Phys Character 1904;203. https://doi.org/https://doi.org/10.1098/rsta.1904.0013.

[66] Andersen L. Linear Elastodynamic Analysis. DCE Lecture Notes No. 3. Aalborg, Denmark: Aalborg University; 2006.

[67] Mosleh A, Alves Costa P, Calçada R. A new strategy to estimate static loads for the dynamic weighing in motion of railway vehicles. Proc Inst Mech Eng Part F J Rail Rapid Transit 2020;234:183–200. https://doi.org/10.1177/0954409719838115.

[68] Sheng X, Jones CJC, Petyt M. Ground vibration generated by a harmonic load acting on a railway track. J Sound Vib 1999;225:3–28. https://doi.org/https://doi.org/10.1006/jsvi.1999.2232.

[69] Verruijt A. An Introduction to Soil Dynamics. 1st ed. Springer Netherlands; 2010. https://doi.org/10.1007/978-90-481-3441-0.

[70] Sheng X, Jones CJC, Petyt M. Ground vibration generated by a load moving along a railway track. J Sound Vib 1999;228:129–56. https://doi.org/10.1006/jsvi.1999.2406.

[71] Alves Costa P, Soares P, Colaço A, Lopes P, Connolly D. Railway critical speed assessment: A simple experimental-analytical approach. Soil Dyn Earthq Eng 2020;134:106156. https://doi.org/10.1016/j.soildyn.2020.106156.

[72] Dong K, Connolly DP, Laghrouche O, Woodward PK, Alves Costa P. Non-linear soil behaviour on high speed rail lines. Comput Geotech 2019;112:302–18. https://doi.org/https://doi.org/10.1016/j.compgeo.2019.03.028.

[73] Gao Y, Huang H, Ho CL, Hyslip JP. High speed railway track dynamic behavior

near critical speed. Soil Dyn Earthq Eng 2017;101:285–94. https://doi.org/10.1016/j.soildyn.2017.08.001.

[74] Mezher SB, Connolly DP, Woodward PK, Laghrouche O, Pombo J, Alves Costa P. Railway critical velocity – Analytical prediction and analysis. Transp Geotech 2016;6:84–96. https://doi.org/10.1016/j.trgeo.2015.09.002.

[75] Dong K, Connolly DP, Laghrouche O, Woodward PK, Alves Costa P. The stiffening of soft soils on railway lines. Transp Geotech 2018;17:178–91. https://doi.org/10.1016/j.trgeo.2018.09.004.

[76] Woodward PK, Laghrouche O, Mezher SB, Connolly DP. Application of Coupled Train-Track Modelling of Critical Speeds for High-Speed Trains using Three-Dimensional Non-Linear Finite Elements. Int. J. Railw. Technol., vol. 4, Lisbon, Portugal: 2015, p. 1–35. https://doi.org/10.4203/ijrt.4.3.1.

[77] Connolly DP, Alves Costa P. Geodynamics of very high speed transport systems. Soil Dyn Earthq Eng 2020;130:1–13. https://doi.org/https://doi.org/10.1016/j.soildyn.2019.105982.

[78] Lombaert G, Degrande G. Ground-borne vibration due to static and dynamic axle loads of InterCity and high-speed trains. J Sound Vib 2009;319:1036–66. https://doi.org/10.1016/j.jsv.2008.07.003.

[79] Kouroussis G, Connolly DP, Alexandrou G, Vogiatzis K. Railway ground vibrations induced by wheel and rail singular defects. Veh Syst Dyn 2015;53:1500–19. https://doi.org/10.1080/00423114.2015.1062116.

[80] Selig ET, Waters JM. Track geotechnology and substructure management. Thomas Telford Publishing; 1994. https://doi.org/10.1680/tgasm.20139.

[81] Mazilu T. Green's functions for analysis of dynamic response of wheel/rail to vertical excitation. J Sound Vib 2007;306:31–58. https://doi.org/10.1016/j.jsv.2007.05.037.

[82] Zhang S, Cheng G, Sheng X, Thompson DJ. Dynamic wheel-rail interaction at high speed based on time-domain moving Green's functions. J Sound Vib 2020;488:115632. https://doi.org/10.1016/j.jsv.2020.115632.

[83] Galvín P, López Mendoza D, Connoll DP, Degrande G, Lombaert G, Romero A. Scoping assessment of free-field vibrations due to railway traffic. Soil Dyn Earthq Eng 2018;114:598–614. https://doi.org/https://doi.org/10.1016/j.soildyn.2018.07.046.

[84] Nordborg A. Vertical Rail Vibrations: Parametric Excitation. Acta Acust United with Acust 1998;84:289–300.

[85] Fărăgău AB, Keijdener C, de Oliveira Barbosa JM, Metrikine A V., van Dalen KN. Transition radiation in a nonlinear and infinite one-dimensional structure: a comparison of solution methods. Nonlinear Dyn 2021. https://doi.org/10.1007/s11071-020-06117-0.

[86] Krzyżyński T. On Continuous Subsystem Modelling in the Dynamic Interaction Problem of a Train-Track-System. Veh Syst Dyn 1995;24:311–24. https://doi.org/10.1080/00423119508969633.

[87] Younesian D, Kargarnovin MH, Thompson DJ, Jones CJC. Parametrically Excited Vibration of a Timoshenko Beam on Random Viscoelastic Foundation jected to a Harmonic Moving Load. Nonlinear Dyn 2006;45:75–93.

https://doi.org/10.1007/s11071-006-1460-4.

[88] Vogiatzis K, Kouroussis G. Airborne and Ground-Borne Noise and Vibration from Urban Rail Transit Systems. Urban Transp. Syst., InTech; 2017, p. 61–87. https://doi.org/10.5772/66571.

[89] Kouroussis G, Vogiatzis KE, Connolly DP. Assessment of railway ground vibration in urban area using in-situ transfer mobilities and simulated vehicle-track interaction. Int J Rail Transp 2018;6:113–30. https://doi.org/10.1080/23248378.2017.1399093.

[90] Jezequel L. Response of Periodic Systems to a Moving Load. J Appl Mech 1981;48:613–8. https://doi.org/10.1115/1.3157683.

[91] Ilias H, Müller S. A discrete-continuous track-model for wheelsets rolling over short wavelength sinusoidal rail irregularities. Veh Syst Dyn 1994;23:221–33. https://doi.org/10.1080/00423119308969517.

[92] Nordborg A. Vertical Rail Vibrations: Pointforce Excitation. Acta Acust United with Acust 1998;84:280-288(9).

[93] Liu Y, Zhang Y, Song C, Gu H, Xu L. Excitation frequency, fastener stiffness and damping, and speed of the moving harmonic load on the dynamic response of the track structure. J Mech Sci Technol 2019;33:11–9. https://doi.org/10.1007/s12206-018-1202-9.

[94] Igeland A, Ilias H. Rail head corrugation growth predictions based on non-linear high frequency vehicle/track interaction. Wear 1997;213:90–7. https://doi.org/https://doi.org/10.1016/S0043-1648(97)00172-5.

[95] Nielsen JCO. Numerical prediction of rail roughness growth on tangent railway tracks. J Sound Vib 2003;267:537–48. https://doi.org/10.1016/S0022-460X(03)00713-2.

[96] Fröhling RD, Scheffel H, Ebersöhn W. The Vertical Dynamic Response of a Rail Vehicle caused by Track Stiffness Variations along the Track. Veh Syst Dyn 1996;25:175–87. https://doi.org/10.1080/00423119608969194.

[97] Johansson A, Nielsen JCO. Out-of-round railway wheels—wheel-rail contact forces and track response derived from field tests and numerical simulations. Proc Inst Mech Eng Part F J Rail Rapid Transit 2003;217:135–46. https://doi.org/https://doi.org/10.1243/095440903765762878.

[98] Hussein MFM, Hunt HEM. Modelling of Floating-Slab Track with Discontinuous Slab: Part 2: Response to Moving Trains. J Low Freq Noise, Vib Act Control 2006;25:111–8. https://doi.org/10.1260/026309206778494283.

[99] Yang Y-B, Yau J-D. Vehicle-Bridge Interaction Element for Dynamic Analysis. J Struct Eng 1997;123:1512–8. https://doi.org/10.1061/(ASCE)0733-9445(1997)123:11(1512).

[100] Galvín P, François S, Schevenels M, Bongini E, Degrande G, Lombaert G. A 2.5D coupled FE-BE model for the prediction of railway induced vibrations. Soil Dyn Earthq Eng 2010;30:1500–12. https://doi.org/https://doi.org/10.1016/j.soildyn.2010.07.001.

[101] Uzzal RUA, Ahmed W, Rakheja S. Dynamic analysis of railway vehicle-track interactions due to wheel flat with a pitch-plane vehicle model. J Mech Eng

1970;39:86–94. https://doi.org/10.3329/jme.v39i2.1851.

[102] Lin CC, Wang JF, Chen BL. Train-Induced Vibration Control of High-Speed Railway Bridges Equipped with Multiple Tuned Mass Dampers. J Bridg Eng 2005;10:398–414. https://doi.org/10.1061/(ASCE)1084-0702(2005)10:4(398).

[103] Zhai WM, Cai CB, Wang QC, Lu Z. W, Wu XS. Dynamic effects of vehicles on tracks in the case of raising train speeds. Proc Inst Mech Eng Part F J Rail Rapid Transit 2001;215:125–35. https://doi.org/10.1243/0954409011531459.

[104] Tao G, Ren D, Wang L, Wen Z, Jin X. Online prediction model for wheel wear considering track flexibility. Multibody Syst Dyn 2018;44:313–34. https://doi.org/10.1007/S11044-018-09633-5.

[105] Cai Y, Cao Z, Sun H, Xu C. Effects of the dynamic wheel–rail interaction on the ground vibration generated by a moving train. Int J Solids Struct 2010;47:2246–59. https://doi.org/10.1016/j.ijsolstr.2010.04.013.

[106] Nielsen JCO, Igeland A. Vertical dynamic interaction between train and track influence of wheel and track imperfections. J Sound Vib 1995;187:825–39. https://doi.org/10.1006/jsvi.1995.0566.

[107] Colaço A, Alves Costa P, Connolly DP. The influence of train properties on railway ground vibrations. Struct Infrastruct Eng Maintenance, Manag Life-Cycle Des Perform 2015;12:517–34. https://doi.org/http://dx.doi.org/10.1080/15732479.2015.1025291.

[108] Ling L, Zhang Q, Xiao X, Wen Z, Jin X. Integration of car-body flexibility into train–track coupling system dynamics analysis. Veh Syst Dyn 2018;56:485–505. https://doi.org/10.1080/00423114.2017.1391397.

[109] Zhou J, Goodall R, Ren L, Zhang H. Influences of car body vertical flexibility on ride quality of passenger railway vehicles. Proc Inst Mech Eng Part F J Rail Rapid Transit 2009;223:461–71. https://doi.org/10.1243/09544097JRRT272.

[110] Wang K, Xia H, Xu M, Guo W. Dynamic analysis of train-bridge interaction system with flexible car-body. J Mech Sci Technol 2015;29:3571–80. https://doi.org/10.1007/s12206-015-0801-y.

[111] Doyle JF. Wave Propagation in Structures. New York, NY: Springer New York; 1997. https://doi.org/10.1007/978-1-4612-1832-6.

[112] Chopra AK. Dynamics of Structures: Theory and Applications to Earthquake Engineering. Fourth Edi. Prentice Hall; 2012.

[113] Baron (Lord) Rayleigh JWS. Theory of Sound. 2nd ed. New York : Dover; 1877.

[114] Petyt M. Introduction to Finite Element Vibration Analysis. 2nd Editio. Cambridge: Cambridge University Press; 2010. https://doi.org/10.1017/CBO9780511761195.

[115] Wang H-F, Lou M-L, Zhang R-L. Selection of Rayleigh Damping Coefficients for Seismic Response Analysis of Soil Layers. World Acad Sci Eng Technol Int J Geol Environ Eng 2017;11:158–63. https://doi.org/doi.org/10.5281/zenodo.10.5281/zenodo.1128809.

[116] Caughey TK. Classical Normal Modes in Damped Linear Dynamic Systems. J Appl Mech 1960;27:269–71. https://doi.org/10.1115/1.3643949.

212

[117] Caughey TK, O'Kelly MEJ. Classical Normal Modes in Damped Linear Dynamic Systems. J Appl Mech 1965;32:583–8. https://doi.org/10.1115/1.3627262.

[118] Makris N. Causal Hysteretic Element. J Eng Mech 1997;123:1209–14. https://doi.org/10.1061/(ASCE)0733-9399(1997)123:11(1209).

[119] Crandall SH. The role of damping in vibration theory. J Sound Vib 1970;11:3-IN1. https://doi.org/10.1016/S0022-460X(70)80105-5.

[120] Maia N. Reflections on the Hysteretic Damping Model. Shock Vib 2009;16:529–42. https://doi.org/10.1155/2009/674758.

[121] Inaudi JA, Kelly JM. Linear Hysteretic Damping and the Hilbert Transform. J Eng Mech 1995;121:626–32. https://doi.org/10.1061/(ASCE)0733-9399(1995)121:5(626).

[122] Chen JT, You DW. Hysteretic damping revisited. Adv Eng Softw 1997;28:165–71. https://doi.org/10.1016/S0965-9978(96)00052-X.

[123] Hanson CE, P.E. JC, Ross PE, David A. Towers PE. High-Speed Ground Transportation Noise and Vibration Impact Assessment. Washington, DC: 2012.

[124] Liu GR, Quek SS. The Finite Element Method: A Practical Course. Butterworth-Heinemann; 2013.

[125] Duhamel D, Mace BR, Brennan MJ. Finite element analysis of the vibrations of waveguides and periodic structures. J Sound Vib 2006;294:205–20. https://doi.org/10.1016/j.jsv.2005.11.014.

[126] Li D, Hyslip J, Sussmann TR, Chrismer S. Railway Geotechnics. 1st Editio. London: CRC Press; 2002. https://doi.org/10.1201/b18982.

[127] Paixão A, Fortunato E, Calçada R. Transition zones to railway bridges: Track measurements and numerical modelling. Eng Struct 2014;80:435–43. https://doi.org/10.1016/j.engstruct.2014.09.024.

[128] Prakoso PB. The Basic Concepts of Modelling Railway Track Systems using Conventional and Finite Element Methods 2012;13:57–65.

[129] Kece E, Reikalas V, DeBold R, Ho CL, Robertson I, Forde MC. Evaluating ground vibrations induced by high-speed trains. Transp Geotech 2019;20:100236. https://doi.org/10.1016/j.trgeo.2019.03.004.

[130] Alves Ribeiro C, Calçada R, Delgado R. Calibration and experimental validation of a dynamic model of the train-track system at a culvert transition zone. Struct Infrastruct Eng 2018;14:604–18. https://doi.org/10.1080/15732479.2017.1380674.

[131] Xu Q, Xiao Z, Liu T, Lou P, Song X. Comparison of 2D and 3D prediction models for environmental vibration induced by underground railway with two types of tracks. Comput Geotech 2015;68:169–83. https://doi.org/10.1016/j.compgeo.2015.04.011.

[132] Powrie W, Yang LA, Clayton CRI. Stress changes in the ground below ballasted railway track during train passage. Proc Inst Mech Eng Part F J Rail Rapid Transit 2007;221:247–62. https://doi.org/10.1243/0954409JRRT95.

[133] Real T, Zamorano C, Ribes F, Real JI. Train-induced vibration prediction in tunnels using 2D and 3D FEM models in time domain. Tunn Undergr Sp

Technol 2015;49:376–83. https://doi.org/10.1016/j.tust.2015.05.004.

[134] Giner IG, López-Pita A. Numerical simulation of embankment—structure transition design. Proc Inst Mech Eng Part F J Rail Rapid Transit 2009;223:331–43.
https://doi.org/https://doi.org/10.1243/09544097JRRT234.

[135] Wang H, Markine V. Modelling of the long-term behaviour of transition zones: Prediction of track settlement. Eng Struct 2018;156:294–304. https://doi.org/10.1016/j.engstruct.2017.11.038.

[136] Shan Y, Zhou S, Wang B, Ho CL. Differential Settlement Prediction of Ballasted Tracks in Bridge–Embankment Transition Zones. J Geotech Geoenvironmental Eng 2020;146:04020075. https://doi.org/10.1061/(ASCE)GT.1943-5606.0002307.

[137] Ju SH. A frictional contact finite element for wheel/rail dynamic simulations. Nonlinear Dyn 2016;85:365–74. https://doi.org/10.1007/s11071-016-2691-7.

[138] El-sayed HM, Lotfy M, El-din Zohny HN, Riad HS. A three dimensional finite element analysis of insulated rail joints deterioration. Eng Fail Anal 2018;91:201–15. https://doi.org/10.1016/j.engfailanal.2018.04.042.

[139] El-sayed HM, Lotfy M, El-din Zohny HN, Riad HS. Prediction of fatigue crack initiation life in railheads using finite element analysis. Ain Shams Eng J 2018;9:2329–42. https://doi.org/10.1016/j.asej.2017.06.003.

[140] Bandula-Heva TM, Dhanasekar M, Boyd P. Experimental Investigation of Wheel/Rail Rolling Contact at Railhead Edge. Exp Mech 2013;53:943–57. https://doi.org/10.1007/s11340-012-9701-6.

[141] Ma Y, Markine VL, Mashal AA, Ren M. Effect of wheel–rail interface parameters on contact stability in explicit finite element analysis. Proc Inst Mech Eng Part F J Rail Rapid Transit 2018;232:1879–94. https://doi.org/10.1177/0954409718754941.

[142] Mahdavi SH, Abdul Razak H. Indirect Time Integration Scheme for Dynamic Analysis of Space Structures Using Wavelet Functions. J Eng Mech 2015;141:1–15. https://doi.org/https://doi.org/10.1061/(ASCE)EM.1943-7889.0000914.

[143] Raymond GP. Analysis of track support and determination of track modulus. Transp Res Rec 1985;0:80–90.

[144] Meacham HC, Prause RH, Ahlbeck DR, Kasuba JA. Studies for Rail Vehicle Track Structures. Washington, DC, USA: 1970.

[145] Smith CC, Wormley DN. Response of Continuous Periodically Supported Guideway Beams to Traveling Vehicle Loads. J Dyn Syst Meas Control 1975;97:21–9. https://doi.org/10.1115/1.3426867.

[146] Filon LNG. On a Quadrature Formula for Trigonometric Integrals. Proc R Soc Edinburgh 1930;49:38–47. https://doi.org/10.1017/S0370164600026262.

[147] Huybrechs D. Filon Quadrature. Encycl. Appl. Comput. Math., Berlin, Heidelberg: Springer Berlin Heidelberg; 2015, p. 513–6. https://doi.org/10.1007/978-3-540-70529-1_395.

[148] Flinn EA. A Modification of Filon's Method of Numerical Integration. J ACM

1960;7:181–4. https://doi.org/10.1145/321021.321029.

[149] Lombaert G, François S, Degrande G. Traffic MATLAB toolbox for traffic induced vibrations, user's guide traffic 5.2 report BWM-2012-10. Leuven, Belgium: 2012.

[150] Chase SM, Fosdick LD. An algorithm for Filon quadrature. Commun ACM 1969;12:453–7. https://doi.org/10.1145/363196.363209.

[151] Le Floc'h F. An adaptive Filon quadrature for stochastic volatility models. J Comput Financ 2018;22:65–88. https://doi.org/10.21314/JCF.2018.356.

[152] Brown JW, Churchill R V. Complex Variables and Applications. 8th ed. McGraw-Hill Education; 2017.

[153] Hussein MFM. Vibration from underground railways. University of Cambridge, 2004. https://doi.org/https://doi.org/10.17863/CAM.19122.

[154] Kouroussis G, Verlinden O. Prediction of railway ground vibrations: Accuracy of a coupled lumped mass model for representing the track/soil interaction. Soil Dyn Earthq Eng 2015;69:220–6. https://doi.org/10.1016/j.soildyn.2014.11.007.

[155] Kouroussis G, Verlinden O, Conti C. Free field vibrations caused by high-speed lines: Measurement and time domain simulation. Soil Dyn Earthq Eng 2011;31:692–707. https://doi.org/10.1016/j.soildyn.2010.11.012.

[156] Connolly DP, Galvín P, Olivier B, Romero A, Kouroussis G. A 2.5D time-frequency domain model for railway induced soil-building vibration due to railway defects. Soil Dyn Earthq Eng 2019;120:332–44. https://doi.org/10.1016/j.soildyn.2019.01.030.

[157] Zakeri J-A, Xia H, Fan JJ. Dynamic responses of train-track system to single rail irregularity. Lat Am J Solids Struct 2009;6:89–104.

[158] Haskell NA. The dispersion of surface waves on multilayered media. Vincit Verit. A Portrait Life Work Norman Abraham Haskell, 1905–1970, Washington, D. C.: American Geophysical Union; 1990, p. 86–103. https://doi.org/10.1029/SP030p0086.

[159] Thomson WT. Transmission of Elastic Waves through a Stratified Solid Medium. J Appl Phys 1950;21:89–93. https://doi.org/10.1063/1.1699629.

[160] Kausel E, Roësset JM. Stiffness matrices for layered soils. vol. 71. 1981.

[161] Kausel E. Fundamental Solutions in Elastodynamics: a Compendium. Cambridge: Cambridge University Press; 2006. https://doi.org/10.1017/CBO9780511546112.

[162] Kaynia AM, Madshus C, Zackrisson P. Ground Vibration from High-Speed Trains: Prediction and Countermeasure. J Geotech Geoenvironmental Eng 2000;126:531–7. https://doi.org/10.1061/(ASCE)1090-0241(2000)126:6(531).

[163] Kausel E. Thin-layer method: Formulation in the time domain. Int J Numer Methods Eng 1994;37:927–41. https://doi.org/https://doi.org/10.1002/nme.1620370604.

[164] Kausel E. Wave propagation in anisotropic layered media. Int J Numer Methods Eng 1986;23:1567–78. https://doi.org/10.1002/nme.1620230811.

[165] Schevenels M, François S, Degrande G. EDT: ElastoDynamics Toolbox for MATLAB, manual. K.U.Leuven, Structural Mechanics; 2009.

[166] Dieterman HA, Metrikine A. The equivalent stiffness of a half-space interacting with a beam. Critical velocities of a moving load along the beam. Eur J Mech A/Solids 1996;15:67–90.

[167] Alves Costa PMB. Vibrações do sistema via-maciço induzidas por tráfego ferroviário. Modelação numérica e validação experimental. Universidade do Porto, 2011.

[168] Steenbergen MJMM, Metrikine A V. The effect of the interface conditions on the dynamic response of a beam on a half-space to a moving load. Eur J Mech - A/Solids 2007;26:33–54. https://doi.org/10.1016/j.euromechsol.2006.03.003.

[169] Alves Costa P, Colaço A, Calçada R, Cardoso AS. Critical speed of railway tracks. Detailed and simplified approaches. Transp Geotech 2015;2:30–46. https://doi.org/10.1016/j.trgeo.2014.09.003.

[170] Sheng X, Jones CJC, Thompson DJ. A theoretical model for ground vibration from trains generated by vertical track irregularities. J Sound Vib 2004;272:937–65. https://doi.org/10.1016/S0022-460X(03)00782-X.

[171] Thompson DJ. Wheel-rail Noise Generation, Part I: Introduction And Interaction Model. J Sound Vib 1993;161:387–400. https://doi.org/https://doi.org/10.1006/jsvi.1993.1082.

[172] Pieringer A. Time-domain modelling of high-frequency wheel/rail interaction. Chalmers University of Technology, 2011.

[173] Zhai WM. Two simple fast integration methods for large-scale dynamic problems in engineering. Int J Numer Methods Eng 1996;39:4199–214. https://doi.org/https://doi.org/10.1002/(SICI)1097-0207(19961230)39:24<4199::AID-NME39>3.0.CO;2-Y.

[174] Zhai W, Cai Z. Dynamic interaction between a lumped mass vehicle and a discretely supported continuous rail track. Comput Struct 1997;63:987–97. https://doi.org/https://doi.org/10.1016/S0045-7949(96)00401-4.

[175] Zhang J, Gao Q, Tan SJ, Zhong WX. A precise integration method for solving coupled vehicle–track dynamics with nonlinear wheel–rail contact. J Sound Vib 2012;331:4763–73. https://doi.org/https://doi.org/10.1016/j.jsv.2012.05.033.

[176] Sadeghi J, Khajehdezfuly A, Esmaeili M, Poorveis D. Investigation of rail irregularity effects on wheel/rail dynamic force in slab track: Comparison of two and three dimensional models. J Sound Vib 2015;374:228–44. https://doi.org/https://doi.org/10.1016/j.jsv.2016.03.033.

[177] Nielsen JCO, Abrahamsson TJS. Coupling of physical and modal components for analysis of moving non-linear dynamic systems on general beam structures. Int J Numer Methods Eng 1992;33:1843–59. https://doi.org/10.1002/nme.1620330906.

[178] Lei X, Noda N-A. Analyses of Dynamic Response of Vehicle and Track Coupling System with Random Irregularity of Track Vertical Profile. J Sound Vib 2002;258:147–65. https://doi.org/10.1006/jsvi.2002.5107.

[179] Sheng X, Xiao X, Zhang S. The time domain moving Green function of a railway track and its application to wheel–rail interactions. J Sound Vib 2016;377:133–54. https://doi.org/10.1016/j.jsv.2016.05.011.

[180] Wu TX, Thompson DJ. Theoretical Investigation of Wheel/Rail Non-Linear Interaction due to Roughness Excitation. vol. 34. Southampton, England: 2000. https://doi.org//10.1076/vesd.34.4.261.2060.

[181] Sadeghi J, Khajehdezfuly A, Esmaeili M, Poorveis D. An Efficient Algorithm for Nonlinear Analysis of Vehicle/Track Interaction Problems. Int J Struct Stab Dyn 2016;16:1550040 (20 pages). https://doi.org/https://doi.org/10.1142/S0219455415500406.

[182] Sadeghi J, Khajehdezfuly A, Esmaeili M, Poorveis D. Dynamic Interaction of Vehicle and Discontinuous Slab Track Considering Nonlinear Hertz Contact Model. J Transp Eng 2016;142:04016011. https://doi.org/10.1061/(ASCE)TE.1943-5436.0000823.

[183] Zhong WX, Williams FW. A Precise Time Step Integration Method. Proc Inst Mech Eng Part C J Mech Eng Sci 1994;208:427–30. https://doi.org/https://doi.org/10.1243/PIME_PROC_1994_208_148_02.

[184] Alves Costa P, Calçada R, Silva Cardoso A. Ballast mats for the reduction of railway traffic vibrations. Numerical study. Soil Dyn Earthq Eng 2012;42:137–50. https://doi.org/10.1016/j.soildyn.2012.06.014.

[185] Grassie SL, Gregory RW, Johnson KL. The Behaviour of Railway Wheelsets and Track at High Frequencies of Excitation. J Mech Eng Sci 1982;24:103–11. https://doi.org/https://doi.org/10.1243/JMES_JOUR_1982_024_019_02.

[186] Remington PJ. Wheel/rail noise— Part I: Characterization of the wheel/rail dynamic system. J Sound Vib 1976;46:359–79. https://doi.org/https://doi.org/10.1016/0022-460X(76)90861-0.

[187] Wehbi M, Bezgin NÖ. Proposal and Application of a New Technique to Forecast Railway Track Damage Because of Track Profile Variations. Transp Res Rec J Transp Res Board 2019;2673:568–82. https://doi.org/10.1177/0361198119836973.

[188] Wu T., Thompson DJ. A hybrid model for the noise generation due to railway wheel flats. J Sound Vib 2002;251:115–39. https://doi.org/https://doi.org/10.1006/jsvi.2001.3980.

[189] Pieringer A, Kropp W, Nielsen JCO. The influence of contact modelling on simulated wheel/rail interaction due to wheel flats. Wear 2014;314:273–81. https://doi.org/10.1016/j.wear.2013.12.005.

[190] Thompson DJ. Theoretical Modelling of Wheel-Rail Noise Generation. Proc Inst Mech Eng Part F J Rail Rapid Transit 1991;205:137–49. https://doi.org/10.1243/PIME_PROC_1991_205_227_02.

[191] Thompson DJ, Gautier P-E. Review of research into wheel/rail rolling noise reduction. Proc Inst Mech Eng Part F J Rail Rapid Transit 2006;220:385–408. https://doi.org/10.1243/0954409JRRT79.

[192] Thompson D, Armstrong T, Wu T. Wheel/rail rolling noise - the effects of nonlinearities in the contact zone. 10th Int. Congr. Sound Vib. ICSV2003, Stockholm, Sweden: 2003.

[193] Johnson KL. Normal contact of elastic solids – Hertz theory. Contact Mech., Cambridge University Press; 1985, p. 84–106. https://doi.org/https://doi.org/10.1017/CBO9781139171731.005.

[194] Baeza L, Roda A, Carballeira J, Giner E. Railway Train-Track Dynamics for Wheelflats with Improved Contact Models. Nonlinear Dyn 2006;45:385–397. https://doi.org/10.1007/s11071-005-9014-8.

[195] Kalker JJ. Three-Dimensional Elastic Bodies in Rolling Contact. Springer Netherlands; 1990. https://doi.org/10.1007/978-94-015-7889-9.

[196] Johnson KL. Non-Hertzian normal contact of elastic bodies. Contact Mech., Cambridge University Press; 1985, p. 107–52. https://doi.org/https://doi.org/10.1017/CBO9781139171731.006.

[197] Sun Y, Zhai W, Guo Y. A robust non-Hertzian contact method for wheel–rail normal contact analysis. Veh Syst Dyn 2018;56:1899–921. https://doi.org/https://doi.org/10.1080/00423114.2018.1439587.

[198] Pombo J, Ambrósio J. An alternative method to include track irregularities in railway vehicle dynamic analyses. Nonlinear Dyn 2012;68:161–76. https://doi.org/10.1007/s11071-011-0212-2.

[199] Haigermoser A, Luber B, Rauh J, Gräfe G. Road and track irregularities: measurement, assessment and simulation. Veh Syst Dyn 2015;53:878–957. https://doi.org/10.1080/00423114.2015.1037312.

[200] Karis T, Berg M, Stichel S, Li M, Thomas D, Dirks B. Correlation of track irregularities and vehicle responses based on measured data. Veh Syst Dyn 2018;56:967–81. https://doi.org/10.1080/00423114.2017.1403634.

[201] Zhiping Z, Shouhua J. PSD Analysis of Slab Ballastless Track Irregularity of Qinhuangdao-Shenyang Dedicated Passenger Railway Line. 2009 Second Int. Conf. Intell. Comput. Technol. Autom., IEEE; 2009, p. 669–72. https://doi.org/10.1109/ICICTA.2009.627.

[202] Berawi ARB. Improving Railway Track Maintenance Using Power Spectral Density (PSD). Universidade do Porto, 2013.

[203] Grassie SL, Kalousek J. Rail Corrugation: Characteristics, Causes and Treatments. Proc Inst Mech Eng Part F J Rail Rapid Transit 1993;207:57–68. https://doi.org/https://journals.sagepub.com/doi/10.1243/PIME_PROC_1993_207_227_02.

[204] Grassie SL. Rail corrugation: Characteristics, causes, and treatments. Proc Inst Mech Eng Part F J Rail Rapid Transit 2009;223:581–96. https://doi.org/10.1243/09544097JRRT264.

[205] Grassie SL. Rail irregularities, corrugation and acoustic roughness: characteristics, significance and effects of reprofiling. Proc Inst Mech Eng Part F J Rail Rapid Transit 2012;226:542–57. https://doi.org/10.1177/0954409712443492.

[206] Remennikov AM, Kaewunruen S. A review of loading conditions for railway track structures due to train and track vertical interaction. Struct Control Heal Monit 2008;15:207–34. https://doi.org/10.1002/stc.227.

[207] Zhao X, Li Z, Liu J. Wheel–rail impact and the dynamic forces at discrete supports of rails in the presence of singular rail surface defects. Proc Inst

Mech Eng Part F J Rail Rapid Transit 2012;226:124–39. https://doi.org/10.1177/0954409711413975.

[208] López-Mendoza D, Connolly DP, Romero A, Kouroussis G, Galvín P. A transfer function method to predict building vibration and its application to railway defects. Constr Build Mater 2020;232:1–16. https://doi.org/https://doi.org/10.1016/j.conbuildmat.2019.117217.

[209] Nielsen JCO, Johansson A. Out-of-round railway wheels-a literature survey. Proc Inst Mech Eng Part F J Rail Rapid Transit 2000;214:79–91. https://doi.org/https://doi.org/10.1243/0954409001531351.

[210] Tao G, Wen Z, Chen G, Luo Y, Jin X. Locomotive wheel polygonisation due to discrete irregularities: simulation and mechanism. Int J Veh Mech Mobil 2020. https://doi.org/https://doi.org/10.1080/00423114.2020.1737148.

[211] Steenbergen MJMM. Wheel-rail interaction at short-wave irregularities. 2008.

[212] Connolly DP, Dong K, Alves Costa P, Soares P, Woodward PK. High speed railway ground dynamics: a multi-model analysis. Int J Rail Transp 2020;8:324–46. https://doi.org/10.1080/23248378.2020.1712267.

[213] Kuhlemeyer RL, Lysmer J. Finite Element Method Accuracy for Wave Propagation Problems. J Soil Mech Found Div 1973;99:421–7. https://doi.org/10.1061/JSFEAQ.0001885.

[214] Shih J-Y. Models of vehicle/track/ground interaction in the time domain. University of Southampton, 2017.

[215] Auersch L. Simple and fast prediction of train-induced track forces, ground and building vibrations. Railw Eng Sci 2020;28:232–50. https://doi.org/10.1007/s40534-020-00218-7.

[216] Auersch L. Train-induced ground vibration due to the irregularities of the soil. Soil Dyn Earthq Eng 2021;140:106438. https://doi.org/10.1016/j.soildyn.2020.106438.

[217] Corbin JC. Statistical Representations of Track Geometry Volume I. Washington, United States: 1980.

[218] Thompson DJ, Kouroussis G, Ntotsios E. Modelling, simulation and evaluation of ground vibration caused by rail vehicles. Veh Syst Dyn 2019;57:936–83. https://doi.org/10.1080/00423114.2019.1602274.

[219] Standard B. BS 6472: 1992, Guide to Evaluation of Human Exposure to Vibration in Buildings (1 Hz to 80 Hz). BSI; 1992.

[220] Fernández Ruiz J, Soares PJ, Alves Costa P, Connolly DP. The effect of tunnel construction on future underground railway vibrations. Soil Dyn Earthq Eng 2019;125. https://doi.org/https://doi.org/10.1016/j.soildyn.2019.105756.

[221] Kouroussis G, Gazetas G, Anastasopoulos I, Conti C, Verlinden O. Discrete modelling of vertical track–soil coupling for vehicle–track dynamics. Soil Dyn Earthq Eng 2011;31:1711–23. https://doi.org/10.1016/j.soildyn.2011.07.007.

[222] Farooq MA, Nimbalkar S, Fatahi B. Three-dimensional finite element analyses of tyre derived aggregates in ballasted and ballastless tracks. Comput Geotech 2021;136:104220. https://doi.org/10.1016/j.compgeo.2021.104220.

[223] Sadri M, Lu T, Steenbergen M. Railway track degradation: The contribution of a spatially variant support stiffness - Local variation. J Sound Vib 2019;455:203–20. https://doi.org/10.1016/j.jsv.2019.05.006.

[224] Sadri M, Lu T, Steenbergen M. Railway track degradation: The contribution of a spatially variant support stiffness - Global variation. J Sound Vib 2020;464:114992. https://doi.org/10.1016/j.jsv.2019.114992.

[225] Gupta S, Degrande G, Chebli H, Clouteau D, Hussein MFM, Hunt HEM. A coupled periodic FE-BE model for ground-borne vibrations from underground railways. III Eur. Conf. Comput. Mech., Lisbon, Portugal: 2006, p. 212–212. https://doi.org/10.1007/1-4020-5370-3_212.

[226] Chebli H, Othman R, Clouteau D, Arnst M, Degrande G. 3D periodic BE–FE model for various transportation structures interacting with soil. Comput Geotech 2008;35:22–32. https://doi.org/10.1016/j.compgeo.2007.03.008.

[227] Hussein MFM. A comparison between the performance of floating-slab track with continuous and discontinuous slabs in reducing vibration from underground railway tunnels. 16th Int. Congr. Sound Vib. Pol., Krakow: 2009.

[228] Forrest JA. Modelling of Ground Vibration from Underground Railways. University of Cambridge, 1999.

[229] Heckl MA. Railway Noise - Can Random Sleeper Spacings Help? Acustica 1995;81:559–64.

[230] Squicciarini G, Toward MGR, Thompson DJ. Experimental procedures for testing the performance of rail dampers. J Sound Vib 2015;359:21–39. https://doi.org/10.1016/j.jsv.2015.07.007.

[231] Heckl MA. Coupled waves on a periodically supported Timoshenko beam. J Sound Vib 2002;252:849–82. https://doi.org/10.1006/jsvi.2001.3823.

[232] Jones CJC, Thompson DJ, Diehl RJ. The use of decay rates to analyse the performance of railway track in rolling noise generation. J Sound Vib 2006;293:485–95. https://doi.org/10.1016/j.jsv.2005.08.060.

[233] Hima BS, Thompson D, Squicciarini G, Ntotsios E, Herron D. Estimation of track decay rates from laboratory measurements on a baseplate fastening system. 13th Int. Work. Railw. Noise, Belgium: 2019, p. 1–8.

[234] Lu S, Xuejun D. Dynamic analysis to infinite beam under a moving line load with uniform velocity. Appl Math Mech 1998;19:367–73. https://doi.org/10.1007/BF02457541.

[235] Moser W, Antes H, Beer G. A Duhamel integral based approach to one-dimensional wave propagation analysis in layered media. Comput Mech 2005;35:115–26. https://doi.org/10.1007/s00466-004-0607-8.

[236] Mace BR, Duhamel D, Brennan MJ, Hinke L. Finite element prediction of wave motion in structural waveguides. J Acoust Soc Am 2005;117:2835–43. https://doi.org/10.1121/1.1887126.

[237] Manconi E, Mace BR. Modelling Wave Propagation in Two-dimensional Structures using a Wave/Finite Element Technique. ISVR Technical Memorandum 966. Southampton, UK: 2007.

[238] Mercer CA, Seavey MC. Prediction of natural frequencies and normal modes of skin-stringer panel rows. J Sound Vib 1967;6:149–62.

https://doi.org/10.1016/0022-460X(67)90167-8.

[239] Netz P. Dynamic Stiffness Method: A Fast Design Tool of High Accuracy. Spacecr Struct Mater Mech Testing, Proc a Eur Conf Held Braunschweig, Ger 4-6 Novemb Paris Eur Sp Agency (ESA), ESA-SP 1999;428:205.

[240] Stephen N. Transfer matrix analysis of the elastostatics of one-dimensional repetitive structures. Proc R Soc A Math Phys Eng Sci 2006;462:2245–70. https://doi.org/10.1098/rspa.2006.1669.

[241] Poole D. Linear Algebra: A Modern Introduction. Fourth Edi. Brooks Cole; 2014.

[242] Andersen L. Wave Propagation in Infinite Structures and Media. Aalborg University, 2002.

[243] Liu L, Hussein MI. Wave Motion in Periodic Flexural Beams and Characterization of the Transition Between Bragg Scattering and Local Resonance. J Appl Mech 2012;79. https://doi.org/10.1115/1.4004592.

[244] Floquet G. Sur les équations différentielles linéaires à coefficients périodiques. Ann Sci l'École Norm Supérieure 1883;12:47–88. https://doi.org/10.24033/asens.220.

[245] Gupta S, Hussein MFM, Degrande G, Hunt HEM, Clouteau D. A comparison of two numerical models for the prediction of vibrations from underground railway traffic. Soil Dyn Earthq Eng 2007;27:608–24. https://doi.org/10.1016/j.soildyn.2006.12.007.

[246] Chebli H, Clouteau D, Modaressi A. Three-dimensional periodic model for the simulation of vibrations induced by high speed trains. Riv Ital DI Geotec 2004;4:26–31.

[247] Clouteau D, Elhabre ML, Aubry D. Periodic BEM and FEM-BEM coupling. Comput Mech 2000;25:567–77. https://doi.org/10.1007/s004660050504.

[248] Chebli H, Othman R, Clouteau D. Response of periodic structures due to moving loads. Comptes Rendus Mécanique 2006;334:347–52. https://doi.org/10.1016/j.crme.2006.04.001.

[249] Clouteau D, Arnst M, Al-Hussaini TM, Degrande G. Freefield vibrations due to dynamic loading on a tunnel embedded in a stratified medium. J Sound Vib 2005;283:173–99. https://doi.org/10.1016/j.jsv.2004.04.010.

[250] Mead DJ. Free wave propagation in periodically supported, infinite beams. J Sound Vib 1970;11:181–97. https://doi.org/https://doi.org/10.1016/S0022-460X(70)80062-1.

[251] Mead DJ. Wave propagation and natural modes in periodic systems II. Multi-coupled systems, with and without damping. J Sound Vib 1975;40:19–39. https://doi.org/https://doi.org/10.1016/S0022-460X(75)80228-8.

[252] Mead DJ. The forced vibration of one-dimensional multi-coupled periodic structures: An application to finite element analysis. J Sound Vib 2009;319:282–304. https://doi.org/10.1016/j.jsv.2008.05.026.

[253] Thompson DJ. Wheel-rail Noise Generation, Part III: Rail Vibration. J Sound Vib 1993;161:421–46. https://doi.org/10.1006/jsvi.1993.1084.

[254] Germonpré M. The effect of parametric excitation on the prediction of railway

induced vibration in the built environment. Katholieke Universiteit te Leuven, 2018.

[255] Liu W, Du L, Liu W, Thompson DJ. Dynamic response of a curved railway track subjected to harmonic loads based on the periodic structure theory. Proc Inst Mech Eng Part F J Rail Rapid Transit 2018;232:1932–50. https://doi.org/10.1177/0954409718754470.

[256] Castanheira-Pinto A, Colaço A, Ruiz JF, Alves Costa P, Godinho L. Simplified approach for ground reinforcement design to enhance critical speed. Soil Dyn Earthq Eng 2022;153:107078. https://doi.org/10.1016/j.soildyn.2021.107078.

[257] Johnson SG. Notes on Perfectly Matched Layers (PMLs). ArXiv 2021;abs/2108.0:1–16. https://doi.org/10969193.

[258] Basu U. Explicit finite element perfectly matched layer for transient three-dimensional elastic waves. Int J Numer Methods Eng 2009;77:151–76. https://doi.org/10.1002/nme.2397.

[259] Basu U, Chopra AK. Perfectly matched layers for time-harmonic elastodynamics of unbounded domains: theory and finite-element implementation. Comput Methods Appl Mech Eng 2003;192:1337–75. https://doi.org/10.1016/S0045-7825(02)00642-4.

[260] Lopes P, Alves-Costa P, Calçada R, Silva Cardoso A. Numerical modeling of vibrations induced in tunnels: A 2.5D FEM-PML approach. Traffic Induc. Environ. Vib. Control. Theory Appl., 2013, p. 133–66.

[261] François S, Schevenels M, Lombaert G, Degrande G. A 2.5D displacement-based PML for elastodynamic wave propagation. Comput Mech 2010:2–3.

[262] Lopes P, Alves Costa P, Ferraz M, Calçada R, Cardoso AS. Numerical modeling of vibrations induced by railway traffic in tunnels: From the source to the nearby buildings. Soil Dyn Earthq Eng 2014;61–62:269–85. https://doi.org/10.1016/j.soildyn.2014.02.013.

[263] Dahlberg T. Track issues. In: Iwnicki S, editor. Handb. Railw. Veh. Dyn. 2nd ed., 2006, p. 552. https://doi.org/https://doi.org/10.1201/9781420004892.

[264] Zeng Y, Shen C, Núñez A, Dollevoet R, Zhang W, Li Z. An Interpretable Method for Operational Modal Analysis in Time-Frequency Representation and Its Applications to Railway Sleepers. Struct Control Heal Monit 2023;2023:1–26. https://doi.org/10.1155/2023/6420772.

[265] Shen C, Dollevoet R, Li Z. Fast and robust identification of railway track stiffness from simple field measurement. Mech Syst Signal Process 2021;152:107431. https://doi.org/10.1016/j.ymssp.2020.107431.

[266] Berggren EG, Jahlénius Å, Bengtsson B-E. Continuous Track Stiffness Measurement: An Effective Method to Investigate the Structural Conditions of the Track. 5th Int. Conf. Railw. Eng., Edinburgh: Engineering Technics Press; 2002.

[267] Wangqing W, Geming Z, Kaiming Z, Lin L. Development of Inspection Car for Measuring Railway Track Elasticity. 6th Int. Heavy Haul Conf., Cape Town: 1997.

[268] The MathWorks I. MATLAB and Statistics Toolbox 2020.

[269] EUROPEAN COMMITTEE FOR STANDARDIZATION. BS EN 13674-1, Railway applications. Track. Rail Vignole railway rails 46 kg/m and above. British Standards Institution; n.d.

[270] Çati Y, Gökçeli S, Anil Ö, Korkmaz CS. Experimental and numerical investigation of usp for optimization of transition zone of railway. Eng Struct 2020;209:109971. https://doi.org/10.1016/j.engstruct.2019.109971.

[271] Qu X, Ma M, Li M, Cao Y, Liu W. Analysis of the Vibration Mitigation Characteristics of the Ballasted Ladder Track with Elastic Elements. Sustainability 2019;11:6780. https://doi.org/10.3390/su11236780.

[272] Ntotsios E, Thompson DJ, Hussein MFM. A comparison of ground vibration due to ballasted and slab tracks. Transp Geotech 2019;21:100256. https://doi.org/10.1016/j.trgeo.2019.100256.

[273] Sadri M, Steenbergen M. Effects of railway track design on the expected degradation: Parametric study on energy dissipation. J Sound Vib 2018;419:281–301. https://doi.org/10.1016/j.jsv.2018.01.029.

[274] Naeimi M, Li Z, Petrov RH, Sietsma J, Dollevoet R. Development of a New Downscale Setup for Wheel-Rail Contact Experiments under Impact Loading Conditions. Exp Tech 2018;42:1–17. https://doi.org/10.1007/s40799-017-0216-z.

[275] Nguyen K, Goicolea J, Galbadón F. Comparison of dynamic effects of high-speed traffic load on ballasted track using a simplified two-dimensional and full three-dimensional model. Proc Inst Mech Eng Part F J Rail Rapid Transit 2014;228:128–42. https://doi.org/10.1177/0954409712465710.

[276] Li L, Nimbalkar S, Zhong R. Finite element model of ballasted railway with infinite boundaries considering effects of moving train loads and Rayleigh waves. Soil Dyn Earthq Eng 2018;114:147–53. https://doi.org/10.1016/j.soildyn.2018.06.033.

[277] Othman MIH, Abdul Wahab AM, Hadi MS, Mohamad Noor N. Assessing the nonlinear static stiffness of rail pad using finite element method. J Vibroengineering 2022;24:921–35. https://doi.org/10.21595/jve.2022.22293.

[278] Wei K, Liu Z, Liang Y, Wang P. An investigation into the effect of temperature-dependent stiffness of rail pads on vehicle-track coupled vibrations. Proc Inst Mech Eng Part F J Rail Rapid Transit 2017;231:444–54. https://doi.org/10.1177/0954409716631786.

[279] Plastics Pipe Institute. HDPE & Propylene Materials. Poisson. High-density Polyethyl. or Polyethyl. high-density, n.d.

[280] Ferdous W, Manalo A, Muttashar M, Yu P, Kakarla R, Salih C, et al. Composites for Alternative Railway Sleepers. 16th East Asia-Pacific Conf. Struct. Eng. Constr., 2019, p. 267–76. https://doi.org/10.1007/978-981-15-8079-6_26.

[281] Ferdous W, Manalo A, Van Erp G, Aravinthan T, Kaewunruen S, Remennikov A. Composite railway sleepers – Recent developments, challenges and future prospects. Compos Struct 2015;134:158–68. https://doi.org/10.1016/j.compstruct.2015.08.058.

[282] Witt S. The Influence of Under Sleeper Pads on Railway Track Dynamics. Linköping university institute of technology, 2008.

[283] Safari Baghsorkhi M, Laryea S, McDowell G, Thom N. An investigation of railway sleeper sections and under sleeper pads using a box test apparatus. Proc Inst Mech Eng Part F J Rail Rapid Transit 2016;230:1722–34. https://doi.org/10.1177/0954409715613818.

[284] Abadi T, Le Pen L, Zervos A, Powrie W. Measuring the Area and Number of Ballast Particle Contacts at Sleeper-Ballast and Ballast-Subgrade Interfaces. Int J Railw Technol 2015;4:45–72. https://doi.org/10.4203/ijrt.4.2.3.

[285] Ferreira TM, Teixeira PF. Rail Track Performance with Different Subballast Solutions: Traffic and Environmental Effects on Subgrade Service Life. J Transp Eng 2012;138:1541–50. https://doi.org/10.1061/(ASCE)TE.1943-5436.0000470.

[286] Grossoni I, Hawksbee S, Jorge P, Bezin Y, Magalhaes H. Prediction of track settlement at high-speed railway transitions between embankment and bridge in the proximity of a turnout. Transp Geotech 2022;37:100879. https://doi.org/10.1016/j.trgeo.2022.100879.

Other Activities

My research period involved multiple activities, including participating in railway engineering international conferences and the Derby Railway Engineering Society Peter Parking competition. Details of these activities are provided below.

Activity No. 1

Details:	**A.C. Lamprea-Pineda**, C. Charoenwong, P. Chumyen, D.P. Connolly, P. K. Woodward, and P. Alves-Costa, 'Track-ground coupling techniques for the analysis of railway track vibrations'.
Type of Activity:	Conference participation
Activity:	ICSV27 – 27th International Congress on Sound and Vibration. The annual congress of the International Institute of Acoustic and Vibration (IIAV).
Type of Presentation:	Virtual presentation
Presenter:	A.C. Lamprea-Pineda
Date:	11-16 July 2021
Location:	-

Activity No. 2

Details:	**A.C. Lamprea-Pineda**, D.P. Connolly, P.K. Woodward, M.F.M. Hussein, and P. Alves-Costa, 'Semi-analytical study of train induced ground borne-vibrations effects'.
Type of Activity:	Conference participation
Activity:	ICSV28 – 28th International Congress on Sound and Vibration. The annual congress of the International Institute of Acoustic and Vibration (IIAV).
Type of Presentation:	Virtual presentation
Presenter:	A.C. Lamprea-Pineda
Date:	04-05 August 2022
Location:	-

Activity No. 3

Details:	**A.C. Lamprea-Pineda**, D. P. Connolly, M.F.M. Hussein, P. Alves-Costa, and P. K. Woodward, 'Modelling the Critical Speed Amplification Effect on Railway Track-Ground Systems'.
Type of Activity:	Conference participation
Activity:	The fifth International Conference on Railway Technology: Research, Development and Maintenance.
Type:	Oral Presentation
Presenter:	A.C. Lamprea-Pineda
Date:	22-25 August 2022
Location:	Montpellier, France

Activity No. 4

Details:	**A. C. Lamprea-Pineda**, A. Castanheira-Pinto, P. Alves-Costa, P. K. Woodward, M. F.M. Hussein, and D. P. Connolly, 'Railway track structural dynamics via periodic approaches'.
Type of Activity:	Conference participation
Activity:	COMPDYN 2023, 9th ECCOMAS Thematic Conference on Computational Methods in Structural Dynamics and Earthquake Engineering.
Type:	Oral Presentation
Presenter:	D. P. Connolly
Date:	12-14 June 2023
Location:	Athens, Greece

Activity No. 5

Details:	**A. C. Lamprea-Pineda**, 'Railway Track Assessment Via Periodic Approaches'.
Type of Activity:	Lecture Competition
Activity:	Peter Parkin Memorial Lecture. The Derby Railway Engineering Society (DRES) – **Winner**.
Type:	Online Presentation
Presenter:	A.C. Lamprea-Pineda
Date:	8 June 2023
Location:	Derby, UK